ABSTRACT

Title of Dissertation: QUANTIFYING PHOTOLYSIS RATES IN THE TROPOSPHERE AND STRATOSPHERE

William Howard Swartz, Doctor of Philosophy, 2002

Dissertation directed by: Professor Russell R. Dickerson
Department of Meteorology

Solar radiation drives the chemistry and dynamics of the atmosphere. An accurate and precise knowledge of the rates of photochemical reactions throughout the atmosphere is essential to understanding the state of the atmosphere and its future changes (e.g., in photochemical smog, aerosol formation, and stratospheric ozone depletion) on all timescales. This dissertation uses state-of-the-art instruments and radiative transfer models to quantify photolysis rate coefficients (j-values) in the troposphere and stratosphere during recent field campaigns. A UMD chemical actinometer was used to measure j_{NO_2} at the surface during the IPMMI intercomparison. The JHU/APL radiative transfer model was also used to calculate cloud-free j_{NO_2} and j_{O_3} ($\rightarrow O_2 + O(^1D)$, or $j_{O(^1D)}$). Model–spectroradiometer agreement is within 2% for both j_{NO_2} and j_{O_3}, and model–actinometer agreement is within 1% for j_{O_3} and about 14% for j_{NO_2}. Comparisons suggest that currently accepted NO_2 absorption cross sections may be too small.

Treatments of aerosols and the extraterrestrial solar irradiance are shown to have a significant effect on j_{NO_2} and j_{O_3}. During POLARIS, agreement of modeled j_{NO_2} and j_{O_3} with data from a spectroradiometer flown on the NASA ER-2 near 20 km is shown to be within 6% and 1% on average, respectively, depending on the input albedo and overhead ozone. The model is also used to explore the sensitivity of *j*-values to surface height, surface albedo, and ozone column, with the variability in *j*-value measurements related to variations in the geophysical environment. During SOLVE, modeled *j*-values are shown to agree with a spectroradiometer on the NASA DC-8 near 11 km to within 6% for j_{NO_2} and 15% for j_{O_3}, even at solar zenith angles beyond 85°. Intermittent attenuation of measured j_{NO_2} at 11 km of up to 75% is presented, attributed to the optical effects of polar stratospheric clouds (PSCs). Inferred PSCs are shown to have a significant (up to 10%) impact on daily polar vortex–averaged ClOOCl photolysis in late January 2000. PSC attenuation of ClOOCl photolysis is estimated to lead to a maximum reduction in ozone loss of about 2%. Photochemical ozone loss rates in the Arctic during SOLVE are determined by MSX/UVISI satellite stellar occultation measurements combined with diabatic trajectory analyses of airmass subsidence within the polar vortex, with a maximum of $\sim$1 ppmv ozone loss in the lower stratosphere during January 23–March 4, 2000.

QUANTIFYING PHOTOLYSIS RATES IN THE

TROPOSPHERE AND STRATOSPHERE

by

William Howard Swartz

Dissertation submitted to the Faculty of the Graduate School of the
University of Maryland, College Park in partial fulfillment
of the requirements for the degree of
Doctor of Philosophy
2002

Advisory Committee:

Professor Russell R. Dickerson, Chair/Advisor
Professor Millard H. Alexander
Dr. Donald E. Anderson, Jr.
Professor Neil V. Blough
Professor Robert D. Hudson
Dr. Steven A. Lloyd
Professor John M. Ondov

PREFACE

This dissertation focuses on the quantification of photolysis, or photodissociation, rates in the atmosphere, from Earth's surface to about 25 km in the lower stratosphere. The photolysis rates discussed have been measured at the surface, in the stratosphere with aircraft instruments, and remotely from space, as well as calculated by radiative transfer models. The investigation focuses on measured and modeled photolysis rate coefficients (*j*-values) from three field campaigns: (1) the International Photolysis Frequency Measurement and Modeling Intercomparison (IPMMI), conducted near Boulder, Colorado, June 1998, (2) the Photochemistry of Ozone Loss in the Arctic Region in Summer (POLARIS) mission, based in Fairbanks, Alaska, April–September 1997, and (3) the SAGE III Ozone Loss and Validation Experiment (SOLVE), based in Kiruna, Sweden, November 1999–March 2000. Following the introduction (chapter 1), the research has been organized into chapters as follows.

Chapter 2 presents results from IPMMI, a blind intercomparison of coincident measurements of *j*-values made at the relatively rural Marshall Field Site of the National Center for Atmospheric Research (NCAR), near Boulder, Colorado, under well-characterized conditions. Of central interest are measurements of the photolysis rate coefficient for NO_2, j_{NO_2}, made with a chemical actinometer developed in the Dickerson air chemistry laboratory at the University of Maryland, College Park. The results are compared with an NCAR j_{NO_2} actinometer, as well as a number of spectroradiometers from around the world. The measurements are also compared with j_{NO_2} calculated by roughly a dozen models, including the JHU/APL radiative transfer model. While the IPMMI findings suggest that, at least under clear-sky conditions, measurements and models of j_{NO_2} are in good agreement, there is also evidence that the larger *Harder et al.* [1997] NO_2 cross sections are more consistent with the actinometric data than those recommended in the Jet Propulsion Laboratory (JPL) compilations of molecular data [e.g., *DeMore et al.*, 1997]. Comparison of APL model actinic flux calculations with spectroradiometer measurements prompted a change in the extraterrestrial flux used in the model, benefitting later calculations during SOLVE. The impacts of aerosols on j_{NO_2} and j_{O_3} ($\rightarrow O_2 + O(^1D)$) are also probed. These and other results from the international effort have been presented at a number of conferences and have been submitted as a series of papers in a special issue to the *Journal of Geophysical Research—Atmospheres (JGR)* by *Cantrell et al.* [2002] (IPMMI overview), *Bais et al.* [2002] (actinic flux), *Shetter et al.* [2002] (j_{NO_2}), and *Hofzumahaus et al.* [2002] (j_{O_3}).

In chapter 3, the theoretical sensitivity of j_{NO_2} and j_{O_3} to the geophysical environment (e.g., ozone profile, surface reflectivity, cloud top height) in the lower stratosphere during POLARIS is examined with the APL model. The model is also applied along the flight tracks of the NASA high-altitude ER-2 research aircraft, flown from Fairbanks, Alaska. The calculated flight track *j*-values are then compared with those derived from Environment Canada's Composition and Photodissociative Flux Spectroradiometer on board the ER-2. Much of the variability in the *j*-values can be attributed to geophysical variability. This sensitivity study appeared in the *JGR* POLARIS special issue ("A Sensitivity Study of Photolysis Rate Coefficients during POLARIS" [*Swartz et al.*, 1999]).

Three related SOLVE projects constitute chapters 4–6. SOLVE posed a challenge to the measurement and modeling of *j*-values, owing to the large solar zenith angles (SZAs) encountered during polar twilight. As shown in chapter 4, the APL model, already improved following the findings of IPMMI (chapter 2), was further enhanced by utilizing input data from a number of climatological, in situ, and remotely sensed datasets. Along–flight track *j*-value calculations are presented for the NASA DC-8 aircraft (see appendix E for ER-2 calculations), which flew from Kiruna, Sweden. Model comparisons with DC-8 *j*-value measurements made by NCAR's Scanning Actinic Flux Spectroradiometer (SAFS) are in good agreement, despite the large SZAs. The comparison of particular flights also provides a compelling suggestion of the optical effects of polar stratospheric clouds (PSCs) on *j*-values. This model–SAFS comparison will ultimately be published, likely in *JGR* (R. E. Shetter et al., manuscript in preparation, 2002).

In chapter 5, photochemical ozone loss is inferred from remote sensing data from the Ultraviolet Imagers and Spectrographic Imagers (UVISI) instrument on board the Midcourse Space Experiment (MSX) satellite. A newly developed stellar occultation technique is used in combination with atmospheric dynamics calculations to infer ozone loss in January, February, and March 2000 during SOLVE. This work represents the first science application of space-based stellar occultation to probe Earth's atmosphere, a technique that could be used to study long-term ozone trends. The ozone loss rates determined are later used in chapter 6 as the basis for an estimation of the absolute impact of PSC optical effects on photolysis and ozone loss during SOLVE. The stellar occultation determination of ozone loss appeared in the *JGR* SOLVE special issue ("Photochemical Ozone Loss in the Arctic as Determined by MSX/UVISI Stellar Occultation Observations during the 1999/2000 Winter" [*Swartz et al.*, 2002]).

PSCs were prevalent during the 1999/2000 winter studied by SOLVE. While the heterogeneous chemistry occurring on PSCs is well understood, the impact of the optical effects of PSCs, which attenuate the weak actinic flux in polar twilight, on photolysis and ozone loss is only poorly understood. The high-SZA observations of SOLVE in the Arctic lower stratosphere provided a unique dataset for studying the optical effects of PSCs on photolysis. In chapter 6, the impact of PSCs on actinic flux and *j*-values during SOLVE is investigated in a preliminary study by comparing SAFS in situ measurements of *j*-values with clear-sky model calculations. From these comparisons, empirical relationships of PSC attenuation of *j*-values with temperature, light path, and the local radiative transfer environment are developed, allowing for estimates of the PSC effect on j_{ClOOCl} (and thus ozone loss) throughout the lower stratosphere, combining results of chapters 4 and 5.

Chapter 1 contains general introductory material, including the atmospheric chemical context of photodissociation, definitions of radiometric terms used throughout this work, a physical basis for understanding radiative transfer, and a brief overview of IPMMI, POLARIS, and SOLVE. Final concluding remarks are in chapter 7.

Several appendices contain supplemental information. A detailed description of the APL radiative transfer model, including its inputs, is in appendix A. Ancillary material from IPMMI, POLARIS, and SOLVE, including flight track maps, are in appendices B–D, respectively. Extensive model–model and model–measurement comparisons of *j*-values from SOLVE (including the ER-2 flights) are reported in appendix E. Appendix F contains definitions and descriptions of meteorological terminology that is employed, primarily in chapters 5 and 6. Finally, a “photolysis atlas” of 76 wavelength-dependent *j*-values over 0–40 km calculated with the APL model appears in appendix G.

The author has also collaborated on a number of other, related publications as co-author (or principal author), providing modeling calculations and analyses not specifically reported in this dissertation. From the POLARIS campaign, modeled j_{NO_2} was extensively compared with that inferred from trace gas measurements made aboard the ER-2 (see "Comparison of Modeled and Observed Values of NO_2 and j_{NO_2} during the Photochemistry of Ozone Loss in the Arctic Region in Summer (POLARIS) Mission" [*Del Negro et al.*, 1999]). APL model *j*-values were also utilized to test our ability to model j_{NO_2} near sunset (see "J_{NO_2} at High Solar Zenith Angles in the Lower Stratosphere" [*Gao et al.*, 2001]), to postulate unknown HO_x sources (see "Twilight Observations Suggest Unknown Sources of HO_x" [*Wennberg et al.*, 1999]), and to study ozone photochemistry (see "Ozone Destruction and Production Rates between Spring and Autumn in the Arctic Stratosphere" [*Fahey et al.*, 2000]) during POLARIS. In advance of the SOLVE campaign, several potential flight bases were considered, leading to the selection of Kiruna, Sweden (see "SOLVE Flight Base Analysis" [*Swartz and Newman*, 1998]). Finally, APL model calculations were employed to test the new POAM III O_3–PV reconstructions utilized during SOLVE (see chapter 4; "Reconstruction of Three-Dimensional Ozone Fields using POAM III during SOLVE" [*Randall et al.*, 2002]).

DEDICATION

To the Family

ACKNOWLEDGMENTS

While this dissertation is my own work, there are many who have materially made this research possible. From Russ's group, I thank Shobha Kondragunta (now at NOAA/NESDIS) and Kristen Hallock-Waters (now at Stockton College) for lending their field experience in connection with IPMMI. I am also truly indebted to Jeff Stehr for his above-and-beyond-the-call assistance in readying my j_{NO_2} actinometer for the field. My participation in IPMMI would not have been possible without his willing sacrifice of two weeks of his time before the campaign. I appreciate the use of a microbalance in Neil Blough's lab for measuring mass loss from my NO_2 permeation tube. Rick Shetter (NCAR) and his group graciously met all of my on-the-ground instrument needs at IPMMI (e.g., several bulkhead fittings, an NO calibration standard, use of a flow meter)—a life-saver. Post-IPMMI, Tom Ryerson (NOAA/Aeronomy Laboratory) very generously offered to make a calibration measurement of my NO_2 permeation tube emission rate after the campaign and then shipped my instrument back for me(!). Thanks also to Sasha Madronich (NCAR) for his TUV model calculations of the downwelling contribution to the radiation field so I could test my downwelling approximation using the APL model. In addition to the j_{NO_2} measurements I personally made during the campaign, I am grateful for the j-value data collected by Rick and the other IPMMI participants, along with their model calculations, supplementing my own to make a compelling story.

My POLARIS analysis relied in part on Tom McElroy's (Environment Canada) ER-2 CPFM spectroradiometer data. Tom is always very willing to lend support in the analysis of his data. And he and his group are always fun to go to dinner with.

Tom Kusterer (JHU/APL) worked diligently to adapt the APL radiative transfer model for POLARIS and SOLVE, including coding many of the modifications I envisioned for the latter campaign. Tom's intellectual input in addition to his programming prowess has greatly improved the model. As inputs to the APL model, Stacey Hollandsworth Frith and Gordon Labow (both at NASA/Goddard) developed a set of ozone/pressure/temperature climatologies for when all else failed. In addition, Karl Hoppel (Naval Research Laboratory) and Cora Randall (LASP, University if Colorado) generated daily ozone fields during SOLVE based on POAM III satellite O_3–PV reconstructions, for my own nearly exclusive personal use. Finally, Rick Shetter provided the measurement part of the model–measurement comparison with DC-8 SAFS spectroradiometer data during SOLVE.

The MSX/UVISI stellar occultation retrievals were provided by Ron Vervack, Bob DeMajistre, and Sam Yee, with the help of Frank Morgan, Gerry Romick, and Steve Lloyd (all at JHU/APL). These ozone profiles, combined with custom-made diabatic trajectory calculations by Paul Newman (NASA/Goddard), made the calculation of photochemical ozone loss during SOLVE possible.

Special thanks goes to the mission scientists, pilots, and flight crew of the POLARIS and SOLVE missions. As a mere theory team member during SOLVE, I was given a coveted empty seat on the SOLVE January 25, 2000 DC-8 flight, one of the best for encounters with PSCs. I first had the idea of investigating the impact of PSCs on j-values while gazing at them out my window.

In connection with my data analyses, I thank Chris Chase (JHU/APL, now at AT&T)

for helping me make better use of Interactive Data Language (IDL) and Emacs. I have also benefitted from the occasional IDL function liberated from the NASA/Goddard Atmospheric Chemistry and Dynamics Branch IDL library, rather than re-inventing the wheel, for which I am very grateful.

Now, at the academic level, I greatly appreciate my research advisor, Prof. Russ Dickerson, for providing me with a tremendous opportunity to develop in the field of atmospheric science while nourishing my roots in traditional chemistry. Working with him in this confluence of chemistry, physics, and meteorology has shown me the truth of Norbert Wiener's statement, "The most fruitful areas for growth of the sciences are those between established fields." Russ displayed a remarkable confidence in me and my skills encouraging me to take the plunge and run with the best during IPMMI. That support has never waned. Russ has been an excellent mentor and advocate, and I look forward to a lifelong association with him and his work. I have also enjoyed my scientific and personal association with the members of the Dickerson Group (and larger research family).

I further thank the other members of my dissertation committee from the University of Maryland who have given their time, encouragement, and advice to improve the quality of my work: Profs. Neil Blough, John Ondov, and Millard Alexander, from the Department of Chemistry and Biochemistry, and Prof. Bob Hudson from the Department of Meteorology.

There are also several individuals at APL who have made this work possible. My thanks of course goes to Don Anderson (now at NASA/Headquarters) for taking a chance on an organic chemist. To say that Don has vision would be quite an understatement. I hope I've put his radiative transfer model to good use. And I will never forget that "Before there was multiple scattering, there was single scattering" (or his occasional

2×4s!). I also thank colleague and mini-advisor Steve Lloyd for taking me under his wing and allowing me into the ER-2 community for my POLARIS and SOLVE work. His encouragement along the way has made this dissertation possible. I thank Don and Steve for being willing to serve on my committee, as well. In the post-Don era, Sam Yee has given me great opportunities for interesting work, not least of which the chance to do some fun science with stellar occultation data. A special thanks to Xun Zhu for answering my questions about atmospheric dynamics while taking METO 600/610 (it is always nice to have a former Jim Holton student around when studying dynamic meteorology). I cannot forget Ken Potocki, whose suggestion it was, back in 1995, to talk to Ray Greenwald, the head of what is now the Atmospheric Remote Sensing Group, and see what opportunities might exist for atmospheric research in the group. That fateful suggestion has indeed borne fruit. APL (in general, and specifically the SRA Group) should be commended for its commitment to education in allowing me the flexibility required to pursue my doctorate at UMCP.

I have had great opportunities to work with a number of exceptional atmospheric scientists at the NASA/Goddard Space Flight Center. I owe special thanks to Paul Newman, Randy Kawa, and Anne Thompson. I have had the privilege of working with Paul in the field during both POLARIS and SOLVE, and in some of the planning and data analysis for the SOLVE campaign. I thank Randy for allowing me to spend several months on-site at Goddard, helping me learn how to use the Goddard trajectory chemistry model. And though I have only nibbled around the edges of a bona fide scientific collaboration with Anne, she has been a long and steady source of encouragement and friendship.

IPMMI also provided a great opportunity to work with the NCAR crowd in addition to Rick Shetter, including Chris Cantrell, Jack Calvert (now retired), and Sasha

Madronich. There I also got to know Jim Crawford (NASA/Langley), whose path I have crossed several times now.

As for the dissertation itself, the UMCP dissertation LaTeX class file created by those who have gone before me has, with only a few minor improvements, made my job a lot easier. I cannot imagine a more rational way to produce a technical dissertation. I thank Ron Vervack for Figure 5.1. And I am very grateful to my principal proof-readers. Steve took the earliest, roughest versions of this dissertation to task, something I wouldn't wish on anyone. Russ's and Sam's comments have helped me add more sizzle to the steak.

I also thank those agencies and program managers supporting me over the last seven years. The majority of the research in this dissertation was funded by the Atmospheric Chemistry Modeling and Analysis Program (ACMAP) and the Upper Atmosphere Research Program (UARP), both part of NASA's Office of Earth Science, with additional funding of my IPMMI measurements from the NSF-funded Center the Clouds, Chemistry and Climate. My research and I have also received support directly and indirectly from NASA's Atmospheric Effects of Aviation Project (AEAP), NOAA's Office of Global Programs, the DoD, and several APL internal projects.

My gratitude and thanks also extend to previous chapters in my chemistry career. I sincerely thank my former research advisors as well. At Harvard, Prof. Dave Evans for nearly three years taught me many principles of organic chemistry, which have enriched my potential as an atmospheric chemist. Though I ultimately found a greater passion for a field other than organic synthesis, I think some of my greatest lessons in chemistry (*and life!*) so far were learned while in the Evans Group.

The genesis of my graduate career occurred when UM's Prof. Pat Mariano (who, with his wife Prof. Debra Dunaway-Mariano, is now at the University of New Mexico), near the end of my first semester in sophomore organic chemistry, offered me the chance to work in his lab. For the next two and half years I shared in the research of Profs. Mariano's and Dunaway-Mariano's labs in both organic and biochemistry. The opening of so many doors of opportunity before me in chemistry can be traced to their generosity. I also thank Prof. Mariano for his parting admonition in the summer of 1991, prior to heading for Cambridge, Massachusetts, to *Work hard. Don't get discouraged.* This has proved invaluable advice.

"With the development of the science of chemistry, ... there has arisen a considerable body of general principles which can serve as the basis for deduction, and the profound change in the character of chemical research during the last generation bears witness to the development of the [modern] type of scientist, the one who seeks causes, and aims to develop means for predicting and controlling phenomena" [*Hildebrand*, 1919, p. vii]. My ultimate gratitude will always go to my family, especially my wife, Brecken. Any accomplishments of mine have, in the Family, been many years in the making, with much love and support.

TABLE OF CONTENTS

LIST OF TABLES

LIST OF FIGURES

Chapter 1

Introduction

1.1 Atmospheric Chemistry Background

To understand the influence of human activities on our environment, it is essential to understand both the natural and anthropogenic sources, cycles, and sinks of trace gases and particles in the atmosphere. Ozone, O_3, plays a central role in atmospheric chemistry by regulating conditions in the biosphere that make life on Earth possible. Ninety percent of the ozone in the atmosphere resides in the stratosphere in a layer between roughly 15 and 30 km, absorbing effectively all solar radiation between 240 and 290 nm at the surface, thus shielding living organisms from harmful ultraviolet radiation. Stratospheric ozone, which releases absorbed sunlight as thermal energy, produces the stable thermal structure of the stratosphere and hence has a profound influence on atmospheric dynamics. In contrast, ozone in the underlying troposphere plays a deleterious role as an oxidizing agent, negatively impacting the health of humans, other animals, and plant life. Its large infrared absorption cross section also makes ozone an important greenhouse gas with a significant impact on global climate. A principal focus and motivation for the study of atmospheric chemistry is the abundance of ozone and the forces controlling its production, cycling, and distribution.

It had long been assumed that, due to its large volume, Earth's atmosphere would be impervious to any significant change caused by human activities. During the latter half of the twentieth century, however, this assumption was shown to be wrong. Near the Earth's surface, we have learned how hydrocarbons and nitrogen oxides (e.g., NO_x = NO + NO_2) from fossil fuel combustion can lead to dangerously high levels of tropospheric ozone, or "photochemical smog." NO and NO_2 are two of the most important trace species in atmospheric chemistry and are intimately related to ozone production and loss. Anthropogenic emissions account for approximately three quarters of the estimated annual global emissions of NO_x over the last decade of the twentieth century [*Seinfeld and Pandis*, 1998]. Fossil fuel combustion alone accounts for half of the total source and is increasing. Aircraft emissions make up a relatively small part of the total, but occur in the upper troposphere, a climate-sensitive region of the atmosphere.

While tropospheric ozone has been increasing, statistically significant loss of stratospheric ozone of several percent has been observed with ground- and space-based instruments at mid- and high-latitudes in both the Northern and Southern Hemispheres during all seasons since 1970 (up to 50% loss at the South Pole in austral spring). There has been significant elucidation of the mechanisms of stratospheric ozone depletion, due to the emissions of CFCs and other chemicals used in industry and agriculture.

1.1.1 Motivation for the Study of Photochemistry

Solar radiation is vital for the regulation of the atmosphere's structure and composition. The absorption of radiation by the atmosphere and Earth's surface, which is in near-equilibrium, results in relatively warm surface temperatures, weather, and general atmospheric circulation. The spectral opacity of the atmosphere itself controls the amount of radiation reaching the surface and re-radiating to space. Solar radiation also drives the chemistry of the atmosphere, both directly and indirectly. Trace gases absorb sunlight and dissociate to form energetic species that effect complex chemical processes and have a profound impact on the terrestrial environment.

The most fundamental photochemical processes affecting the troposphere and stratosphere are the photolysis of NO_2 and O_3 and the photochemical process driving the depletion of stratospheric ozone through catalytic cycles. A simplified view of several important chemical cycles is shown in Figure 1.1. The modeling and analysis of atmospheric chemistry requires the accurate determination of photolysis rates controlling the production, cycling, and loss of reactive radicals. The photolysis of NO_2, O_3, and ClOOCl are the key reactions discussed in this dissertation.

1.1.2 NO_2 Photolysis

The photolysis of nitrogen dioxide, NO_2,

$$NO_2 + h\nu \xrightarrow{\lambda < 424\mathrm{nm}} NO + O(^3P), \tag{R1.1}$$

is the main source of atomic O in the troposphere, which directly leads to the production of O_3 via the termolecular reaction

$$O + O_2 \xrightarrow{M} O_3. \tag{R1.2}$$

Oxidation of NO by ozone,

$$NO + O_3 \longrightarrow NO_2 + O_2, \tag{R1.3}$$

to form NO_2, completes a null cycle, (R1.1)–(R1.3). The NO_2 photodissociation rate coefficient, j_{NO_2}, controls the steady-state partitioning of NO_x and ozone [*Leighton*, 1961].

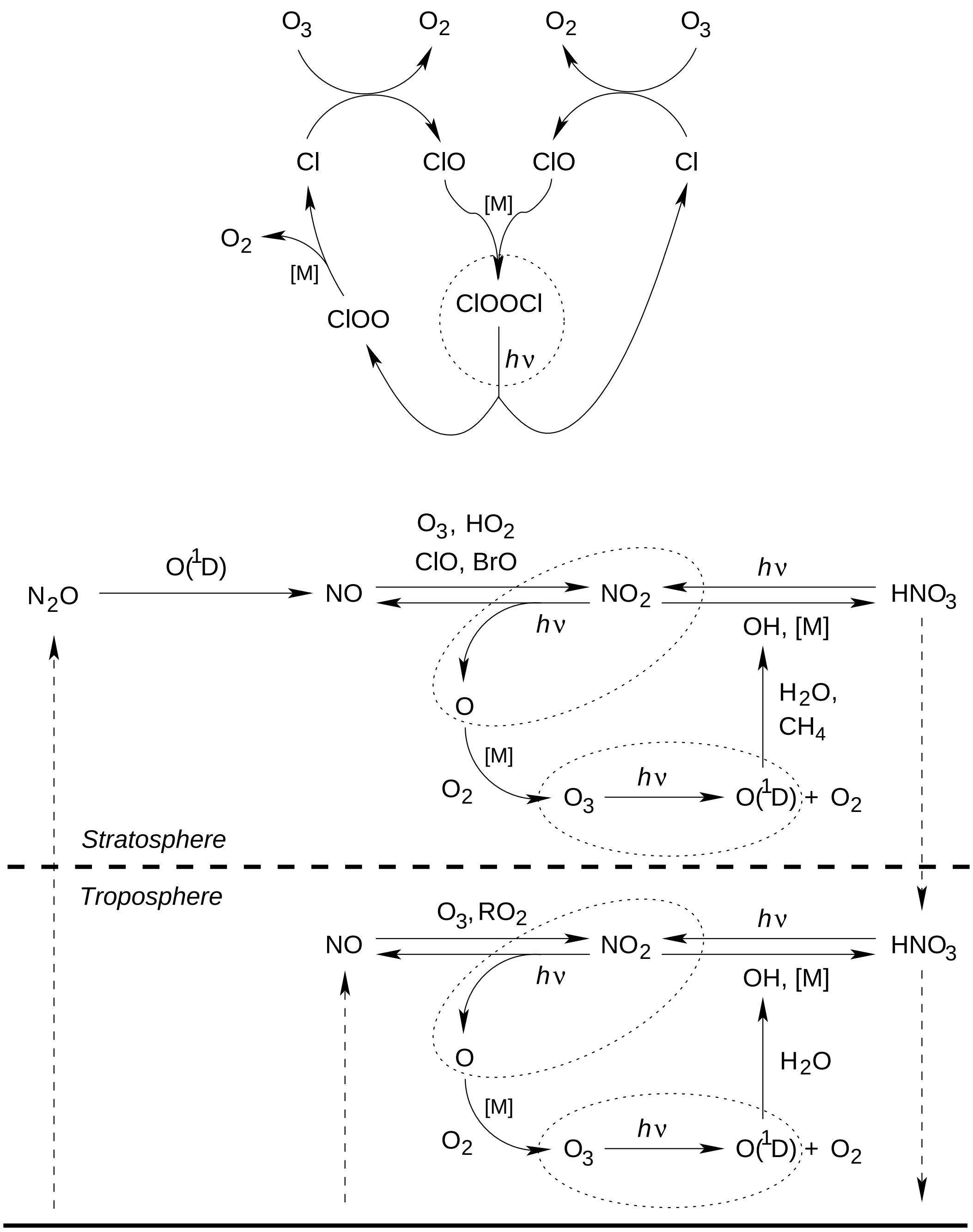

Figure 1.1. Simplified view of important chemical processes in the troposphere and stratosphere. Key photolysis processes are circled.

Under photochemical smog conditions (high concentrations of NO_x and volatile organic compounds, combined with warm temperatures and sunlight), organic compounds are oxidized by O_2 (catalyzed by OH) to form peroxy radicals, which oxidize NO to NO_2 in competition with (R1.3),

$$NO + RO_2 \longrightarrow NO_2 + RO, \tag{R1.4}$$

where R = (H or organic moiety), enhancing ozone concentrations via NO_2 photolysis (R1.1) [*Leighton*, 1961; *Chameides and Walker*, 1973].

1.1.3 O_3 Photolysis

Ozone is an oxidant and source of the oxidizing capacity of the atmosphere. Ozone is photolyzed in the atmosphere, producing both ground-state and electronically excited oxygen atoms:

$$O_3 + h\nu \xrightarrow{\lambda < 730\text{nm}} O_2 + O(^3P) \tag{R1.5a}$$

$$O_3 + h\nu \xrightarrow{\lambda < 345\text{nm}} O_2 + O(^1D). \tag{R1.5b}$$

$O(^1D)$ is the most important electronically excited species in the atmosphere. Its reaction with water vapor,

$$O(^1D) + H_2O \longrightarrow 2\,OH, \tag{R1.6}$$

is the principal source of OH throughout the atmosphere [*Levy*, 1971], which is largely responsible for the cleansing of the atmosphere, reacting with hydrocarbons and other reduced species [*Thompson*, 1992]. $O(^1D)$ reacts with N_2O in the stratosphere as the main source of stratospheric NO_x

$$O(^1D) + N_2O \longrightarrow 2\,NO. \tag{R1.7}$$

1.1.4 Stratospheric Ozone Loss

On the global scale, ozone is photochemically produced mainly in the upper stratosphere at low latitudes and is transported throughout the rest of the stratosphere. Ozone is lost from the stratosphere by natural chemical loss processes, chemical depletion enhanced by anthropogenic emissions, and by transport to the troposphere. Current understanding of the photochemical formation, cycling, and destruction of stratospheric ozone has evolved through several distinct stages, increasing in complexity from a simple oxygen-only mechanism to relatively complicated processes involving heterogeneous reactions and controlled by the temperature and dynamics of the polar stratosphere [*Solomon*, 1999].

Chapman Chemistry

Chapman [1930] first posited an oxygen-only mechanism for the photochemical regulation of ozone in the stratosphere:

$$O_2 + h\nu \longrightarrow 2\,O \tag{R1.8}$$

$$O + O_2 \xrightarrow{M} O_3 \tag{R1.2}$$

$$O_3 + h\nu \longrightarrow O + O_2 \tag{R1.5}$$

$$O + O_3 \longrightarrow 2\,O_2. \tag{R1.9}$$

Reactions (R1.2) and (R1.5), which interchange reactive O (predominantly $O(^3P)$) and O_3, are fast relative to the rest of the cycle. Atomic O and O_3 may be considered collectively as "odd oxygen." Reactions (R1.2) and (R1.5) therefore do not contribute to net production or loss of odd oxygen.

Catalytic Loss Cycles

It was discovered subsequently that the Chapman mechanism alone is not sufficient to explain observed ozone abundance, which over-predicts ozone concentrations. Several *catalytic* ozone loss cycles were proposed based on "odd hydrogen" ($HO_x = OH + HO_2$) [*Bates and Nicolet*, 1950], "odd nitrogen" (NO_x) [*Crutzen*, 1970; *Johnston*, 1971], "odd chlorine" ($ClO_x = Cl + ClO$)[1] [*Stolarski and Cicerone*, 1974], and "odd bromine" ($BrO_x = Br + BrO$) [*Wofsy et al.*, 1975] chemistry. *Molina and Rowland* [1974] correctly identified man-made CFCs as the major source of stratospheric chlorine, which is responsible for the majority of catalytic ozone loss in the lower stratosphere. At the heart of these cycles, reactive radicals destroy odd oxygen by the following couplet:

$$\mathrm{X} + \mathrm{O_3} \longrightarrow \mathrm{XO} + \mathrm{O_2} \qquad \text{(R1.10)}$$

$$\mathrm{XO} + \mathrm{O} \longrightarrow \mathrm{X} + \mathrm{O_2} \qquad \text{(R1.11)}$$

$$[\ \mathit{net}\colon \mathrm{O} + \mathrm{O_3} \longrightarrow 2\,\mathrm{O_2}\ ], \qquad \text{(R1.9)}$$

where X = (H, NO, Cl, or Br), with a net destruction of two odd oxygen molecules. There are several other important reactions that are a part of these cycles (not shown), which connect these reactive species with less-reactive reservoirs and interconnect the HO_x, NO_x, ClO_x, BrO_x, and related cycles (see *Solomon* [1999]).

Heterogeneous Processing

Gas-phase ozone destruction by (R1.10)–(R1.11) alone would predict maximum losses in ozone near 40 km, where O atoms are relatively abundant, higher than where most of the ozone resides. Measurable ozone depletions over the Antarctic (the so-called "ozone

[1] ClO_x now typically includes $2\times ClOOCl$ as well, as a source of ClO.

hole") were first presented by *Chubachi* [1985], documented in the peer-reviewed literature by *Farman et al.* [1985], and confirmed with space-based observations by *Stolarski et al.* [1986]. Elevated ClO within the ozone hole was established with ground-based observations by *de Zafra et al.* [1987, 1989] and with in situ airborne measurements made by *Anderson et al.* [1989]. Subsequent detailed analyses have shown that ozone depletion occurs over the poles in spring, largely confined to altitudes between 12 and 25 km. It is precisely at these altitudes that polar stratospheric clouds (PSCs) exist, which are present over the Antarctic during June–September and over the Arctic during December–March, when temperatures drop below about 200 K [*McCormick et al.*, 1982; *Poole and Pitts*, 1994].

PSC aerosol particles exist in both solid and liquid forms and are composed of nitric acid hydrates, water ice, and mixtures of HNO_3, H_2SO_4, and water, and form when the lower stratosphere is extremely cold, mostly during the several-month-long polar night. *Solomon et al.* [1986] suggested that heterogeneous processes on the surfaces of PSCs activate chlorine from its dominant reservoir forms, HCl and $ClONO_2$,

$$\mathrm{HCl} + \mathrm{ClONO_2} \xrightarrow{\mathrm{PSC}} \mathrm{HNO_{3(s)}} + \mathrm{Cl_{2(g)}}. \tag{R1.12}$$

In the springtime, as the Sun slowly begins to illuminate the polar stratosphere, Cl_2 is photolyzed and ozone depletion is initiated,

$$\mathrm{Cl_2} + h\nu \longrightarrow 2\,\mathrm{Cl} \tag{R1.13}$$

$$2 \times (\mathrm{Cl} + \mathrm{O_3} \longrightarrow \mathrm{ClO} + \mathrm{O_2}). \tag{R1.14}$$

There is insufficient atomic O in the polar lower stratosphere, however, for catalytic ozone loss to propagate via (R1.10)–(R1.11).

ClO Dimer Cycle

Once chlorine has been activated by PSCs in polar winter and ClO_x is produced in early spring, rapid ozone depletion occurs by way of a pathway involving the recycling of ClO via the formation and photolysis of the ClO dimer, ClOOCl [*Molina and Molina*, 1987],

$$ClO + ClO \xrightarrow{M} ClOOCl \quad (R1.15)$$

$$ClOOCl + h\nu \longrightarrow ClOO + Cl \quad (R1.16)$$

$$ClOO \xrightarrow{M} Cl + O_2 \quad (R1.17)$$

$$2 \times (Cl + O_3 \longrightarrow ClO + O_2) \quad (R1.14)$$

$$[\ net\colon 2\,O_3 \longrightarrow 3\,O_2\ ], \quad (R1.18)$$

in the absence of significant concentrations of atomic O. The photolysis of ClOOCl (R1.16) is a key step of the cycle, limiting the overall rate of ozone destruction [*Lloyd*, 1993; *Vömel et al.*, 2001].

Though simplified, the preceding description summarizes many of the key aspects of halogen-catalyzed stratospheric ozone depletion. Other gas-phase and heterogenous processes are also important for ozone depletion, as well as the dynamical conditions of the polar regions (i.e., the polar vortex, which isolates the polar airmass from the rest of the atmosphere [*Schoeberl et al.* [1992]; see appendix F.4]) and gravitational PSC sedimentation, which leads to denitrification of the vortex [*Fahey et al.*, 1990; *Popp et al.*, 2001], inhibiting the deactivation of active chlorine via

$$ClO + NO_2 \xrightarrow{M} ClONO_2 \quad (R1.19)$$

as NO_2 is removed from the gas phase (see [*Solomon*, 1999]).

There is significant inter-annual variability in the degree of ozone depletion in the

Arctic. Improved understanding of the chemical, dynamic, and radiative processes involved is required to more accurately predict future changes (especially recovery) of stratospheric ozone.

1.2 Atmospheric Photochemistry

1.2.1 Definitions of Radiometric Quantities

Any discussion of solar radiation and its transfer (i.e., propagation) in the atmosphere must begin with definitions of the key physical quantities involved. There are a number of excellent introductions to the subject [*Chandrasekhar*, 1960; *Liou*, 1980; *Madronich*, 1987b, 1993; *Seinfeld and Pandis*, 1998; *Finlayson-Pitts and Pitts*, 2000].

The propagation of light may be quantified in terms of the *radiant flux*, which is simply the flux or quantity of light per unit time crossing a surface element, irrespective of direction. *Radiance* or radiant intensity, $I(\theta,\phi)$, is the radiant flux from a beam or "pencil" of light of infinitesimal solid angle Ω from the direction specified by zenith angle θ (angle from local vertical) and azimuth angle ϕ (about a surface in the local frame of reference, such as the Earth's surface). $I(\theta,\phi)$ is measured in units of photons s^{-1} cm^{-2} sr^{-1} (or similarly W cm^{-2} sr $^{-1}$), where sr (steradians) is the unit of solid angle. The sunlight the Earth receives is not monochromatic and neither are any of the radiometric quantities discussed. Thus, we are really concerned with the *spectral* radiance $I_\lambda(\theta,\phi)$ (photons s^{-1} cm^{-2} sr^{-1} nm^{-1}), the subscript λ indicating that radiance in the atmosphere is a function of wavelength. Except for polarization, which is not considered here, radiance gives a complete description of the radiation field at any point in the atmosphere. For simplicity, the subscript λ will be assumed and dropped here.

Another useful quantity, particularly when considering many instruments that measure light, is *irradiance* or vector irradiance, E, which describes the radiant flux received on a flat surface. E is measured in units of photons s^{-1} cm^{-2}. Irradiance on a surface element dS is related to the radiance by integration over all solid angles:

$$E = \int_{\phi} \int_{\theta} I(\theta, \phi) \cos\theta \sin\theta d\theta d\phi, \tag{1.1}$$

where θ is the angle between the light beam and the normal to the surface dS, and ϕ is the azimuth. If the surface is horizontal and near the Earth's surface, the irradiance is sometimes termed the "global" irradiance E_g. If dS were an instrument collecting light with a flat surface parallel to the ground, the (global) irradiance is

$$E_g = \int_0^{2\pi} \int_0^{\frac{\pi}{2}} I(\theta, \phi) \cos\theta \sin\theta d\theta d\phi, \tag{1.2}$$

where the zenith angle is limited to the upper hemisphere.

Irradiance as a function of altitude describes the flow of energy through the atmosphere, but when considering photochemical processes, what we are concerned with precisely is the probability of a molecule encountering a photon. Except in special cases where absorption by the photoreacting molecule is much greater than scattering in the atmosphere and absorption by other molecules, another radiometric quantity is invoked: *actinic flux* (literally meaning capable of causing photochemical reaction) or scalar irradiance, F. A molecule can be thought of as roughly spherical. The actinic flux is the radiant flux from all directions incident onto a spherical volume and is expressed in units of photons s^{-1} cm^{-2}. Actinic flux is related to radiance by

$$F = \int_{\phi} \int_{\theta} I(\theta, \phi) \sin\theta d\theta d\phi = 4\pi\bar{I}, \tag{1.3}$$

where $\bar{I}$ is the mean radiance over all 4π steradians of solid angle. Note that the only difference between actinic flux (1.3) and irradiance (1.1) is the $\cos\theta$ weighting of the radiance. The spherical volume element presents a surface normal to all angles of incidence, hence $\cos\theta = 1$ for all angles.

Table 1.1. Summary of radiometric quantities

Quantity	Symbol	Units	Definition	Alternate Names
radiance	$I(\theta,\phi)$	photons s^{-1} cm^{-2} sr^{-1}		intensity (specific, spectral[a])
irradiance	E	photons s^{-1} cm^{-2}	(1.1)	spectral[a] flux, vector irradiance
actinic flux	F	photons s^{-1} cm^{-2}	(1.3)	scalar irradiance, beam irradiance, actinic irradiance, energy density $\times$ c, fluence rate, mean intensity $\times$ 4π, spherical intensity, flux

[a] nm^{-1}

Ideally, an instrument's optics are designed in such a way as to measure actinic flux directly [e.g., *Hofzumahaus et al.*, 1999; *Shetter and Müller*, 1999], but many are flat-plate detectors and are limited to measuring irradiance. F and E are related, but not identical (see *Cotte et al.* [1997] and *McKenzie et al.* [2002] for techniques to derive approximations of the actinic flux from irradiance measurements).

The literature presents a disconcerting lack of consensus as to the names and even definitions of these radiometric quantities. Table 1.1 summarizes the principal radiometric quantities used throughout this study, along with alternate terminology found in the literature.

1.2.2 Basic Principles of Radiative Transfer

The intensity and spectral distribution of radiation traveling through the atmosphere is modified by three processes: absorption, scattering, and emission. The change in intensity of a pencil of radiation traversing a thickness ds is

$$dI = -knI\,ds + Jn\,ds, \tag{1.4}$$

where k is the extinction coefficient (cm^2) describing light loss due to absorption and scattering and n denotes the number density of molecules or particles (cm^{-3}) at that point in the atmosphere. The term J is referred to as the source function coefficient and represents increases in intensity due to scattering and emission *into* the pencil of light. Eq. (1.4) is the general equation of radiative transfer. Thermal and other forms of emission are insignificant at ultraviolet (UV)/visible wavelengths in the troposphere and stratosphere and will be neglected here.

If the consideration of scattering into the light path is momentarily suspended and only light *attenuation* by absorption and scattering is considered, (1.4) reduces to the familiar Beer–Lambert law

$$I = I_0 e^{-knl}, \tag{1.5}$$

where I_0 is the intensity of light incident on the top of the atmosphere and l is the path length, $\int_x ds$, of the atmosphere along the light path. A homogeneous absorbing/scattering medium reduces light intensity exponentially. We may also define transmissivity $\mathscr{T}$ as

$$\mathscr{T} = I/I_0 = e^{-knl}. \tag{1.6}$$

Another concept that can be gleaned from (1.5) is that of *optical depth* $\tau = knl$, which is often the most effective coordinate for describing radiative transfer in atmospheres. Optical depth describes the largely separable extinctive processes causing the opacity of the atmosphere:

$$\tau = (\tau_{\mathrm{ag}} + \tau_{\mathrm{ap}}) + (\tau_{\mathrm{sg}} + \tau_{\mathrm{sp}}), \tag{1.7}$$

where τ_{ag} and τ_{ap} represent absorption by gases and particles and τ_{sg} and τ_{sp} are the corresponding optical depths due to scattering.

Scattering Processes

The scattering of light by molecules and aerosol particles is a fundamental process in the atmosphere, particularly in the lower atmosphere. Scattering is a physical process by which a particle (molecule or aerosol) continuously extracts energy from incident light and re-radiates that energy, at the same wavelength, in all directions (though not necessarily equally). Thus the atmosphere can be thought of as an ensemble of point sources. Scattering is isotropic if it is independent of direction. Small particles, much smaller than the wavelength of the incident light (e.g., molecules), cause what is known as molecular, or Rayleigh, scattering, which is approximately isotropic. For particles that are similar to λ in size, Mie scattering theory applies. Mie scattering can be highly anisotropic, generally favoring forward or backward scattering relative to the direction of propagation of the light incident on the particle.

In reality, both absorption and scattering processes are important. The *single-scattering albedo*, ω_0, of a particle is the fraction of extincted photons it scatters. The fraction absorbed is thus $1 - \omega_0$. Light in the atmosphere has the opportunity to scatter more than once, a process known as multiple scattering. Photons removed from a pencil of light by scattering may reappear traveling in the same direction as a consequence of multiple scattering.

If the second, $Jnds$ term in the equation of transfer (1.4) were not considered, calculation of the actinic flux at the surface would fall short of the actual light intensity because light scattered from the path of the pencil of light contributes to the radiation field in the form of *diffuse* radiation. Thus, an accurate description of scattering processes is necessary. Eq. (1.3) may be expanded to delineate the direct and diffuse (scattered) components of the radiation field as

$$F = F_0 e^{-\tau} + \int_0^{2\pi} \int_0^{\frac{\pi}{2}} I_{\downarrow}(\theta,\phi) \sin\theta d\theta d\phi + \int_0^{2\pi} \int_{-\frac{\pi}{2}}^{0} I_{\uparrow}(\theta,\phi) \sin\theta d\theta d\phi, \qquad (1.8)$$

where F_0 is the top-of-the-atmosphere solar flux,[2] $F_0 e^{-\tau}$ is the direct, attenuated actinic flux, and $I_{\downarrow}$ and $I_{\uparrow}$ are the downward and upward parts of the diffuse radiation field. The relative contributions of the direct and diffuse components of the radiation field vary with wavelength and atmospheric conditions.

While the direct attenuated flux may be easily treated by the Beer–Lambert Law, scattered flux requires solution of the equation of transfer (1.4). The radiative transfer model (including scattering) used in this study is described in section 1.3 and appendix A.

1.2.3 Photolysis Rate Coefficients: "*j*-Values"

The primary step of any photochemical reaction is the absorption of a photon of light:

$$\mathrm{AB} + h\nu \longrightarrow \mathrm{AB^*}]^{\ddagger}, \qquad \text{(R1.20)}$$

where molecule AB absorbs a photon of light energy E denoted by $h\nu$ and AB* represents an excited state of AB, which may not be stable ($\mathrm{AB^{*\ddagger}}$). The efficiency with which a molecule absorbs light is described by its absorption cross section, σ ($\mathrm{cm^2}$). Excited AB* may collisionally deactivate, thus heating the atmosphere, react directly with another molecule, re-emit radiation by fluorescence or phosphorescence, ionize, or photodissociate. Photodissociation, or photolysis, is what is of most interest here:

$$\mathrm{AB^*}]^{\ddagger} \longrightarrow \mathrm{A} + \mathrm{B}. \qquad \text{(R1.21)}$$

[2]Outside the atmosphere, the actinic flux is equivalent to the solar irradiance: $F_0 = E_0$.

The branching fraction for each primary photochemical process i is the quantum yield, ϕ_i (photons^{-1}), for that process, where $\sum_i \phi_i = 1$. Photodissociation can occur only if $E_{h\nu}$ (combined with excess vibrational/rotational energy already present in AB) exceeds the bond strength of A–B. For many molecules, σ and ϕ are functions of wavelength and temperature T (and pressure).

The enthalpic barriers to many important atmospheric photochemical reactions, namely the bond strengths in photodissociating molecules, correspond roughly to energies at which electronic transitions occur. This energy is provided by solar photons at UV and visible wavelengths. For example, in NO_2, the ON–O bond dissociation energy is about 300 kJ/mol, which corresponds to photons with wavelengths of about 400 nm. Of course, for significant photolysis to occur in the atmosphere, not only must there be photons of sufficient energy, but the wavelength dependence of the molecule's absorption cross section and photolysis quantum yield must also accommodate photolysis.

In the study of atmospheric chemistry, the rate of photodissociation of AB is

$$-\frac{d[\mathrm{AB}]}{dt} = j_{\mathrm{AB}}[\mathrm{AB}], \tag{1.9}$$

where j_{AB} is the first-order photolysis rate coefficient[3] (s^{-1}), which is mathematically equivalent and analogous to the chemical rate coefficient k for a unimolecular decomposition or simple first-order decay process. The "j-value" j_{AB} may be represented as

$$j_{\mathrm{AB}} = \int_{\lambda} F(\lambda,\ldots)\sigma_{\mathrm{AB}}(\lambda,T)\phi_{\mathrm{AB}\to\mathrm{A+B}}(\lambda,T)d\lambda. \tag{1.10}$$

For use in computer models, this may be approximated as the finite sum

$$j_{\mathrm{AB}} \approx \sum_i \overline{F}(\lambda_i,\ldots)\overline{\sigma}_{\mathrm{AB}}(\lambda_i,T)\overline{\phi}_{\mathrm{AB}\to\mathrm{A+B}}(\lambda_i,T)\Delta\lambda_i, \tag{1.11}$$

[3]Photolysis rate coefficient or photolysis *frequency,* but not photolysis rate *constant*.

where the overbars indicate average quantities within wavelength intervals i that span the photolysis wavelength range. The wavelength resolution of approximation (1.11) must be fine enough to adequately sample F_λ, σ_λ, and ϕ_λ, which may vary logarithmically in some wavelength regions, especially the UV-B region (280–320 nm). Errors due to coarse gridding can lead to significant inaccuracies in j-value calculation (see *Madronich and Weller* [1990] and appendix A.3.4).

1.2.4 Measurement and Modeling of Actinic Flux and *j*-Values

j-Values have been measured numerous times at different point locations in the atmosphere and under specific conditions, but a qualitative and quantitative understanding of atmospheric photochemistry also requires a knowledge of j-values over considerable length- and timescales. Measurements of this scope are not always practical, so it is therefore necessary to also calculate photolysis rates in the atmosphere.

Quantitative assessment of j-values in the real atmosphere is a daunting problem. Actinic flux is a function not only of wavelength, but it is also sensitive to location in the atmosphere and varies with time, as the position and orientation of the Earth changes relative to the Sun. It is attenuated by absorption caused by O_2, O_3, and to a lesser degree by NO_2 and SO_2, and further modified by molecular scattering, principally by N_2 and O_2. Scattering and absorption by aerosol particles, including clouds, means the morphology and microphysics of aerosol distributions, though complicated, must also be considered. The three-dimensional distributions of aerosols and clouds are difficult to measure and are constantly changing. Actinic flux and j-values also depend on boundary conditions. At the top of the atmosphere there is the extraterrestrial solar irradiance, and at the bottom the surface reflectance (e.g., of the surface of the Earth or optically thick clouds below). Due to the effective impossibility of completely characterizing the atmosphere at any point in time, the interpretation of j-value measurements and the modeling of j-values rely on assumptions and physical simplifications.

An accurate and precise knowledge of actinic flux throughout the atmosphere is essential to understanding the state of the atmosphere and its future changes on all timescales. Measurements and modeling are used individually to quantify j-values. When used together, not only do measurements validate model calculations, but additional insights into the physics of gases and particles, their interaction with light, and their impacts on atmospheric chemistry and composition may be gleaned. There exists a great need for additional measurements and model development, validation, and intercomparison [*Albritton et al.*, 1990; *Meier et al.*, 1997].

1.3 APL Radiative Transfer Model

1.3.1 Model Heritage

The radiative transfer model used throughout this dissertation and for the calculation of photolysis rate coefficients published during the IPMMI, POLARIS, and SOLVE campaigns is based on radiative transfer algorithms originally developed at the Naval Research Laboratory (NRL), which are described in some detail by *Anderson and Meier* [1979] and *Meier et al.* [1982] (for modeling radiative transfer in general) and by *Anderson* [1983] (for the model's specific application to polar twilight conditions). The motivation for the model's development was the need for calculation of the radiation field of the stratosphere and troposphere in the photochemically active 175–850-nm region and, more importantly, the photolysis rate coefficients for key photochemical reactions. Some initial results of the algorithm were presented by *Nicolet et al.* [1982].

With the discovery of the ozone hole over Earth's southern pole and the recognition of the photochemical mechanism of ozone destruction (see section 1.1.4), an urgent need for the reliable calculation of photolysis rate coefficients in polar twilight in the stratosphere emerged for which the NRL model was well-suited. The effect of atmospheric refraction was added and characteristics of the polar twilight UV/visible radiation field were described by *Anderson and Lloyd* [1990], *Anderson et al.* [1995], and *DeMajistre et al.* [1995]. (The NRL model migrated to APL in the early 1990s and thus became the "APL" model.)

Versions of the APL model have been applied to a number of NASA aircraft campaigns studying polar ozone loss (see summary in section 1.4.2). The accuracy of the model has been validated in these missions in comparisons with observations and has been the subject of extensive evaluation. Modeled *j*-values, particularly for NO_2, O_3, and $ClONO_2$ photolysis, have been compared with those obtained from UV/visible spectroradiometers aboard aircraft, from other models, and *j*-values calculated from observed species concentrations, most recently during POLARIS [*Swartz et al.*, 1999; *Del Negro et al.*, 1999; *Stimpfle et al.*, 1999; *Gao et al.*, 2001; see chapter 3] and SOLVE (R. E. Shetter et al., manuscript in preparation, 2002; see chapter 4).

1.3.2 Physical Model

Since the 1960s, two principal physical/mathematical approaches have been used for calculating solar-induced radiation fields. The first, *discrete-ordinates* model is now more commonly used and involves calculating radiances at a given point from a number of discrete angles, or ordinates [*Chandrasekhar*, 1960; *Stamnes et al.*, 1988]. The actinic flux is determined after integrating the intensities over the various angles. It is important to note that the accuracy of this method depends strongly on the number of angles (or "streams") [e.g., *Ruggaber et al.*, 1993; *Kylling et al.*, 1995; *Olson et al.*, 1997]. The second approach has been termed the *source function*[4] model. The calculated "source function," as defined here, is simply the ratio of the actinic flux to the top-of-the-atmosphere flux, $S = F/F_0$. S is proportional to the integral of radiance over all directions and is a scalar, unitless quantity [*Meier et al.*, 1982]. The APL model utilizes the source function, integral approach and does not directly calculate the angular dependence of the radiation field.

The different contributions to the radiation field may be considered by writing the actinic flux F (again with the subscript λ dropped for clarity) as

$$F = \underbrace{F_0 e^{-\tau}}_{\text{direct attenuated flux}} + \underbrace{\int_\phi \int_\theta I_{\text{diffuse}}(\theta, \phi) \sin\theta d\theta d\phi}_{\text{scattered flux}}, \tag{1.12}$$

equivalent to (1.8), where I_{diffuse} is the diffuse radiance. The first term in (1.12) represents the direct attenuated flux into a volume element and the second term is the diffuse flux scattered from all other points in the atmosphere. In the APL model, the scattering field is solved by constructing a wavelength–altitude matrix of atmospheric optical depths, which is a function only of atmospheric properties, namely profiles of absorbers and scatterers (e.g., density, O_2, O_3, aerosols) and not F_0. The matrix is inverted to solve for the total source function S throughout the entire atmosphere, which when multiplied by the top-of-the-atmosphere solar irradiance gives the actinic flux directly. Note that the scattering field is determined for all layers of the atmosphere at once, so the actinic fluxes at all altitudes are calculated simultaneously.

Model details, including the model algorithm derivation, are presented in appendix A.

---

[4]The "source function" defined here should not be confused with the source function discussed by *Chandrasekhar* [1960] or the source function coefficient in the equation of transfer (1.4).

Figure 1.2. Flux and j-value examples from the APL radiative transfer model (see figure on page 22). (a) Four π–sr actinic flux at five altitudes throughout the atmosphere with a solar zenith angle (SZA) of 60° and also at the surface at three additional SZAs representing sunrise/sunset. (b) Source functions (F/F_0) as a function of altitude for wavelengths of 305 and 370 nm, at three SZAs. (c) Spectrally resolved (normalized) j-values for $NO_2 \rightarrow NO + O(^3P)$ and $O_3 \rightarrow O_2 + O(^1D)$ at three SZAs at 10 km. (d) Scattering contributions to j_{NO_2} and j_{O_3} ($j_{scattered}/j_{total}$) at three SZAs (with the same linestyles as in (b)). This model calculation used the U. S. Standard Atmosphere [*COESA*, 1976], with a surface reflectivity of 0.5.

1.3.3 Examples of Actinic Flux and *j*-Values in the Atmosphere

The APL model is used to demonstrate some of the characteristics of the atmosphere in Figure 1.2. In Figure 1.2a, the total (4π-sr) actinic flux is shown at a number of altitudes, from 120 km, which is the top of the model atmosphere and represents the top-of-the-atmosphere extraterrestrial flux (equivalent to the solar irradiance), to the Earth's surface. As one descends through the atmosphere, absorption by the O_2 Schumann–Runge system attenuates solar flux at wavelengths shortward of 205 nm. Between 200 and 300 nm, the O_2 Herzberg and O_3 Hartley bands are, fortunately for life on Earth, very effective at reducing ultraviolet light penetrating the upper atmosphere. At altitudes even as low as the upper troposphere, however, there remains a "window" near 200 nm in the overlap region between the O_2 and O_3 absorption curves that allows for significant photolysis of species, such as nitric acid, that are sensitive to such high-energy photons. At the surface, the atmosphere appears black at wavelengths less than about 290 nm. Figure 1.2a also shows the change in actinic flux at the surface at higher solar zenith angles (SZAs). Absorption by the O_3 Chappuis bands centered near 600 nm are evident when the Sun is close to the horizon.

Examples of source functions, F/F_0, or the ratio of actinic flux to the extraterrestrial flux, are shown in Figure 1.2b for wavelengths of 305 and 370 nm, which are close

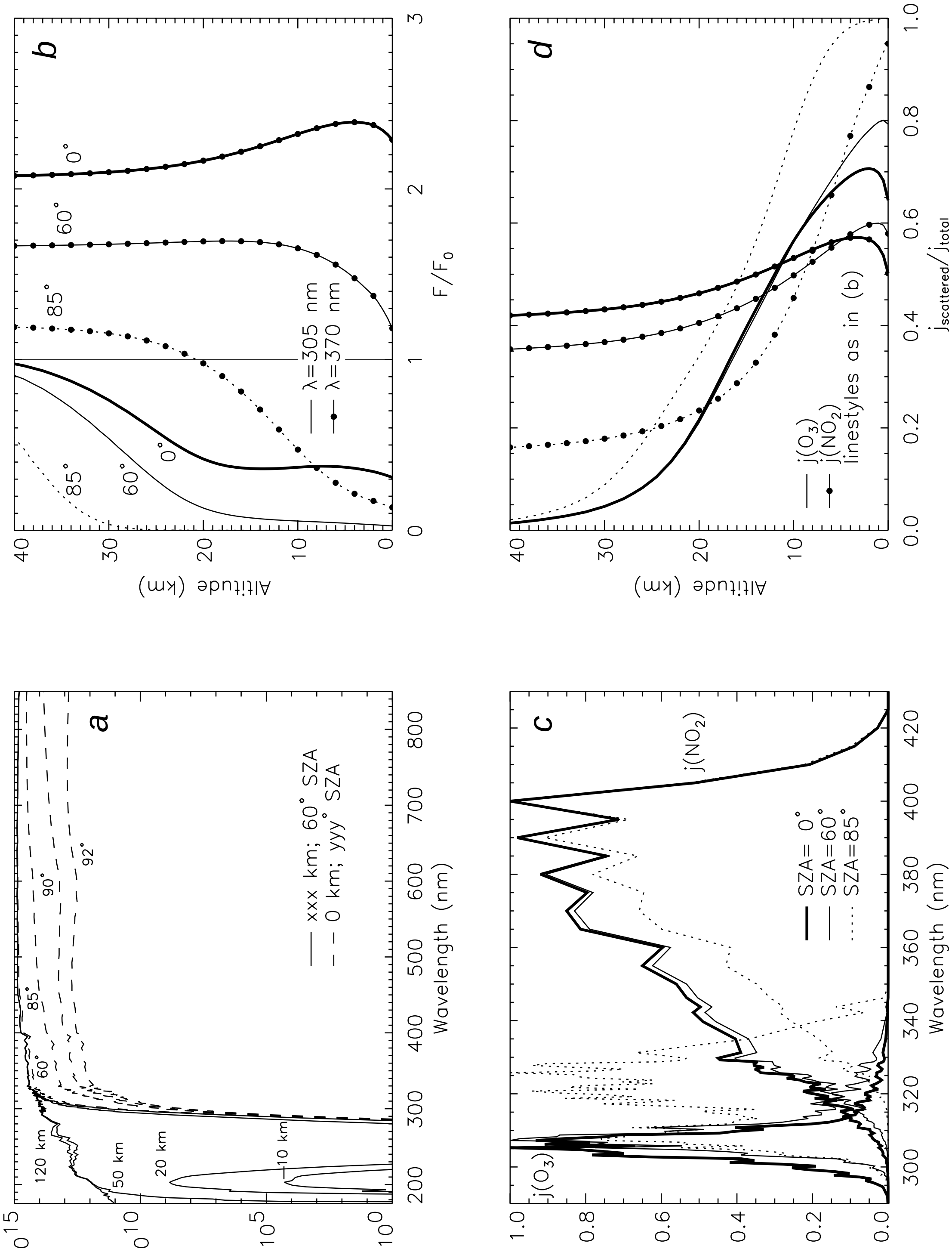

Figure 1.2. Flux and *j*-value examples from the APL model (see caption on page 21).

to the centers of the photolysis ranges for j_{O_3}[5] and j_{NO_2}, respectively, at all but the highest SZAs. Absorption by ozone attenuates 305-nm light as it passes thought the atmosphere, while 4π-sr light at 370 nm is actually enhanced relative to the top of the atmosphere. This phenomenon is due in part to multiple scattering and the relative transparency of the atmosphere in the near-UV. With an overhead Sun and a surface reflecting 50% of the light reaching it, the actinic flux at 370 nm in the troposphere and lower stratosphere is more than *double* the extraterrestrial solar irradiance.[6] This may seem counter-intuitive, but in fact illustrates the geometry of actinic flux. Unlike a flat-plate collector, a molecule receives light spherically, equally from all directions, without cosine weighting.

The *j*-value is a marriage of actinic flux, absorption cross section, and photolysis quantum yield (see section 1.2.3), and is a function of wavelength. Figure 1.2c shows the wavelength dependence of j_{NO_2} and j_{O_3} at 10 km, at three different SZAs. The long-wavelength end of the O_3 Hartley bands and the Huggins bands allow for j_{O_3}. The long-wavelength tail of the $O_3 \rightarrow O_2 + O(^1D)$ quantum yield [*Sander et al.*, 2000] leads to significant photolysis even at large SZAs, where the shorter wavelengths are effectively filtered by high slant ozone columns. The centroid wavelength for NO_2 photolysis shifts to longer wavelengths at large SZAs, with the long-wavelength cutoff for photolysis determined by its quantum yield.

Finally, the relative contributions of scattered light (to the total *j*-value) to j_{NO_2} and j_{O_3} are illustrated in Figure 1.2d. The scattered component of j_{O_3} dominates at the surface and decreases rapidly with altitude, whereas the scattering contribution to j_{NO_2}

---

[5] Also referred to as $j_{O(^1D)}$ in the literature.

[6] In the absence of absorption and scattering, S can reach values up to 3, due to the geometry of actinic flux. Scattering in optically thin atmospheres also enhances the source function.

is more constant throughout the lower atmosphere.

1.4 Overview of Field Campaigns

This dissertation comprises analyses of measured and modeled photochemical data from three field campaigns (described below). The results have been reported in a number of published papers as well as manuscripts submitted or in preparation for publication (see Preface for details).

1.4.1 IPMMI

The International Photolysis Frequency Measurement and Modeling Intercomparison (IPMMI) was designed to address five major objectives: (1) to compare in blind experiments the results of different techniques measuring j_{NO_2} and j_{O_3} ($\rightarrow O_2 + O(^1D)$) under identical, well-defined experimental conditions, (2) to compare results of blind modeling calculations of j_{NO_2} and j_{O_3} with current models using physical input data (e.g., albedo, ozone profile) as measured at the IPMMI site, (3) to compare the blind measurement and modeling j-value results, (4) to compare measured and modeled actinic flux, and (5) based on the results of the intercomparison, to make recommendations as to which of the various model input data (e.g., absorption cross sections, extraterrestrial solar irradiance) lead to the greatest consistency between measurements and modeling [*Cantrell et al.*, 2002].

IPMMI was conducted during a one-week intensive at the Marshall Field Site of the National Center for Atmospheric Research (NCAR) (40°N, 105°W) near Boulder, Colorado, June 15–19, 1998. Without special funding, 21 researchers from eight different institutions participated in the measurement portion of the intercomparison and, with 18 modelers from 13 groups providing modeling calculations. IPMMI was a blind intercomparison, with measurement and modeling results submitted to independent referees. A number of ancillary measurements were also made during the campaign, including ozone profiles and aerosol properties.

1.4.2 Brief History of Aircraft Campaigns in the Polar Stratosphere

Following the discovery of the Antarctic ozone hole in 1984, there was immediate interest in how large depletions of stratospheric ozone over both poles would affect humans, particularly in the populous Northern Hemisphere. This concern stimulated a series of elaborate aircraft field missions (summarized in Table 1.2) that sought to quantify natural and anthropogenically enhanced polar ozone depletion and to elucidate the physical–chemical mechanisms controlling ozone production and loss. A number of independent ground- and balloon-based campaigns have also been conducted to study ozone loss over the poles (not listed in Table 1.2).

Chapters 3–6 focus on the photochemistry of the Arctic stratosphere during the Photochemistry of Ozone Loss in the Arctic Region in Spring (POLARIS) and SAGE III Ozone Loss and Validation Experiment (SOLVE) campaigns.

POLARIS

The high-latitude Northern Hemisphere experiences a naturally occurring seasonal cycle of ozone, in which approximately 40% of the stratospheric ozone disappears each summer. The main scientific objective of the POLARIS campaign was to evaluate the reduction of stratospheric ozone over a range of altitudes and latitudes in the summertime Northern Hemisphere. The measurement and modeling efforts sought to determine the contributions of the various ozone loss cycles and the interplay of chemistry and

Table 1.2. Summary of major polar aircraft campaigns

Abbreviation	Campaign	Hemisphere	Year
AAOE[a]	Airborne Antarctic Ozone Experiment	Southern	1987
AASE[a]	Airborne Arctic Stratospheric Experiment	Northern	1989
EASOE	European Arctic Stratospheric Ozone Experiment	Northern	1991–2
AASE-II[a]	Second Airborne Arctic Stratospheric Experiment	Northern	1991–2
ASHOE/MAESA[a]	Airborne Southern Hemisphere Ozone Experiment/Measurements for Assessing the Effects of Stratospheric Aircraft	Southern	1994
SESAME	Second European Stratospheric Arctic and Mid-latitude Experiment	Northern	1994–5
POLARIS[a,b]	Photochemistry of Ozone Loss in the Arctic Region in Summer	Northern	1997
THESEO	Third European Stratospheric Experiment on Ozone	Northern	1997–9
SOLVE[a,c]	SAGE III Ozone Loss and Validation Experiment	Northern	1999–2000
THESEO 2000	Third European Stratospheric Experiment on Ozone 2000	Northern	1999–2000
SOLVE-2	Second SAGE III Ozone Loss and Validation Experiment	Northern	2003

[a]The JHU/APL radiative transfer model or its predecessors were used for the modeling and analysis of aircraft data.
[b]Subject of chapter 3.
[c]Subject of chapters 5–6.

transport in controling ozone [*Newman et al.*, 1999].

POLARIS was a coordinated NASA high-altitude ER-2 aircraft mission based in Fairbank, Alaska (65°N, 148°W). A total of 28 ER-2 flights were flown during three field deployments, from the equator to the North Pole, during April–September 1997, flying instruments measuring O_3, HO_x, H_2O, NO, NO_2, total reactive nitrogen (NO_y[7]), HNO_3, N_2O, ClO, $ClONO_2$, HCl, CO_2, CO, CH_4, hydrocarbons, halocarbons, solar radiation, overhead ozone column, aerosols, pressure, temperature, and winds. A number of balloon payloads were also launched during the campaign, along with ground- and space-based measurements.

SOLVE

The primary scientific objectives of SOLVE were to (1) study the transport and dynamics of the development and break-up of the polar vortex, (2) study the formation and composition of PSCs, (3) improve quantification of the activation and deactivation of ClO_x, and (4) evaluate empirical and modeled calculations of chemical ozone loss [*Newman et al.*, 2002]. Delays in the launch of the Stratospheric Aerosol and Gas Experiment (SAGE) III satellite instrument prevented validation of the solar occultation limb profiler.

In concert with the Third Europoean Stratospheric Experiment on Ozone 2000 (THESEO 2000), SOLVE employed the NASA ER-2 and DC-8 aircraft, based in Kiruna, Sweden (68°N, 20°E) [*Swartz and Newman*, 1998]. The ER-2 flew 15 flights in two (of three) field deployments during January–March 2000, and the DC-8 flew 23 flights in three deployments during November 1999–March 2000. The ER-2 pay-

[7] NO_y is operationally defined as nitrogen compounds that are reduced to NO by MoO_x or CO on gold, e.g., $NO + NO_2 + NO_3 + 2N_2O_5 + ClONO_2 + HNO_3 + HONO + HO_2NO_2 + BrONO_2 + \cdots$.

load was similar to that in POLARIS, with the notable addition of ClOOCl and BrO measurements. The DC-8 payload was roughly similar (less the NO_2 and ClOOCl measurements), with the addition of lidar profiles of ozone, water vapor, and aerosols (see *Newman et al.* [2002] for details). Both aircraft were equipped with Global Positioning System (GPS) altitude instruments, an improvement over POLARIS. The aircraft measurements were supplemented with numerous ground-, balloon-, and space-based observations.

1.5 Summary

Photochemical processes are at the heart of atmospheric chemistry. The production and loss of ozone in the troposphere and stratosphere are key to understanding the impacts of anthropogenic emissions and global change on the biosphere. The quantification, through measurement and modeling, of the photolysis rates of NO_2, O_3, and ClOOCl, along with the rate of photochemical destruction of ozone in the stratosphere, are essential components of efforts to analyze and predict the chemical composition of the atmosphere.

The basic parameters and principles of radiative transfer in the atmosphere have been outlined, along with a description of the APL radiative transfer model. A context for the IPMMI, POLARIS, and SOLVE field campaigns studied in this dissertation was also outlined.

Chapter 2

International Photolysis Frequency Measurement and Modeling Intercomparison (IPMMI)

2.1 Introduction

2.1.1 Measurement and Modeling of j_{NO_2} and j_{O_3}

The photolysis of nitrogen dioxide, NO_2, is the main source of atomic O in the troposphere, leading directly to the formation of ozone [*Chameides and Walker*, 1973]. Thus, it has been the subject of many measurement efforts, beginning in 1973 [e.g., *Stedman and Niki*, 1973; *Jackson et al.*, 1975; *Harvey et al.*, 1977; *Zafonte et al.*, 1977; *Ritter et al.*, 1979; *Bahe et al.*, 1980; *Dickerson and Stedman*, 1980; *Dickerson et al.*, 1982; *Parrish et al.*, 1983; *Madronich et al.*, 1983; *Madronich*, 1987a; *Junkermann et al.*, 1989; *Shetter et al.*, 1992; *Brauers and Hofzumahaus*, 1992; *Kelley et al.*, 1995; *Volz-Thomas et al.*, 1996; *Lantz et al.*, 1996; *Cotte et al.*, 1997; *Kraus and Hofzumahaus*, 1998].

Ultimately the principal source of the important OH radical [*Levy*, 1971], the photolysis of ozone to produce $O(^1D)$ has also been measured numerous times since the 1970s [e.g., *Dickerson et al.*, 1979; *Bahe et al.*, 1979, 1980; *Ritter et al.*, 1979; *Dickerson et al.*, 1982; *Junkermann et al.*, 1989; *Bairai and Stedman*, 1992; *Blackburn et al.*, 1992; *Hofzumahaus et al.*, 1992; *Müller et al.*, 1995; *Shetter et al.*, 1996; *Cotte et al.*, 1997; *Kraus and Hofzumahaus*, 1998; *Kraus et al.*, 2000].

The modeling and analysis of atmospheric chemistry requires the accurate determination of rate coefficients of NO_2 and O_3 photolysis. These *j*-values have been measured using chemical actinometry, spectroradiometry, and filter radiometry. Chemical actinometry directly measures the rate of change of a chemical system perturbed by the photolysis of one of its components (see section 2.3.1). An actinometer depends on chemical calibration but not on laboratory measurements of molecular parameters, such as absorption cross sections and photolysis quantum yields. Radiometers measure incident radiation with a photoelectric device and rely on photometric calibration. *Spectro*radiometers measure spectrally resolved, absolute radiation (either irradiance or actinic flux). *j*-Values are then derived from spectroradiometer measurements using laboratory measurements of cross sections and quantum yields. *Filter* radiometers use bandpass filters that are designed to mimic the photolysis wavelength dependence, $\sigma(\lambda)\phi(\lambda)$, of a particular species and rely on absolute calibration with an absolute technique (e.g., actinometry).

The modeling of actinic flux and *j*-values has also received a great deal of attention for several decades [e.g, *Leighton*, 1961; *Peterson*, 1977; *Demerjian et al.*, 1980; *Meier et al.*, 1982; *Madronich*, 1987b; *Stamnes et al.*, 1988; *Ruggaber et al.*, 1993; *Kylling et al.*, 1995; *Wild et al.*, 2000, and references therein]. Radiative transfer/*j*-value modeling is an integral part of photochemical modeling in general, which plays an important role in the analysis of atmospheric measurements and the prediction of the future evolution of the atmosphere.

While measurement techniques are limited by experimental uncertainties, even with a perfect theoretical model of radiative transfer, uncertainties remain in the input parameters, such as absorption cross sections, photolysis quantum yields, and extraterrestrial solar irradiance. There are in fact numerous assessments of each of these quantities in the literature. For example, two commonly used sets of NO_2 cross sections are those of *Davidson et al.* [1988] (the basis for the recommendation in JPL's "Chemical Kinetics and Photochemical Data for Use in Stratospheric Modeling" [*DeMore et al.*, 1997]) and *Harder et al.* [1997]. The average ratio of these cross sections, $\sigma_{NO_2,\mathrm{Harder}}/\sigma_{NO_2,\mathrm{Davidson}}$, over 350–425 nm (where NO_2 is largely photolyzed) is about 1.07. The use of the *Harder et al.* cross sections in a model (or when combined with actinic flux measurements) leads to estimates of j_{NO_2} roughly 7% larger than when using the JPL recommendation. *Mérienne et al.* [1995] have reported NO_2 cross sections that are intermediate between the *Davidson et al.* and *Harder et al.* determinations. The cross sections of *Schneider et al.* [1987] are also used in modeling calculations of j_{NO_2}, but are more similar to the *DeMore et al.* recommendations, leading to j_{NO_2} of less than 3% smaller.

The significant differences in the variety of molecular data available poses a problem for *j*-value computation. Measurement–measurement and model–measurement intercomparison are means by which improved recommendations may be made regarding the applicability of extant molecular data.

2.1.2 Intercomparison

The term "intercomparison" is used in the context of the International Photolysis Frequency Measurement and Modeling Intercomparison (IPMMI) to describe an experiment specifically designed to address the level of quantitative agreement between techniques employed to determine a particular quantity. Well-conceived intercomparisons will meaningfully compare observations and/or theory. Increased understanding of differences between techniques helps to characterize differences between separate datasets, which can lead to the more reliable merger of results from separate campaigns into larger datasets and the connection of time series from different measurement networks to establish longer-term trends (see *Albritton et al.* [1990]). As mentioned above, evidence of the best determinations of input data used for *j*-value calculations can also be gleaned from a good intercomparison.

There have been a number of intercomparison (or intercomparison-like) campaigns that have addressed the measurement and modeling of j_{NO_2} and j_{O_3}, including: the MLOPEX experiments [*Shetter et al.*, 1992; *Lantz et al.*, 1996; *Shetter et al.*, 1996], the work of *Müller et al.* [1995], Photo-Oxidant Formation by Plant Emitted Compounds (POPCORN) [*Kraus and Hofzumahaus*, 1998], the j_{NO_2} COMparison 1997 (JCOM97) [*Kraus et al.*, 2000], and the work of *Früh et al.* [2000]. While these intercomparisons often led to j_{NO_2} and j_{O_3} agreements of 10% or better among limited sets of measurement/model determinations, there were also huge discrepancies, well beyond the experimental uncertainties (e.g., the measurement of j_{NO_2} during MLOPEX 2, which exceeded theoretical estimates by up to nearly 50%, regardless of the range of aerosol and other environmental factors accounted for in the model [*Lantz et al.*, 1996]). There exists a great need for high-quality intercomparison of measured and modeled *j*-values [*Albritton et al.*, 1990; *Meier et al.*, 1997].

IPMMI is unique in that it was the first blind, simultaneous intercomparison of *j*-values from a large number of independent measurement and modeling efforts, where the conditions at the measurement site were well characterized and used as input to the models [*Cantrell et al.*, 2002; *Bais et al.*, 2002; *Shetter et al.*, 2002; *Hofzumahaus et al.*, 2002].[1]

---

[1]These four papers constitute the core papers describing the IPMMI campaign and its principal findings and will be referred to as "the IPMMI papers." The first is an overview paper; the others focus on actinic flux, j_{NO_2}, and j_{O_3}, respectively.

2.2 IPMMI: Overview

IPMMI was conducted during a one-week intensive at the Marshall Field Site of the National Center for Atmospheric Research (NCAR), near Boulder, Colorado, June 15–19, 1998. Without special funding, 21 researchers from eight different institutions participated in the measurement portion of the intercomparison (see Tables 2.2 and B.1), with 18 modelers from 13 groups providing modeling calculations (see Table 2.3). IPMMI was a blind intercomparison, with measurement and modeling results submitted to independent referees. After the final data were received, the results were shared between the referees and then the participating investigators.

2.2.1 Objectives

IPMMI was designed to address five major objectives: (1) to compare in blind experiments the results of different techniques measuring j_{NO_2} and j_{O_3} ($\rightarrow O_2 + O(^1D)$) under identical, well-defined experimental conditions, (2) to compare results of blind modeling calculations of j_{NO_2} and j_{O_3} with current models using physical input data (e.g., albedo, ozone profile) as measured at the IPMMI site, (3) to compare the blind measurement and modeling j-value results, (4) to compare measured and modeled actinic flux, and (5) based on the results of the intercomparison, to make recommendations as to which of the various model input data (e.g., absorption cross sections, extraterrestrial solar irradiance) lead to the greatest consistency between measurements and modeling [*Cantrell et al.*, 2002].

2.2.2 The Site

The NCAR Marshall Field Site (39°57′N, 105°12′W; surface elevation: 1.8 km asl[2]) is situated about 8 km southeast of the main NCAR facility in Boulder, Colorado. The local topography is relatively flat for 50 miles to the north, east, and south, with the ground covered with short prairie grass. The surface albedo was measured to be 0.029 ± 0.002 (1-σ) in the near-UV ($\lambda < 420$ nm) in diffuse sunlight and 0.026 ± 0.002 under scattered clouds. A north–south mountain range is located about five miles to the west, but extends less than 3° above the horizon. All of the instruments were mounted on towers on the tops of four white Seacontainers, 5 m above the surface, oriented in a line roughly north–south.

Clouds

Typical of a summer day in Boulder, there were periods of partial cumulus cloud cover. June 15 and 16 were clear in the mornings but clouded over in the afternoons. (June 17 was a down-day.) June 18 was partly cloudy throughout day, and June 19 proved to be virtually cloud-free. Several modeling groups attempted to account for cloud cover in calculations of *j*-values on June 15. Clear-sky *j*-values are much simpler to quantify than when clouds are present, and the June 19 data will be the primary focus here.

Ancillary Measurements

Several sets of ancillary measurements were also made, to aid in the data modeling and analysis. W. Junkermann (Fraunhofer Institut für Atmosphärische Umweltforschung, Germany) took all-sky photographs of cloud cover every 5 min. These cloud images

[2] asl = above sea level.

were used by some of the modelers to account for the effects of clouds on actinic flux on June 15. The NASA/Langley group took measurements with several Eppley radiometers mounted with the primary instruments (listed in Table 2.2) for comparison.

Particularly for the j_{O_3} modeling, the atmospheric ozone burden was measured by a number of techniques: ozonesondes launched daily from the site during the intensive measurement days; total column measurements with a hand-held Microtops II photometer instrument;[3] Dobson total ozone measurements by the NOAA/Climate Monitoring and Diagnostics Laboratory (CMDL) Ozone and Water Vapor Group, located 8 km northwest of the IPMMI site; and total column ozone from the Earth Probe Total Ozone Mapping Spectrometer, within $\pm 0.5^\circ$ latitude/longitude of the site. The total ozone derived from the various techniques agreed to within about $\pm 5\%$ each day.

Unlike the Washington, D. C. area, Boulder enjoys air largely free of aerosol particles. To characterize the thin aerosols present during IPMMI, several measurements were made: direct aerosol optical depth (AOD) at 1020 nm using the Microtops photometer; AOD derived from Langley plots obtained by the NOAA/CMDL Aerosols Group; aerosol optical properties from a ground level–sampling nephelometer, also by the Aerosols Group; and ground-level horizontal visibility from an instrument located at the nearby Jefferson County Airport.

Ambient temperature ranged on the intensive days from an average low of 9.9°C to an average high of 25.6°C. Atmospheric pressure ranged from 820 to 828 mb.

Table 2.1 contains a summary of the IPMMI site conditions and ancillary measurements for June 19, along with corresponding model input parameters discussed in section 2.2.4.

---

[3] See `http://www.solar.com`.

Table 2.1. IPMMI measurement and modeling conditions for June 19, 1998

Parameter	Measured Value	IPMMI Model Protocol	APL[a] Model Settings
Geographic position	39°57′N, 105°12′W	SZA defined	SZA defined
Minimum solar zenith angle	16.5°	(16.5°)	(16.5°)
Surface elevation (km)	1.8	1.8	1.8
Measurement height (m)	5	(0)	(0)
Viewing angle (sr)	downwelling 2π	downwelling 2π	downwelling 2π
Surface albedo	~0.026 ($\lambda < 420$ nm)	0.03 ($\lambda \leq 420$ nm), 0.10 ($\lambda > 420$ nm)	0.03 ($\lambda \leq 420$ nm), 0.10 ($\lambda > 420$ nm)
Total column ozone (Dobson units)	~306	306	306
Ozone profile	ozonesonde	ozonesonde	ozonesonde
Atmospheric profiles	—	U. S. Standard 1976	U. S. Standard 1976
Ambient temperature (°C)	11.7°–23.3°	ambient	ambient
Cloud cover	clear	clear	clear
Aerosol optical depth (550 nm)	~0.03	0.03	0.004–0.18
Aerosol single-scattering albedo	~0.5	0.5	0.94 (1.8–4.5 km)
Aerosol asymmetry factor, g	~0.45	0.45	0.65 (1.8–4.5 km)
Aerosol Ångström parameter, α[b]	~1.7	1.7	0.81–0.91

[a]The final, “APL” IPMMI submission used the model settings shown. The model recalculations also considered in this chapter, “APL*,” utilized the IPMMI model protocol aerosol specifications (see section 2.4.1).

[b]See description of Ångström parameter α in footnote 14 on page 61.

2.2.3 Measurement Protocol

The general measurement protocol was negotiated during planning meetings prior to the intercomparison.[4] Site preparations were made by C. A. Cantrell and R. E. Shetter (NCAR), and the IPMMI participants arrived during the week prior to the intercomparison to install their equipment at the site. Table 2.2 summarizes the instruments used during IPMMI to measure j_{NO_2} (see Table B.1 for a list of the j_{O_3} instruments).

June 15, 16, 18, and 19 were selected for intensive measurements, with June 17 specified as a down-day during which calibration and other instrument maintenance could be performed. Each intensive day, measurements were made continuously from before sunrise ($\sim$4:30 MST[5]) to after sunset ($\sim$19:30 MST). IPMMI was a *blind* intercomparison, so there was no exchange of data among the experimenters. At the end of each day, preliminary data collected were processed and submitted to the measurement referee, J. G. Calvert (NCAR). The referee analyzed the data for obvious errors. Several anomalous problems were detected, and the referee privately alerted the individual participants that there were likely problems with their equipment or data treatment, without disclosing the nature of the anomalies.[6] Daily all-hands meetings allowed for discussions of general issues and scheduling.

Final data were reported by all of the participants by October 1998, with no major changes from the preliminary submissions (corrected for problems encountered in the field). The data were reported as 1-, 10-, and 30-min averages, starting at the top of each hour. The final results were shared among the measurement participants, after which

[4]The author was absent at these meetings.

[5]MST = Mountain Standard Time.

[6]This is how the author became aware of a positive bias in his j_{NO_2} measurements that was due to a system leak that led to a flow rate error (see below). By learning of this problem in the field, it was possible to characterize the leak and make a correction.

Table 2.2. j_{NO_2} instruments participating in IPMMI[a]

Instrument/Institution	Technique[b]	Determination	j_{NO_2} Uncertainty (%, 2-σ)	IPMMI ID
Chemical Actinometers				
National Center for Atmospheric Research	Flow tube/NO detection	j_{NO_2}	9	NCAR
University of Maryland, College Park	Flow tube/NO detection	j_{NO_2}	12	UMD
Spectroradiometers				
Institut für Atmosphärische Chemie, Forschungszentrum, Jülich (Germany)	Double MC/PMT	Actinic flux	12	FZJ
Meteorologie Consult, Glashütten (Germany)	Single MC/PDA	Actinic flux	13–15	MET[2]
National Center for Atmospheric Research	Double MC/PMT	Actinic flux	12	NCAR
University of Leicester (United Kingdom)	Single MC/PDA	Actinic flux	13–15	ULI
National Institute of Water and Atmospheric Research, Lauder (New Zealand)	Double MC/PMT	Irradiance	12	NIWA
Filter Radiometers				
Institut für Atmosphärische Chemie, Forschungszentrum, Jülich (Germany)	Filter/PMT	Broadband j_{NO_2}	10–11	FZJ
Fraunhofer Institut für Atmosphärische Umweltforschung, Garmisch-Partenkirchen (Germany)	Filter/PMT	Broadband j_{NO_2}	21–22	IFU
Meteorologie Consult, Glashütten (Germany)	Filter/PMT	Broadband j_{NO_2}	10–11	MET1
Meteorologie Consult, Glashütten (Germany)	Filter/PMT	Broadband j_{NO_2}	10–11	MET2
NASA/Langley Research Center	Filter/PMT	Broadband j_{NO_2}	10–11	NAL1
NASA/Langley Research Center	Filter/PMT	Broadband j_{NO_2}	10–11	NAL2
University of Leicester (United Kingdom)	Filter/PMT	Broadband j_{NO_2}	10–11	ULI

[a]Other instrument details reported by *Cantrell et al.* [2002], *Bais et al.* [2002], *Shetter et al.* [2002], and *Hofzumahaus et al.* [2002].

[b]MC = monochromator, PDA = photodiode array, PMT = photomultiplier tube.

time no resubmissions could be made.

2.2.4 Modeling Protocol

The modeling effort was divided into two phases. The first, which was optional, was performed before the measurement intensive with a set of estimated geophysical conditions. For the second, geophysical parameters were specified based on ancillary measurements made during IPMMI (see Table 2.1).[7] Table 2.3 lists the modelers that participated in IPMMI. Similar to the measurement protocol, modeling calculations were submitted privately to the modeling referee, A. Bais (Aristotle University of Thesseloniki, Greece).

Two of the intensive days were the focus of the modeling effort. Of primary interest was the clear-sky day, June 19. The modeling outputs requested for comparison with both the other models and the IPMMI measurements are shown in Table 2.4. There were additional requests of those modeling the cloudy June 15, but these are not considered here. The downwelling 2π sr of the actinic flux (and j-values) was the primary focus of the intercomparison, since the instruments involved measured only the upper hemisphere of the radiation field (which is the majority of the radiation field close to the Earth's surface). It should be noted, however, that the 4π-sr actinic flux is what is most relevant for atmospheric chemistry, as molecules are three-dimensional. Aircraft measurements often combine two 2π-sr instruments to determine the total, 4π-sr j-value [e.g., *Kelley et al.*, 1995; *Shetter and Müller*, 1999].

Other intercomparisons [e.g., *van Weele et al.*, 2000] have sought to isolate underlying differences among models and have therefore specified input molecular data, ex-

---

[7] Unfortunately, miscommunication of the modeling parameter specifications for the second phase resulted in several of the modelers using input data that were not consistent with the modeling protocol, but which they felt were appropriate.

Table 2.3. Models participating in IPMMI[a]

ID	Modeler (Institution)	Model	Extraterrestrial Spectrum[b,c]	σ_{O_3}[b,c] [σ_{O_3} for j_{O_3}][d]	$\phi_{O(^1D)}$[b]	σ_{NO_2}[b]
ACD	S. Madronich (NCAR)	TUV 4.0	ATLAS-3 (λ<400), Nec84 (λ>400)	M&M86 (λ<350), WMO86 (λ>350)	JPL97	JPL97
AES	E. Griffloen (Environment Canada)	JMAM	WMO86	M&M86 (λ<325), GOME (λ>325)	JPL97	JPL97
APL[e]	W. H. Swartz (University of Maryland)	JHU/APL	MODTRAN3	M&M86 (λ<350), WMO86 (λ>350)	JPL97	JPL97
BAS	T. Martin and B. Gardner (British Antarctic Survey)	BASRTM	ATLAS-2[f] (λ<419.9), Arv69 (λ>419.9)	Mal95 [JPL97]	JPL97	JPL97
BM1	B. Mayer (NCAR)	libRadtran[g]	ATLAS-3 (λ<407.8), ATLAS-2 (407.8<λ<419.9), MODTRAN3.5 (λ>419.9)	M&M86	Tal98	Sch87
BM2	B. Mayer (NCAR)	libRadtran[g]	ATLAS-3 (λ<407.8), ATLAS-2 (407.8<λ<419.9), MODTRAN3.5 (λ>419.9)	M&M86	Tal98	Sch87
BM3	B. Mayer (NCAR)	libRadtran[g]	ATLAS-3 (λ<407.8), ATLAS-2 (407.8<λ<419.9), MODTRAN3.5 (λ>419.9)	M&M86	Tal98	Sch87

[a] Other model details reported by *Cantrell et al.* [2002], *Bais et al.* [2002], *Shetter et al.* [2002], and *Hofzumahaus et al.* [2002].

[b] Arv69 = *Arvesen et al.* [1969], GOME = *Burrows et al.* [1999], JPL97 = *DeMore et al.* [1997], Mal95 = *Malicet et al.* [1995], Mic94 = *Michelsen et al.* [1994], M&M86 = *Molina and Molina* [1986], Nec84 = *Neckel and Labs* [1984], P&B85 = *Paur and Bass* [1985]/*Bass and Paur* [1985], Sch87 = *Schneider et al.* [1987], She96 = *Shetter et al.* [1996], Sto90 = *Stockwell et al.* [1990], Tal98 = *Talukdar et al.* [1998], WMO86 = *WMO* [1986].

[c] All wavelengths (λ) in nm.

[d] In most cases, the same σ_{O_3} was used both in the radiative transfer calculations and in the computation of j_{O_3}. In the instances where a different σ_{O_3} was used for j_{O_3} it is thus noted.

[e] APL calculations denoted as "JHU" in the IPMMI papers.

[f] Shifted from vacuum to air wavelengths.

[g] libRadtran run in Monte Carlo (BM1), pseudo-spherical DISORT (BM2), and DISORT (BM3) modes.

Table 2.3. Models participating in IPMMI (continued)

ID	Modeler (Institution)	Model	Extraterrestrial Spectrum[b,c]	σ_{O_3}[b,c] [σ_{O_3} for j_{O_3}][d]	$\phi_{O(^1D)}$[b]	σ_{NO_2}[b]
KFA	E. P. Röth (Institut für Atmosphärische Chemie, Jülich, Germany)	ART	WMO86	WMO86 [Mal95]	Mic94	Sch87
KFU	G. Pfister (Karl-Franzens University, Graz, Austria)	TUV 3.9	SUSIM SL2 (λ<350), Nec84 (λ>350)	P&B85 (λ<340), WMO86 (λ>340) [M&M86]	JPL97	JPL97
KNM	M. van Weele (Royal Netherlands Meteorological Institute, Debilt)	DAK	ATLAS-3 (λ<400), Nec84 (λ>400)	P&B85	She96	JPL97
LOA	J. Lenoble (LOA/UJSTL, Grenoble, France)	USTL-SOS	ATLAS-3	P&B85	n/a	n/a
MAR	M. Krol (Institute for Marine and Atmospheric Research, Utrecht, The Netherlands)	(parametric)	SUSIM, Nec84	M&M86 (λ<350), WMO86 (λ>350)	She96	JPL97
NIL	A. Kylling (Norweigan Institute for Air Research, Kjeller, Norway)	libRadtran	ATLAS-3 (λ<407.8), ATLAS-2 (407.8<λ<419.9), MODTRAN 3.5 (λ>419.9)	P&B85	Tal98	JPL97
NI2	A. Kylling (Norwegian Institute for Air Research, Kjeller, Norway)	photodis		M&M86	JPL97	

Table 2.3. Models participating in IPMMI (continued)

ID	Modeler (Institution)	Model	Extraterrestrial Spectrum^{b,c}	$\sigma_{O_3}{}^{b,c}$ [σ_{O_3} for j_{O_3}]^{d}	$\phi_{O(^1D)}{}^{b}$	$\sigma_{NO_2}{}^{b}$
NOA	G. Frost (NOAA/Aeronomy Laboratory)	TUV 3.8	SUSIM hi-res ($\lambda<350$), Nec84 ($\lambda>350$)	M&M86 ($\lambda<350$), WMO86 ($\lambda>350$)	JPL97	JPL97
UMU	A. Ruggaber and P. Koepke (Meteorologisches Institut, Universität München, Germany)	STAR	ATLAS-3 ($\lambda<400$), Nec84 ($\lambda>400$)	GOME	Sto90	Sch87

Table 2.4. IPMMI modeling output tasks for June 19, 1998

Model Output	Radiation	Geometry	Wavelength Range (nm) [Resolution]	Time Period (MST) [Increment]
j_{NO_2}	direct + diffuse	downwelling 2π sr	—	04:35–19:35 [10-min]
j_{O_3}	direct + diffuse	downwelling 2π sr	—	04:35–19:35 [10-min]
Spectral actinic flux	direct + diffuse	downwelling 2π sr	280–700 [1-nm]	05:05–12:05 [1-hr]
Spectral actinic flux	direct + diffuse	4π sr	280–700 [1-nm]	05:05–12:05 [1-hr]
Spectral global irradiance[a]	direct + diffuse	downwelling 2π sr	280–700 [1-nm]	05:05–12:05 [1-hr]
Spectral direct irradiance	direct	2π sr, normal to beam	280–700 [1-nm]	05:05–12:05 [1-hr]

[a]Spectral global irradiance = spectral irradiance on a horizontal surface.

traterrestrial flux [*Ritter et al.*, 1987], etc. as much as possible. This was not, however, the purpose of IPMMI, which strove rather the ascertain how various models (and modelers) calculated spectral actinic flux and j-values under "real" conditions, as they would in the course of normal scientific investigation. *van Weele et al.* [2000] found that, when the model inputs are strictly controlled, various models commonly in use today vary on the order of 10% at 310 nm and by less than 3% at wavelengths greater than 320 nm in the calculation of direct and global irradiance.

Final data were reported by August 1998. Several modeling groups discovered errors in their calculations after the final deadline. These groups were allowed to re-submit their calculations with an explanation for the change (to be published, [*Cantrell et al.*, 2002]). After the resubmission, the referee distributed the theoretical results among the modelers and no further changes were permitted.

2.3 Measurement of j_{NO_2}

2.3.1 Principles of Chemical Actinometry

Perhaps the most direct measurement of the photolysis of a species in the atmosphere involves the observation of the formation rate of a photolysis product. Chemical actinometry determines essentially the amount of light effecting photodissociation by measuring the rate of resultant chemical change in a controlled volume of air (or liquid). The actinometer apparatus produces a known concentration of a reactant gas, exposes it to ambient sunlight, and measures the amount of photolysis products formed. An advantage of actinometry is that it is independent of laboratory measurements of absorption cross sections and quantum yields and measurements of the extraterrestrial solar flux.

The two j_{NO_2} actinometers used during IPMMI, UMD and NCAR, are similar in that they both measure the photolysis of NO_2,

$$NO_2 + h\nu \longrightarrow NO + O(^3P), \tag{R2.1}$$

in an O_2-rich atmosphere in a quartz flow tube exposed to sunlight. The NO_2 photolysis rate coefficient, j_{NO_2}, is inferred based on the amount of NO formed relative to the duration of solar exposure:

$$j_{NO_2} \approx \frac{\Delta[NO]}{[NO_2]_0\,\Delta t}, \tag{2.1}$$

where $[NO_2]_0$ is the initial NO_2 concentration, Δt is the flow tube residence (solar exposure) time, and Δ[NO] is the concentration of photolytically produced NO, given that $\Delta NO \ll [NO_2]_0 \approx$ constant.

2.3.2 University of Maryland j_{NO_2} Chemical Actinometer

The original version of the University of Maryland j_{NO_2} chemical actinometer was designed and fabricated by *Kelley et al.* [1995], and versions thereof have been used previously for measuring j_{NO_2} [*Kondragunta*, 1997; *Dickerson et al.*, 1997; *Rhoads et al.*, 1997].

Instrument Description

The UMD actinometer is shown schematically in Figure 2.1, adapted for the intercomparison. A permeation tube (VICI Metronics, Inc., Santa Clara, California), maintained at a constant 35.0°C, evolved NO_2, which was diluted in zero air to a nominal concentration of 4940 ppbv. This reported concentration was based on an average of four measurement determinations: permeation tube manufacturer certification of the NO_2 permeation rate (by gravimetric determination, i.e., measured mass loss), permeation

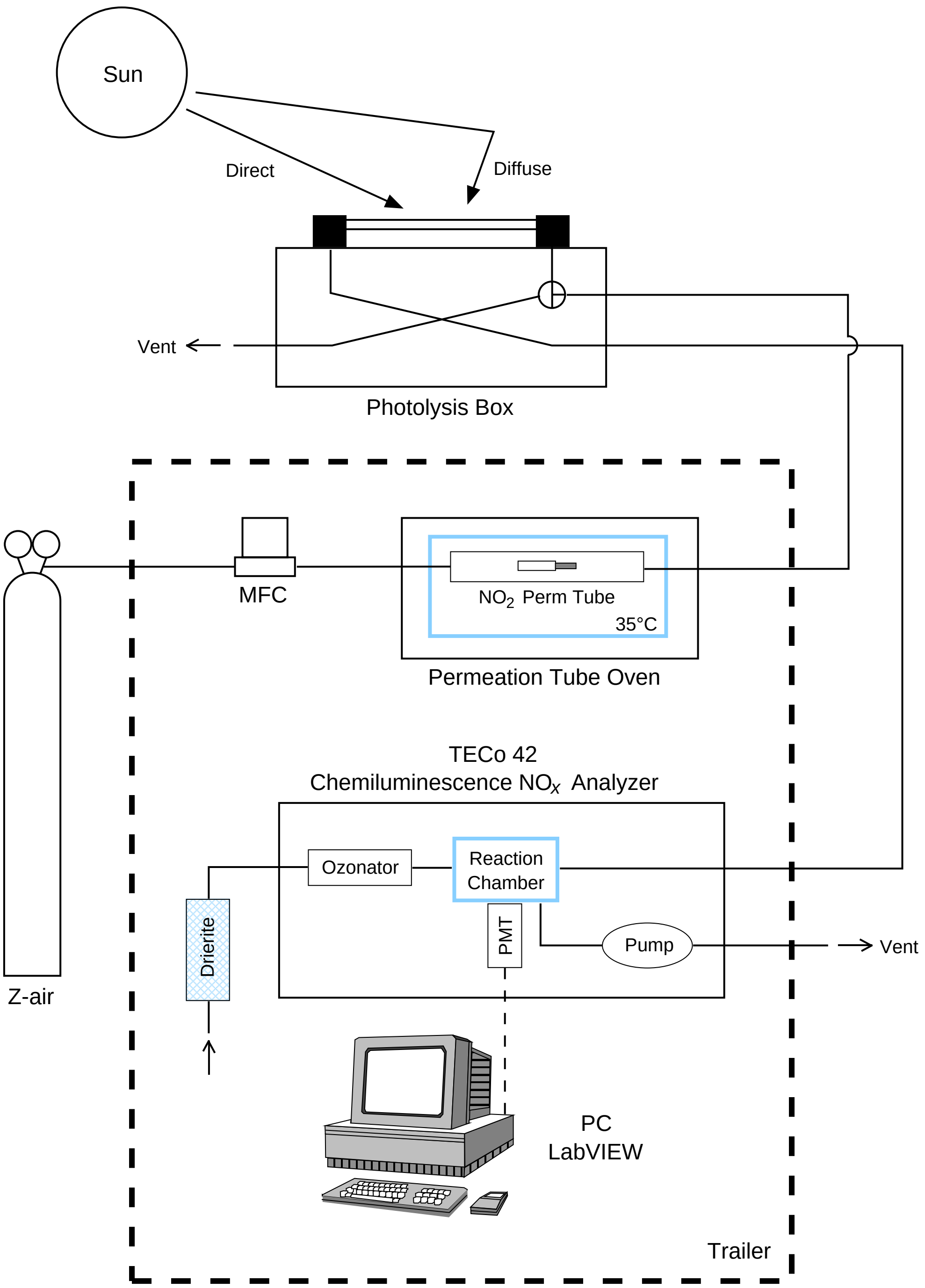

Figure 2.1. Schematic diagram of the University of Maryland j_{NO_2} chemical actinometer (MFC = mass flow controller; PMT = photomultiplier tube).

rate by observed mass loss, NO_2 concentration measured in the field with the actinometer NO_x analyzer, and NO_2 concentration measured using the NOAA/AL P-3 aircraft NO_y instrument (T. Ryerson, NOAA/Aeronomy Laboratory, personal communication, 1998),[8] which measures NO_2 by NO–O_3 chemiluminescence after reduction to NO [*Ryerson et al.*, 1999]. Based on the standard deviation of the these determinations, the uncertainty of the NO_2 concentration was 8% (2-σ).

The quartz photolysis tube (9.9 mm OD $\times$ 8.0 mm ID $\times$ 179.9 mm exposed length) was mounted 4 mm above a flat black[9] plate. This configuration limits the field-of-view of the actinometer to the downwelling 2π sr of the radiation field. It has been estimated that 5% of the lower 2π sr of the radiation field is still visible to the photolysis tube [*Kondragunta*, 1997] and that 1.8% of the sky is invisible to the system due to tube-end effects [*Kelley et al.*, 1995]. The calculated residence time in the illuminated portion of the photolysis tube, assuming plug flow, was roughly 0.7 s, accounting for atmospheric temperature and pressure. Black Teflon tubing was used throughout the system for the gas flow, protecting NO_2 from unwanted photolytic decomposition.

A modified chemiluminescence NO_x analyzer (Thermo Environmental Instruments, Inc., Model 42, Franklin, Massachusetts) was used to measure NO generated by NO_2 photolysis in the quartz photolysis tube, integrating over 10-s intervals. The analyzer was calibrated in the field immediately before and after the campaign and once on June 17, the down-day during the intercomparison, against a 2.0-ppmv NO standard (Scott Specialty Gases, Inc., Plumsteadville, Pennsylvania).[10]

Background measurements of NO in the NO_2 reaction mixture were made twice

[8]The permeation tube analysis was graciously performed by Tom Ryerson (NOAA/AL) at the NOAA Aeronomy Laboratory, Boulder, Colorado, following the intercomparison.

[9]Rustoleum flat black spray paint was used, identical to that used on the NCAR actinometers.

[10]The NO standard was provided by R. E. Shetter (NCAR), at the intercomparison field site.

each hour for 3 min. During the background periods, a solenoid valve was actuated, bypassing the photolysis tube and thus providing a "dark path" to the NO_x analyzer. Data from the 2-min periods immediately following changes in the gas flow were ignored, allowing the system to equilibrate. Background concentrations of NO were typically near 10 ppbv (roughly 30% of the NO produced by NO_2 photolysis near local noon, or a j_{NO_2} of 0.009 s^{-1}). These were smaller NO background levels than were seen in a recent configuration of the actinometer [*Kondragunta*, 1997].

Side Reaction Correction

The production of reactive NO and atomic oxygen within the actinometer flow leads to several side reactions in the photolysis tube:

$$O + O_2 \xrightarrow{M} O_3 \tag{R2.2}$$

$$O + NO_2 \longrightarrow NO + O_2 \tag{R2.3}$$

$$NO + O_3 \longrightarrow NO_2 + O_2, \tag{R2.4}$$

where M is a third body (mostly N_2 or O_2). An error term was calculated in order to compensate for (R2.2)–(R2.4) [*Harvey et al.*, 1977; *Dickerson*, 1980]. The correction, which was less than 2% during IPMMI, was iteratively computed starting with the uncorrected j_{NO_2}, initial NO_2 concentration, and photolysis residence time. The return path from the photolysis tube to the NO_x analyzer was approximately 16 m, with a residence time about about 5.5 s. There was thus an opportunity for NO oxidation by reaction with ozone (R2.4) after photolysis but before detection. This reaction was also corrected for and was always less than 2%. The combined impact of the photolysis tube side reactions and post-photolysis NO titration was less than 2%, and the reported j_{NO_2} was adjusted accordingly.

Table 2.5. Sources of uncertainty in the UMD j_{NO_2} chemical actinometer

Source	Estimated Uncertainty (%, 2-σ)
Photolysis tube geometry	4.0
Permeation tube emission rate ($[NO_2]_0$)	8.0
Mass flow rate	2.0
System leak	7.0
Temperature	2.0
[NO]	2.0
Side reaction correction	0.4
Total uncertainty (added in quadrature)	12

Uncertainty Analysis

The absolute uncertainty of this instrument has typically been on the order of 8% [*Kelley et al.*, 1995; *Kondragunta*, 1997; *Rhoads et al.*, 1997]. During the intercomparison, a system leak was discovered down-stream of the permeation oven. While this leak would not have affected $[NO_2]_0$, the reduced flow through the photolysis tube increased the photolysis residence time (and the apparent j_{NO_2} computed from (2.1)). The source of the leak was not identified during the intensive, but by measuring the flow rate at several places in the apparatus, the effect of the leak was characterized, and the residence time was corrected. After the intercomparison, the leak was discovered in the exit fitting of the permeation tube housing within the oven, accounting for an approximately 14% reduction in flow through the photolysis tube.

The various uncertainties affecting the actinometer measurements are shown in Table 2.5. Despite the larger-than-normal absolute uncertainty (12%, 95% confidence), the excellent day-to-day precision was estimated to be on the order of 3–4%.

2.3.3 Results

The measurements of j_{NO_2} made with the UMD chemical actinometer are shown in Figure 2.2. These data are shown at the finest instrument resolution of 10 s. The data were averaged over 1-, 10-, and 30-min intervals for submission in the intercomparison.

The effects of clouds are immediately apparent. The mornings of June 15 and 16 were mostly clear until 08:00 MST. After noon on June 15 and 16, extensive cloud cover reduced the available actinic flux considerably. Scattered clouds were present midday on June 15 and 16 and occasionally on June 18, causing both reduction and enhancement of j_{NO_2}. This phenomenon was first explained by *Nack and Green* [1974] and is discussed in great detail for the IPMMI campaign by *Crawford et al.* [2002]. Simply, cloud cover that occults the solar disk reduces the direct contribution to the radiation field, while clouds in the rest of the sky may either enhance or attenuate the diffuse radiation field, depending on their extent and optical thickness. Partial cloud cover that does not block the Sun will likely increase actinic flux at the surface relative to clear-sky conditions. As those clouds occasionally cover the Sun, the flux may drop below clear-sky values (hence the j_{NO_2} noise midday on the June 15 and 16 and during June 18). Except for one instance near 16:30 MST, June 19 was cloud-free. Small modulations of the clear-sky data by aerosols are discussed in section 2.6.3.

Measurements of j_{NO_2} from all four intensive days are overlaid in Figure 2.3. The excellent precision of the instrument is apparent in the day-to-day agreement during clear-sky intervals. This reproducibility of the j_{NO_2} measurements suggests that the system leak was constant throughout the intercomparison.

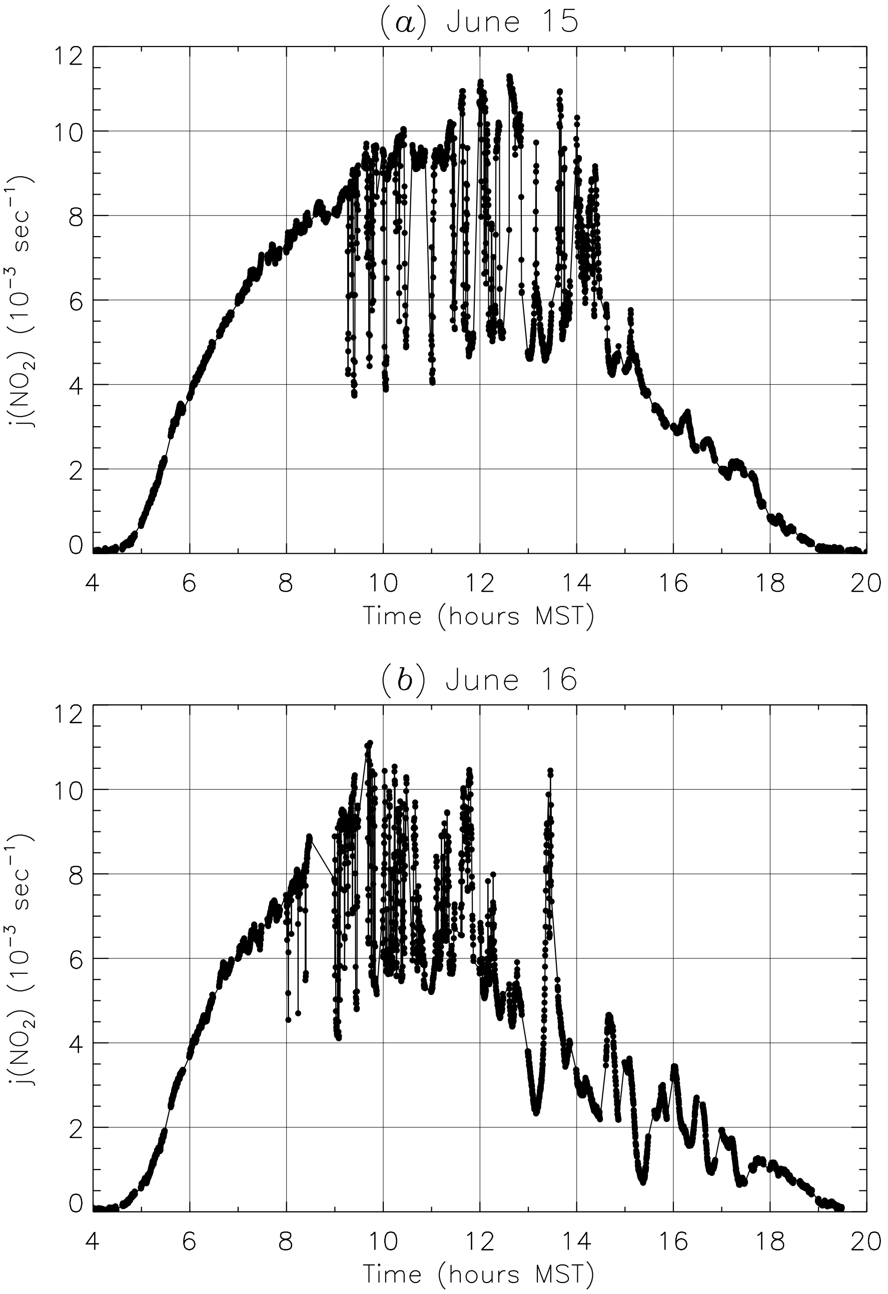

Figure 2.2. Measurements of j_{NO_2} made with the UMD chemical actinometer during IPMMI. The data are presented at the finest, 10-s resolution.

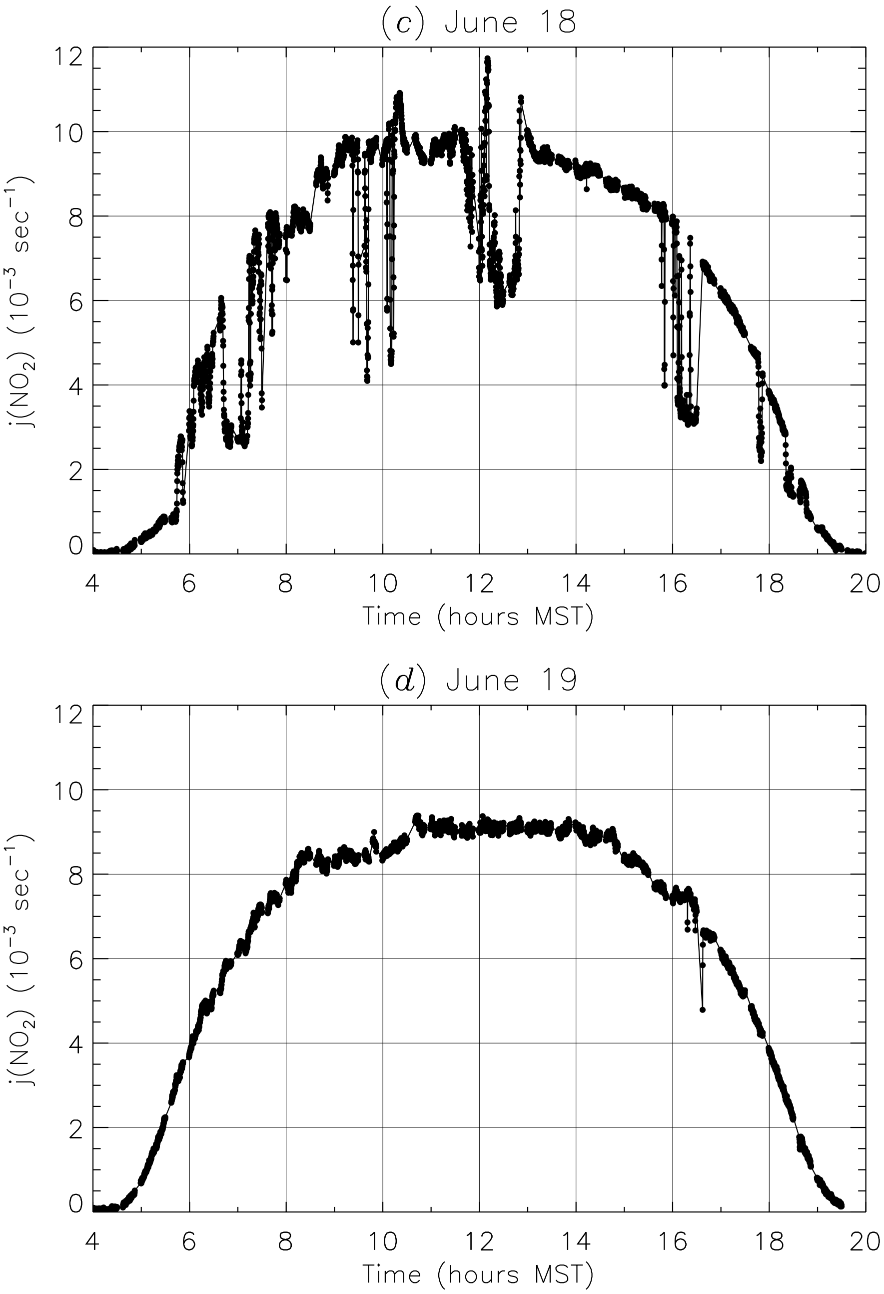

Figure 2.2. Measurements of j_{NO_2} made with the UMD chemical actinometer during IPMMI (continued).

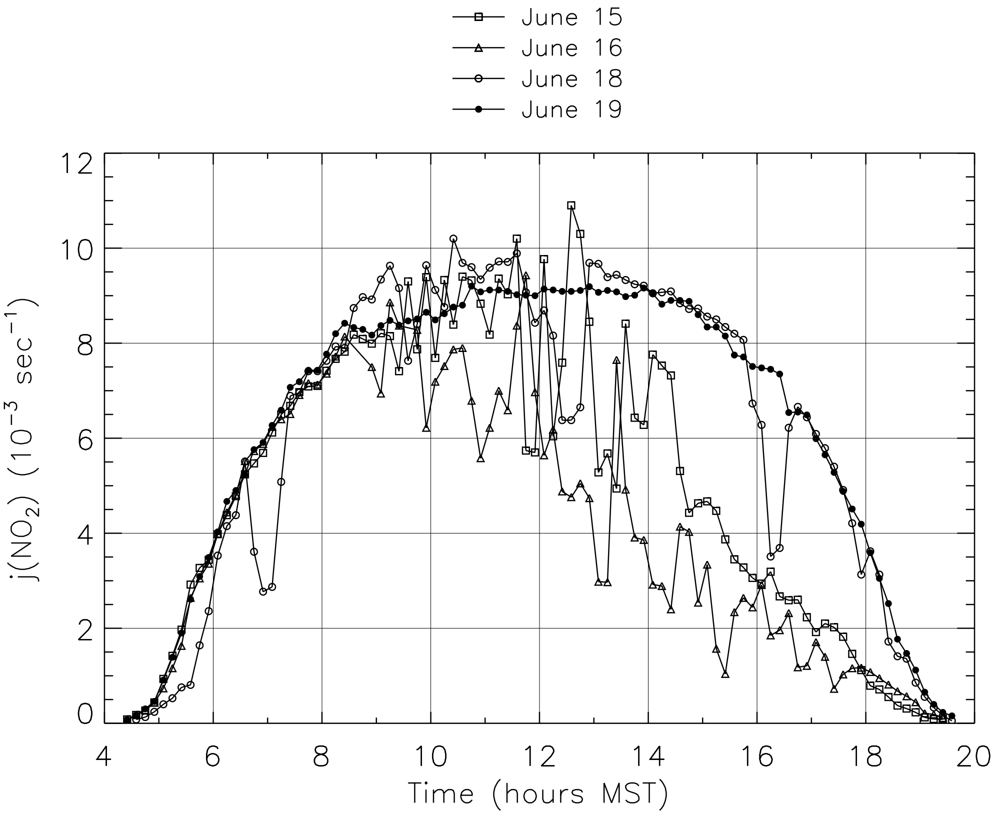

Figure 2.3. Measurements of j_{NO_2} made with the UMD chemical actinometer during IPMMI, for June 15–19, overlaid. The data are 10-min averages.

2.3.4 Comparison with NCAR j_{NO_2} Chemical Actinometer and Spectroradiometers

Brief Description of Other Instruments

While similar in operating principle, the NCAR j_{NO_2} actinometer differed from the UMD instrument in a several respects [*Shetter et al.*, 2002]. The NO_2 source in the NCAR instrument was a calibrated, high-pressure tank mixture of NO_2 in N_2. This was diluted in O_2, and the system was maintained at a pressure of 50 Torr. NO_2, at a concentration two orders of magnitude smaller than the UMD actinometer, flowed through a larger photolysis tube ($1.00 \times \sim 50$ cm) in about 0.3 s. The NCAR group also made an attempt to create a more sophisticated artificial horizon to restrict the field of view to the upper hemisphere of the radiation field with a short lip around the perimeter of the box on which the photolysis tube was mounted.

Four of the scanning spectroradiometers utilized all-quartz 2π-sr detector heads that measured actinic flux directly (rather than irradiance across a flat plate). This made the instruments sensitive to flux independent of angle of incidence, similar to a molecule in the atmosphere. Flat-plate light collectors suffer a cosine–solar zenith angle (SZA) dependence and have large errors when the Sun is near the horizon and illuminating the detector obliquely. Actinic flux was scanned over the wavelength range of interest ($\sim$290–420 nm) using either a single or double monochromator and a photomultiplier tube or photodiode array detector. The spectroradiometers were calibrated using calibration lamps.

The NIWA spectroradiometer (measuring irradiance) and the filter radiometers have other caveats and limitations and are not considered here. Details of all instruments were reported in the IPMMI papers.

Table 2.6. Statistical comparison of UMD and NCAR actinometer measurements of j_{NO_2} (1-min data)

Date	Slope	y-intercept	r^2	n	Mean Ratio [06–18][b]	Slope[a] [06–18][b]	n [06–18][b]
June 15	0.94	$-1.2E-04$	0.981	614	0.93	0.93	515
June 16	0.95	$-1.6E-04$	0.984	613	0.90	0.92	502
June 18	0.92	$-1.0E-04$	0.991	636	0.90	0.90	522
June 19	0.91	$-2.9E-04$	0.995	194	0.86	0.87	132

[a]Forced through the origin.
[b]Of data during 06:00–18:00 MST.

Instrument Comparison

The j_{NO_2} measurements made by the UMD and NCAR actinometers on June 16 are shown in Figure 2.4 (see Figures B.1–B.3 for the other intensive days). In general, the UMD actinometer reported j_{NO_2} larger than the NCAR instrument, with greater disagreement at large SZAs. Some of the "noise" in the ratio plot results when the two instruments were inconsistently sampling the time interval (e.g., one of the instruments was taking a background determination for part of the interval). The statistical comparison shown in Table 2.6 for all four intensive days is based on 1-min data when both instruments reported data, minimizing such biases (Figures 2.4 and B.1–B.3 show 10-min data, for clarity). The actinometer measurements were largely consistent throughout the campaign. Unfortunately, the NCAR actinometer failed before 09:00 MST on June 19, so the comparison for that day is biased toward dawn.

"Composite" Actinometer j_{NO_2}

As a basis for comparison for the other instruments and models, the data from the two j_{NO_2} actinometers were averaged to form a "composite" reference. The actinometers were chosen for this purpose because the best absolute accuracy likely comes from

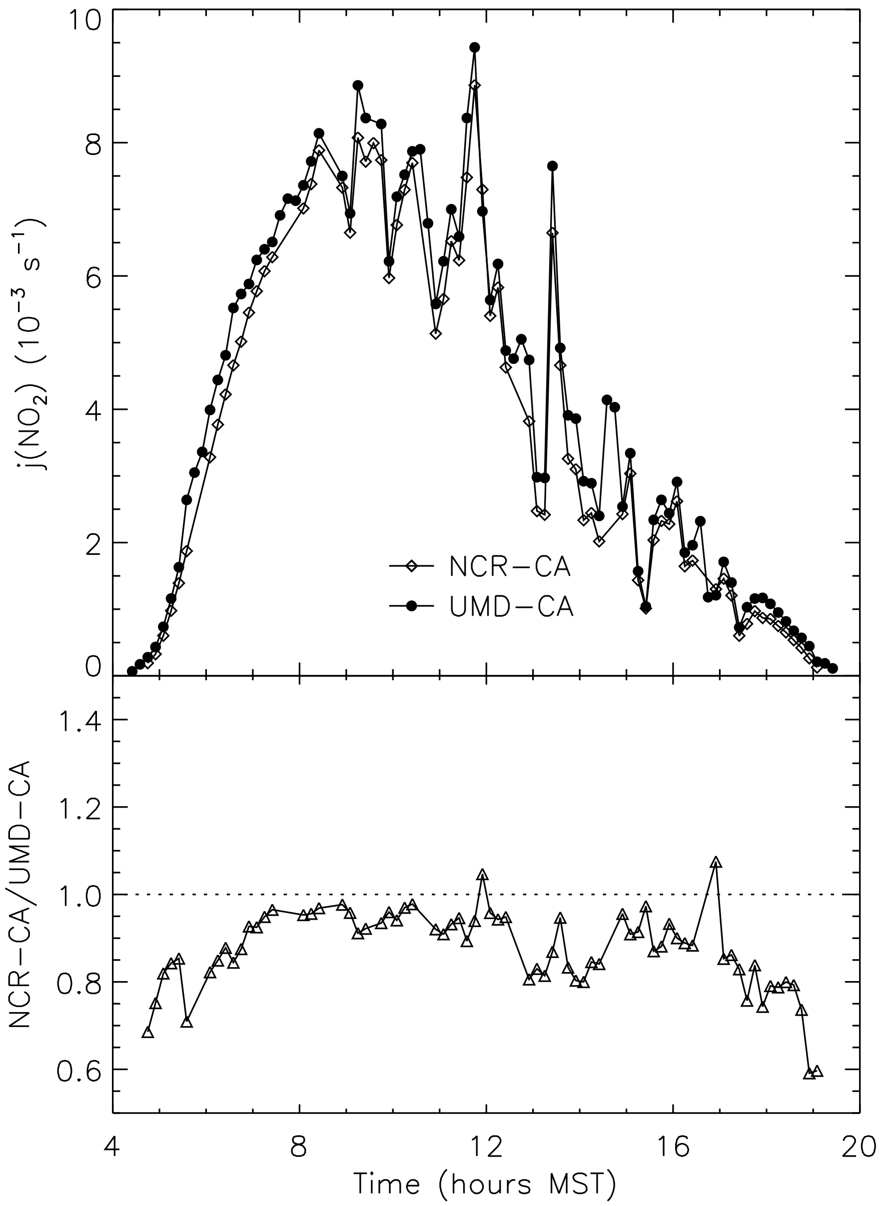

Figure 2.4. Comparison of UMD and NCAR actinometer measurements of j_{NO_2} for June 16 (10-min data).

chemical actinometer measurements, which are independent of laboratory measurements of molecular parameters. The combination of the two actinometers also results in lower absolute uncertainty, added in quadrature, than the individual instruments, or about 7% (2-σ). While an intercomparison seeks to compare individual instruments, a key objective of IPMMI was also to make recommendations of molecular data based on measurement–measurement and model–measurement agreement. The use of composite actinometer data as a stable reference allows for the variation of molecular data used in the derivation of j_{NO_2} from spectroradiometer and model data.[11]

Table 2.7 shows the statistical comparison of all of the actinometers and spectroradiometers with the composite actinometer for June 15–19 (the filter radiometers are not considered). For June 19, pseudo-composite actinometer data were employed as the basis for comparison. The NCAR actinometer failed mid-morning, so the UMD data alone were used, reduced by 4%, since the UMD actinometer was generally about 8% higher than the NCAR instrument during the previous three days. The agreement is excellent, and in general, spectroradiometer j_{NO_2} derived with the *Harder et al.* [1997] NO_2 absorption cross sections leads to better agreement throughout the campaign with the actinometer measurements (individually and as a UMD/NCAR composite) than the smaller *DeMore et al.* [1997] values. The actinometers and spectroradiometers (using *Harder et al.* [1997] NO_2 cross sections) all agreed to within the individual uncertainties of the various instruments on all four days.

[11] In contrast, *Shetter et al.* [2002] make comparisons with a single spectroradiometer. This approach, however, makes conclusions about NO_2 cross sections less transparent since the basis for comparison (the denominator) changes from case to case (the spectroradiometer j_{NO_2} changes with the different input cross sections compared).

Table 2.7. Statistical comparison of measurements with composite actinometer j_{NO_2} (10-min data)

Instrument[a] (σ_{NO_2})[b]	Slope	y-intercept	r^2	n	Mean Ratio [06–18][d]	Slope[c] [06–18][d]	n [06–18][d]
June 15:							
UMD-CA	1.04	3.3E – 05	0.988	68	1.04	1.04	56
NCAR-CA	0.96	–3.3E – 05	0.985	68	0.96	0.96	56
FZJ-SR (JPL)	0.91	–6.6E – 06	0.986	60	0.91	0.91	56
FZJ-SR (Har)	0.98	–6.5E – 06	0.986	60	0.98	0.98	56
NCAR-SR (JPL)	0.87	–2.1E – 05	0.988	68	0.86	0.87	56
NCAR-SR (Har)	0.94	–2.3E – 05	0.988	68	0.93	0.93	56
ULI-SR (JPL)	0.94	1.5E – 04	0.978	63	0.98	0.97	52
ULI-SR (Har)	1.02	1.6E – 04	0.978	63	1.05	1.04	52
June 16:							
UMD-CA	1.02	1.0E – 04	0.998	71	1.05	1.04	58
NCAR-CA	0.98	–1.0E – 04	0.998	71	0.95	0.96	58
FZJ-SR (JPL)	0.92	4.2E – 05	0.994	71	0.94	0.93	58
FZJ-SR (Har)	1.00	4.5E – 05	0.994	71	1.01	1.00	58
NCAR-SR (JPL)	0.86	5.4E – 06	0.999	71	0.87	0.87	58
NCAR-SR (Har)	0.93	5.6E – 06	0.999	71	0.93	0.93	58
ULI-SR (JPL)	0.88	2.9E – 04	0.951	56	0.96	0.93	50
ULI-SR (Har)	0.94	3.1E – 04	0.951	56	1.04	1.00	50

[a]CA = chemical actinometer; SR = spectroradiometer.
[b]JPL = *DeMore et al.* [1997]; Har = *Harder et al.* [1997].
[c]Forced through the origin.
[d]Of data during 06:00–18:00 MST.

Table 2.7. Statistical comparison of measurements with composite actinometer j_{NO_2} (continued)

Instrument[a] (σ_{NO_2})[b]	Slope	y-intercept	r^2	n	Mean Ratio [06–18][d]	Slope[c] [06–18][d]	n [06–18][d]
June 18:							
UMD-CA	1.04	5.9E – 05	0.998	72	1.06	1.05	59
NCAR-CA	0.96	−5.9E – 05	0.997	72	0.94	0.95	59
FZJ-SR (JPL)	0.88	−4.6E – 06	0.995	72	0.88	0.88	59
FZJ-SR (Har)	0.95	−7.9E – 06	0.995	72	0.95	0.95	59
NCAR-SR (JPL)	0.87	8.0E – 06	0.996	72	0.88	0.87	59
NCAR-SR (Har)	0.94	6.8E – 06	0.996	72	0.94	0.94	59
ULI-SR (JPL)	0.87	2.8E – 04	0.944	71	0.92	0.91	58
ULI-SR (Har)	0.93	1.4E – 04	0.945	71	0.96	0.95	58
June 19:							
UMD-CA	1.04	−5.0E – 18	1.000	92	1.04	1.04	72
NCAR-CA	0.95	−2.9E – 04	0.997	23	0.90	0.91	15
FZJ-SR (JPL)	0.88	−1.2E – 04	0.996	92	0.86	0.86	72
FZJ-SR (Har)	0.95	−1.3E – 04	0.996	92	0.93	0.93	72
NCAR-SR (JPL)	0.86	−1.0E – 04	0.992	92	0.85	0.85	72
NCAR-SR (Har)	0.93	−1.1E – 04	0.992	92	0.91	0.92	72
ULI-SR (JPL)	0.92	1.2E – 04	0.989	71	0.94	0.94	67
ULI-SR (Har)	0.99	1.1E – 04	0.989	71	1.01	1.01	67

2.4 Actinic Flux and *j*-Value Modeling

2.4.1 APL Radiative Transfer Model

The APL model (described in section 1.3, with ancillary information in appendix A) has been developed over a period of nearly two decades specifically for the calculation of twilight *j*-values (175–850 nm) in the lower stratosphere and troposphere. The model solves the integral equation of radiative transfer, in which direct solar deposition and reflection from a Lambertian reflecting surface are calculated in a spherical, refracting atmosphere, and isotropic multiple scattering is calculated using a plane-parallel approximation.

For the IPMMI calculations, the APL model calculated spectral actinic flux at 0.5-nm resolution. Adjacent spectral bins were summed to arrive at the 1-nm resolution required for the data submission. *j*-Values were computed from the 0.5-nm spectral flux.

Adaptation of APL Model for Downwelling 2π-Steradian Calculation

The primary product of the APL model is the 4π-sr actinic flux. For comparison with measurements (and other models) of the downwelling 2π-sr flux during IPMMI, an approximation of the downwelling radiation field was used:

$$S_{2\pi(\downarrow)} \approx S_{4\pi} - S_{0\mathrm{g}}, \tag{2.2}$$

where $S_{4\pi}$ and $S_{0\mathrm{g}}$ are the source functions for the total radiation field (defined in section 1.3.2 and (A.7)) and the direct attenuated solar flux reflected from the surface (defined in (A.11), or "C" in Figure A.1), respectively.[12] This approximation predicts

[12]It should be noted that the surface albedo should not simply be set to zero. This would eliminate multiply scattered downwelling flux following reflection from the surface.

that less than about 3% of the total radiation field at 310 and 380 nm near the surface comes from the upwelling 2π sr (the surface albedo is 3%). This approximation agrees to within 2% of the downwelling fraction calculated with NCAR's Tropospheric Ultraviolet-Visible (TUV) model with a discrete-ordinates code operating in four-stream mode with delta-M scaling (calculations by S. Madronich, NCAR, personal communication, 1998), suggesting that the major contributor to the upwelling field is indeed from the direct reflection from the surface.

IPMMI Final Submission and Recalculation

The IPMMI papers utilize the final submissions of model calculations for the intercomparison proper. Miscommunication of the IPMMI model parameters (see Table 2.1) led to a misunderstanding regarding the aerosol specifications in the APL[13] final submission. As a result, the APL model calculations deviated from the IPMMI specification by using MODTRAN rural aerosol optical parameters [*Berk et al.*, 1989] in the boundary layer, scaled to the 1020-nm AOD measured by the Microtops photometer.

For this work, APL calculations were repeated, identical to the final submission, except that the IPMMI aerosol specifications were used,[14] along with the ATLAS ex-

---

[13]Denoted "JHU" in the IPMMI papers.

[14]For the aerosol specification, the AOD_{550nm}, single-scattering albedo, and asymmetry parameter were all set to match the IPMMI protocol (see Table 2.1). The Ångström parameter comes from the empirical Ångström law, $AOD = \beta\lambda^{-\alpha}$, where β is the Ångström turbidity coefficient and α is the Ångström parameter [*Shifrin*, 1995]. The parameter α describes the wavelength dependence of the AOD:

$$\alpha = -\frac{d[\ln \mathrm{AOD}(\lambda)]}{d[\ln \lambda]},$$

assuming here that α and β are roughly constant over the wavelength range of interest. For the APL* recalculations, the wavelength dependence of the MODTRAN rural aerosol optical extinction used in the boundary layer was scaled such that a linear fit of $-d[\ln \mathrm{AOD}(\lambda)]/d[\ln \lambda]$ matched the specified α.

traterrestrial flux[15] [*Kaye and Miller*, 1996; *Woods et al.*, 1996] (see sections 2.6.3 and 2.7.2 for an analysis of the impact of these various input parameters on j_{NO_2} and j_{O_3}). The model recalculations are denoted "APL*."

2.4.2 Other Models

Differences among the models (listed in Table 2.3) resulted from differing theoretical approaches, different input molecular data, different extraterrestrial fluxes, and different applications of the "specified" input geophysical parameters. For example, the surface albedo was specified over different wavelength ranges (see Table 2.1), but some of the modelers varied the albedo linearly to avoid a discontinuity at 420 nm. Despite the specification of aerosol parameters, the intentions of the referee were not communicated clearly. Several modelers used different aerosol profiles and scaling factors.

Model–model comparisons serve only to uncover relative biases and not absolute accuracy. It must also be kept in mind that a number of the models used during IPMMI are in fact related, and would be expected to produce similar results.

2.5 Modeling of Actinic Flux

A majority of models in IPMMI used the ATLAS extraterrestrial solar spectra [*Kaye and Miller*, 1996; *Woods et al.*, 1996]. The APL model, in contrast, used the MODTRAN3 spectrum [*Berk et al.*, 1989], and this difference led to some significant deviations from the other models. The ratio of the MODTRAN to the ATLAS spectra is shown in Figure 2.5a. Over 300–315 nm, where ozone photolysis occurs, the MODTRAN flux ex-

[15]For 200.0–407.8 nm (ATLAS-3), 407.8–419.9 nm (ATLAS-2), and 419.9–700.0 nm (MODTRAN) (also see section A.3.2).

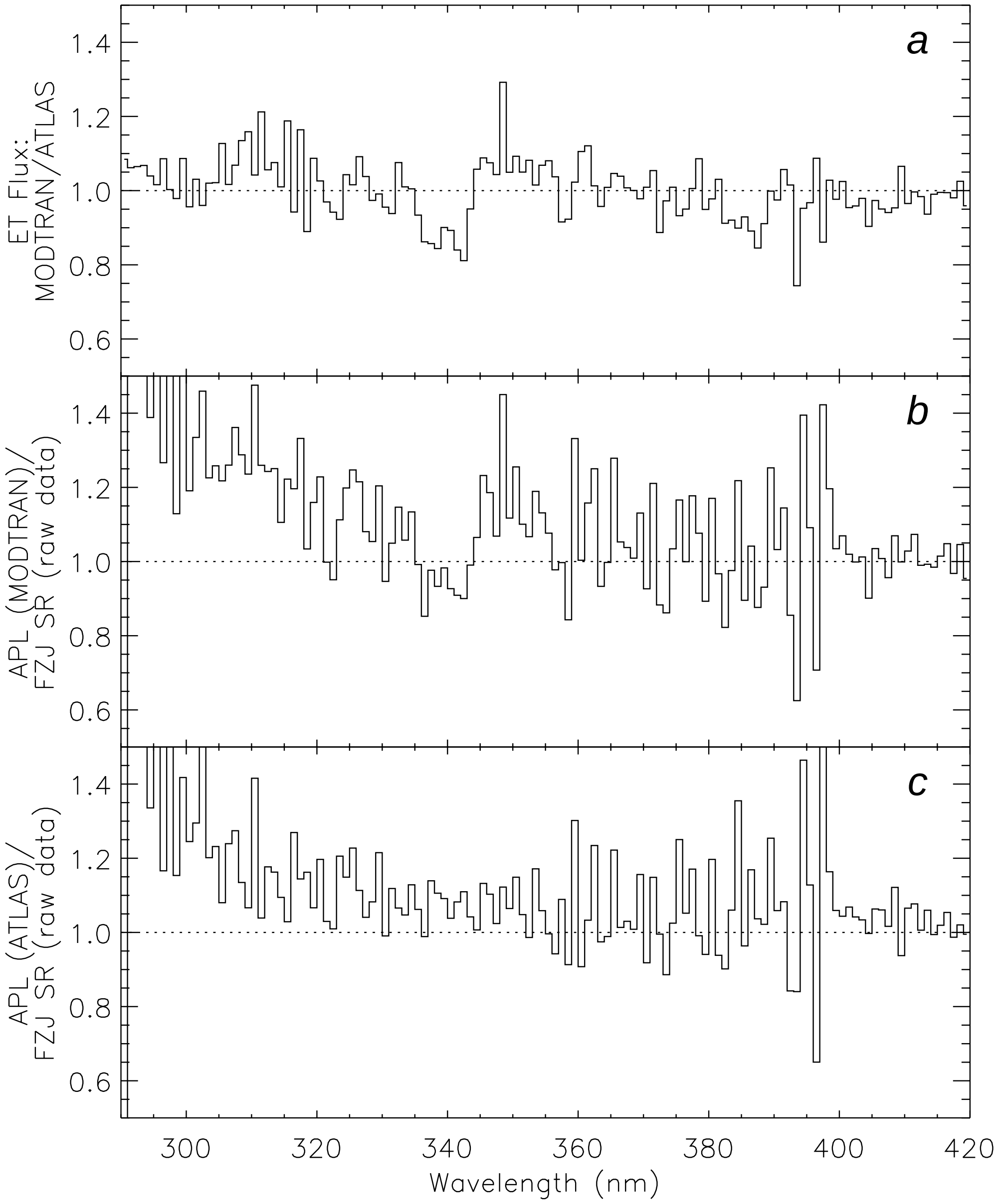

Figure 2.5. Effect of extraterrestrial flux on modeled downwelling 2π-sr spectral actinic flux. Compared are (a) the MODTRAN3 and ATLAS-2/-3 extraterrestrial (ET) solar irradiance, (b) the APL model (using the MODTRAN ET flux; calculated for 12:05 UT on June 19) and "raw" (not corrected for instrument slit function) spectral flux measured by the FZJ spectroradiometer (averaged over 12:00–12:10 UT on June 19), and (c) same as (b), but with the APL model using the ATLAS ET flux.

ceeds ATLAS by roughly 7%, with excursions of up to 20%. Thus, the selection of the solar spectrum alone increased APL in this region, which is important for ozone photolysis, by several percent (see section 2.7.2).

2.5.1 Comparison with Measurements

Strictly speaking, direct comparison of the modeled with measured spectral flux is not entirely valid, since the models reported flux across a uniform 1-nm wavelength grid with a rectangular slit function, while the shape of the spectroradiometer spectra were affected by the instruments' actual slit functions, wavelength steps, etc. The FZJ spectroradiometer had the narrowest slit function and best wavelength stability [*Bais et al.*, 2002] and was thus used in the comparison with the APL model shown in Figures 2.5b and c. *Bais et al.* used a deconvolution and convolution technique to account for instrument slit functions, yielding measured spectra appropriate for direct comparison with the modeled data.

Since atmospheric transmission is generally a smooth function of wavelength, structure in the measured or modeled actinic flux is largely due to structure in the extraterrestrial solar flux. The wavelength discontinuity near 345-nm in the APL (MODTRAN)/FZJ spectral ratio corresponds to that in the MODTRAN/ATLAS comparison in Figure 2.5a. When the ATLAS extraterrestrial flux is used instead (Figure 2.5c), the discontinuity disappears, and the model also agrees better in the 300–320-nm region.

2.5.2 Finding: Support for ATLAS Extraterrestrial Flux

The relatively better agreement of the ATLAS-derived model calculations with the measured spectra (compare Figure 2.5c with Figure 2.5b) confirms the superiority of the ATLAS spectrum for model calculations (see also *Bais et al.* [2002]). This supports the general trend toward using the ATLAS extraterrestrial flux found in the literature [*Gröbner and Kerr*, 2001, and references therein]. The ATLAS flux (290–420 nm) should be used in j-value modeling.[16]

2.6 Modeling of j_{NO_2}

2.6.1 Comparison with Measurements and Other Models

Comparisons of the various modeled j_{NO_2} with that of the (pseudo-)composite actinometer (i.e., UMD actinometer reduced by 4%) for June 19 is shown in Figure 2.6. All of the models utilized the *DeMore et al.* [1997] or comparable NO_2 cross sections. The majority of the models occupy a small envelope, agreeing to within about $\pm 5\%$ near noon. The core of this envelope remains intact to SZAs of about 80°. Beyond 85°, several of the models diverge markedly from the actinometer measurements. The APL[*] model performs well, even at the largest SZAs.

A statistical summary of the model–actinometer comparison is shown in Table 2.8. APL* underestimated the measured j_{NO_2} by about 14% (considering the slope for the 06:00–18:00 MST data, at SZA $\leq 75°$, forced through the origin), consistent with the average of all the models, which was 0.85 with an rms error[17] of $\pm 4\%$ (relative to the mean of the models). *Olson et al.* [1997] found an rms error of $\pm 6\%$ for j_{NO_2} at the surface at SZA=23° under clear-sky, aerosol-free conditions among 20 radiative transfer models during the PhotoComp (model-only) intercomparison. APL* agreement with the NCAR and FZJ spectroradiometers, using the same NO_2 cross sections, was

[16]In subsequent campaigns (SOLVE, see chapters 4 and 6), the ATLAS extraterrestrial flux has been used in APL model calculations as a result of the IPMMI findings.

[17]Root-mean-square (rms) error = $\sqrt{\sum_i (c_i - c_{\text{mean}})^2/n}$, where c_i and c_{mean} are the individual and mean values, respectively, and n is the number of values.

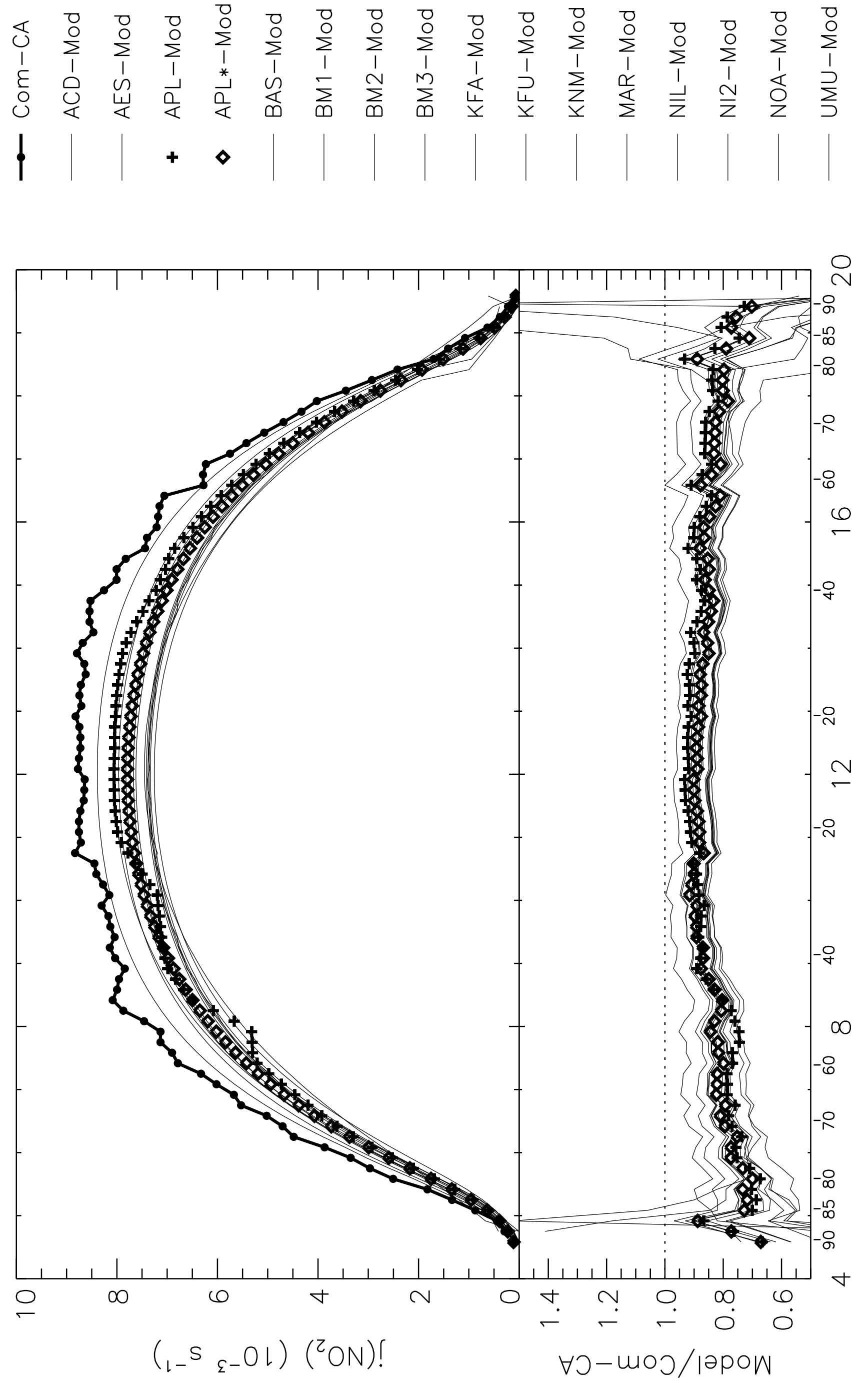

Figure 2.6. Comparison of models with composite actinometer (UMD measurements reduced by 4%), "Com-CA," j_{NO_2}: June 19. Models other than APL/APL* are not specifically identified in the figure, but the statistical summary is shown in Table 2.8. Ratios of the various models to the actinometer are shown in the lower panel. Selected SZAs are also indicated on the abscissa for reference.

Table 2.8. Statistical comparison of models with composite actinometer j_{NO_2}: June 19

Model	Slope	y-intercept	r^2	n	Mean Ratio [06–18][b]	Slope[a] [06–18][b]	n [06–18][b]
ACD	0.88	−1.7E − 04	0.996	91	0.85	0.86	72
AES	0.93	−2.7E − 04	0.994	91	0.89	0.90	72
APL	0.92	−3.3E − 04	0.984	91	0.86	0.88	72
APL*	0.90	−2.6E − 04	0.993	91	0.86	0.86	72
BAS	0.85	−1.6E − 04	0.994	91	0.82	0.83	72
BM1	0.86	−3.4E − 04	0.995	91	0.81	0.82	72
BM2	0.86	−2.4E − 04	0.995	91	0.82	0.82	72
BM3	0.86	−3.4E − 04	0.995	91	0.81	0.82	72
KFA	0.81	−4.5E − 05	0.979	91	0.80	0.81	72
KFU	0.90	−2.1E − 04	0.995	91	0.87	0.88	72
KNM	0.91	−3.8E − 04	0.995	91	0.86	0.86	72
MAR	0.97	−1.3E − 04	0.997	91	0.95	0.95	72
NIL	0.85	−2.9E − 04	0.994	91	0.81	0.82	72
NI2	0.91	−7.9E − 05	0.997	91	0.90	0.90	72
NOA	0.86	−5.1E − 04	0.990	91	0.78	0.80	72
UMU	0.87	−6.0E − 05	0.996	89	0.86	0.87	72
average:[c]	*0.88*	*−2.3E − 04*	*0.994*		*0.85*	*0.85*[d]	

[a]Forced through the origin.
[b]Of data during 06:00–18:00 MST.
[c]Including APL*, but not APL.
[d]rms error: ±4% (relative to the mean of the models).

within 1–2% (not shown).

2.6.2 Finding: Support for Larger NO_2 Cross Sections

If a rough uncertainty of 10% for the model calculations is assumed [*Shetter et al.*, 1992; *Weihs and Webb*, 1997], along with 7% for the pseudo-composite actinometer, only nine of 15 (counting APL*, not APL) models agree with the measured j_{NO_2} to within the combined model–measurement uncertainty (considering the slope for the 06:00–18:00 MST data forced through the origin). If larger NO_2 cross sections were used, however, like those of *Harder et al.* [1997], which lead to a j_{NO_2} of about 7% higher, all of the models would agree with the measurement within the combined uncertainties, and eight of the models would agree to within the measurement uncertainty alone.

This finding is consistent with the results of better spectroradiometer–actinometer agreement when using the *Harder et al.* [1997] cross sections (section 2.3.4) and suggests that the community should consider using larger NO_2 cross sections and/or further laboratory evaluation of σ_{NO_2}.[18,19] This conclusion also confirms results from the limited spectroradiometer–actinometer comparisons of *Kraus et al.* [2000], which showed better agreement when using the *Mérienne et al.* [1995] cross sections, in comparison with those of *DeMore et al.* [1997].

[18] Use of the larger *Harder et al.* [1997] NO_2 cross sections during POLARIS would reduce the steady-state [NO_2] inferred from modeled j_{NO_2} (see chapter 3) and in situ species concentrations by *Del Negro et al.* [1999], improving agreement with measured [NO_2].

[19] Unlike the finding supporting the ATLAS extraterrestrial flux, the *Harder et al.* [1997] NO_2 cross sections were not used during SOLVE. This is because while many modelers had already adopted the ATLAS extraterrestrial flux when SOLVE was conducted, the *DeMore et al.* [1997] NO_2 cross sections were almost universally accepted. The findings of IPMMI were also as yet unpublished.

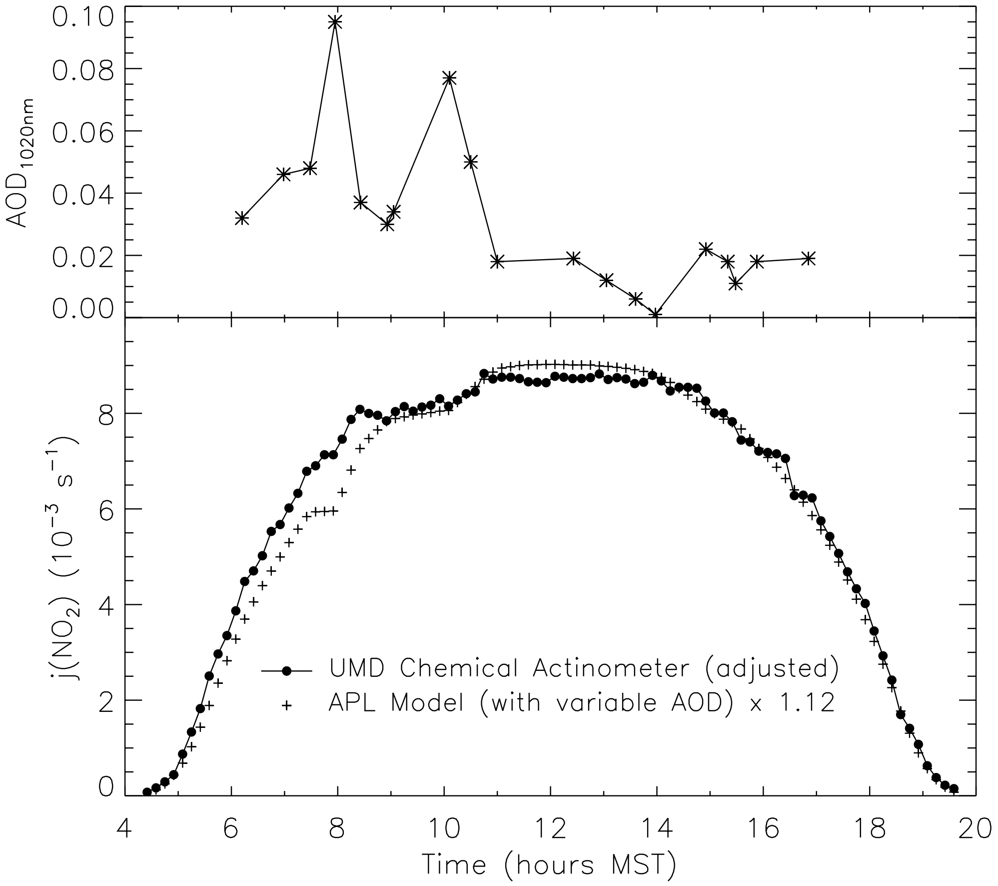

Figure 2.7. Effect of aerosol attenuation on j_{NO_2}. In the upper panel, the AOD at 1020 nm measured by a Microtops II photometer on June 19 is shown. In the lower panel, the corresponding composite actinometer (UMD measurements reduced by 4%) data are shown along with calculations with the APL model (scaled by 1.12 for comparison), which utilized the diurnal AOD_{1020nm} as input.

2.6.3 Effects of Aerosols and Extraterrestrial Flux on j_{NO_2}

Aerosols have been shown to have dramatic effects on the photochemistry of the atmosphere, both increasing and decreasing photolysis, depending on local conditions [e.g., *Dickerson et al.*, 1997; *Liao et al.*, 1999; *He and Carmichael*, 1999; *Castro et al.*, 2001]. While the aerosol loading at the IPMMI site was relatively light and the prevailing view was that the impact of aerosols was minor, the effects of aerosols on radiative transfer and photolysis were not immeasurable. Figure 2.7 shows UMD actinometer data for June 19, when clouds were not present, along with APL model calculations (final IPMMI submission, with aerosol scaling). Though there were questions regarding the reliability of the Microtops AOD during IPMMI, the diurnal variability of the measured AOD (especially the spikes in the morning) and corresponding model calculations correlated nicely with the actinometer measurements, showing how aerosols did indeed modulate j_{NO_2}.

To explore the aerosol effects further, the APL model was used to recalculate IPMMI j_{NO_2} with the AOD_{550nm} set to 0.03 and also with the complete IPMMI aerosol specification (from Table 2.1). These calculations, along with APL*, are shown in Figure 2.8. Comparing modifications (1) and (2), Figure 2.8 shows the effects of reducing the single-scattering albedo (which means greater aerosol absorption of radiation), increasing α (which increases the AOD at wavelengths shorter than 550 nm, where NO_2 and ozone photolyze), and reducing the asymmetry factor (which reduces the relative forward scattering of the aerosols). These three parameters combine to produce a 5–10% reduction in j_{NO_2} in this case. The use of the ATLAS extraterrestrial flux (APL*) has a relatively small impact on j_{NO_2}.

2.7 Modeling of j_{O_3}

2.7.1 Comparison with Measurements and Other Models

Most of the modelers chose to the use either the *Molina and Molina* [1986] or *Paur and Bass* [1985] (see also *Bass and Paur* [1985]) ozone cross sections, which differ very little (<2%) for j_{O_3}. For the $O(^1D)$ quantum yields chosen, there is reasonable agreement, at least at smaller SZAs. Curiously, some modelers used different O_3 cross sections for their calculations of solar transmission and absorption leading to photolysis.

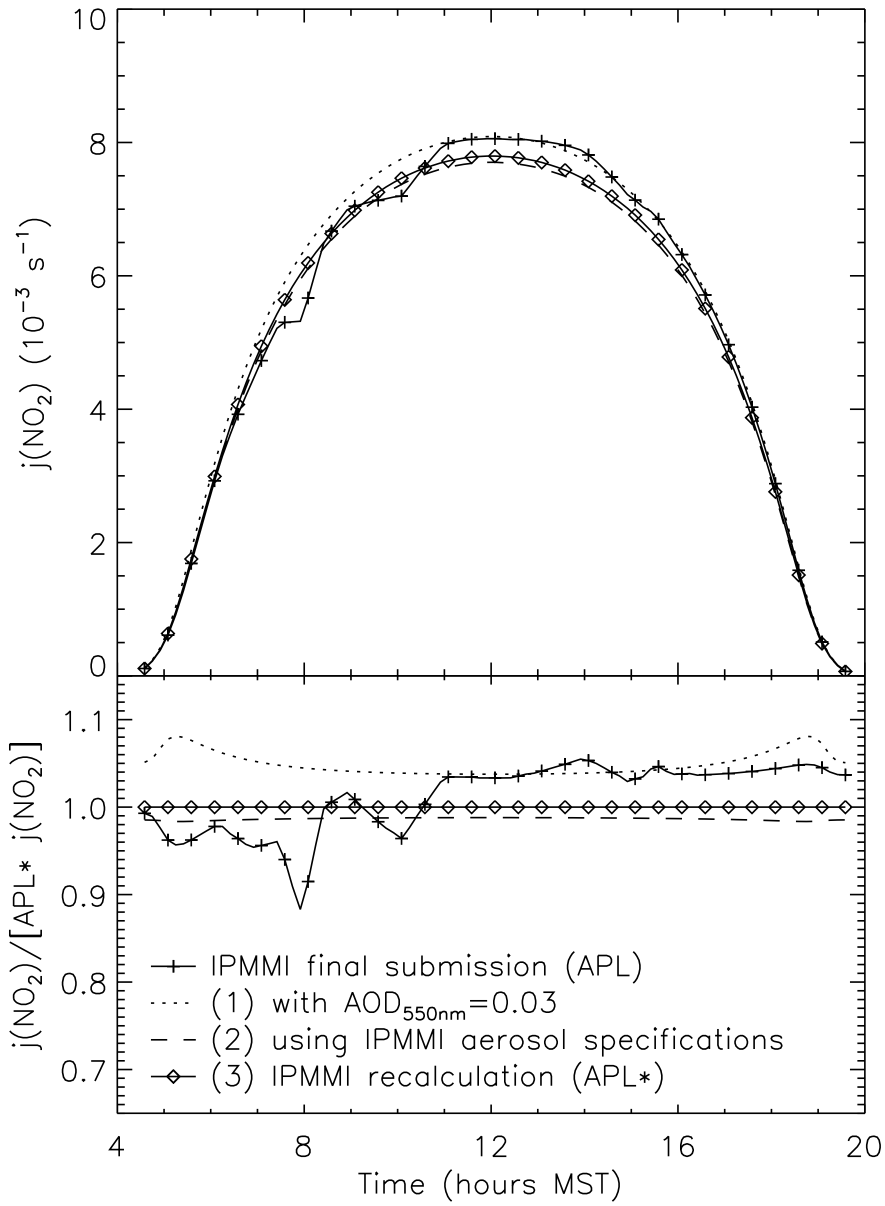

Figure 2.8. APL model j_{NO_2} with various aerosol and extraterrestrial flux inputs: June 19. The final IPMMI submission is shown, along with identical calculations except for (1) scaling the aerosol optical depth at 550 nm to 0.03 (to partially match IPMMI specifications), (2) matching the complete IPMMI aerosol specification, and (3) the APL* IPMMI recalculation, which used the IPMMI specification and the ATLAS extraterrestrial flux. The ratios are relative to the APL* calculation.

Table 2.9. Statistical comparison of models with NCAR actinometer j_{O_3}: June 19

Model	Slope	y-intercept	r^2	n	Mean Ratio [06–18][b]	Slope[a] [06–18][b]	n [06–18][b]
ACD	0.99	$-3.0E-07$	0.993	63	0.95	0.98	53
AES	0.99	$-4.0E-07$	0.997	63	0.94	0.97	53
APL	1.14	$-5.2E-07$	0.983	63	1.08	1.12	53
APL*	1.01	$-3.5E-07$	0.994	63	0.97	1.00	53
BAS	0.93	$-3.6E-07$	0.995	63	0.88	0.92	53
BM1	1.00	$-6.8E-08$	0.993	63	0.98	0.99	53
BM2	0.99	$3.1E-08$	0.993	63	0.99	1.00	53
BM3	1.00	$-6.3E-08$	0.993	63	0.98	1.00	53
KFA	0.98	$-5.6E-07$	0.993	63	0.92	0.96	53
KFU	1.06	$-4.2E-07$	0.997	63	1.00	1.04	53
KNM	0.89	$-7.0E-07$	0.997	63	0.81	0.87	53
MAR	1.14	$-2.7E-07$	0.993	63	1.10	1.13	53
NIL	0.99	$-6.3E-08$	0.993	63	0.98	0.99	53
NI2	1.22	$-2.4E-07$	0.996	63	1.18	1.21	53
NOA	1.02	$-4.6E-07$	0.994	63	0.96	1.00	53
UMU	0.86	$-8.9E-07$	0.997	63	0.75	0.82	53
average:[c]	*1.00*	*$-3.4E-07$*	*0.995*		*0.96*	*0.99*[d]	

[a]Forced through the origin.
[b]Of data during 06:00–18:00 MST.
[c]Including APL*, but not APL.
[d]rms error: ±9% (relative to the mean of the models).

Several modelers also used surface temperatures and temperature profiles other than those prescribed.[20]

The results of the j_{O_3} modeling in comparison with the NCAR j_{O_3} chemical actinometer is presented in Table 2.9.[21] The final APL submission for j_{O_3} was significantly higher than the actinometer measurements. With the IPMMI aerosol parameters and

[20]See Figure B.4 for the modeled dependence of j_{O_3} on surface temperature.

[21]While the modelers were asked to calculate j_{O_3} based on ambient surface temperature, the temperature inside the large NCAR j_{O_3} actinometer photolysis tube was generally a few degrees warmer due to solar heating. Therefore, the modeled j_{O_3} had a negative bias relative to the actinometer (and the spectroradiometers, which computed j_{O_3} based on actinometer temperature). The negative bias is estimated to be less than about 4% at noon on June 19.

using an extraterrestrial flux similar to the other models, however, the APL* calculations of j_{O_3} were in excellent agreement with the other models and with the NCAR j_{O_3} actinometer measurements (within 1% on average) and the NCAR and FZJ spectroradiometers (1%, not shown). The average of all the models was $0.99 \pm 9\%$ (considering the slope for the 06:00–18:00 MST data, at SZA $\leq 75°$, forced through the origin), compared to a $\pm 7\%$ rms error in modeled j_{O_3} at SZA=23° found during PhotoComp [*Olson et al.*, 1997].

2.7.2 Effects of Aerosols and Extraterrestrial Flux on j_{O_3}

Similar to the results in section 2.6.3, recalculations using the APL model are shown in Figure 2.9 for j_{O_3}. The APL j_{O_3} final submission was significantly higher than the other models and the measurements. When the aerosols were properly (or at least consistently) handled, j_{O_3} was reduced by 7% at noon, with corrections of up to roughly 10% at some points during the day. Replacing the MODTRAN extraterrestrial flux with the ATLAS data further reduced j_{O_3} by another 7%.[22] This impressive correction brought the APL model into nearly perfect average agreement with the measurements.

2.8 Summary and Conclusions

Despite a system leak, the University of Maryland j_{NO_2} chemical actinometer measured j_{NO_2} during IPMMI with excellent day-to-day precision (clear-sky portions) and was in good agreement with another, NCAR actinometer. Its performance on the only clear

[22] If the POLARIS j_{O_3} calculations in chapter 3 and *Swartz et al.* [1999] were re-computed with the ATLAS extraterrestrial flux, the APL_{CPFM}/CPFM agreement would go from +14% to about +7%, and the APL_{TOMS}/CPFM agreement would drop from +8% to +1%.

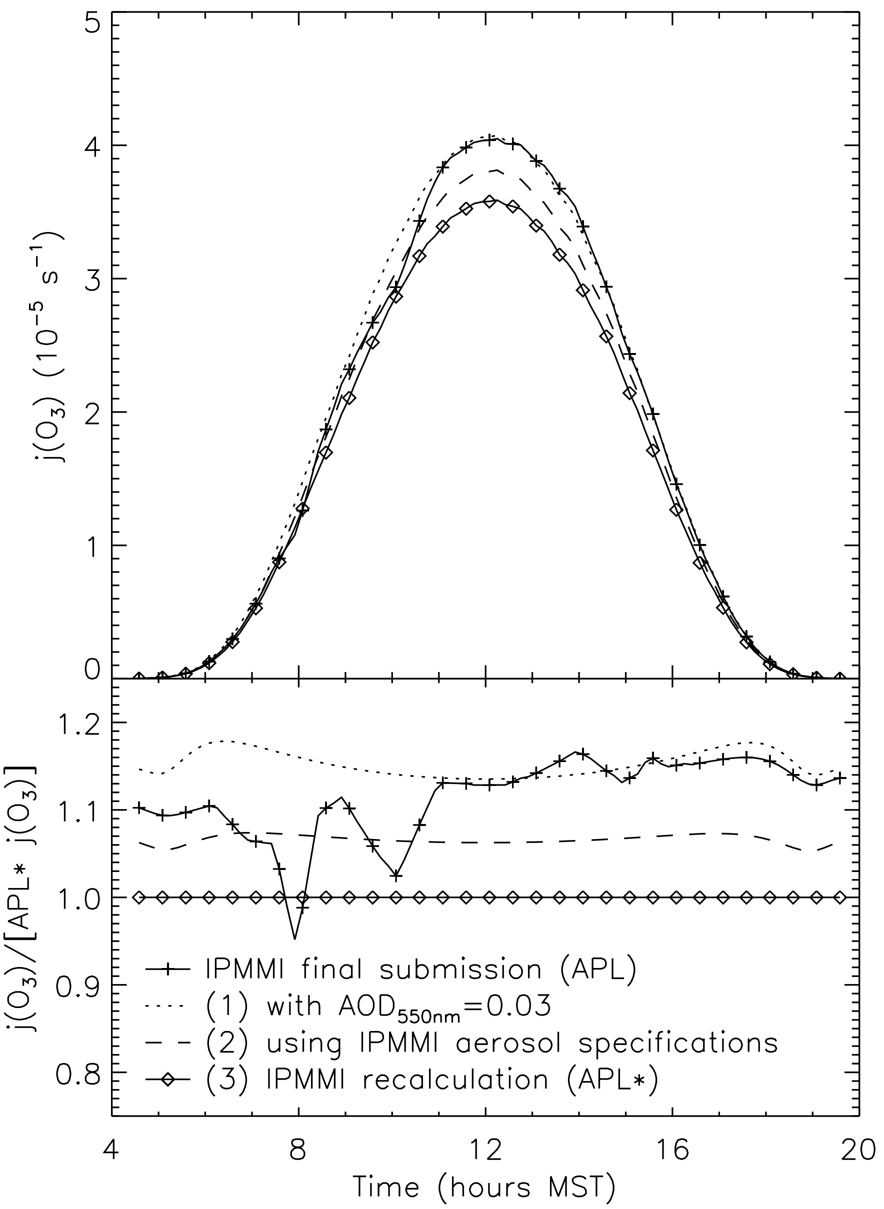

Figure 2.9. Same as Figure 2.8, but for j_{O_3}.

day of the intercomparison (June 19) was critical, since the other actinometer failed mid-morning.

The APL radiative transfer model, particularly when using detailed aerosol optical parameters measured at the IPMMI site and the ATLAS extraterrestrial flux (APL*), was in excellent agreement with a majority of the other models (clear-sky calculations, June 19), which had an rms error of ±4% and ±9% for j_{NO_2} and j_{O_3}, respectively. For solar zenith angles less than 75°, its calculations of j_{NO_2} and j_{O_3} were within 1–2%, on average, of those calculated with the TUV model of S. Madronich (NCAR), which is currently widely used in the literature. APL model j_{NO_2} agreed with the NCAR and FZJ spectroradiometers to with 1–2%, using the same NO_2 cross sections. APL model j_{O_3} also agreed with the NCAR j_{O_3} actinometer (and NCAR and FZJ spectroradiometers) to within about 1%, on average. Estimates of the aerosol optical properties differing from those specified during IPMMI (APL versus APL*), though otherwise reasonable, led to j_{NO_2} and j_{O_3} errors of up to 10%. It is thus essential to have an accurate description of aerosol properties when modeling *j*-values.

APL model j_{NO_2}, similar to the other models, which all used the *DeMore et al.* [1997]–recommended or similar NO_2 absorption cross sections, under-estimated by about 14% j_{NO_2} measured by the (adjusted) UMD chemical actinometer, which is only nominally within the combined uncertainties of the techniques. The use of larger (e.g., *Harder et al.* [1997]) NO_2 cross sections in model calculations would lead to much better agreement with actinometer measurements.[23] Similarly, spectroradiometer–actinometer agreement (with the actinometers individually or as a composite) throughout the intercomparison was better with the *Harder et al.* [1997] cross sections. This

[23]Incidentally, the use of the larger *Harder et al.* [1997] NO_2 cross sections during POLARIS would reduce the steady-state [NO_2] inferred from modeled j_{NO_2} (see chapter 3) and in situ species concentrations by *Del Negro et al.* [1999], improving agreement with measured [NO_2].

important finding suggests that the community should re-evaluate the NO_2 cross sections recommended for use in stratospheric/tropospheric modeling.

Further, it was found that modeling calculations using the ATLAS extraterrestrial flux led to better consistency with spectral actinic flux measured by the spectroradiometers, compared to the MODTRAN3 flux. There was little effect on the total j_{NO_2}, but ATLAS-derived j_{O_3} was about 7% smaller and in better agreement with j_{O_3} actinometer measurements. The ATLAS flux (290–420 nm) should be used in j-value modeling.

Chapter 3

Sensitivity Study of Photolysis Rate Coefficients during POLARIS

3.1 Introduction

In addition to an anomalous springtime ozone loss [*Newman et al.*, 1997], the high-latitude Northern Hemisphere experiences a naturally occurring seasonal cycle in which stratospheric ozone decreases by approximately 40% during the summer [*Lloyd et al.*, 1999], resulting from the balance of chemical loss and production of ozone and atmospheric dynamics [*Fahey et al.*, 2000]. To study the processes effecting ozone loss, the NASA-sponsored Photochemistry of Ozone Loss in the Arctic Region in Summer (POLARIS) high-altitude ER-2 aircraft campaign was conducted from Fairbanks, Alaska (65°N, 148°W), during the late spring and summer of 1997 (see section 1.4.2 for a more complete background of ER-2 missions).

Solar flux measurements were made by the Composition and Photodissociative Flux Measurement (CPFM) spectroradiometer flown on board the ER-2 [*McElroy*, 1995], from which photolysis rate coefficients (j-values) for $NO_2 \rightarrow NO + O(^3P)$ and $O_3 \rightarrow O_2 + O(^1D)$, j_{NO_2} and j_{O_3}, respectively, were derived [*McElroy et al.*, 1995]. The CPFM measurements can be used to validate *j*-values calculated with radiative transfer models. Such models also provide *j*-values for species not addressed by the CPFM instrument (e.g., species that photodissociate at $\lambda < 300$ nm), which are important in photochemical modeling of the upper troposphere/lower stratosphere. The APL radiative transfer model was used to calculate *j*-values for over 70 photochemical reactions of interest in the lower stratosphere and upper troposphere along the ER-2 flight tracks, including j_{NO_2} and j_{O_3}.[1]

The inherent sensitivity of *j*-values to the geophysical environment, as observed during POLARIS, is the principal focus of this chapter. Factors such as surface reflectivity (albedo), baseheight (atmospheric lower boundary altitude), total column ozone, ozone profile shape, solar zenith angle (SZA), and refraction all significantly affect *j*-values, which vary with altitude. Such a sensitivity study delineates the influence on photolysis of the individual factors, gauging their relative importance in the total *j*-values, and suggests the tolerance of model calculations to the simplification of input data. During the 1994 Airborne Southern Hemisphere Ozone Experiment/Measurements for Assessing the Effects of Stratospheric Aircraft (ASHOE/MAESA) ER-2 campaign, calculations of *j*-values with a previous version of the APL model, those with a model developed by *Salawitch et al.* [1994], and *j*-values derived from CPFM observations occasionally differed by as much as 50% for j_{NO_2} and by a factor of 2–3 for j_{O_3} (S. A. Lloyd, JHU/APL, personal communication, 1999). Improvements of both models and observational instrumentation during the POLARIS campaign have dramatically increased *j*-value agreement and thus the extent to which radiative transfer phenomena can be investigated with model–model and model–measurement comparisons.

---

[1] The POLARIS *j*-value calculations are archived at `ftp://espoarchive.nasa.gov`.

3.2 Model Description

The APL model (described in section 1.3, with ancillary information in appendix A) calculated the actinic flux in each wavelength bin: 175–298 nm (500-cm^{-1} bins),[2] 298–320 nm (0.5-nm bins), and 320–850 nm (5-nm), for SZAs of 0°–100°. Albedo was handled by assuming a Lambertian reflecting surface with uniform reflectivity applied at the baseheight, the atmospheric lower boundary altitude.

Four contributions to the actinic flux were calculated by the model: the direct attenuated flux, the multiply scattered flux, the ground (or cloud) reflection of the direct attenuated flux, and the ground (or cloud) reflection of the multiply scattered flux (see Figure A.1). The relative magnitudes of these components of the radiation field determine the sensitivity of *j*-values to albedo, baseheight, and ozone.

The accuracy of radiation field calculations of *j*-values depends on the accuracy of the model inputs. For this study, composite atmospheric profiles containing climatologies of density, temperature, and ozone were each derived by averaging six Fairbanks ozonesonde profiles from each POLARIS deployment (April–May, June–July, and September) (S. A. Lloyd, JHU/APL, personal communication, 1997). Ozone profiles were scaled to the total column ozone value using the profile itself as a weighting function (i.e., most changes in ozone occurred near the ozone peak, and the troposphere and upper stratosphere did not vary significantly). Molecular absorption cross sections and quantum yields were taken from the Jet Propulsion Laboratory compilation of chemical kinetic and photochemical data [*DeMore et al.*, 1997]. A background aerosol climatology was taken from the MODTRAN database [*Berk et al.*, 1989], appropriate for a volcanically quiescent period. A conservative estimate of the uncertainties of the mod-

[2] *Swartz et al.* [1999] erroneously reported 50-cm^{-1} bins at 175–295 nm.

eled j-values at ER-2 flight altitudes (15–22 km) are on the order of 15 and 20% for j_{NO_2} and j_{O_3}, respectively.

3.3 Theoretical Sensitivity

3.3.1 Altitude Profiles

Photolysis rate coefficients vary as a function of altitude in the atmosphere as the optical depth to the Sun, local molecular scattering, and proximity to the reflecting surface change. Wavelength dependencies of the actinic flux, molecular absorption cross sections, and photolysis quantum yields determine the j-value profile characteristics. The focus here is on the j-value sensitivity of two species, NO_2 and O_3 ($\rightarrow O(^1D)$). Not only are these two photolysis processes of principal importance in ozone production and loss, but they are also representative of two regimes of j-value sensitivity, photolyzing mainly in the near-ultraviolet (UV)/visible and at wavelengths less than 345 nm, respectively. Figures 3.1–3.4 show modeled altitude profiles of j_{NO_2} and j_{O_3}, where atmospheric inputs (albedo, baseheight, or ozone) were varied over the ranges observed during the POLARIS campaign. The SZA used in the calculations shown in Figures 3.1–3.4 was 60°, an intermediate value for POLARIS flights. The abscissa ranges of the plots in these figures are fixed to facilitate comparison between figures.

Albedo

The effect of varying the surface albedo from 0 to 1 is shown in Figure 3.1. (The albedo of open ocean in the near-UV/visible is typically less than a few percent; snow/ice/dense cloud cover can approach unity albedo.) The POLARIS June–July climatological atmospheric profile was used (total ozone is 308 Dobson units (DU)), with a baseheight

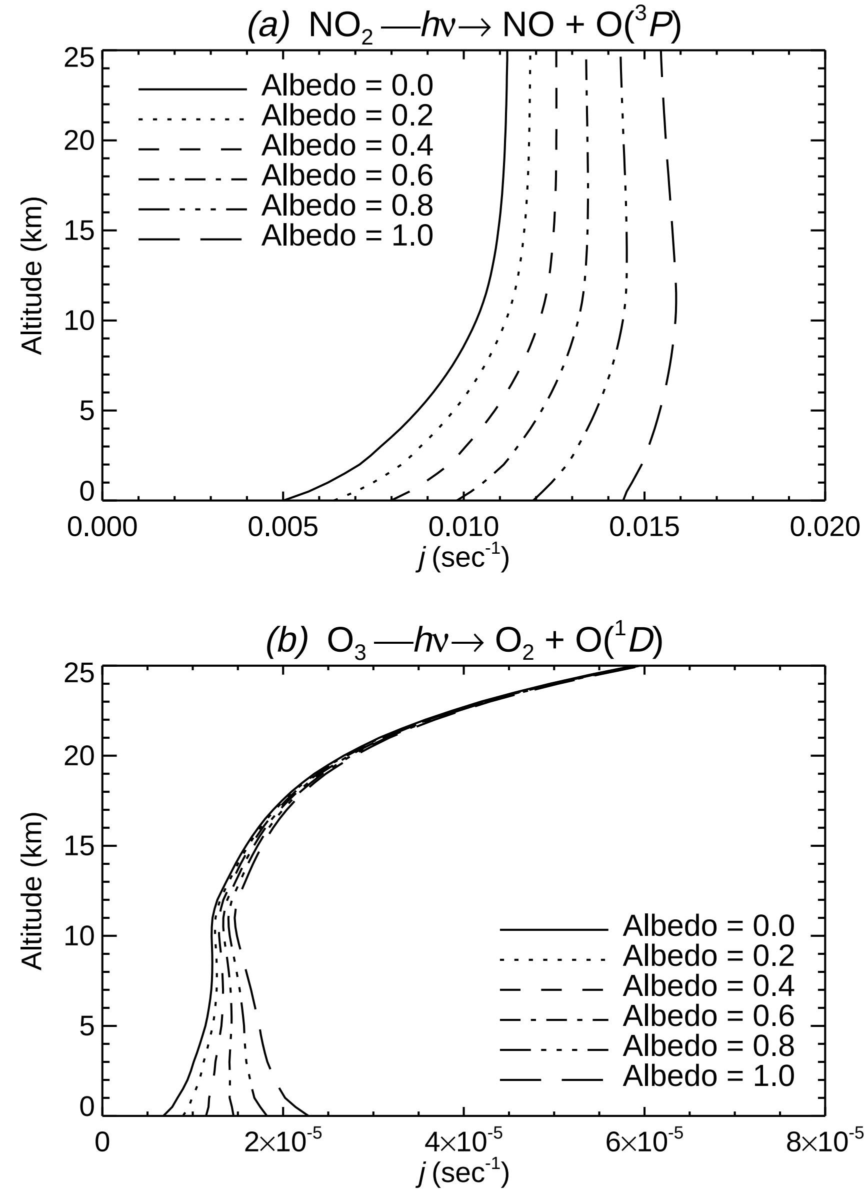

Figure 3.1. The effect of varying surface albedo on (a) $j_{\mathrm{NO_2}}$ and (b) $j_{\mathrm{O_3}}$ altitude profiles. The surface reflectivity (albedo) was sequentially set to 0 (a value close to that of open ocean), 0.2, 0.4, 0.6, 0.8, and 1 (snow/ice/dense cloud). In all cases, the POLARIS June–July climatological atmospheric profile was used (total column ozone is 308 Dobson units (DU)), with the baseheight fixed at 0 km and a SZA of 60°.

of 0 km. The *j*-values show significant enhancement in the troposphere as albedos increase. NO_2 photolyzes in the optically thin near-UV/visible; thus the effect of albedo is significant throughout the troposphere and stratosphere. At a 60° SZA, j_{NO_2} responds strongly to albedo changes, varying by nearly 50% at 20 km. For j_{O_3}, a photolysis process driven primarily by short-wavelength radiation ($\lambda < 320$ nm), the large optical depth of the stratosphere limits the albedo effect primarily to altitudes below the tropopause. While the albedo enhancement is large near the surface (greater than a factor of 2) as the albedo is increased from 0 to 1, its importance at ER-2 altitudes is greatly attenuated by atmospheric absorption below the aircraft (j_{O_3} varies by only a few percent).

Baseheight

The altitude of the lower atmospheric boundary (baseheight) can have an effect on *j*-values comparable to that of moderate changes in surface albedo. For the calculations shown in Figure 3.2, the albedo was fixed at 0.08, the value for terrain used in the Total Ozone Mapping Spectrometer (TOMS) satellite version 7 algorithm [*McPeters et al.*, 1998]. The baseheight was varied from 0 to 6 km (allowing for the possibility of passing over terrain as high as Mt. McKinley). Again, owing to the large optical depth of the atmosphere at shorter wavelengths, j_{O_3} is affected mainly at altitudes below ER-2 cruise altitudes. For these low-albedo cases, when the baseheight is increased, *j*-values at a given altitude decrease. Though raising the baseheight brings the reflective surface closer to the observer, thus reducing the optical path length and extinction of the reflected solar flux, it simultaneously eliminates flux scattered from the lowest layers of the troposphere. At low albedos, this scattering contribution from below dominates the effect on *j*-values due to changes in the baseheight. The effect at 20 km of raising the

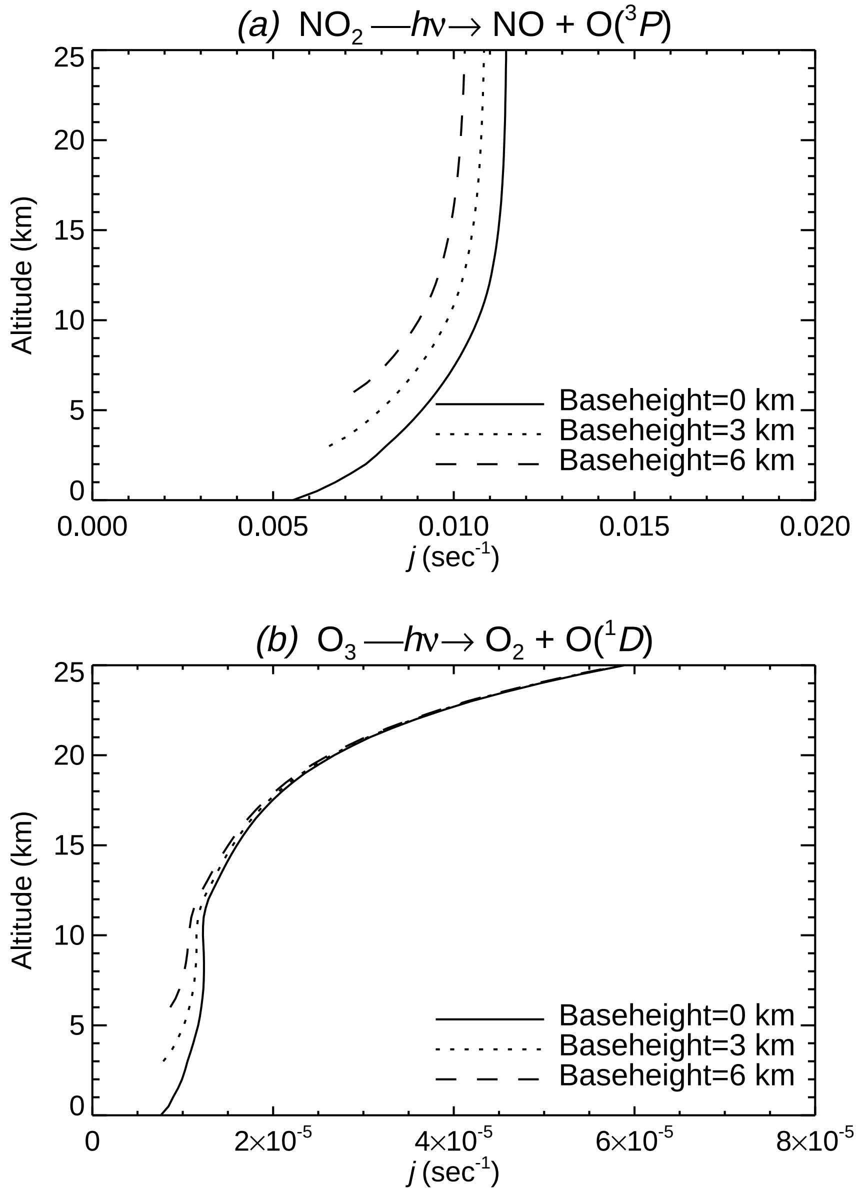

Figure 3.2. The effect of varying baseheight (atmospheric lower boundary altitude) on (a) j_{NO_2} and (b) j_{O_3} altitude profiles. Same as Figure 3.1, but with the albedo fixed at a typical terrain value of 0.08 and the baseheight set to 0 (total column ozone is 308 DU), 3 (ozone is 301 DU), and 6 km (ozone is 292 DU).

baseheight with an albedo of 0.08 from 0 to 6 km is 11% for j_{NO_2} and 2% for j_{O_3}. In contrast, when increasing the baseheight of highly reflective surfaces (not shown), such as snow, ice, or cloud, the increased contribution of the reflected solar flux roughly balances the loss of scattering from below, effectively eliminating baseheight sensitivity. The effect at 20 km of raising the baseheight with an albedo of 0.8 from 0 to 6 km is on the order of 0.1% for j_{NO_2} and 1% for j_{O_3}.

Ozone

The total column ozone and shape of the ozone profile varied over a wide range during POLARIS. Over the three deployments, the total ozone column over Fairbanks was reduced from a springtime high of approximately 450 DU to 250 DU by the end of summer [*Lloyd et al.*, 1999]. Figure 3.3 shows the effect on j_{NO_2} and j_{O_3} when the shape of the atmospheric profiles for density, temperature, and ozone and the total column ozone are varied, corresponding to the trends observed during POLARIS. Ozone photolysis increases by more than a factor of 2 at 20 km from midspring to late summer, whereas photolysis of NO_2, which does not spectrally overlap ozone absorption to any significant extent, increases by only 1.5%. Most of the increase, especially below the ozone density peak near 21 km, is due to the reduction of the partial ozone column above the observer altitude.

To delineate the effects of both the total column ozone and the atmospheric profiles on j_{O_3}, Figure 3.4 indicates how j_{O_3} changes when the total ozone is held fixed at 350 DU and the atmospheric profiles (of density, temperature, and ozone) are varied as they did throughout POLARIS. This is a nonphysical situation but demonstrates the importance of having the correct shapes of the atmospheric profiles as well as the total ozone amount. There is a significant impact near and above ER-2 flight altitudes.

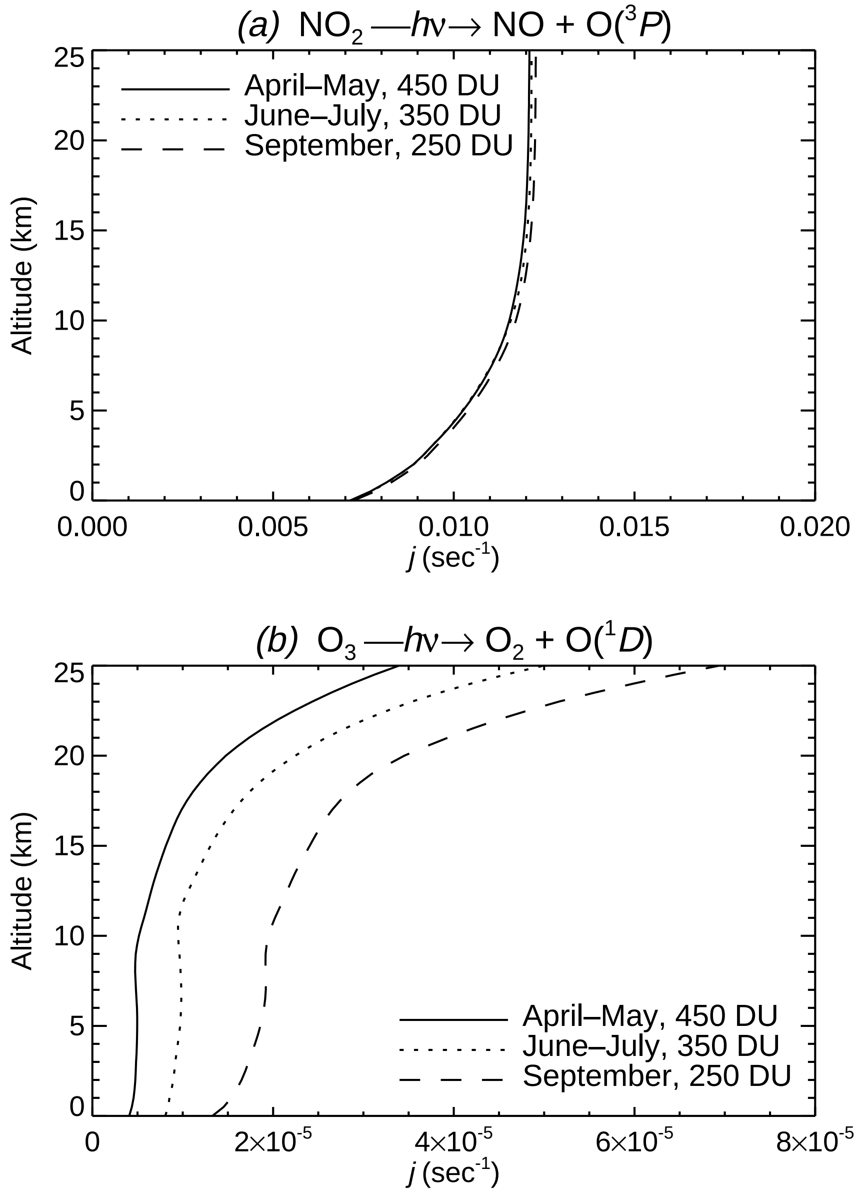

Figure 3.3. The effect of varying atmospheric profiles of density, temperature, and ozone and total column ozone (as they did during POLARIS) on (a) j_{NO_2} and (b) j_{O_3} altitude profiles. Same as Figure 3.1, but with the albedo fixed at the POLARIS average value of 0.3 and using the April–May (total ozone column scaled to 450 DU), June–July (ozone scaled to 350 DU), and September (ozone scaled to 250 DU) profiles.

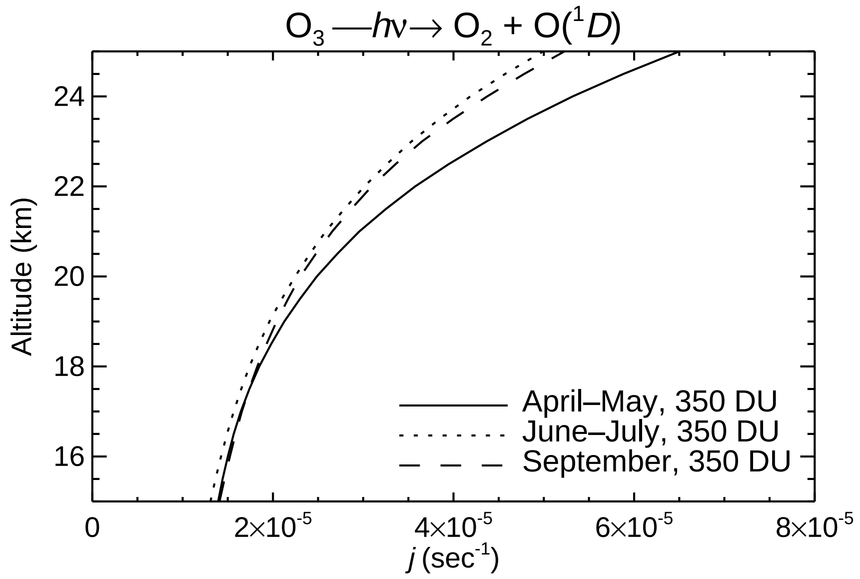

Figure 3.4. The effect of varying only the altitude distributions (i.e., profile shapes) of density, temperature, and ozone, holding total column ozone fixed, on j_{O_3}. Same as Figure 3.3b, but with the total column ozone fixed at 350 DU.

Under these conditions, j_{O_3} decreases by nearly 8% at 20 km and 15% at 22 km from midspring to late summer. This is caused by two factors. First, merely by distributing the ozone with the September rather than the April–May Fairbanks profile reduces j_{O_3}, as the median altitude of the ozone profile and thus the partial ozone column above the observer altitude is raised. Second, falling lower stratospheric temperatures throughout the summer diminish these temperature-dependent j-values. However, with both the total column ozone and atmospheric profile correctly accounted for in Figure 3.3, j_{O_3} is shown to increase throughout POLARIS, driven primarily by the reduction of total column ozone.

3.3.2 Solar Zenith Angle Profiles

As the solar zenith angle changes, so too does the sensitivity of j-values to albedo, base-height, and ozone. SZA profile calculations, ranging from 0° to 95° with the observer altitude fixed at a typical ER-2 cruise altitude (20 km), are shown in Figures 3.5–3.7.

Albedo

As in Figure 3.1, Figure 3.5 shows the effect of varying the albedo from 0 to 1. In general, as the SZA increases, the albedo sensitivity of these *j*-values diminishes. For clarity, the albedo enhancements relative to the cases with the albedo set to 0 are plotted in Figures 3.5c and 3.5d. Beyond 90°, the sensitivity of j_{NO_2} increases. This occurs because the albedo-sensitive surface reflection of the multiply scattered flux becomes relatively more important as the direct solar flux and its surface reflection are largely eliminated at high SZAs. The albedo sensitivity of j_{O_3} similarly increases beyond 80° as the direct flux is attenuated but diminishes beyond 90° as the surface-reflected multiply scattered flux again becomes a smaller fraction of the total actinic flux.

Baseheight

The SZA dependence of the baseheight effect on j_{NO_2} is shown in Figure 3.6. When the albedo is set to 0.08 and the baseheight is increased from 0 to 6 km, j_{NO_2} diminishes at all SZAs. Figure 3.6b shows the effect relative to the case with the baseheight at 0 km. (The maximum baseheight effect on j_{O_3} is on the order of only 3%.) Similar to Figure 3.5c, the sensitivity (*j*-value reduction when increasing the baseheight) of j_{NO_2} is minimized near 90°, beyond which multiple scattering dominates the actinic flux. As mentioned in section 3.3.1, when the surface albedo is large, the effects of scattering from below and the attenuation of the ground reflection largely cancel each other out (not shown). This balance is a function of SZA, with sensitivity to the surface reflection relatively more important at low SZAs. Regardless of SZA, the effect of changing the baseheight of a high-albedo surface is small.

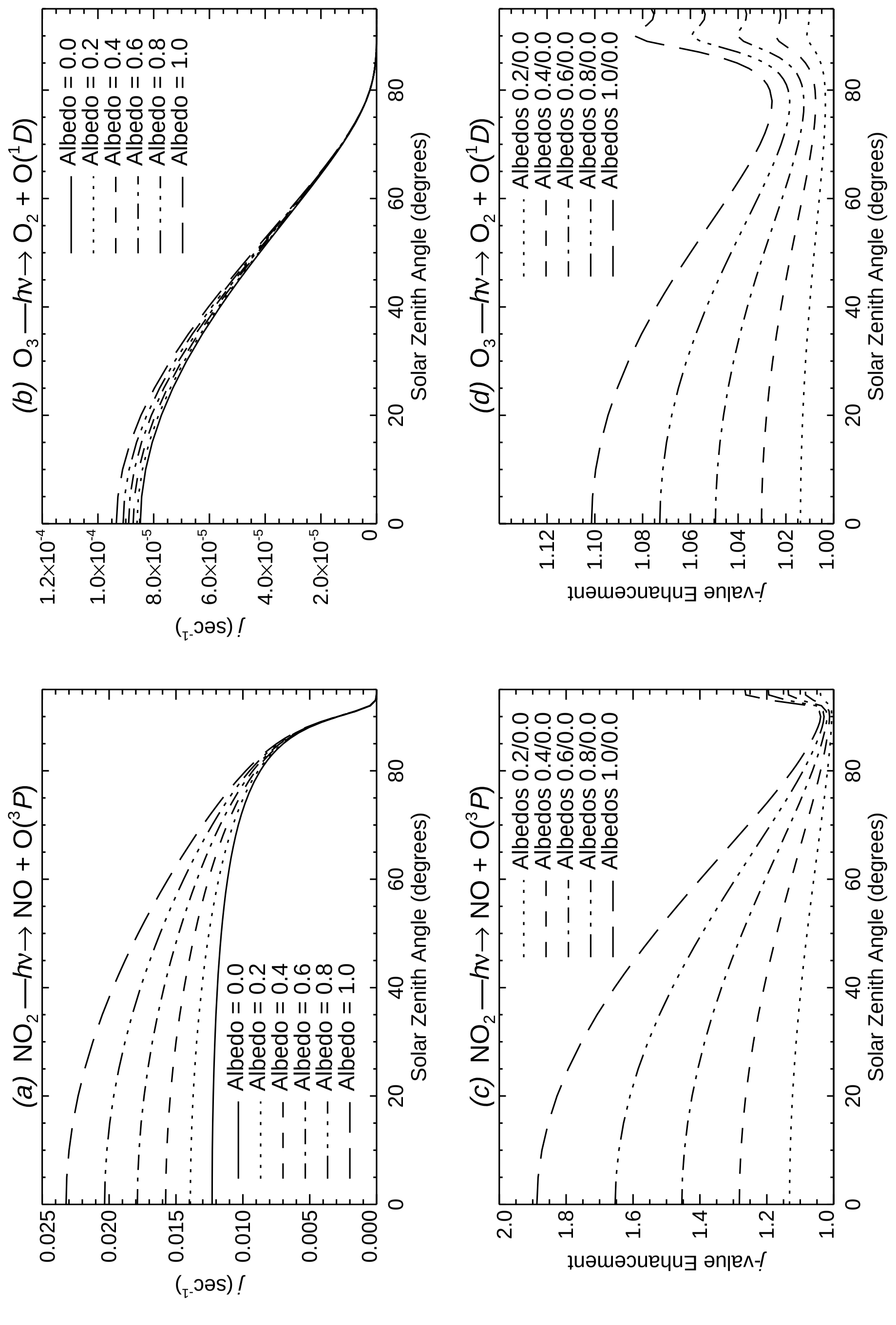

Figure 3.5. The effect of varying surface albedo on (a) $j_{\mathrm{NO_2}}$ and (b) $j_{\mathrm{O_3}}$ SZA profiles. Profiles (from 0° to 95° SZA) were modeled at 20 km. The albedo was sequentially set to 0, 0.2, 0.4, 0.6, 0.8, and 1. In all cases, the POLARIS June–July climatological atmospheric profile was used (total column ozone is 308 DU) with the baseheight fixed at 0 km. The *j*-value albedo enhancements (the ratios of *j*-values to the respective cases with albedo set to 0) are shown in (c) and (d).

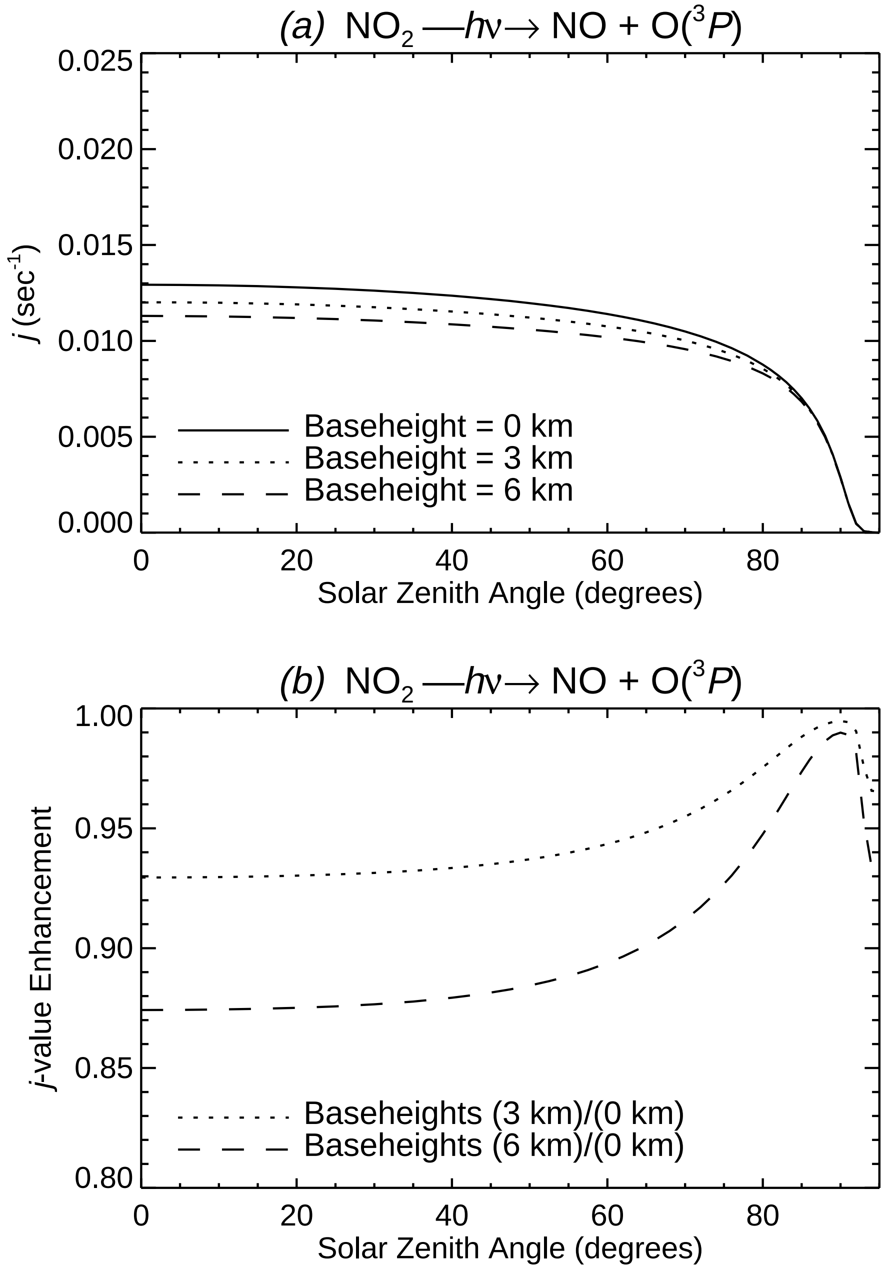

Figure 3.6. The effect of varying baseheight on j_{NO_2} SZA profiles at 20 km. Same as Figures 3.5a and 3.5c, but with the albedo fixed at a typical terrain value of 0.08 and the baseheight set to 0 (total column ozone is 308 DU), 3 (ozone is 301 DU), and 6 km (ozone is 292 DU).

Ozone

In Figure 3.7, the effect of the summertime ozone trend on j_{O_3} is depicted. While j_{NO_2} is insensitive to changes in the ozone profile, j_{O_3} increases by more than a factor of 2 over the entire range of SZAs, from midspring to late summer. At SZAs less than approximately 85°, photolysis of ozone is dominated by the direct solar flux. The slant path to the Sun through the ozone layer increases with SZA, thus increasing the sensitivity of j_{O_3} to the magnitude of the ozone column. At larger SZAs, the multiply scattered portion of the radiation field (a local effect) becomes relatively more important, thus diminishing the sensitivity of j_{O_3} to changes in the ozone column.

3.3.3 Refraction

Under many circumstances, the effect of atmospheric refraction on *j*-values is insignificant and can be neglected. However, at high SZAs, near sunrise/sunset and during the long polar twilight, refractive enhancement of photolysis rates can become important in the stratosphere [*DeMajistre et al.*, 1995; *Anderson et al.*, 1995]. The enhancement of j_{NO_2} due to refraction ($j_{\text{refraction}}/j_{\text{no refraction}}$) under POLARIS conditions is shown in Figure 3.8 at altitudes of 16, 18, 20, and 22 km. Refraction primarily affects the direct component of the actinic flux. As the observer altitude increases, so too does the fraction of the total actinic flux due to the direct component; thus, an effect that is insignificant at the surface (where local scattering often accounts for a majority of the actinic flux in the near-UV/visible) may become important at ER-2 altitudes. Photolysis of ozone (not shown) occurs at short wavelengths dominated by local scattering at high SZAs and is largely insensitive to refraction. NO_2, however, is photolyzed at longer wavelengths (where scattering is less important) and is more sensitive to refraction. At midlatitudes, photolysis at high SZAs is very brief, during sunrise and sunset, with *j*-values much

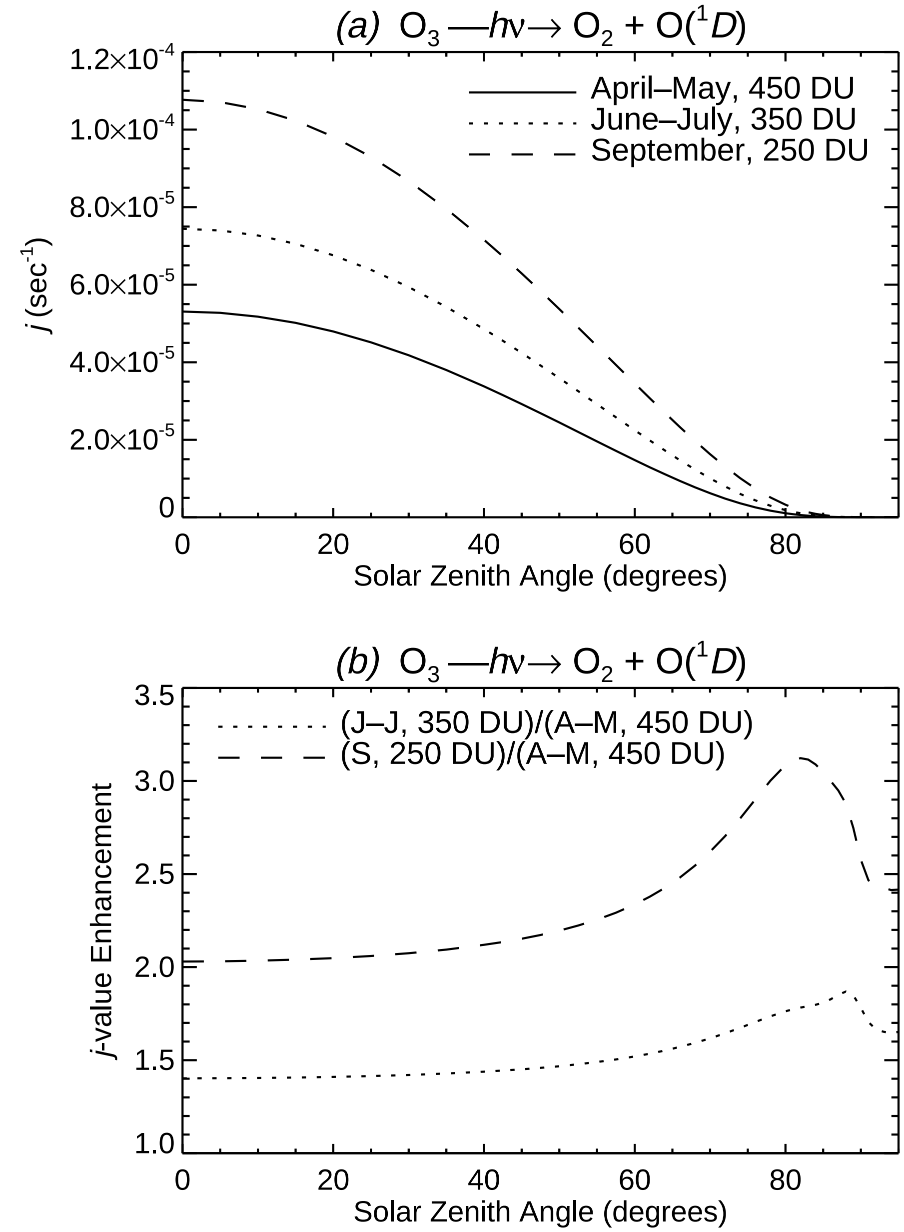

Figure 3.7. The effect of varying atmospheric profiles of density, temperature, and ozone and total column ozone (as they did during POLARIS) on j_{O_3} SZA profiles at 20 km. Same as Figures 3.5b and 3.5d, but with the albedo fixed at the POLARIS average value of 0.3 and using the April–May (total ozone column scaled to 450 DU), June–July (ozone scaled to 350 DU), and September (ozone scaled to 250 DU) profiles.

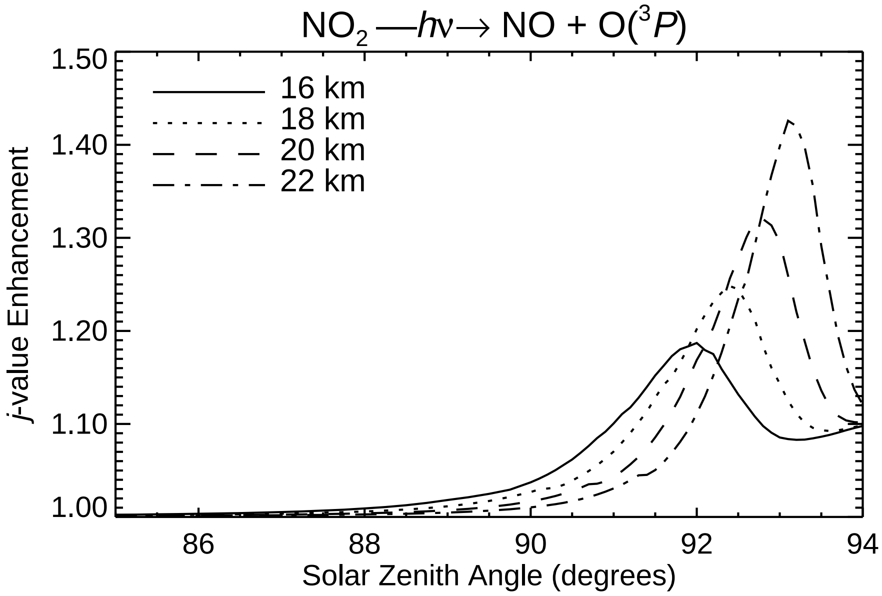

Figure 3.8. The effect of atmospheric refraction on j_{NO_2}. SZA profiles of *j*-value enhancements due to refraction (the ratio of $j_{\mathrm{refraction}}$ to $j_{\mathrm{no\ refraction}}$) were modeled at altitudes of 16, 18, 20, and 22 km, from 85° to 94° SZA. The POLARIS June–July atmospheric profile was used (total column ozone is 308 DU) with an albedo of 0.3.

less than those near noon. However, in the polar regions, which are often in twilight, the effect of refraction cannot be ignored.

3.4 Comparison with Observations along Flight Tracks

For many photolytic processes, *j*-values may be difficult to measure experimentally, for example, in polar twilight where flux measurements are difficult to make due to low light levels. It is generally only feasible to infer *j*-values from solar flux measurements for processes in the lower stratosphere for which there is no significant absorption at $\lambda < 300$ nm (where light levels are exceedingly low). One of the ultimate goals in thoroughly understanding how *j*-values respond to sundry physical variables is the ability to confidently extend *j*-value calculation to processes that cannot be readily measured.

The POLARIS mission has provided an opportunity to extensively compare modeled *j*-values with those derived from in situ solar flux measurements (for previous comparisons with the CPFM spectroradiometer, see *McElroy et al.* [1995]) and chemical constituent measurements [*Del Negro et al.*, 1999].

3.4.1 CPFM Instrument

The CPFM instrument is a compact, holographic grating spectrometer with a 1024-element Reticon photodiode array detector. Band-limiting filters allow operation in either the first order (nominally 375–775 nm) or second order (188–388 nm), with a FWHM of about 1.2 nm at the short end of the spectrum in the first order and about 1 nm in the near-UV in the second order. The instrument is housed in a small pod located on the right wing of the ER-2 aircraft, which allows for the sequential measurement of the downwelling irradiance and nadir and Earth-limb radiances every 2.2 min with only minimal optical interference from the aircraft fuselage. Downwelling irradiance is collected with a Teflon transmission diffuser covered with a quartz dome. A quartz prism driven by a stepping motor allows the rapid redirection of the spectrometer field of view among the various light sources measured. The limb angle range covered is from approximately 3.5° above the horizontal to 10° below in steps of 1.5°. The instrument and its data handling system have a very low noise level and measure with a precision better than 1% and an accuracy of 8% for the visible flux measurements and 9% for the UV [*McElroy*, 1995; *McElroy et al.*, 1995].

Photolysis rate coefficients are calculated from the spectral radiances and irradiances measured by the CPFM instrument. The spectral irradiance on the horizontal diffuser is corrected for the cosine effect and cosine error. Because the sky is essentially black at the altitudes at which the ER-2 flies (∼20 km), the direct solar beam component is approximately the total contribution from above the aircraft. A correction to the apparent horizontal irradiance is made to account for the small contribution from the limb before making the cosine correction. The apparent radiance within the nadir field of view (0.1° along-track × 5° across-track) is taken as representative of the upwelling radiation within a solid angle of π steradians, half of the solid angle below the aircraft, and a representative value from the limb scan is taken as representative of the light from the horizon, the other π steradians. A correction to the limb radiance is made that accounts for the expected (modeled) variation of the two components of limb polarization as a function of the solar elevation and azimuth angles, assuming a Rayleigh atmosphere [*McElroy*, 1984]. The horizontal irradiance and the nadir and limb radiances are integrated and convolved with the cross sections and quantum yields for the photodissociation of NO_2 and of O_3 ($\rightarrow O(^1D)$) to produce the total j-values. The ozone cross sections used for the POLARIS data were those measured by *Paur and Bass* [1985] (see also *Bass and Paur* [1985]), but all other molecular data follow the recommendations of *DeMore et al.* [1997]. The j-values for NO_2 are estimated to be accurate to about 10%, while j_{O_3} results are accurate to 15%. The accuracy of the latter is less because the signal-to-noise ratio near 300 nm is less than at longer wavelengths.

3.4.2 Model Implementation along the ER-2 Flight Track

Model input parameters, albedo and column ozone, were derived from measurements made during POLARIS, either from the CPFM spectroradiometer along the ER-2 flight track or from the TOMS satellite. Two sets of j-values were generated with the model. The first, APL_{CPFM}, utilized the inferred vertical ozone column above the ER-2 and (nadir) 600-nm albedo as measured by the CPFM (Rayleigh scattering is relatively unimportant at 600 nm). The other set of j-values, denoted APL_{TOMS}, used high-resolution (level 2) TOMS total ozone measurements and TOMS UV effective reflectivity for the surface albedo (the TOMS retrieval algorithm derives an effective surface reflectivity from the 360-nm channel by removing the calculated effect of Rayleigh scattering from the signal [*McPeters et al.*, 1998]). In both cases, the POLARIS climatological ozone profiles were scaled to the column ozone measurements, as described in section 3.2. The terrain and cloud top heights used in the model calculations were from the National Oceanic and Atmospheric Administration National Centers for Environmental Prediction (formerly National Meteorological Center) and the International Satellite Cloud Climatology Project, respectively, as used in the TOMS version 7 algorithm [*McPeters et al.*, 1998]. The following approach has been adopted for handling surface albedo/reflectivity and cloud top/terrain heights, consistent with the TOMS algorithm. If the albedo was less than 0.08, the baseheight was set to the terrain height. If the albedo was greater than 0.8, the baseheight was set to the cloud top height, from the TOMS climatology. When the albedo was between 0.08 and 0.8, two calculations were performed, one at the terrain height with an albedo of 0.08 and the other at the cloud top height with an albedo of 0.8. The effective cloud fraction (as defined in the TOMS algorithm) was then used to provide a weighted average of these two calculations, yielding the total j-values. If the surface climatology used in the TOMS retrieval indicated that there was a greater-than-50% chance of snow or ice on the ground, the reflectivities were recalculated accordingly (for more details, see *McPeters et al.* [1998]).

A comprehensive synopsis of each of the science flights[3] is found in Figure 3.9, including input data availability for each of the different model modes, SZA, j_{NO_2}, j_{O_3}, surface albedo, overhead ozone, temperature, and flight altitude. Other flight track information, including maps, is in appendix C.

[3]Dates are represented in YYYYMMDD format. 19970629 denotes June 29, 1997.

Figure 3.9. POLARIS ER-2 flight synopsis (see figure on page 97). Time from each science flight has been concatenated, and the beginning of each flight indicated with a labeled, full-figure vertical line. The two horizontal bands at the top of the figure indicate exactly when input data corresponding to each of the model modes were available (e.g., CPFM was not available for the 19970430 flight). The next panel shows the solar zenith angle (SZA) at the aircraft, with 93° indicated with a dotted line, which is the approximate SZA of sunrise/sunset in the lower stratosphere. APL_{TOMS} values of j_{NO_2} and j_{O_3} are shown in the next two panels as points of reference. TOMS albedo is shown next, followed by the APL_{TOMS} overhead ozone column above the ER-2. The air temperature at the aircraft is next shown, and the altitude of each flight is indicated.

3.4.3 General POLARIS Model–CPFM Comparison

The agreement between the j_{NO_2} and j_{O_3} calculated by the model (APL_{CPFM}) and that derived from CPFM flux measurements is shown in Figure 3.10. The data were taken from 17 Fairbanks-based POLARIS flights (i.e., excluding transit flights, where ozone profiles are less well represented by the Fairbanks ozonesonde-based climatologies). To eliminate issues associated with ER-2 takeoff and landing, the data compared were limited to pressures between 50 and 100 mb. Data where the SZA was greater than 85° were also excluded, to ensure the CPFM spectroradiometer had an adequate signal-to-noise ratio. On average, APL_{CPFM} calculations exceeded the CPFM flux-derived measurements by 6% for j_{NO_2} and 14%[4] for j_{O_3}, and APL_{TOMS} exceeded CPFM by 9% for j_{NO_2} and 8%[4] for j_{O_3} (not shown). Differences between modeled and CPFM flux-derived j-values may in part be due to uncertainties associated with convolving the rapidly changing actinic flux, cross sections, and quantum yields as a function of wavelength, especially for j_{O_3} in the 300–310-nm region.

[4]The use of the ATLAS extraterrestrial solar flux would reduce the model overestimate of j_{O_3} to approximately 7% for APL_{CPFM} and 1% for APL_{TOMS}, respectively (see section 2.7.2).

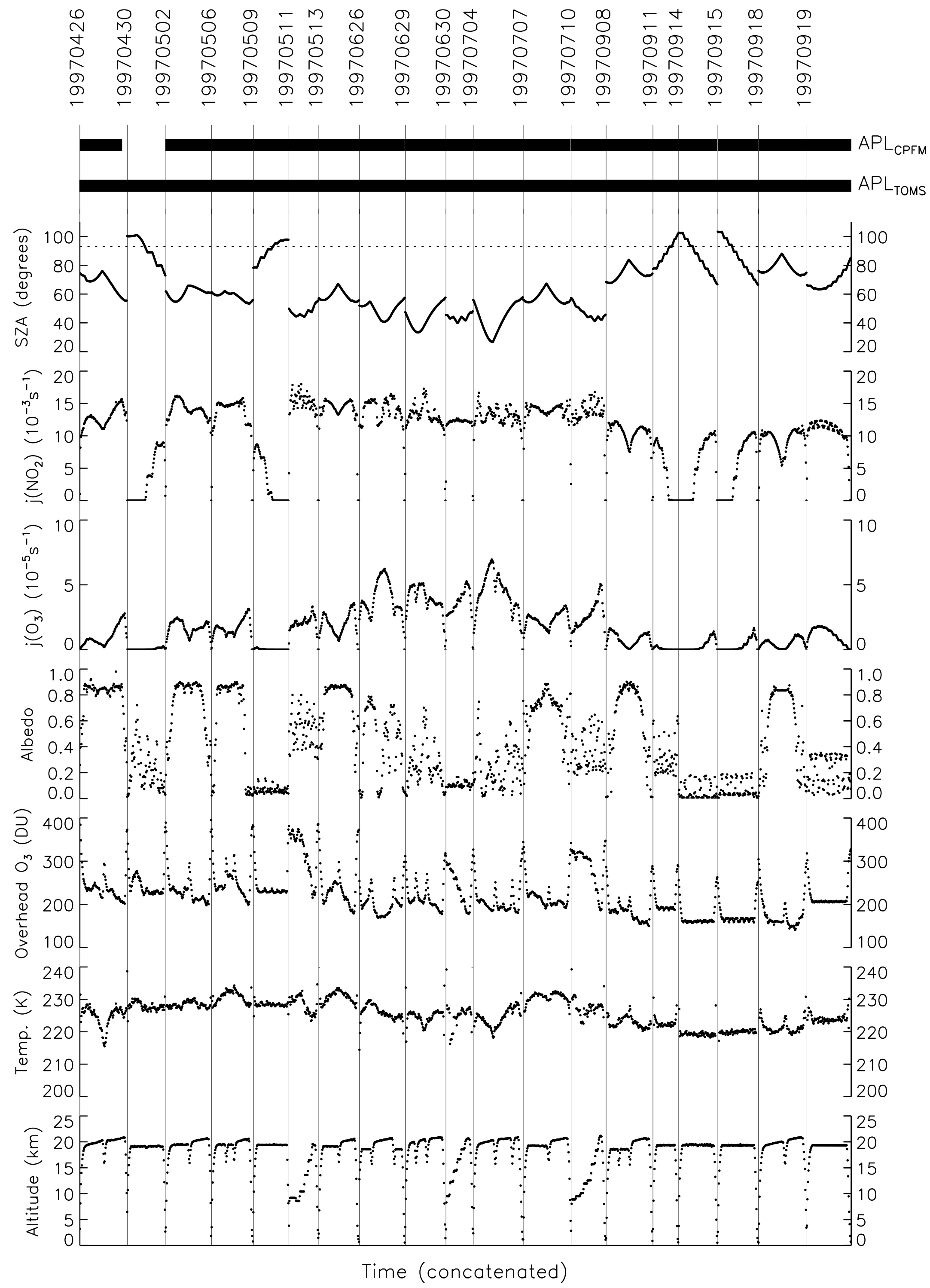

Figure 3.9. POLARIS ER-2 flight synopsis (see caption on page 96).

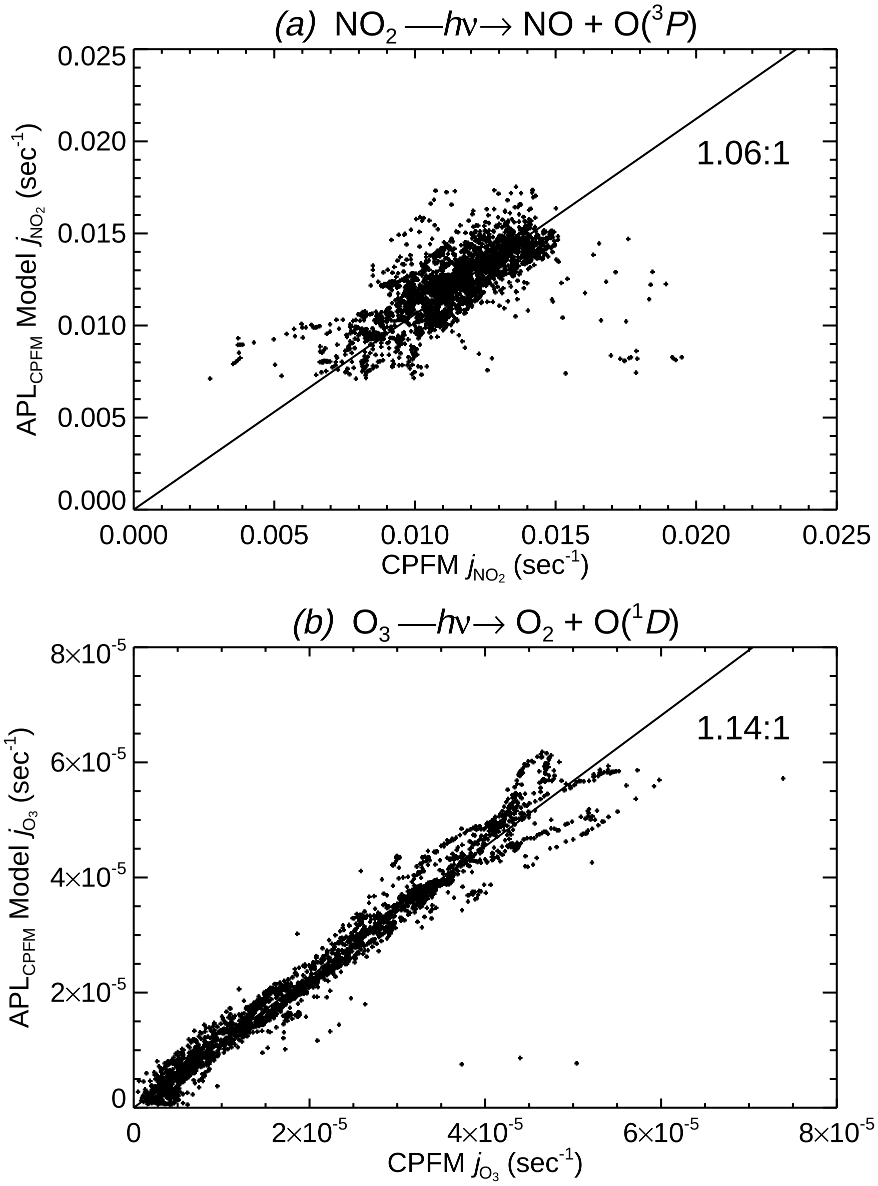

Figure 3.10. Agreement of APL_{CPFM} model and CPFM flux-derived (a) j_{NO_2} and (b) j_{O_3}. The data were taken from 17 POLARIS flights based from Fairbanks, at 50 mb < pressure < 100 mb and SZA < 85°. The solid lines represent the best fits through the data, when forced through the origin, with the slopes noted. The linear regression coefficients, r^2, are 0.56 (a) and 0.96 (b).

3.4.4 Specific Flight Comparison

To put the present sensitivity study in context, Figures 3.11 and 3.12 show comparisons of modeled and measured j-values along the 19970629 and 19970710 POLARIS flight tracks. Flight 19970629 was a constant-altitude flight with two dives, traveling from Fairbanks to Washington State and back. SZAs ranged from about 33° to 58°; albedos ranged from nearly 0 to 0.8; terrain heights ranged from 0 to 1.5 km; cloud top heights ranged from 3.5 to 5.5 km; and total column ozone ranged from 325 to 380 DU. Flight 19970710 was a step flight where the ER-2 flew a series of constant-altitude legs, from 9 to 21 km, in the vicinity of Fairbanks. The SZAs ranged from about 41° to 57°; albedos ranged from 0.1 to 0.7; terrain heights ranged from 0 to 1 km; cloud top heights ranged from 3.3 to 4.1 km; and total column ozone ranged from 325 to 360 DU. Only the at-altitude portions of the flights are discussed.

In Figure 3.11, j_{NO_2} along the ER-2 19970629 flight track is displayed. The CPFM-derived model j_{NO_2} and that derived from CPFM flux measurements are shown, along with CPFM albedo observations, in Figure 3.11a to emphasize the dependence of j_{NO_2} on albedo. The structure in j_{NO_2} along the flight track is well correlated with changes in albedo. The APL_{TOMS} calculations are plotted with the TOMS albedo in Figure 3.11b. The TOMS-derived calculations are occasionally somewhat "blocky" when compared with CPFM spectroradiometer measurements, due to the Earth Probe TOMS nadir footprint of approximately 26×26 km on the ground (during POLARIS, prior to the December 1997 Earth Probe orbit change). The CPFM data, which were collected on a 2.2-min timescale, and APL_{CPFM}, which uses CPFM albedo as input, show finer spatial variability than that seen in the TOMS data. The CPFM illustrates real-time temporal variability, whereas the TOMS data are a once-a-day snapshot near local noon, presumed to be a reasonable approximation for the entire flight.

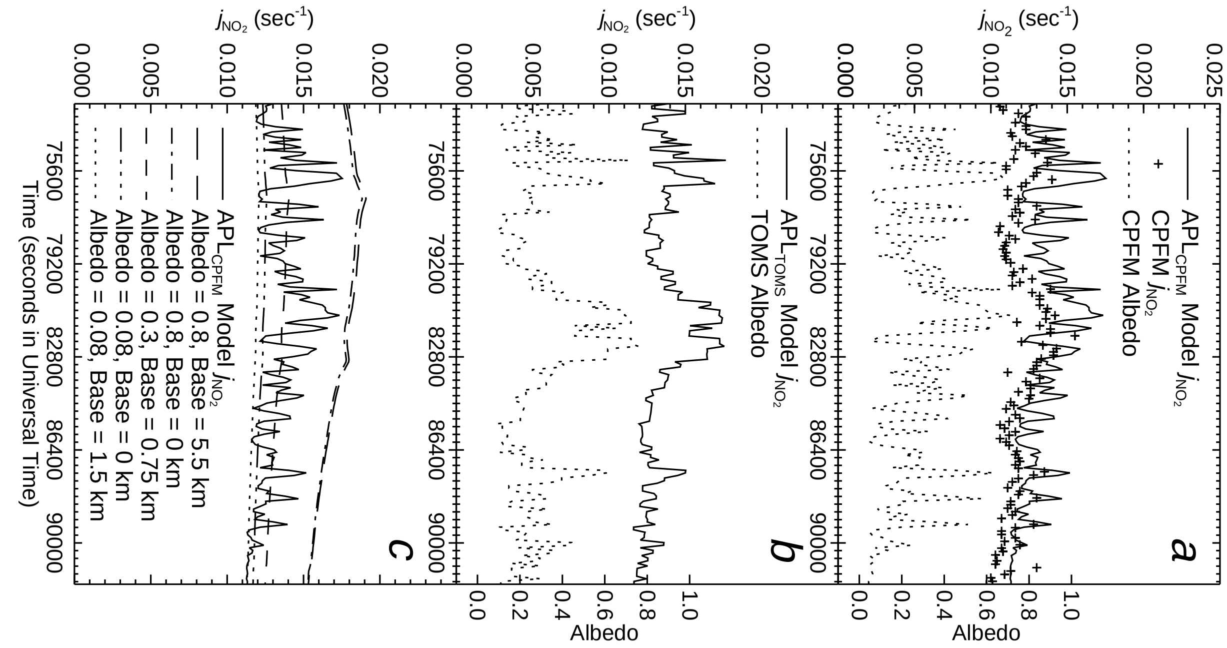

Figure 3.11. Modeled and measured j_{NO_2} from POLARIS flight 19970629. (a) Modeled j_{NO_2} using CPFM-derived albedo and overhead ozone. The CPFM flux-derived j_{NO_2} and albedo observations are overplotted. (b) Modeled j_{NO_2}, same as (a), but using TOMS albedo and derived overhead ozone. (c) The modeled APL$_{CPFM}$ j_{NO_2} (same as that in (a)) is compared with a series of model runs holding the albedo and baseheight fixed as shown.

In order to separate and illustrate the major physical parameters that control j_{NO_2} and to put them into the context of specific POLARIS conditions, Figure 3.11c shows a series of j_{NO_2} model calculations along with the APL_{CPFM} model j_{NO_2} from Figure 3.11a. With the baseheight set to 0 km, two sets of model j-values were generated with albedos of 0.08 and 0.8, that of terrain and snow/ice/cloud in the TOMS version 7 algorithm [*McPeters et al.*, 1998]. (An albedo of 0.8 at 0 km represents snow/ice cover.) To demonstrate the range of terrain and high-albedo baseheights, calculations were also made with an albedo of 0.08 at 1.5 km and with an albedo of 0.8 at 5.5 km. To simulate generic conditions, a sixth model calculation is included with an albedo of 0.3 and terrain height of 0.75 km, intermediate values for the flight. Though this generic set of physical inputs produces j_{NO_2} values that are reasonable, ignoring the sensitivity of j_{NO_2} to albedo and baseheight could result in errors of 20% for some parts of the flight. Changes in albedo account for most of the j_{NO_2} variability. As discussed in sections 3.3.1 and 3.3.2, baseheight has the greatest effect at low albedo. The dependence of the albedo sensitivity on SZA can also be seen as the low-to-high albedo difference was greatest when the SZA reached a minimum for the flight near 76800 s UT. The sensitivity diminished throughout the rest of the flight as the SZA increased.

In Figure 3.12, j_{O_3} is similarly displayed for the 19970710 flight. Model calculations using both CPFM and TOMS albedo/ozone and the CPFM flux-derived values are shown in Figure 3.12a. Unlike j_{NO_2}, j_{O_3} is very sensitive to altitude (i.e., the partial ozone column above the ER-2). The ER-2 altitude is included for comparison. There are two major factors that impacted j_{O_3} along this flight track: albedo and ozone absorption (either in terms of total column ozone or ozone above the ER-2). The CPFM albedo, CPFM measurements of ozone above the ER-2, and the ozone above the ER-2 derived from TOMS total ozone are shown in Figure 3.12b. The CPFM and TOMS-derived

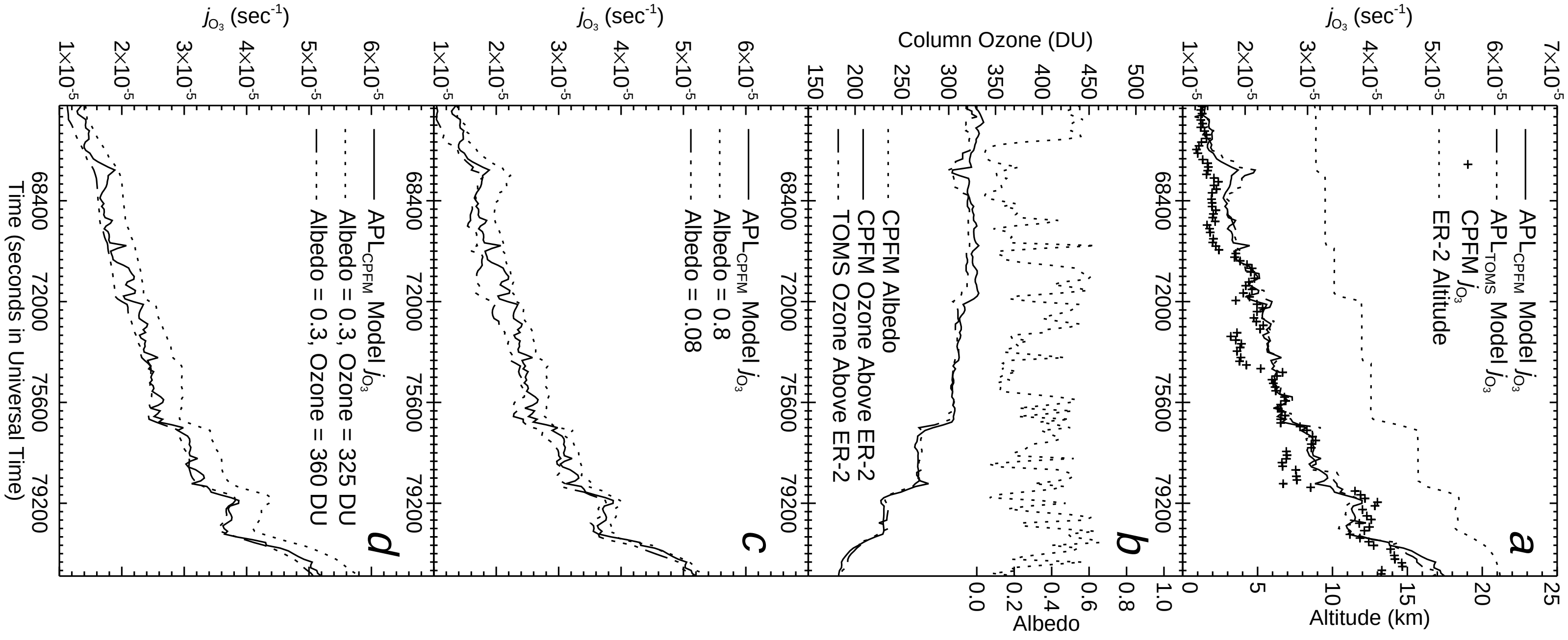

Figure 3.12. Modeled and measured j_{O_3} from POLARIS flight 19970710. (a) Modeled j_{O_3} using both CPFM and TOMS albedo and overhead ozone. CPFM flux-derived j_{O_3} and ER-2 altitude are overplotted. (b) Observed CPFM albedo with overhead ozone amounts measured by CPFM and also that derived from TOMS total ozone measurements. (c) The modeled APL$_{CPFM}$ j_{O_3} (same as that in (a)) is compared with model runs fixing the albedo at 0.08 and 0.8. (d) APL$_{CPFM}$ j_{O_3} compared with model results with the albedo fixed at 0.3 and the total ozone set to 325 and 360 DU.

ozone above the ER-2 are in excellent agreement and can be used interchangeably. To examine the relative impact of albedo and ozone variability on j_{O_3} for this POLARIS flight, the model is again used with particular parameters fixed. Figure 3.12c shows results with albedos set to 0.08 and 0.8 along with the standard APL_{CPFM} model calculations. As the ER-2 altitude increased during the flight, the sensitivity to albedo diminished and the high- and low-albedo curves converge throughout the flight (compare with Figure 3.1b). The maximum impact of the range of total ozone for the 19970710 flight on j_{O_3} is depicted in Figure 3.12d, with the total ozone set to the extremes observed by CPFM.

Departures of CPFM j_{O_3} from the model calculations arise largely from solar scattering from an inhomogeneous cloud field along the horizon, which is not represented in either the measured surface albedo or the partial ozone column or thus in the isotropic model calculations. For example, from 74700–77400 s UT, CPFM j_{O_3} rose by nearly 20% while there were no significant changes in the model j_{O_3}. This variability, which is particularly evident in the 19970710 flight, is due to changes in the limb contribution to the CPFM flux measurements (not shown). In contrast, the model assumes a uniform Lambertian reflecting surface with an albedo determined by either CPFM or TOMS observations. The surface albedo derived from the CPFM is deduced from the apparent upwelling radiance from within a limited, nadir field of view. Real variability on the limb (e.g., from reflections from scattered clouds), however, does not appear in these surface albedo measurements. Therefore some of the geophysical variability observed by the CPFM is not captured in model calculations.

3.5 Summary and Conclusions

The sensitivity of j_{NO_2} and j_{O_3} to surface albedo, atmospheric baseheight, total ozone, ozone and temperature altitude profile shape, solar zenith angle, refraction, and observer altitude were explored in the context of the POLARIS mission at a theoretical level by varying physical input parameters to the APL radiative transfer model over the ranges observed during the campaign. In general, j-values were most sensitive to albedo in the troposphere, where optical depths to the surface were relatively small. Changing a low-albedo baseheight from sea level to mountain top height decreased j-values, due to the reduction of upwelling Rayleigh scattering. The effect was significant throughout the troposphere and lower stratosphere for NO_2, which photodissociates in the optically thin near-UV/visible. The j-values studied were insensitive, however, to the baseheight of high-albedo surfaces (e.g., clouds). The effect on j-values of variations in albedo and baseheight decreased with SZA, except near twilight where j-values actually were more sensitive. Ozone, which photodissociates at wavelengths less than 345 nm, was sensitive to both the magnitude and the shape of the ozone altitude profile. The sensitivity of j_{O_3} to ozone reached a maximum at approximately 85° SZA.

At typical ER-2 cruise altitudes (15–22 km) with a SZA of 60°, the relative magnitudes of the j-value sensitivities to physical parameters (varying as they did during the entire POLARIS campaign) are albedo $>$ baseheight $\gg$ total ozone for j_{NO_2} and total ozone $\gg$ albedo $>$ baseheight for j_{O_3}. The enhancement of j-values due to atmospheric refraction at high SZAs increases with altitude through the lower stratosphere. Refraction has a negligible effect on j_{O_3} but can enhance j_{NO_2} by up to 40% at 22 km relative to the no-refraction case, peaking at a SZA of 93°.

On average, APL_{CPFM} calculations exceeded the CPFM flux-derived measurements by 6% for j_{NO_2} and 14%[5] for j_{O_3}, and APL_{TOMS} exceeded CPFM by 9% for j_{NO_2} and 8% for j_{O_3}.[5] The sensitivity of j-values was further illustrated by varying physical inputs in the context of specific flights and comparing these results with observation-derived j-values. Model calculations of j_{NO_2} and j_{O_3} along specific ER-2 flight tracks show excellent agreement with those derived from CPFM flux measurements on board the ER-2. Some disagreements stem from fundamental limitations of the model input data, underlining the need for complete, measured descriptions of the geophysical environment. Variations in j_{NO_2} were principally due to and are well correlated with changes in surface albedo. Ozone above the ER-2 and albedo have the greatest impact on j_{O_3}.

[5]The use of the ATLAS extraterrestrial solar flux would reduce the model overestimate of j_{O_3} to approximately 7% for APL_{CPFM} and 1% for APL_{TOMS}, respectively (see section 2.7.2).

Chapter 4

Comparison of Modeled and Measured *j*-Values during SOLVE

4.1 Introduction

The SAGE III Ozone Loss and Validation Experiment (SOLVE) was the most recent of a series of NASA field missions to study the lower stratosphere in connection with polar ozone depletion (see section 1.4.2 for a summary of polar field missions). The NASA ER-2 and DC-8 aircraft, flying above and near the tropopause, were used along with a number of remote sensing satellite-, balloon-, and ground-based instruments to characterize the atmosphere of the wintertime high northern latitudes. The SOLVE mission, in concert with the Third European Stratospheric Experiment on Ozone 2000 (THESEO 2000), was based in Kiruna, Sweden (68°N, 20°E), from November 1999 through March 2000 in three intensive deployments.

As in POLARIS, the model calculation of *j*-values, in addition to those derived from in situ flux measurements, played an important role in the photochemical analysis of the chemistry of ozone. Building upon the success of POLARIS (chapter 3), the sophistication of the geophysical data input to the APL radiative transfer model was increased in order to cope with the high–solar zenith angle (SZA) conditions found in polar winter and due to a lack of secondary observations at high latitudes. A comprehensive ozone/pressure/temperature/albedo climatology (S. Hollandsworth Frith, NASA/Goddard, personal communication, 1999) was adopted as a baseline description of the atmosphere. Earth Probe Total Ozone Mapping Spectrometer (TOMS) satellite [*McPeters et al.*, 1998] and Composition and Photodissociative Flux Measurement (CPFM) spectroradiometer [*McElroy*, 1995] (ER-2 only) data were utilized, as in POLARIS, along with remote sensing data from the Polar Ozone and Aerosol Measurement (POAM) III satellite instrument [*Lucke et al.*, 1999] and in situ ozone data from the ER-2 [*Proffitt and McLaughlin*, 1983; *Richard et al.*, 2001] and DC-8.[1]

This chapter contains some details of the model development for SOLVE and its application along DC-8 flight tracks.[2] j-Values computed using different model inputs are compared and the impacts of using various inputs are examined. The DC-8 j-values are also compared with the results from the Scanning Actinic Flux Spectroradiometer (SAFS) [*Shetter and Müller*, 1999], which measured the 4π-sr actinic flux on board the DC-8. In section 4.5.2, the attenuation of j-values, likely by polar stratospheric clouds (PSCs), is also presented.

Model–model comparisons for the ER-2 flight tracks are presented separately in appendix E.

[1] See `http://www-gte.larc.nasa.gov/trace/TP_Avery_Vay_Instrument.htm` and references therein.

[2] The SOLVE j-value calculations are archived at `ftp://espoarchive.nasa.gov`.

4.2 Model Input Changes since POLARIS

For the SOLVE campaign, the *Molina and Molina* [1986] temperature-dependent ozone cross sections were replaced with those of *Paur and Bass* [1985] (see also *Bass and Paur* [1985]) from 245 to 345 nm.[3] The APL model was used to demonstrate the relative effect of using the *Paur and Bass* measurements. Figure 4.1a shows that this change had only a minor effect (<2%) on j_{O_3}. A much more important modification came with the realization of the importance of the long wavelength tail of the $O_3 \rightarrow O_2$ + O(^1D) quantum yield out to 345 nm [*Sander et al.*, 2000]. Inclusion of this tail is crucial, particularly at high SZAs, when the relative contribution of long wavelengths to j_{O_3} becomes important. This substantial effect (up to nearly a factor of 4) can be seen in Figure 4.1b. In this case, *Molina and Molina* cross sections were used and only the quantum yields were changed, from the *DeMore et al.* [1997] recommendation to that of *Sander et al.*, extending the long-wavelength limit of ozone photolysis (to produce O(^1D)) from 325 to 345 nm.

Due to the findings of the IPMMI investigation (see sections 2.5.2 and 2.7.2), the MODTRAN high-resolution extraterrestrial flux [*Berk et al.*, 1989] was replaced with the more realistic ATLAS flux [*Kaye and Miller*, 1996; *Woods et al.*, 1996] over the following wavelength ranges: 175.4–200.0 nm (*WMO* [1986]), 200.0–407.8 nm (ATLAS-3[4]), and 407.8–419.9 nm (ATLAS-2[4]).

---

[3]Though the most recent recommendation from the Jet Propulsion Laboratory [*DeMore et al.*, 1997] calls for the use of the *Molina and Molina* [1986] data, the *Paur and Bass* [1985] (see also *Bass and Paur* [1985]) cross sections are generally accepted within the ER-2 community as the best estimate for ozone absorption in this wavelength range because of the more complete parameterization of the temperature dependence of the cross sections.

[4]From B. Mayer (German Aerospace Center), in the `atlas_plus_modtran` file in A. Kylling's (Norwegian Institute for Air Research) LibRadtran v0.14 model. For a current version of the model, see `http://www.libradtran.org`.

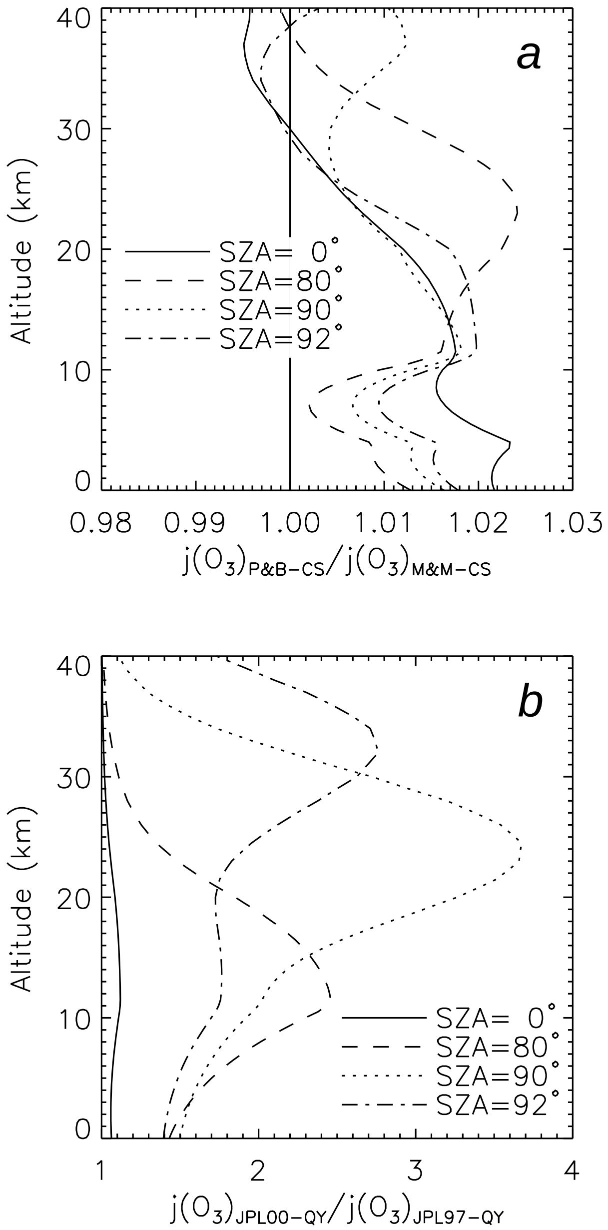

Figure 4.1. Sensitivity of j_{O_3} to cross sections and quantum yields. The APL model was used to calculate j_{O_3} using different molecular data in the U. S. Standard Atmosphere [*COESA*, 1976] with a surface reflectivity of 0.3. Calculations at four different solar zenith angles are shown. (a) Ratios of j_{O_3} using ozone absorption cross sections of *Paur and Bass* [1985] (SOLVE version) compared with those of *Molina and Molina* [1986] (POLARIS version), both using *Sander et al.* [2000] quantum yields. (b) Ratios of j_{O_3} using quantum yields of *Sander et al.* [2000] (JPL00, SOLVE version) compared with *DeMore et al.* [1997] (JPL97, POLARIS version), both using *Molina and Molina* [1986] cross sections.

The wavelength binning over which the model calculated flux (and consequently j-values) was modified to increase the resolution in the critical 295- to 300-nm range. High wavelength resolution is necessary where actinic flux and molecular data change very rapidly [*Madronich and Weller*, 1990]. The binning was as follows: 175–295 nm (500-cm^{-1} bins), 295–330 nm (0.5-nm bins), 330–347.5 nm (2.5-nm bins), 347.5–427.5 nm (5-nm bins), and 427.5–852.5 nm (10-nm bins).

A detailed accounting of these and other inputs is in appendix A.

Finally, the DC-8 and ER-2 were fitted with Global Positioning System (GPS) receivers for the first time, and the altitude registration came from these measurements instead of the pressure altitude (i.e., altitude derived from flight pressure and an assumed pressure–altitude relationship) as during POLARIS. Errors in the pressure altitude of more than 0.5 km were found during SOLVE, compared with the GPS.

4.3 Description of the Application of the Model

The APL radiative transfer model was used in a number of different "modes" to simulate photolysis rate coefficients along the DC-8 and ER-2 flight tracks during SOLVE. The differences between the various j-value modes ($APL_{clim[*]}$, $APL_{TOMS[*]}$, $APL_{CPFM[*]}$, $APL_{POAM[*]}$) reflect how different model inputs were utilized. The APL_{TOMS} mode was based on TOMS level 2 data (total column ozone, ultraviolet (UV) effective reflectivity, and cloud fraction); the APL_{CPFM} calculation (ER-2 only) was based on CPFM data (partial column ozone above the ER-2 and 600-nm albedo); the APL_{POAM} mode was based on POAM III O_3–potential vorticity (PV)[5] reconstruction data (ozone profiles; temperature and pressure from the United Kingdom Meteorological Office (UKMO))

[5]See section F.2 for the definition of PV.

[*Randall et al.*, 2002], with the APL_{clim} mode relying wholly on climatological data. The variants of each model mode marked with an asterisk also incorporated in situ ozone data from the DC-8 or ER-2, with the ozone profiles constrained to agree with the in situ ozone at the aircraft altitude.

Every effort has been made to ensure the quality of these inputs. However, the twilight illumination conditions encountered during SOLVE made many of these observations difficult or impossible. For instance, TOMS data were only reported for SZAs of less than 84°. Therefore, for many of the December 1999–February 2000 flights, TOMS data were only available when the aircraft traveled to the southernmost portions of the region and sometimes were not available at all for northbound flights. Similarly, the quality of the CPFM data at high SZAs diminished with signal-to-noise ratio, especially in the near-UV. The inputs and how they were handled in each of these model modes are described in detail in sections E.1 and E.2 and also summarized in Table 4.1.

4.4 Data Filtering

Complete sets (from take-off to landing) of *j*-values in all model modes were reported for each and every DC-8 and ER-2 flight during SOLVE. However, in order to assess the efficacy of each of the modes, the data analyzed in the model–measurement and model–model comparisons reported in the following sections were filtered to exclude data that would render the results of the analysis more difficult to interpret.

There were 17 DC-8 science flights spanning three deployments in Kiruna, Sweden, in November–December 1999, January 2000, and February–March 2000. Similarly, there were 11 ER-2 science flights during two deployments during SOLVE, in January–February and February–March 2000, coinciding with the latter two DC-8 intensives.

Table 4.1. Description of APL model modes used during SOLVE

Name	Temperature/ Pressure Profiles	Overhead Column Ozone	Total Column Ozone	In Situ Ozone	Default Ozone Profile	Albedo	Default Albedo
ER-2:							
$\mathrm{APL}_{\mathrm{CPFM}*}$	clim[a]	CPFM[b]	TOMS[c]	NOAA[d]	clim[a]	CPFM[b]	clim[a]
$\mathrm{APL}_{\mathrm{POAM}*}$	POAM[e]	—	—	NOAA	POAM[e]	TOMS[c]	clim
$\mathrm{APL}_{\mathrm{TOMS}*}$	clim	—	TOMS	NOAA	clim	TOMS	clim
$\mathrm{APL}_{\mathrm{clim}*}$	clim	—	—	NOAA	clim	clim[a]	clim
$\mathrm{APL}_{\mathrm{CPFM}}$	clim	CPFM	TOMS	—	clim	CPFM	clim
$\mathrm{APL}_{\mathrm{POAM}}$	POAM	—	—	—	POAM	TOMS	clim
$\mathrm{APL}_{\mathrm{TOMS}}$	clim	—	TOMS	—	clim	TOMS	clim
$\mathrm{APL}_{\mathrm{clim}}$	clim	—	—	—	clim	clim	clim
DC-8:							
$\mathrm{APL}_{\mathrm{POAM}*}$	POAM	—	—	LaRC[f]	POAM	TOMS	clim
$\mathrm{APL}_{\mathrm{TOMS}*}$	clim	—	TOMS	LaRC	clim	TOMS	clim
$\mathrm{APL}_{\mathrm{clim}*}$	clim	—	—	LaRC	clim	clim	clim
$\mathrm{APL}_{\mathrm{POAM}}$	POAM	—	—	—	POAM	TOMS	clim
$\mathrm{APL}_{\mathrm{TOMS}}$	clim	—	TOMS	—	clim	TOMS	clim
$\mathrm{APL}_{\mathrm{clim}}$	clim	—	—	—	clim	clim	clim

[a] Derived from climatologies described in section E.1.1.

[b] Environment Canada's Composition and Photodissociative Flux Spectroradiometer [*McElroy*, 1995].

[c] Earth Probe Total Ozone Mapping Spectrometer (TOMS) satellite instrument [*McPeters et al.*, 1998].

[d] ER-2 in situ O_3 measured by NOAA/Aeronomy Laboratory by UV absorption [*Proffitt and McLaughlin*, 1983; *Richard et al.*, 2001].

[e] Derived from POAM III O_3–PV reconstruction [*Randall et al.*, 2002]. At altitudes below 14 and above 60 km, POAM III–reconstructed data were typically not available, so climatological profiles were used instead at these altitudes, as in the other *j*-value modes.

[f] DC-8 in situ O_3 measured by NASA/Langley by chemiluminescence (see `http://www-gte.larc.nasa.gov/trace/TP_Avery_Vay_Instrument.htm` and references therein).

For the j-value comparisons, all transit flights (and test flights) were excluded, limiting the analysis to high latitudes centered around Kiruna.

Data shortly after takeoff and just before landing, when the aircraft were potentially below tropospheric clouds or banked, were excluded, below 8 and 15 km for the DC-8 and ER-2, respectively. Also excluded were modeled or measured j-values smaller than those typical at SZAs beyond sunrise/sunset (92°–93°): 10^{-4} s^{-1} and 5×10^{-8} s^{-1} for j_{NO_2} and j_{O_3}, respectively, which also kept the analyzed j-values above the SAFS limits of detection.

The j-value comparisons are subdivided broadly into two regimes by SZA, those at relatively low ($< 85°$) and high ($\geq 85°$) SZA, with the high SZAs traditionally posing a significant challenge to the modeling and measurement of near-twilight photolysis rate coefficients.

When unique input data were unavailable, the model relied on climatological values. Thus, j-values are included in the comparison only when the relevant input data were available. $APL_{CPFM[*]}$ j-values are compared only when CPFM data were available, and $APL_{TOMS[*]}$ are considered only when TOMS data were available. $APL_{POAM[*]}$ are compared when POAM ozone profiles were available for j_{O_3} and TOMS albedo input for j_{NO_2}, since j_{NO_2} depends importantly on albedo and j_{O_3} on the overhead ozone column, as demonstrated in chapter 3. For example, when APL_{TOMS} are compared with APL_{CPFM} calculations, only points where *both* TOMS and CPFM data were available are considered. The criterion for comparing APL_{CPFM} and APL_{CPFM*} is CPFM-only, though $APL_{CPFM[*]}$ also use TOMS total ozone. At low SZAs, both CPFM and TOMS data were typically available at the same time, but there are instances at high SZAs when CPFM but not TOMS data were valid. Therefore, in the comparisons, some of the high-SZA $APL_{CPFM[*]}$ values were not scaled to TOMS total ozone. Since the overhead

Figure 4.2. SOLVE DC-8 flight synopsis (see figure on page 115). Time from each science flight has been concatenated, and the beginning of each flight indicated with a labeled, full-figure vertical line. The three horizontal bands at the top of the figure indicate exactly when input data corresponding to each of the different model modes (e.g., $\mathrm{APL_{POAM[*]}}$) were available. The next panel shows the solar zenith angle (SZA) at the aircraft, with 93° indicated with a dotted line, which is the approximate SZA of sunrise/sunset in the lower stratosphere. $\mathrm{APL_{POAM}}$ values of $j_{\mathrm{NO_2}}$ and $j_{\mathrm{O_3}}$ are shown in the next two panels as points of reference. TOMS albedo (or climatology when TOMS data are unavailable) is shown next, followed by the $\mathrm{APL_{POAM}}$ overhead ozone column above the DC-8. The air temperature at the aircraft is next shown, along with the nominal saturation points of type I and type II PSCs (195 and 188 K, respectively), noted with dotted lines. Finally, the altitude of each flight is indicated, with the minimum altitude considered in the j-value comparisons noted with a dotted line.

ozone is the primary factor controlling $j_{\mathrm{O_3}}$, this detail should not have a significant effect.

Finally, SAFS reported measurements every 20 s and the model j-values at a 100-s time step, so all the data were interpolated to a 10-s grid and averaged over consecutive 300-s (5-min) bins.

4.5 DC-8: Model–Model and Model–Measurement *j*-Value Comparisons

A comprehensive synopsis of each of the science flights[6] (from the standpoint of the key determinants of j-values) is found in Figure 4.2, including input data availability for each of the different model modes,[7] SZA, $j_{\mathrm{NO_2}}$, $j_{\mathrm{O_3}}$, surface albedo, overhead ozone,

[6]Dates are represented in YYYYMMDD format. 20000123 denotes January 23, 2000.

[7]The availability of $\mathrm{APL_{POAM}}$ data is shown in Figure 4.2. Due to a processing problem, $\mathrm{APL_{POAM*}}$ data from the 20000123 and 20000125 flights are not available and are not included in the comparisons. The $\mathrm{APL_{POAM*}}$–SAFS comparisons contain slightly fewer data points than those for $\mathrm{APL_{POAM}}$–SAFS. The bias thus introduced is on the order of only 1–2%, however.

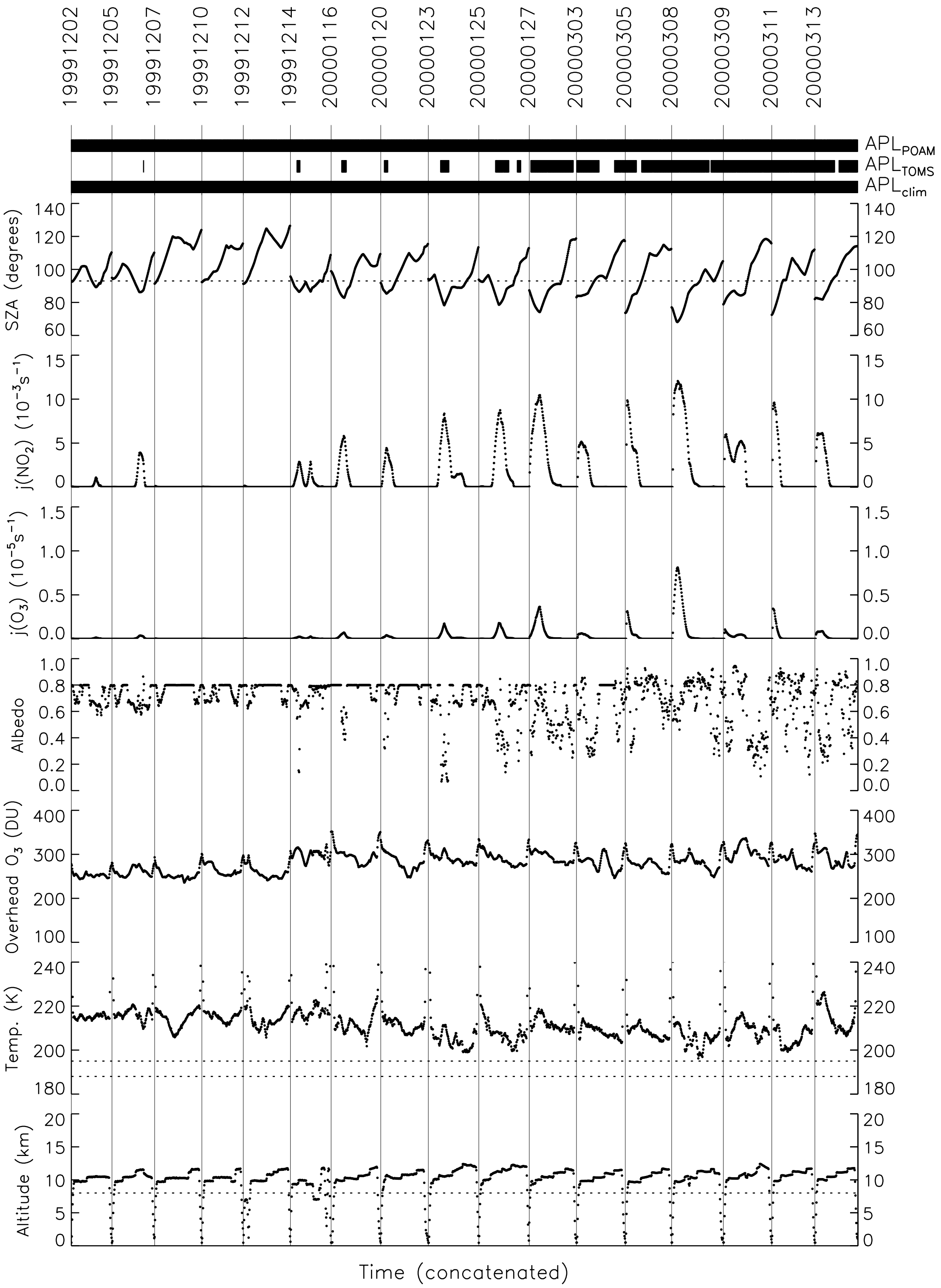

Figure 4.2. SOLVE DC-8 flight synopsis (see caption on page 114).

temperature, and flight altitude. Other flight track information, including maps, is in appendix D. The data represented in Figure 4.2 form the basis for the following model–model and model–measurement j-value comparisons. $APL_{TOMS[*]}$ and $APL_{POAM[*]}$ model data both reverted to climatology when their specific input data were not available, producing a complete set of j-values for each flight. For this comparison, as described in section 4.4, just the data represented by the bands in Figure 4.2 are used, further limited by flight altitude and so forth. This data filtering prevents the comparison from being diluted by climatological defaults when geophysical data were not available.

Though it did not provide measurements of surface albedo or overhead ozone column, the SAFS instrument on board the DC-8 did provide flux-derived measurements of j_{NO_2} and j_{O_3} for direct comparison with the model calculations.

Tables showing comparisons of DC-8 j_{NO_2} and j_{O_3} appear in this section, and tables of the corresponding correlation coefficients and comparisons/correlations of surface albedo and overhead and total ozone column appear in appendix E.

4.5.1 SAFS Instrument

The SAFS instrument provided j-values derived from in situ measurements of the 4π-sr actinic flux from the DC-8 (see *Shetter and Müller* [1999]). It is a double-pass spectroradiometer, making spectrally resolved actinic flux measurements over 280–420 nm[8] using hemispherical quartz light collectors and low–dark current photomultiplier tubes with a FWHM resolution of 1 nm. SAFS actually comprises two independent spectroradiometer systems, mounted on the top and bottom of the aircraft, sampling the downwelling and upwelling hemispheres of the radiation field, respectively, including

[8]Extended to 280–535 nm during the January and February–March 2000 SOLVE intensives.

the direct solar beam.

SAFS has a time response of <10 s, with ∼10% accuracy and ∼5% precision in the flux measurement. The detection limits for j_{NO_2} and j_{O_3} are roughly 2.6×10^{-7} and 1.3×10^{-8} s^{-1}, respectively, with uncertainties of 15–20%. SAFS j_{NO_2} computation was based on *DeMore et al.* [1997] NO_2 cross sections and *Gardner et al.* [1987] quantum yields (similar to that used in the APL model); for j_{O_3}, the O_3 cross sections of *WMO* [1986] and *Molina and Molina* [1986] were used (the same as the POLARIS version of the APL model), with the O(^1D) quantum yields of *Talukdar et al.* [1998], which includes the long-wavelength tail. These molecular data are identical or comparable to those used for the modeling results discussed.

4.5.2 j_{NO_2}: Attenuation of j_{NO_2} by Polar Stratospheric Clouds

The j_{NO_2} matrix in Table 4.2 relates the various model modes and compares them with the SAFS measurements. The first data column in the table shows the overall accuracy of the different modes, capturing j_{NO_2} to within only a few percent, even at high SZAs. The better agreement of $APL_{TOMS[*]}$ and $APL_{POAM[*]}$ with SAFS is likely due to the more accurate TOMS measurements of albedo than the climatology. A 25% difference between the TOMS and climatological albedos translates into a 3% difference in j_{NO_2}.

Evidence of Polar Stratospheric Clouds

Though the DC-8 never sampled air at altitudes high enough for the equilibrium formation of PSCs, the ER-2 certainly did (see Figure E.2). In fact, the ER-2 sampled PSCs on several flights (see flight descriptions in Table D.2), and they were also visible from the

Table 4.2. SOLVE model–model and model–SAFS DC-8 j_{NO_2} comparison matrix

	SAFS	APL_{clim}	APL_{TOMS}	APL_{POAM}	APL_{clim*}	APL_{TOMS*}	APL_{POAM*}
SZA $<$ 85°:							
APL_{POAM*}	1.02	0.97	1.00	1.00	0.97	1.00	—
APL_{TOMS*}	1.04	0.97	1.00	1.00	0.97	—	1.00
APL_{clim*}	1.07	1.00	1.03	1.03	—	1.03	1.03
APL_{POAM}	1.04	0.97	1.00	—	0.97	1.00	1.00
APL_{TOMS}	1.04	0.97	—	1.00	0.97	1.00	1.00
APL_{clim}	1.07	—	1.03	1.03	1.00	1.03	1.03
SAFS	—	0.92	0.95	0.96	0.92	0.95	0.97
SZA $\geq$ 85°:							
APL_{POAM*}	1.04	0.99	1.00	1.00	0.99	1.00	—
APL_{TOMS*}	1.06	0.99	1.00	1.01	0.99	—	1.00
APL_{clim*}	1.10	1.00	1.01	1.02	—	1.01	1.01
APL_{POAM}	1.05	0.98	0.99	—	0.98	0.99	1.00
APL_{TOMS}	1.06	0.99	—	1.01	0.99	1.00	1.00
APL_{clim}	1.10	—	1.01	1.02	1.00	1.01	1.01
SAFS	—	0.87	0.92	0.93	0.87	0.92	0.94

Numbers represent the slopes of the least squares fits (forced through the origin) of scatter plots of *j*-value data with the ordinates and abscissas indicated by the SAFS/model mode labels along the corresponding edges of the matrix. The data have been separated into low- and high-SZA regimes and filtered as described in section 4.4. Table E.4 contains the corresponding matrix of correlation coefficients.

DC-8.[9] Figure 4.3 shows the how APL_{TOMS} (low-SZA) and APL_{clim} (high-SZA) j_{NO_2} compared with SAFS. The agreement is excellent, but biased high, particularly at the highest SZAs. Flights from 20000123, 20000125, and 20000308, when PSCs were especially evident in the stratosphere, show the most pronounced positive deviations from the measurements. It is possible that optically thick PSCs (especially when viewed at long slant paths, close to the horizon) occasionally blocked the Sun, reducing the direct solar flux and diminishing in situ *j*-values.

Climatological model inputs are needed for probing the high-SZA behavior, since TOMS data were not always available. The climatological albedo may have had greater errors (though the magnitude of this effect on *j*-values cannot be too great at such high SZAs; see section 3.3.2). To test the magnitude of such errors, the APL_{clim} calculations for the anomalous flights were repeated with the albedo set to 0, producing the theoretical minimum j_{NO_2}. The results are shown in Figure 4.4. Even if the surface had been black, the model calculations would have still been significantly larger than the SAFS observations, consistent with attenuation of j_{NO_2} by PSCs. The exact positions and optical properties of the putative PSCs are not known, but these *j*-value data are used in chapter 6 to estimate the optical impact of PSCs on photolysis and ozone loss.

4.5.3 j_{O_3}

Table 4.3 shows the model–model and model–SAFS comparisons for j_{O_3}. $APL_{POAM[*]}$ and $APL_{TOMS[*]}$ agree well with SAFS, with APL_{POAM*} agreeing identically with SAFS

[9] The author was not only present in Kiruna, Sweden, for the middle SOLVE deployment, but also had the privilege of flying in one of the few empty seats on the DC-8 for the 20000125 flight, primarily in search of PSCs formed as a result of lee waves forced by the Scandinavian mountains. He observed extensive PSCs, which certainly attenuated the sunlight reaching the aircraft. PSCs were also routinely visible from the surface as well.

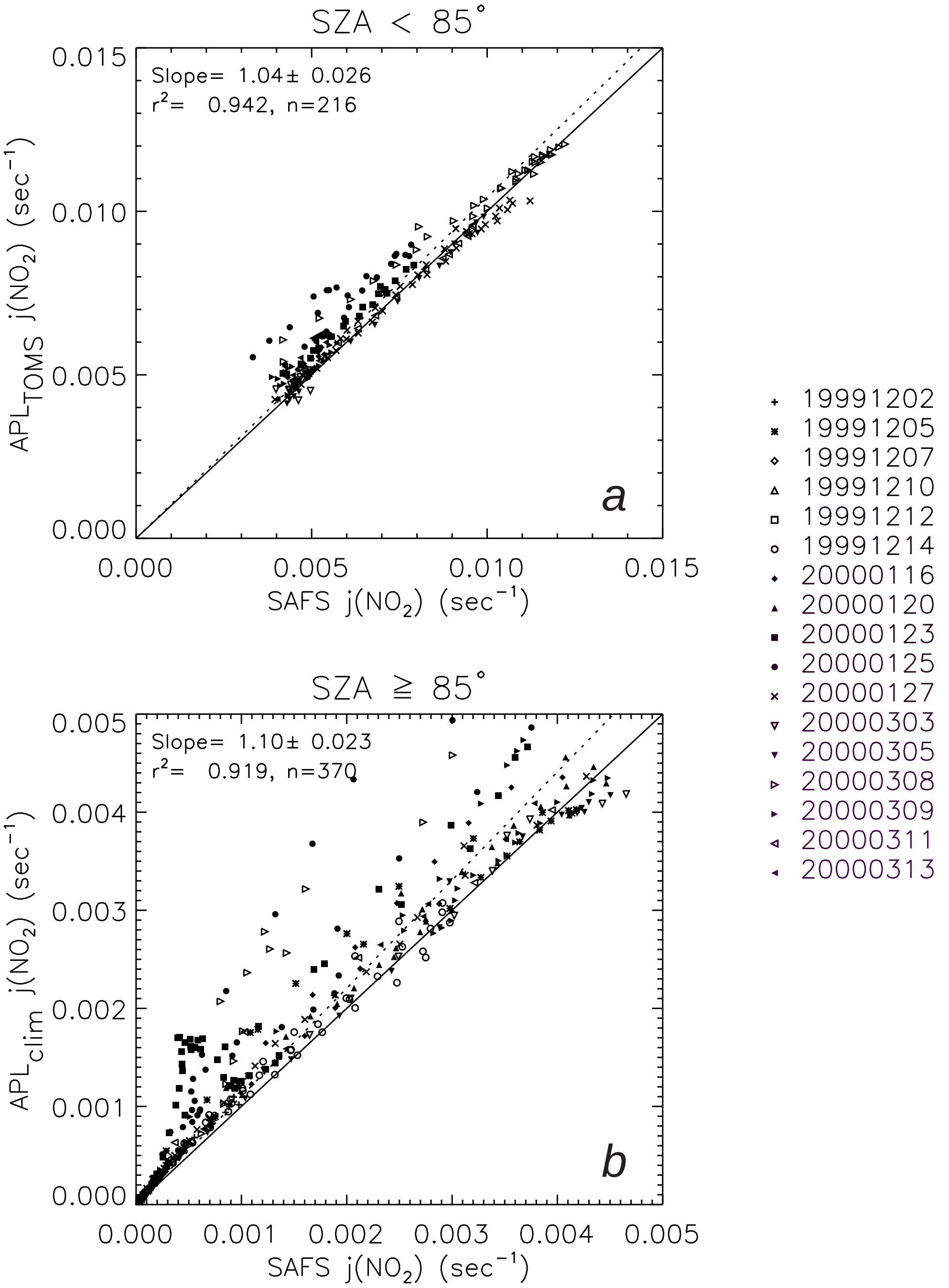

Figure 4.3. Comparison of (a) APL_{TOMS} (modeled) and SAFS (measured), SZA $< 85°$, and (b) APL_{clim} (modeled) and SAFS (measured), SZA $\geq 85°$, j_{NO_2} along DC-8 flight tracks during SOLVE. Each science flight is identified by a unique symbol, as keyed at right. The data were filtered as described in section 4.4. The slopes and correlation coefficients, r^2, are also indicated, corresponding to those recorded, for example, in Tables 4.2 and E.4.

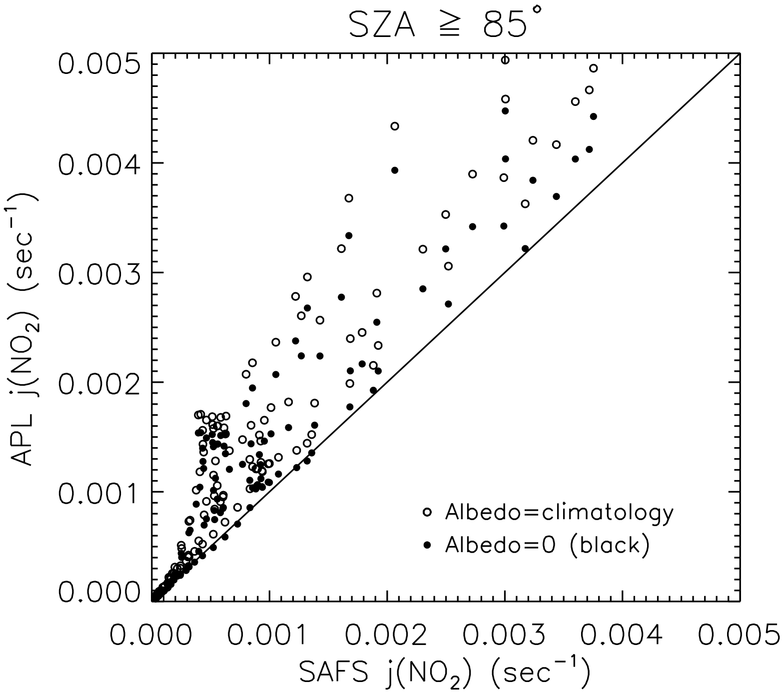

Figure 4.4. Comparison of APL_{clim}-type (modeled) and SAFS (measured) j_{NO_2} at SZA $\geq 85°$ during DC-8 flights 20000123, 20000125, and 20000308. The open circles (○) represent APL_{clim} data from all 3 flights (corresponding to ■, ●, and ▷ in Figure 4.3), and the filled circles (●) represent the same calculations, but with the surface albedo set to 0 (black surface).

Table 4.3. SOLVE model–model and model–SAFS DC-8 j_{O_3} comparison matrix

SZA $<$ 85°:							
APL_{POAM*}	1.00	1.58	0.89	1.06	1.51	0.91	—
APL_{TOMS*}	1.10	1.72	0.98	1.17	1.62	—	1.09
APL_{clim*}	0.67	1.06	0.60	0.71	—	0.61	0.66
APL_{POAM}	0.93	1.47	0.82	—	1.37	0.85	0.93
APL_{TOMS}	1.13	1.76	—	1.20	1.66	1.02	1.11
APL_{clim}	0.63	—	0.56	0.68	0.94	0.57	0.62
SAFS	—	1.56	0.88	1.06	1.47	0.90	0.99
SZA $\geq$ 85°:							
APL_{POAM*}	1.08	1.20	0.93	1.03	1.16	0.94	—
APL_{TOMS*}	1.13	1.31	0.98	1.11	1.26	—	1.06
APL_{clim*}	0.95	1.07	0.76	0.91	—	0.78	0.85
APL_{POAM}	1.03	1.16	0.87	—	1.07	0.89	0.96
APL_{TOMS}	1.15	1.33	—	1.13	1.28	1.02	1.07
APL_{clim}	0.88	—	0.73	0.85	0.92	0.75	0.82
SAFS	—	1.12	0.86	0.96	1.03	0.87	0.91
	SAFS	APL_{clim}	APL_{TOMS}	APL_{POAM}	APL_{clim*}	APL_{TOMS*}	APL_{POAM*}

Same as Table 4.2, but for j_{O_3}. Table E.5 contains the corresponding matrix of correlation coefficients.

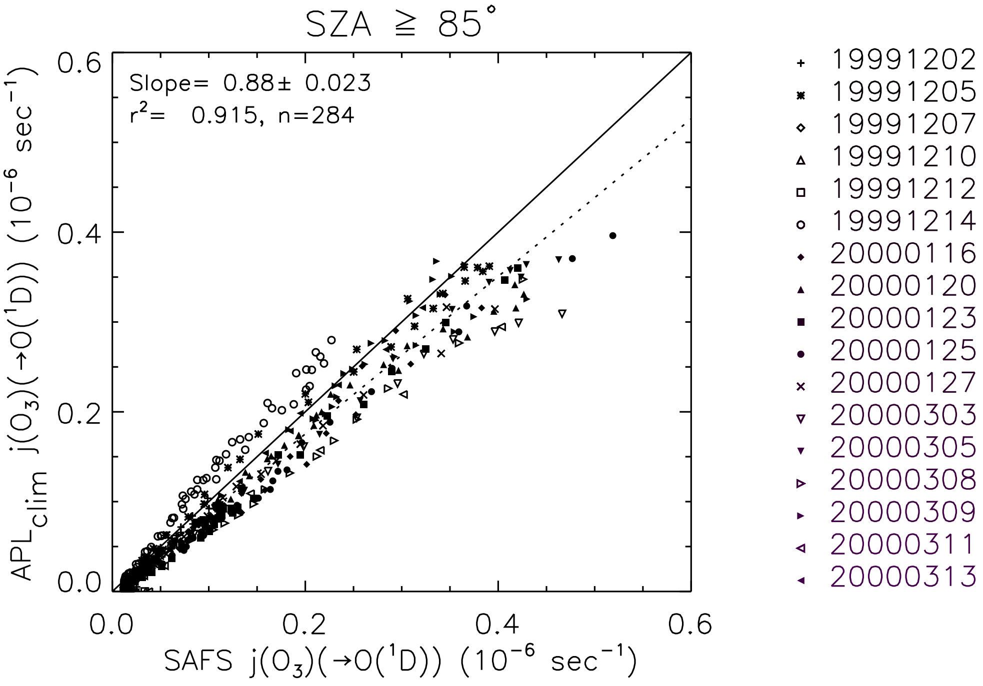

Figure 4.5. Same as Figure 4.3b, but for j_{O_3}.

on average for SZAs $< 85°$. APL_{clim} is low by nearly 40%, due to an overestimation of the overhead ozone (see Table E.10).

Figure 4.5 (corresponding to Figure 4.3b for j_{NO_2}) shows the level of agreement of APL_{clim} and SAFS j_{O_3} at high SZAs. Those flights that likely were influenced by PSCs (as indicated in Figures 4.3 and 4.4) show no significant deviation from the other flights. j_{O_3}, which is dominated by scattering under these conditions, suffers less from PSC attenuation of the direct solar beam than j_{NO_2}.

In Situ Ozone Scaling

The agreement of model j_{O_3} with SAFS measurements was enhanced by the use of in situ data for all modes (except APL_{POAM} at high SZAs). There is thus a clear advantage in using the DC-8 in situ ozone for j-value calculation.

4.6 Summary and Conclusions

SOLVE presented a modeling (and measurement) challenge beyond POLARIS that required changes to the APL radiative transfer model. Based on the conclusions from IPMMI and POLARIS, several key pieces of input data were updated. New climatologies of ozone, pressure, temperature, and albedo were incorporated into the model, along with POAM III satellite and in situ ozone data, in order to more accurately capture the physical characteristics of the atmosphere. Some of the details and nuances of the data application were reported (see also appendix E).

Though it did not provide measurements of ozone or albedo as model inputs, the SAFS instrument on the DC-8 did provide flux measurement–derived j-values for comparison with the APL model. Comparisons with $\mathrm{APL}_{\mathrm{TOMS}[*]}$ and $\mathrm{APL}_{\mathrm{POAM}[*]}$ j_{NO_2} (utilizing TOMS measured albedos) showed excellent agreement, within 4% and 6% for SZAs smaller or larger than 85°, respectively. For j_{O_3}, $\mathrm{APL}_{\mathrm{POAM}*}$ agreed exactly with SAFS, on average, with $\mathrm{APL}_{\mathrm{TOMS}*}$ 10% higher at SZAs $< 85°$. $\mathrm{APL}_{\mathrm{POAM}*}$ and $\mathrm{APL}_{\mathrm{TOMS}*}$ were 8 and 13% higher at SZAs $\geq 85°$, respectively (and $\mathrm{APL}_{\mathrm{POAM}}$ was within 3%). In all of these cases, the APL model agreed with SAFS j-values to within the 15–20% SAFS uncertainties.

Use of the measured albedo led to better agreement of modeled j_{NO_2} with SAFS measurements than the albedo climatology. The climatological overhead ozone was significantly overestimated. The use of POAM III potential vorticity reconstructions for ozone provided input data for SOLVE that were decidedly superior to climatologies. The advantage of using in situ ozone data was apparent with the DC-8, with the model–measurement agreement of j_{O_3} improved in all cases except high-SZA $\mathrm{APL}_{\mathrm{POAM}}$.

Overall, the APL model, with new SOLVE-driven features including the use of in situ ozone data, provided accurate calculations of j-values for the campaign, even at very large SZAs. The comparisons have also uncovered an interesting phenomenon as well. For several DC-8 flights that observed polar stratospheric clouds at higher altitudes, the model predicted significantly greater flux at 350–380 nm than was observed by SAFS (which also accounts for some of the high-bias in the overall j_{NO_2} comparisons). Model calculations show that the bias could not be due to errors in the albedo input. Comparisons from these flights were presented as evidence of the direct attenuation of j_{NO_2} by PSCs (see also chapter 6 for an analysis of the PSC j-value effect).

Chapter 5

Photochemical Ozone Loss in the Arctic Lower Stratosphere as Determined by MSX/UVISI Stellar Occultation Observations

5.1 Introduction

The increased frequency of cold Northern Hemisphere stratospheric winters during the 1990s [*Pawson and Naujokat*, 1999] leading to significant photochemical ozone depletion [*Newman et al.*, 1997; *Solomon*, 1999] has heightened interest in modeling and predicting the future of Arctic ozone loss and recovery. To gain a better understanding of the processes controlling stratospheric ozone at mid-to-high northern latitudes, the SAGE III Ozone Loss and Validation Experiment (SOLVE) campaign was conducted simultaneously with the Third European Stratospheric Experiment on Ozone 2000 (THESEO 2000), based in Kiruna, Sweden (68°N, 20°E), from November 1999 through March 2000. The combined campaign coordinated measurements from a wide range of aircraft-, balloon-, ground-, and space-based instruments. A key goal was to assess quantitatively the rate of high-latitude stratospheric ozone loss.

The winter 1999/2000 Arctic polar vortex[1] was particularly stable over a long period of time [*Manney and Sabutis*, 2000]. Trajectory calculations run over the SOLVE time period show that the vortex was well isolated from midlatitude air. Under these conditions, it is possible to remove the effects of subsidence[1] from ozone measurements within the vortex and determine the photochemical loss of ozone. Ozone loss during SOLVE has also been the subject of several other analyses using remotely sensed and in situ data [e.g., *Santee et al.*, 2000; *Sinnhuber et al.*, 2000; *Richard et al.*, 2001; *Hoppel et al.*, 2002; *Lait et al.*, 2002; *Rex et al.*, 2002; *Schoeberl et al.*, 2002].

Remote sensing techniques that rely on backscattered sunlight, which have been used to document springtime polar ozone loss [e.g., *Stolarski et al.*, 1986; *Newman et al.*, 1997], require solar zenith angles of less than 84° for measurement. Other techniques are therefore needed for observing ozone morphology during the polar night or early dawn, as catalytic ozone loss is initiated. Occultation provides a means for studying ozone before and during polar sunrise.

5.1.1 Occultation Techniques

Occultation techniques have been used for many years to characterize the structure and composition of the Earth's atmosphere, as well as those of other planets and their satellites. Occultation provides a self-calibrating method of measuring absorbing species in the atmosphere and monitoring their long-term trends. Traditionally, two distinct approaches have been utilized. Extinctive occultations yield measurements of absorbing/scattering species resulting from wavelength-dependent extinction. For example, the total transmission of sunlight, attenuated as it passes through the atmosphere, is related

[1] The polar vortex and diabatic subsidence therein are described briefly in section F.4.

to the column densities of absorbing species along the light path. A series of measurements made as the Sun rises or sets may be inverted to yield number density profiles of trace gases in the atmosphere as a function of altitude. This technique has been used by a number of space-based solar occultation instruments with great success, including: SAGE II [*McCormick et al.*, 1989], HALOE [*Russell et al.*, 1993], ATMOS [*Gunson et al.*, 1996], and POAM II & III [*Lucke et al.*, 1999]. Another occultation approach, capitalizing on the refraction of light in the atmosphere resulting from vertical density gradients, provides the bulk properties of the atmosphere (i.e., total density, temperature, and pressure). For example, refractive occultation of radio waves from the Global Positioning System has been used to measure temperature profiles in the atmosphere [*Ware et al.*, 1996].

The Sun is a powerful light source and endows solar occultation with an excellent inherent signal-to-noise ratio. With the Sun come certain limitations, however. Measurements are restricted to the terminator, so for space-based solar occultation, this means only two occultations per orbit are possible (i.e., $\sim$30/day). Though a weaker source of light, stars provide numerous point sources, allowing for occultation measurements virtually continuously throughout the nighttime atmosphere. Stellar occultation has been used to measure column ozone abundance from the ground [e.g., *Roscoe et al.*, 1994; *Fish et al.*, 1994; *Roscoe et al.*, 1997; *McDonald et al.*, 1999] and ozone profiles from balloon-based platforms [e.g., *Renard et al.*, 1996; *Payan et al.*, 1999]. *Yee et al.* [2002] have developed a further innovation to this star-based approach by combining the complementary (though historically separate) extinctive and refractive occultation techniques, which simultaneously provides both the bulk properties of the atmosphere and mixing ratio profiles of absorbers, including ozone, in the atmosphere from space.

5.1.2 Combined Extinctive–Refractive Stellar Occultation

High in the atmosphere, where refraction is not significant and airglow contamination is minimal, atmospheric composition may be retrieved from spectrographic information alone, provided the spectral coverage is sufficient for the species of interest. Airglow emissions become significant in a layer from 80 to 100 km, however, and their contamination must be removed from the stellar signal when the tangent altitude of the line of sight is at or below the layer (light passing through a tangent altitude below the source of the emissions still passes through the emission layer on its path to the observer). An instrument with spectrographic imaging capability is therefore required. Knowledge of airglow emissions above and below the tangent altitude allows for suitable background correction.

Refraction becomes significant lower in the atmosphere, below 35 km, changing the apparent position of the star (and thus the altitude registration) and producing a curved light path that leads to enhanced extinction. In addition, refractive attenuation (photon flux divergence) causes a reduction in the overall signal, and small-scale density fluctuations along the line of sight generate refractive scintillation, which introduces noise and additional uncertainty into the retrieval. Though climatologies may be used to approximate the curved light path, the resulting uncertainties would substantially reduce the efficacy of the technique for addressing science issues. A better approach is to measure refraction simultaneously, allowing for accurate calculation of the refracted path and inference of the atmospheric density profile. A high–angular resolution, visible-light imager that measures the apparent position of the star can provide absolute refraction angles from which the atmospheric density profile may be retrieved. This retrieved density profile can be used to account for Rayleigh scattering directly, thereby allowing for ozone measurements in the lower atmosphere with greater accuracy. Because the density profile may be used to infer both pressure and temperature, another benefit gained from this unique, combined extinctive–refractive method is that potential temperature and constituent mixing ratio profiles can be calculated directly, thus eliminating the need for approximations based on climatologies or meteorological analyses. The approach may be summarized as follows:

$$
\begin{aligned}
\text{(1) Refraction Angles} &\Rightarrow \text{Density Profile} \\
&\Rightarrow \text{Pressure/Temperature Profile} \\
&\Rightarrow \text{Potential Temperature Profile,} \\
\text{(2) Absorption Profile} &\Rightarrow \text{Constituent Density Profile} \\
&\overset{(1)}{\Rightarrow} \text{Constituent Mixing Ratio Profile.}
\end{aligned}
$$

5.2 MSX/UVISI Instrument

5.2.1 Instrument Description

The Midcourse Space Experiment (MSX) was launched on April 24, 1996, into a nearly Sun-synchronous, circular orbit with an inclination of 99.4°, an ascending node of 5:38 pm (which had precessed to approximately 7:30 pm during SOLVE), and an altitude of ~900 km [*Mill et al.*, 1994]. MSX is a 3-axis stabilized satellite with extraordinarily accurate and stable pointing. It can point at a fixed inertial position (e.g., a star) with an absolute accuracy of $\sim$100 μrad and relative stability of 10 μrad (1-σ) for several minutes.

The Ultraviolet and Visible Imagers and Spectrographic Imagers (UVISI) instrument suite aboard MSX consists of four visible and ultraviolet imagers and five spectrographic imagers (SPIMs) covering a wavelength range of 100–900 nm [*Carbary et al.*, 1994; *Paxton et al.*, 1996]. All nine instruments constituting UVISI are co-aligned to within 50 μrad on a common optical bench. During SOLVE, the imaging capabilities of the SPIMs were utilized.[2] The SPIMs use a Wadsworth design and have wavelength resolutions of 0.7–2.2 nm and roughly $0.1^\circ \times 1^\circ$ slit fields of view with 0.025° spatial resolution. The slits can be swept by scan mirrors over an additional 1°, for a $1^\circ \times 1^\circ$ total field of regard. The focal plane units consist of intensified photocathodes fiber-optically connected to 2-dimensional charge-coupled devices (CCDs) and have been optimized for the wavelength range of the particular sensor. An automatic gain/gate system, combined with various filters, provides for a total dynamic range on the order of 10^{13}. The SPIMs accumulate data at a rate of 2 or 4 Hz. Though the instrument was not designed for stellar occultation measurements, MSX/UVISI satisfies the general design requirements for extinctive–refractive occultation experiments, described above.

5.2.2 Occultation Procedure

The general MSX/UVISI stellar occultation procedure has been described in detail by *Yee et al.* [2002] and is summarized here, with the aid of Figure 5.1. During a stellar occultation observation, the UVISI boresight remains fixed and centered on the inertial position of the star, with the SPIM slits oriented vertically with respect to the horizon. The star is acquired when it is well above the attenuating atmosphere, and several hundred spectra are collected before atmospheric extinction begins, thus ensuring an accurate description of the unattentuated light source. As the star sets, its position in the

[2]In the past, the narrow field-of-view visible imager was often used to determine the absolute star refraction angles. This imager failed, however, prior to SOLVE, so the imaging capabilities of the SPIMs were utilized instead.

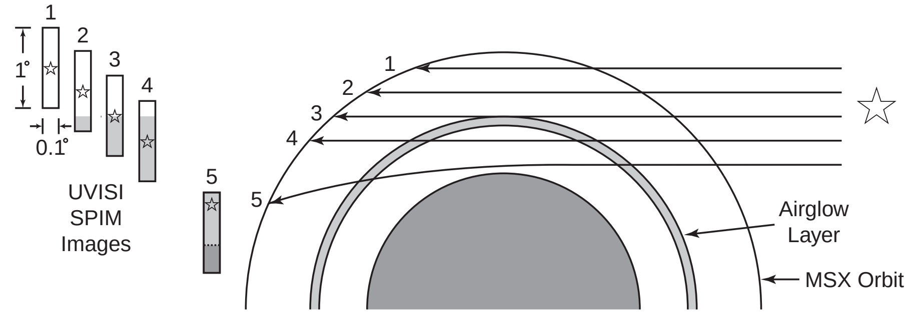

Figure 5.1. Geometry of a typical MSX/UVISI stellar occultation. The light path connecting a setting star and MSX is shown at five points in space and time. As the spacecraft moves in its orbit from point 1 to point 5, the stellar light path enters and descends through the atmosphere. At point 3, the light path enters the airglow layer (at 80–100 km). Significant refraction at point 5 ($<$35 km) is represented with noticable curvature of the light path. At the left side of the figure, the orientation of a SPIM light slit is indicated. The image of the star (refracted at point 5), airglow layer, and solid Earth are depicted within the slit. Reprinted with permission from *Yee et al.* [2002]. Copyright 2002 by the American Geophysical Union.

SPIM slits remains unchanged until refraction becomes significant, below about 35 km. Refraction causes the image of the star to drift slowly up and finally out of the top of the slit at a tangent altitude of about 7–8 km, over a period of roughly 30 s.

5.2.3 Data Reduction and Analysis

The data reduction and analysis procedure for MSX/UVISI extinctive–refractive stellar occultation observations has been described by *Yee et al.* [2002]. Following the determination of the apparent star positions and thus refraction angles, the imaging capabilities of UVISI are used for the identification and subtraction of airglow contamination from the stellar spectra. The refraction angles imply an index of refraction profile, from which density, pressure, and temperature profiles are retrieved [*Vervack et al.*, 2002]. The density profile determines the refracted light path and constrains the amount of Rayleigh scattering, yielding stellar transmission spectra from which atmospheric composition (e.g., ozone profile) is retrieved [*DeMajistre and Yee*, 2002].

5.3 SOLVE Stellar Occultations

There were 31 MSX/UVISI stellar occultation observations during SOLVE, from January 23 through March 4, 2000 (solar contamination precluded observations after this date). The details of each observation are shown in Table 5.1. Each occultation provides profiles of pressure, temperature, and ozone mixing ratio throughout the stratosphere and troposphere, down to an altitude of approximately 7 km. Of the 31 available events, six were found to lie outside the Arctic polar vortex (as indicated in Table 5.1) and have thus been excluded from the analysis. The inside-/outside-vortex distinction was made on the basis of occultation profile potential vorticity (PV)[3] and position relative to streamfunction[4] maxima on the 480- and 550-K potential temperature[5] surfaces [e.g., *Nash et al.*, 1996]. There was a clear separation between relatively high- (inside-vortex) and low-PV (outside-vortex) profiles, as shown in Figure 5.2. At 500 K, for example, the inside- and outside-vortex modified PV[3] [*Lait*, 1994] values lie clustered above 28 and below 22×10^{-6} m^2 km^{-1} s^{-1}, respectively.

5.3.1 Retrieved Temperature

A comparison of MSX/UVISI temperature profiles with that from the analysis reported by the United Kingdom Meteorological Office (UKMO) [*Swinbank and O'Neill*, 1994] is shown in Figure 5.3. The UKMO temperature data have been interpolated onto a 1-km

---

[3] See section F.2 for the definitions of PV and modified PV.

[4] See section F.3 for the definition of streamfunction.

[5] See section F.1 for the definition of potential temperature.

Table 5.1. MSX/UVISI stellar occultation profiles during January–March 2000

Profile	Date[a]		Time (UT hours)	Latitude (°N)	Longitude (°E)	Vortex[b]	Star Name	Visual Magnitude	Spectral Type
1	Jan 23	(23)	0.45	71.3	−63.0	in	α Lep	2.60	F0Ib
2	Jan 24	(24)	0.51	71.2	−65.4	in	α Lep	2.60	F0Ib
3	Jan 24	(24)	17.69	71.2	35.8	in	α Lep	2.60	F0Ib
4	Jan 25	(25)	17.75	71.2	33.4	in	α Lep	2.60	F0Ib
5	Jan 26	(26)	17.80	71.1	31.1	in	α Lep	2.60	F0Ib
6	Jan 27	(27)	16.14	71.1	54.6	in	α Lep	2.60	F0Ib
7	Jan 28	(28)	17.92	71.0	26.4	in	α Lep	2.60	F0Ib
8	Jan 31	(31)	16.37	70.8	45.3	in	α Lep	2.60	F0Ib
9	Feb 01	(32)	16.43	70.8	42.9	in	α Lep	2.60	F0Ib
10	Feb 06	(37)	15.04	79.3	36.6	in	β Ori	0.12	B8Iab:
11	Feb 07	(38)	16.82	79.1	7.2	in	β Ori	0.12	B8Iab:
12	Feb 08	(39)	16.86	79.1	28.0	in	κ Ori	2.05	B0Iab:
13	Feb 09	(40)	16.92	78.9	24.5	in	κ Ori	2.05	B0Iab:
14	Feb 10	(41)	15.26	78.8	47.0	in	κ Ori	2.05	B0Iab:
15	Feb 11	(42)	15.31	78.6	43.6	in	κ Ori	2.05	B0Iab:
16	Feb 12	(43)	15.37	78.4	40.3	in	κ Ori	2.05	B0Iab:
17	Feb 14	(45)	15.44	72.3	65.9	in	α CMa	−1.47	A1V
18	Feb 15	(46)	17.22	72.2	37.6	out	α CMa	−1.47	A1V
19	Feb 16	(47)	17.27	72.1	35.2	out	α CMa	−1.47	A1V
20	Feb 17	(48)	17.33	72.1	32.7	in	α CMa	−1.47	A1V
21	Feb 18	(49)	17.39	72.0	30.3	in	α CMa	−1.47	A1V

[a]Date: MMM DD (day of year).

[b]Profile deemed inside (outside) the vortex by virtue of its relatively high (low) potential vorticity and position relative to streamfunction maxima on the 480- and 550-K potential temperature surfaces.

Table 5.1. MSX/UVISI stellar occultation profiles during January–March 2000 (continued)

Profile	Date		Time (UT hours)	Latitude (°N)	Longitude (°E)	Vortex	Star Name	Visual Magnitude	Spectral Type
22	Feb 19	(50)	17.44	71.9	27.8	in	α CMa	-1.47	A1V
23	Feb 20	(51)	15.78	71.9	51.3	in	α CMa	-1.47	A1V
24	Feb 21	(52)	15.84	71.8	48.8	in	α CMa	-1.47	A1V
25	Feb 21	(52)	17.56	71.8	23.0	out	α CMa	-1.47	A1V
26	Feb 23	(54)	15.95	71.6	44.0	out	α CMa	-1.47	A1V
27	Feb 24	(55)	0.54	71.6	-85.5	in	α CMa	-1.47	A1V
28	Feb 27	(58)	16.13	61.7	45.5	out	δ CMa	1.84	F8Iab:
29	Feb 28	(59)	14.46	59.0	67.7	out	ε CMa	1.51	B2Iab:
30	Mar 02	(62)	16.34	58.7	42.5	in	η CMa	2.40	B5Iab:
31	Mar 04	(64)	16.47	63.9	49.6	in	ρ Pup	2.81	F6IIp...

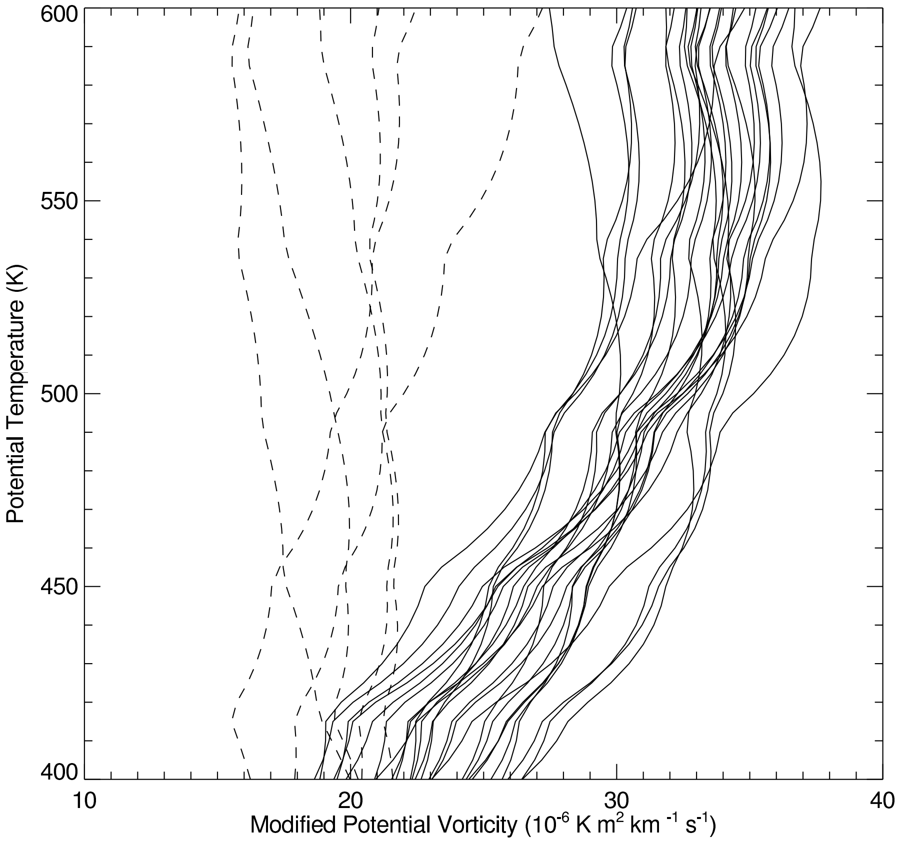

Figure 5.2. Modified potential vorticity (MPV)[3] profiles at times and locations of stellar occultations. Curves correspond to the occultations listed in Table 5.1. The separation between in-vortex and out-of-vortex profiles is distinct at 500 K. Those profiles with relatively high MPV (solid lines) are within the vortex; those with relatively low MPV (dashed lines) lie outside the vortex and are excluded from the ozone loss analysis. See Figure 5.3 for the correspondence of potential temperature to altitude. The geometric altitude range of this figure is 16–24 km.

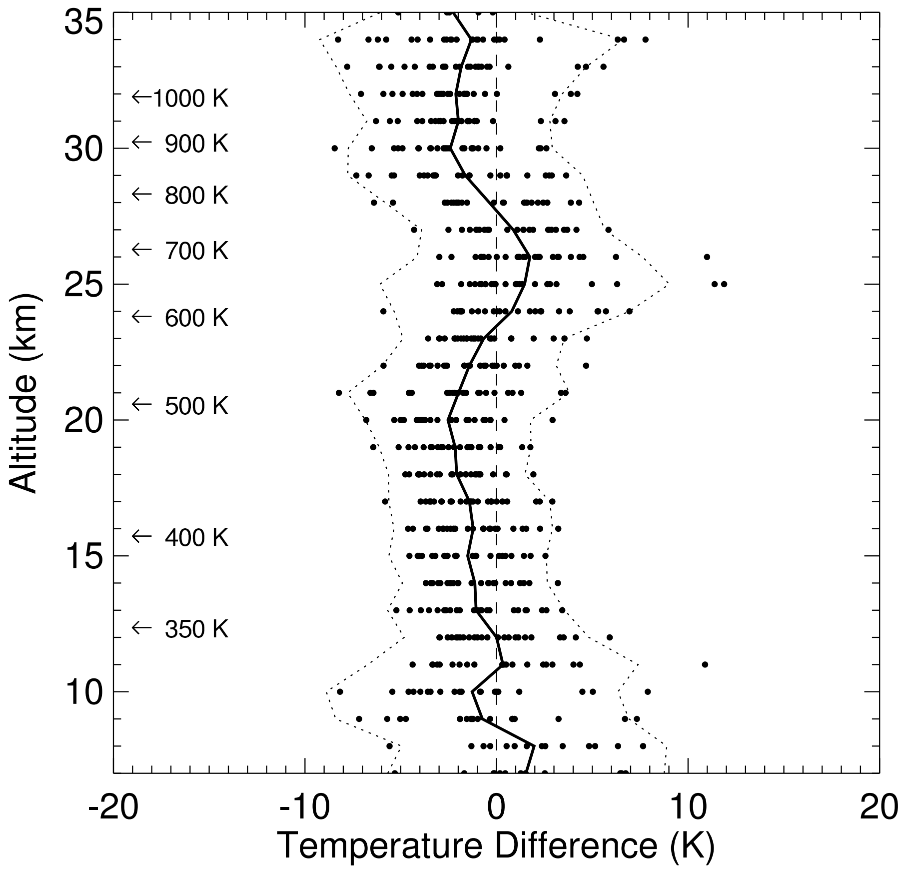

Figure 5.3. MSX/UVISI–UKMO temperature difference. The MSX/UVISI retrieved temperatures from stellar occultations within the vortex (see Table 5.1) are compared with UKMO temperature (MSX/UVISI – UKMO), interpolated onto a 1-km altitude grid. The mean difference as a function of altitude is represented with a thick, solid line, and the mean $\pm$ 2-σ standard deviations at each altitude are represented with dotted lines. The average, calculated 1-σ uncertainty in the temperature profiles due to the stellar occultation measurements and retrieval over 400–600 K is $\pm$1.8 K (not shown). Average potential temperatures corresponding to the geometric altitude scale are included for reference.

altitude grid for this comparison. The envelope represented with dotted lines shows the 2-σ standard deviations around the mean temperature difference at each altitude level. Overall, the agreement is excellent, with an average offset of -0.8 (± 2.7, 1-σ) K for the altitude range shown. A similar, somewhat larger negative temperature bias between 30 and 35 km relative to UKMO has also been observed in aircraft lidar data during the SOLVE campaign [*Burris et al.*, 2002]. In the ozone loss analysis (see below), the focus is on the 400–600-K altitude range ($\sim$16–24 km). Over this range, the temperature difference is -1.4 ± 2.3 K.

Potential Temperature

The MSX/UVISI–UKMO differences in potential temperature exhibit the same general characteristics as temperature (not shown). The average difference is -0.8 (± 7.5, 1-σ) K, with a negative bias from 30 to 35 km, similar to that in Figure 5.3. From 400 to 600 K, the average difference in potential temperature, which provides altitude registration, is -1.0 (± 7.1, 1-σ) K, or -0.04 ± 0.29 km at 500 K.

5.3.2 Retrieved Ozone Mixing Ratio

The results of the MSX/UVISI stellar occultation ozone mixing ratio retrievals for the 25 in-vortex profiles are shown in Figure 5.4 as a function of potential temperature in the lower stratosphere. The ensemble average descent rates for air parcels within the vortex observed by stellar occultation, averaged over 25-K intervals, are shown to indicate the extent of subsidence. Ozone loss is evident, particularly below 500 K. Other commitments of the MSX spacecraft limited the analysis to a relatively sparse sampling of the vortex, compared to other satellite measurements (e.g., POAM III makes approximately 15 solar occultations per day in each hemisphere [*Hoppel et al.*, 2002]).

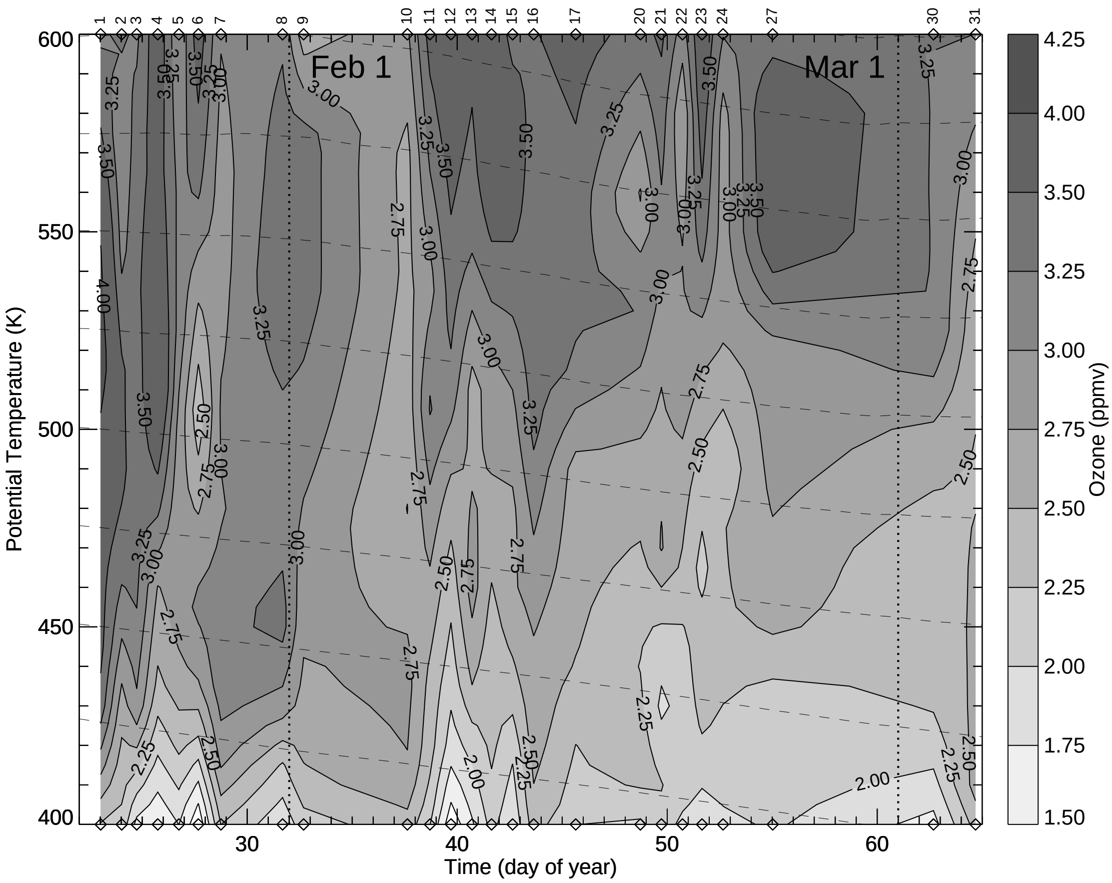

Figure 5.4. Ozone mixing ratio in the lower stratosphere within the Arctic polar vortex as measured by MSX/UVISI using the stellar occultation technique, from late January through early March 2000, during SOLVE. Altitude is represented in terms of potential temperature. The times of the MSX/UVISI stellar occultations are marked with diamonds along the upper and lower abscissas and identified by profile number, corresponding to the listing in Table 5.1. Vertical dotted lines indicate February 1 and March 1. The dashed lines denote the ensemble average diabatic descent of air parcels within the vortex passing through the tangent points of the MSX/UVISI observations. The descent rates, averaged over ±12.5-K intervals, were calculated by diabatic trajectory analysis.

The time of each profile is indicated at the top and bottom of Figure 5.4. Though there are only 25 profiles, the general ozone trend is apparent (this will become more clear in the following section).

Several representative MSX/UVISI ozone profiles have been presented by *Yee et al.* [2002] along with near-coincident ground- and space-based observations for intercomparison, including the February 7, 2000, SOLVE profile (#11 in Table 5.1). This particular profile was centered close to Ny-Ålesund (79°N, 12°E), where lidar data were available from a similar time period. The stellar occultation ozone number density is within roughly 5% of the lidar profile at the ozone peak, with an expected 1-σ statistical uncertainty in the occultation retrieval of $\sim$2.5%. An extensive intercomparison shows the MSX/UVISI ozone and temperature retrievals to be in excellent agreement several with ground- and satellite-based measurements (R. J. Vervack, Jr., manuscript in preparation, 2002).

To demonstrate the accuracy of the stellar occultation technique in the context of the SOLVE campaign, the MSX/UVISI–POAM III ozone mixing ratio differences are shown in Figure 5.5. Three-dimensional ozone fields were reconstructed from POAM III data collected within $\pm$3-day windows around each MSX/UVISI occultation using ozone–PV correlations [*Randall et al.*, 2002] and then interpolated to the occultation geographic location for comparison. While POAM III measures ozone down to the tropopause, ozone fields are not reconstructed below 400 K ($\sim$16 km). The UVISI–POAM ozone difference over the altitude region shown is -0.14 ($\pm$0.60, 1-σ) ppmv. Over 400–600 K, the difference is $+0.02 \pm 0.36$ ppmv ($+1.5 \pm 12.9$%).

Hoppel et al. [2002] found that POAM III ozone measurements during February were not significantly affected by latitudinal sampling (and thus solar exposure) biases. Despite the relative paucity of MSX/UVISI data, which makes it impossible to derive a

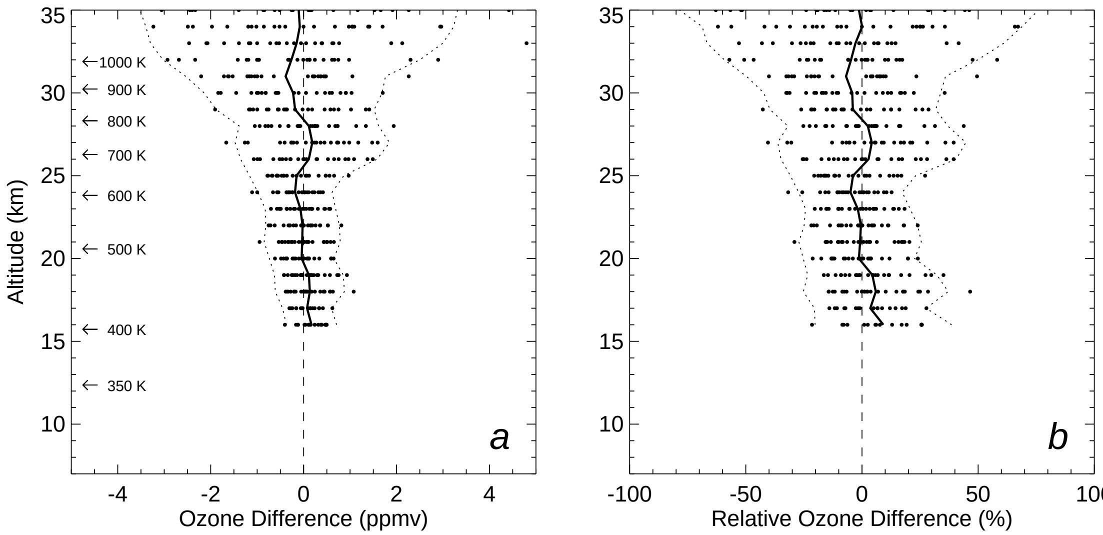

Figure 5.5. MSX/UVISI–POAM III ozone difference. The MSX/UVISI retrieved ozone mixing ratios from stellar occultations within the vortex (see Table 5.1) are compared with ozone derived from POAM III ozone–potential vorticity reconstructions [*Randall et al.*, 2002] in terms of (a) absolute difference (MSX/UVISI – POAM III) and (b) percent difference $((\text{MSX/UVISI} - \text{POAM III})/\text{POAM III} \times 100\%)$. The mean differences as functions of altitude are represented with thick, solid lines, and the means $\pm$ 2-σ standard deviations at each altitude level are represented with dotted lines. The average, calculated 1-σ uncertainty in the ozone mixing ratio profiles due to the stellar occultation measurements and retrieval over 400–600 K is ± 0.11 ppmv (not shown). Average potential temperatures corresponding to the geometric altitude scale are included for reference.

true vortex average ozone morphology from UVISI SOLVE stellar occultations alone, the excellent average UVISI–POAM agreement suggests an absence of substantial solar exposure bias in the air masses remotely sensed by stellar occultation.

5.4 Photochemical Ozone Loss

One goal of SOLVE was to quantify the rate of high-latitude photochemical ozone loss. During the polar winter, there is large-scale, continuous subsidence within the cold vortex [*Schoeberl et al.*, 1992]. Before ozone retrievals, such as those in Figure 5.4, can be used to make any statement about chemical ozone loss, the effects of dynamics within the vortex must be accounted for. Ozone mixing ratios increase with altitude within the lower stratosphere, thus wintertime subsidence tends to increase the ozone mixing ratio at any particular point in the atmosphere with time and mask part of the effect of actual chemical ozone destruction. Diabatic trajectory calculations are used in this analysis to keep track of individual air parcels and relate observed ozone profiles within the vortex after the effective removal of dynamical influence.

5.4.1 Trajectory Analyses

Diabatic back and forward trajectories were calculated[6] with the NASA/Goddard trajectory model [*Schoeberl and Newman*, 1995] using UKMO winds from every vortex profile listed in Table 5.1. Air parcels in 5-K increments from 400 to 800 K ($\sim$16–28 km) were advected back to January 15 and forward to March 31 to produce a continuous 2.5-month history for the parcels (2511 total) in the lower stratosphere at the tangent points of each of the stellar occultation events. Figure 5.6 demonstrates the al-

[6] Trajectories calculated by P. A. Newman (NASA/Goddard).

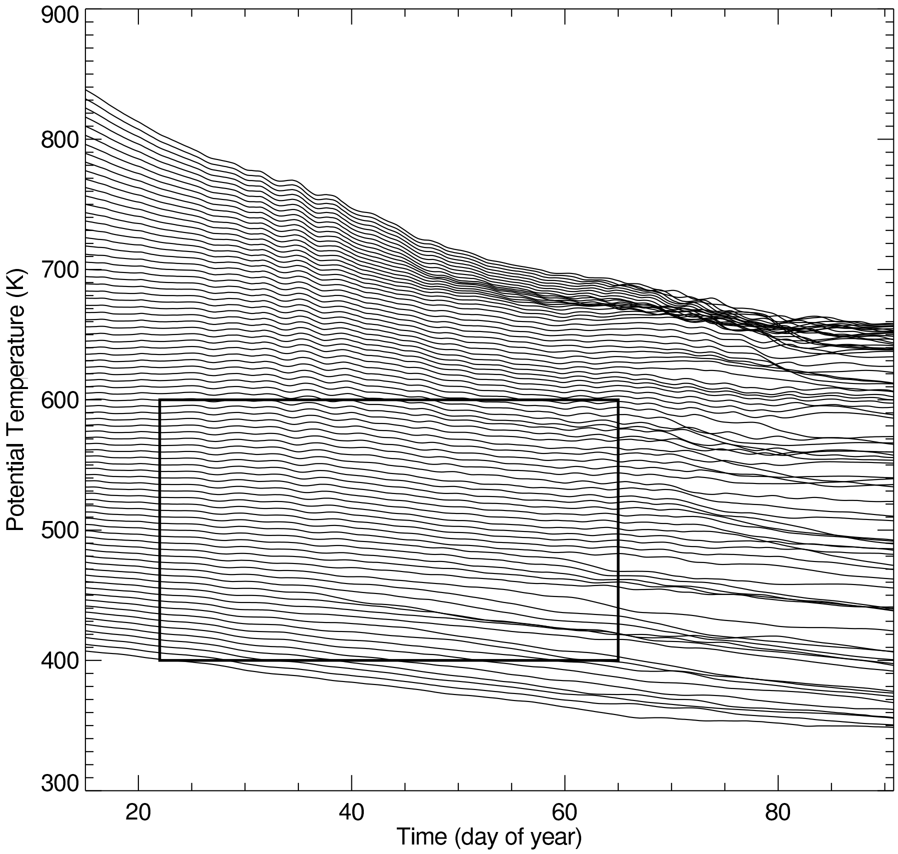

Figure 5.6. Family of diabatic trajectories calculated with the Goddard trajectory model. The curves depict the altitude descent of air parcels sampled by the January 23 stellar occultation (71°N, 63°W), from January 15 through March 31, 2000. The trajectories illustrate how air parcels experienced gradual, uniform descent within the Arctic polar vortex during this period. The thick box encloses the altitude and temporal region used in the ozone loss analysis, as shown in Figures 5.4, 5.8, and 5.9.

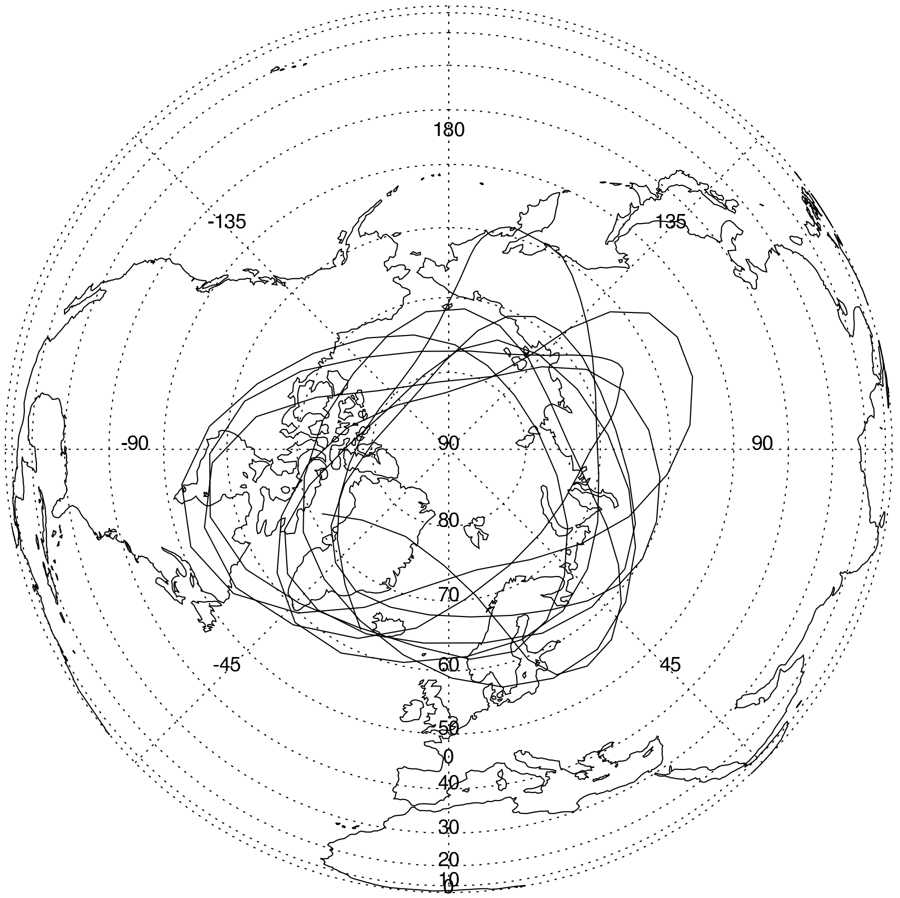

Figure 5.7. Diabatic trajectory calculation using the Goddard trajectory model. The solid curve represents the geographic history in the Northern Hemisphere of an air parcel at 500 K ($\sim$21 km), sampled by the January 23 stellar occultation (71°N, 63°W), through March 4, 2000. The trajectory illustrates how air parcels within the Arctic polar vortex during this period remained isolated from the rest of the atmosphere.

titude history over this period of the air parcels at the tangent point (latitude/longitude) of the January 23 occultation, for example. The geographic isolation of the vortex can be seen in Figure 5.7. There was largely uniform descent within the lower stratosphere vortex, with the 500-K ($\sim$21-km) surface sinking $\sim$40 K from January 15 to March 31 ($\sim$25 K from January 23 to March 4, as illustrated by the mean diabatic descent rates in Figure 5.8). Three different approaches were used to remove the effects of descent.

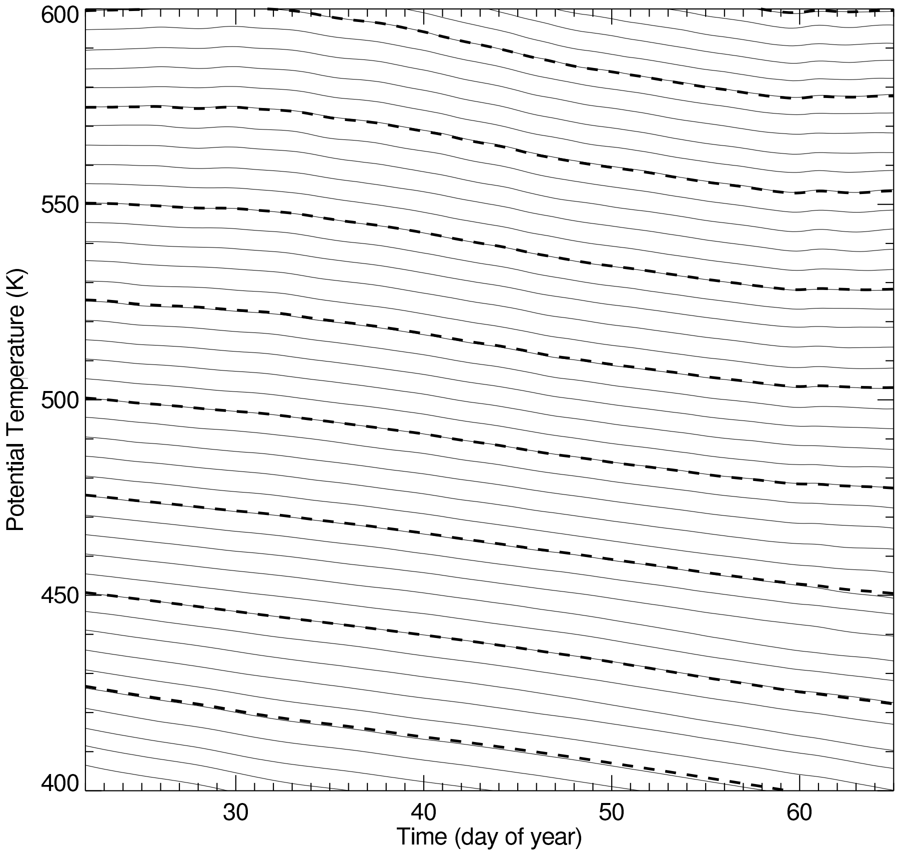

Figure 5.8. Mean diabatic descent rates within the Arctic polar vortex, from January 23 through March 4, 2000. The trajectories sampled by all 25 in-vortex stellar occultations and calculated with the Goddard trajectory model were averaged over the time period shown. The thin solid lines are averages over 5-K intervals. The thick, dashed lines are 25-K averages and are the same as those in Figures 5.4 and 5.9.

Vortex Average Descent Analysis

Diabatic trajectory calculations were used to compute average descent rates within the vortex. Multi-week trajectory calculations are reliable only in a statistical sense, but on average, however, the trajectories accurately describe vortex subsidence. The 2025 parcel trajectories that were calculated for the 25 in-vortex occultations were divided into 5-K layers on January 23 (initial ozone profile), and average descent rates were computed for each layer. With knowledge of the average descent rates, it was then possible to map the initial ozone profile diabatically onto each subsequent profile. The difference in ozone mixing ratio represents the degree of chemical ozone change since January 23. Though the initial condition in this case is composed of a single profile, it lies within the range of vortex profiles derived from POAM III data, thus providing a reasonable representation of the initial state of the vortex for this analysis. The relative differences in the retrieved ozone are shown in Figure 5.9. The contour plot, which is constructed similarly to that in Figure 5.4, reveals the actual, chemical ozone loss within the vortex relative to the January 23 observation computed not along potential temperature surfaces, but along the diabatic descent curves.

Individual Trajectory Analysis

MSX/UVISI data were relatively limited during SOLVE and sampled different parts of the vortex over time. The ozone loss rates implied by the occultations (and corresponding trajectory calculations) over several weeks, however, should provide a good indication of the average loss rate over the time period.

Trajectories were used to follow individual air parcels from the occultation profiles forward to March 4, the date of the final occultation. Diabatic levels were identified by their potential temperatures on March 4. Pairs of adjacent trajectories were used to

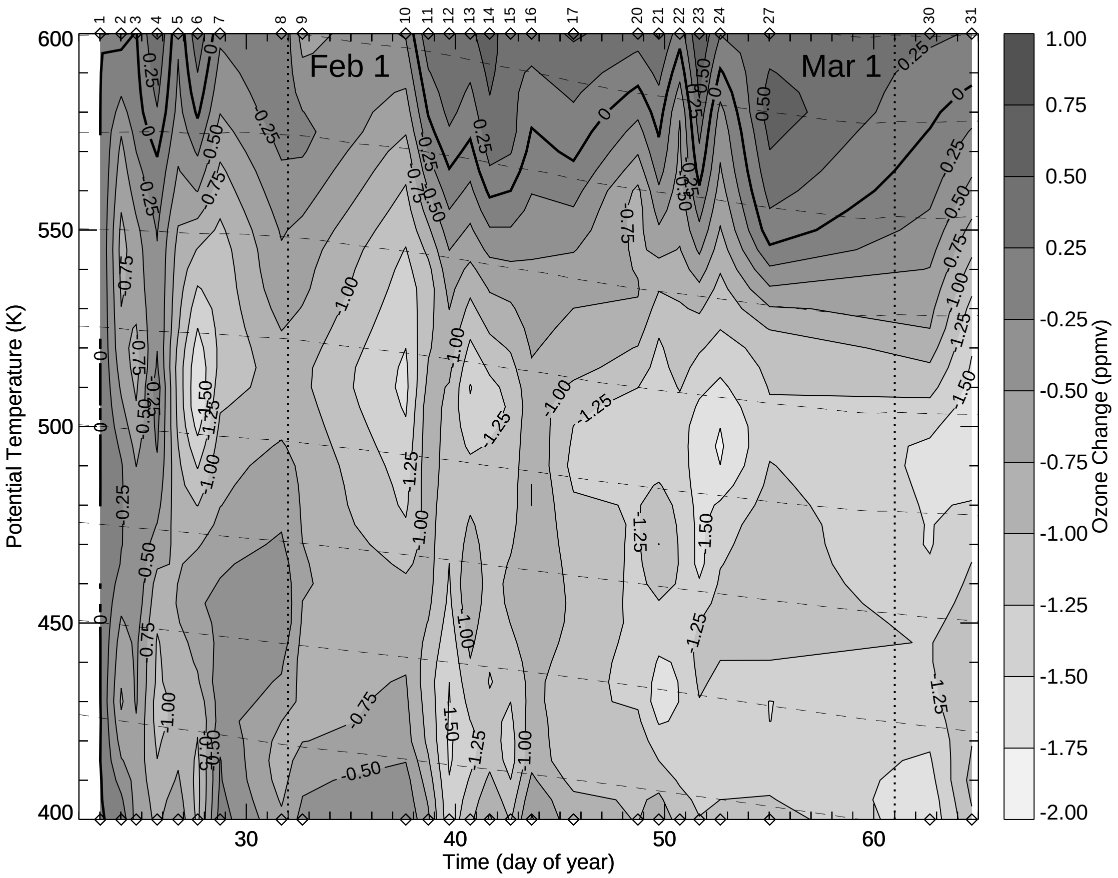

Figure 5.9. Photochemical ozone loss within the polar vortex relative to the first ozone profile, obtained on January 23. The construction of the plot is similar to Figure 5.4. When computing the relative chemical ozone loss, the effects of vortex subsidence were removed by mapping the initial, January 23 occultation onto each subsequent profile using vortex average descent rates and comparing the retrieved ozone mixing ratios.

interpolate each profile onto diabatic levels intersecting a 5-K grid on March 4. Each profile therefore provided a single ozone measurement on every diabatic surface. The results on three such surfaces are shown in Figure 5.10. Each plot represents vertical cross sections parallel (on average) to the dashed diabatic descent curves of Figure 5.4. The diabatic surfaces intersect the 575-, 500-, and 425-K potential temperature surfaces on March 4. The slopes of the measurement points are equivalent to the average daily ozone loss rates at each level during the period and are independent of the initial condition (January 23 occultation). There is little net change in ozone mixing ratio at 575 K, but there is increasing loss with decreasing altitude to a maximum loss near 425 K.

Ozone Time Series Trajectory Analysis

Another, closely related approach utilizing diabatic trajectories has been described by *Schoeberl et al.* [2002], where ozone measurements were injected into a free-running diabatic trajectory calculation. Similar to the preceding analysis, the lower stratosphere on March 4 was divided into 5-K potential temperature layers. All of the parcels within each layer having originated from earlier MSX/UVISI observations were identified using diabatic trajectory calculations. A time series was then constructed for each diabatic layer, with the measured ozone mixing ratios plotted versus the elapsed time from the occultation to March 4. Such an ozone time series is shown in Figure 5.11 for the 425-K surface (analogous to Figure 5.10c). The average ozone loss rate is then simply the slope of the linear regression through the observation points. Because more or fewer than one trajectory air parcel from each occultation may be within each 5-K layer on March 4, not every profile will be represented with a single data point (there may be more or fewer than 25 points on each surface).

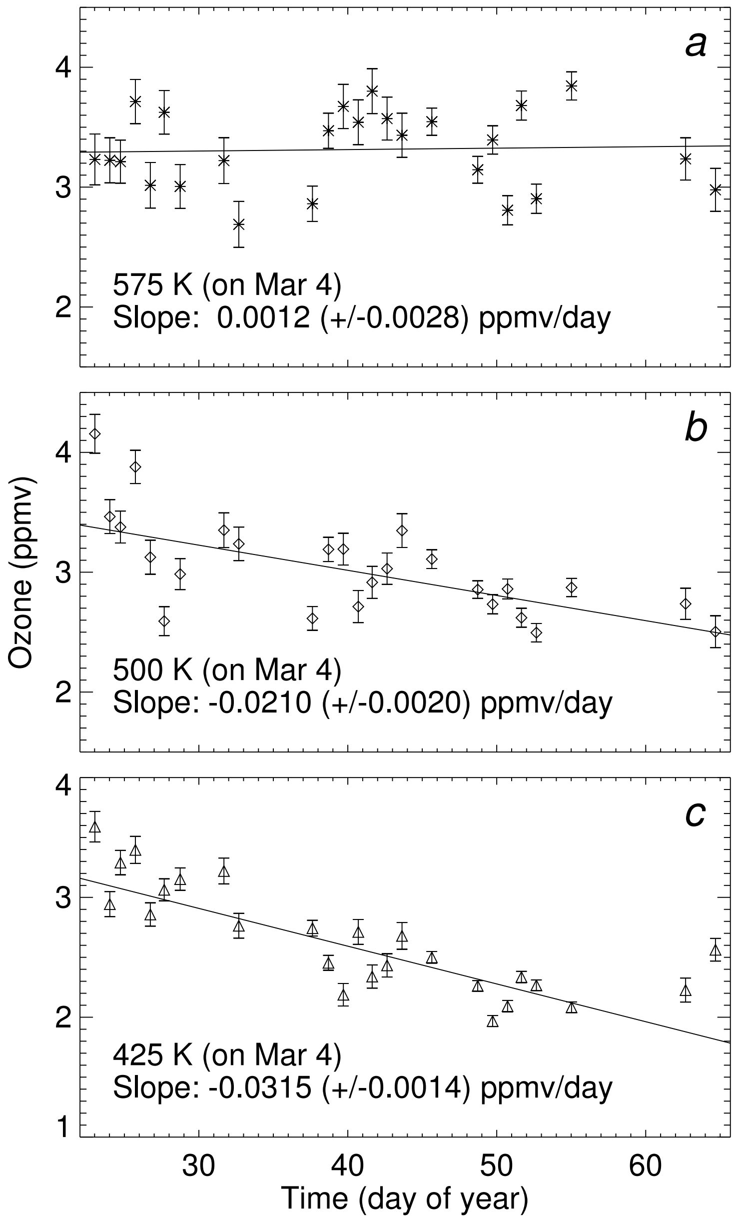

Figure 5.10. Photochemical ozone loss within the polar vortex along three particular diabatic surfaces corresponding to the (a) 575-, (b) 500-, and (c) 425-K potential temperature surfaces on March 4, using diabatic trajectory analysis. The ozone mixing ratios indicated were those measured by each of the 25 stellar occultations within the vortex during SOLVE. The error bars denote the 1-σ uncertainty of the occultation measurements and retrieval and do not include errors in the trajectory calculations. The average daily loss rates for the period (i.e., the absolute values of the slopes resulting from weighted linear regressions through the observations on each surface), are also shown, along with the uncertainties in the fits.

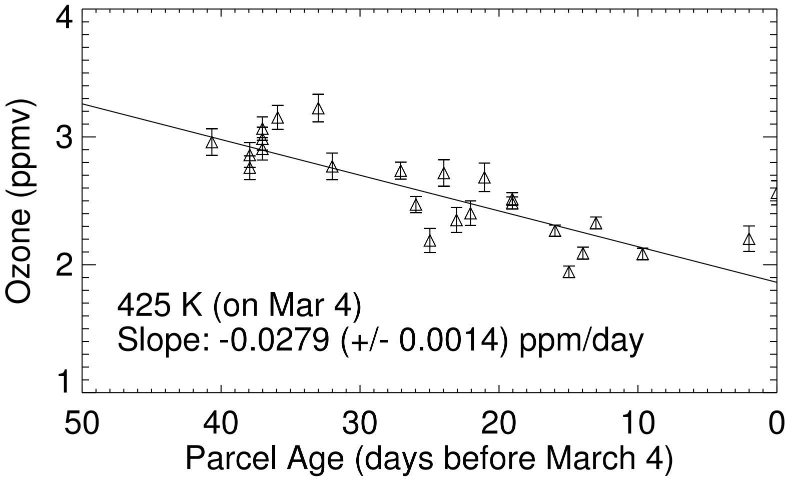

Figure 5.11. Ozone loss inferred from ozone time series at 425 K on March 4. Each symbol represents an air parcel within 2.5 K of 425 K on March 4, the date of the final MSX/UVISI stellar occultation event, that had been sampled by an earlier occultation. The ozone mixing ratios indicated were those measured at the times of the earlier occultations, and the parcel age is simply the elapsed time since those observations on March 4. The error bars denote the 1-σ uncertainty of the stellar occultation measurements and retrieval and do not include errors in the trajectory calculations. In each layer, it is possible for there to be more or fewer than one trajectory parcel sampled in an earlier occultation. The average daily loss rate is inferred from the slope of the weighted linear fit. This diabatic surface corresponds to that in Figure 5.10c.

5.4.2 Ozone Loss Profiles

The ozone loss rates for consecutive layers, which are individually depicted in Figures 5.10 and 5.11, produce a more complete picture of lower stratospheric ozone change when combined to produce a profile, as in Figure 5.12. All three trajectory analysis methods discussed above for deriving ozone loss are represented in the figure. Though they differ at 5-K resolution (compare Figures 5.10c and 5.11), the different analyses provide nearly identical results when averaged over 25-K intervals.

The overall rate of ozone loss below 500 K is very nearly 1 ppmv for this time period, which is consistent with other ozone loss analyses (see Table 5.2). The 450-K average daily loss rate, 0.024 ppmv/day, agrees well with the corresponding loss rate from the ozonesonde analysis of *Schoeberl et al.* [2002], for example, which was $\sim$0.025 ppmv/day at 465 K in mid-February. Ozone change rates diminish above 500 K and even become slightly positive above 575 K, as has been seen by *Hoppel et al.* [2002] and *Schoeberl et al.* [2002], though perhaps only the result of extra-vortex contamination [*Schoeberl et al.*, 2002].

It is important to note that the available MSX/UVISI occultations span only the central portion of the time periods of ozone loss in the other analyses, which report higher total ozone loss over larger portions of the December 1999–late March 2000 period. The quasi-conservative mapping method of *Lait et al.* [2002], when used to derive the ozone loss rate from ozonesonde data over the same time period used in this chapter (January 23 through March 4, 2000), yields an average loss rate of 0.030 $\pm$ 0.008 ppmv/day at 450 K (L. R. Lait, NASA/Goddard, personal communication, 2001).

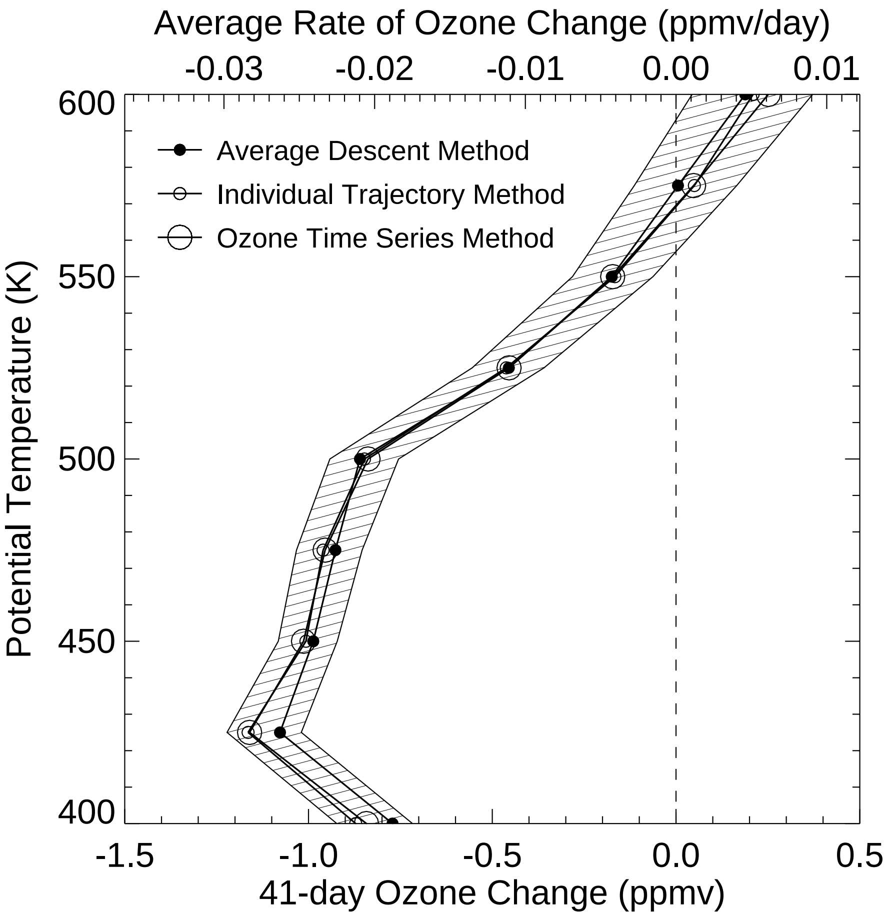

Figure 5.12. Profiles of the average daily rates of ozone change and total ozone destruction, from January 23 to March 4, 2000. The results from three different but related methods, utilizing average vortex descent rates and two analyses using individual diabatic trajectory calculations, are shown. The data have been averaged over 25-K layers, and the lined region contains the average 1-σ uncertainties of the linear fits of the ozone measurements (and thus the rates of ozone change) on the individual diabatic surfaces within each layer.

Table 5.2. Comparison of Arctic polar vortex ozone loss techniques at 450 K on March 12, 2000, estimated from observations from January 20 to March 12, 2000

Reference	O_3 Loss (ppmv)	Uncertainty (ppmv)	Dataset
Bremer et al. [2002]	1.05[a]	±0.1	ASUR
Grant et al. [2001]	1.5	±0.3	LARC DIAL
Hoppel et al. [2002]	1.45	±0.2	POAM III solar occultation
Klein et al. [2002]	0.7[a]	±0.3	Ny-Ålesund microwave radiometer
Kopp et al. [2002]	1.1[a]	±0.2	Kiruna FTIR O_3, N_2O, HF
	1.4	±0.6	Microwave O_3, FTIR N_2O, HF
Lait et al. [2002]	1.7	±0.3	PV–θ analysis–Ozonesondes
Müller et al. [2001]	2.2[b]	±0.3	HALOE and OMS
Rex et al. [2002]	1.7	±0.2	Match–Ozonesondes
Richard et al. [2001]	1.8	±0.3	ER-2 tracer–tracer
Robinson et al. [2001]	1.35[c]	±0.12	Dirac tracer–tracer
	1.10[d]	±0.1	Descartes tracer–tracer
Salawitch et al. [2002]	1.36[e]	±0.21	OMS measurements
	1.76	±0.21	OMS balloon and ER-2 data
Santee et al. [2000]	2.3[f]	±0.6	UARS MLS
Schoeberl et al. [2002]	1.63	±0.3	Vortex average–Ozonesondes
	1.3	±0.1	POAM III
	1.54	±0.15	Forward trajectory
Sinnhuber et al. [2000]	1.7	±0.2	Ny-Ålesund sonde, SLIMCAT model
Swartz et al. [2002]	1.4[g]	±0.08[h]	MSX stellar occultation [this work]

(Adapted from *Newman et al.* [2002].)

[a]Microwave and infrared instruments have ∼10-km vertical resolution at 20 km altitude.

[b]Estimated between November 1999 and 3/(11–14)/2000.

[c]Estimated for 1/23 to 3/7/2000.

[d]Estimated for November 1999 to 3/4/2000.

[e]Estimated for 1/20 to 3/5/2000.

[f]Loss rate (0.04 ppmv/day) estimated at 465 K between 2/2 and 2/13/2000, scaled for 52 days, with a 0.25-ppmv correction for downward advection.

[g]Based on the 1.0-ppmv ozone loss between 1/23 and 3/4/2000. If we assume an average loss rate of 0.05 ppmv/day for the second week in March, consistent with the other analyses, a total loss of 1.4 ppmv for 1/20–3/12/2000 is inferred.

[h]Based solely on the linear fits of the ozone measurements (see Figure 5.12).

Table 5.3. Summary of comparisons of MSX/UVISI stellar occultation retrievals with other analyses

Retrieved Quantity	Difference[a]	Comparison
Temperature	-1.4 ± 2.3 K	UKMO
Potential temperature	-1.0 ± 7.1 K	UKMO
Ozone mixing ratio	$+0.02 \pm 0.36$ ppmv	POAM III[b]
	$(+1.5 \pm 12.9\%)$	

[a]Mean difference (MSX/UVISI − comparison data) $\pm$ 1-σ standard deviation, over 400–600 K potential temperature (∼16–24 km).

[b]Ozone mixing ratio from ozone–PV reconstruction.

5.5 Summary and Conclusions

An innovative, extinctive–refractive stellar occultation technique has been used to measure atmospheric composition within the Arctic polar vortex. This technique allows for the simultaneous retrieval of total density, pressure, temperature, and ozone mixing ratio. Twenty-five profiles within the vortex were derived from MSX/UVISI measurements over a 41-day period during the SOLVE campaign. Table 5.3 summarizes the excellent agreement between the stellar occultation retrievals of temperature, potential temperature, and ozone mixing ratio with other measurements.

Using diabatic trajectory calculations, the effects of large-scale descent within the vortex were removed, allowing the rate of photochemical ozone loss during polar winter to be inferred. A maximum ozone loss of about 1 ppmv at 400–500 K (∼16–21 km) from January 23 through March 4, 2000, was determined, corresponding to an average daily loss rate of ∼0.024 ppmv/day, in agreement with other SOLVE determinations of ozone loss (see the results of several ozone loss analyses during SOLVE summarized in Table 5.2 for comparison [*Newman et al.*, 2002]).

Though the MSX/UVISI instrument was not optimized for stellar occultation and spacecraft commitments limited the number of measurements that could be performed during SOLVE, the dataset demonstrates the utility of stellar occultation from a space-based platform as a means of accurately measuring bulk atmospheric quantities and stratospheric ozone. A dedicated stellar occultation instrument, such as the recently launched Global Ozone Monitoring by Occultation of Stars (GOMOS) instrument [*Bertaux et al.*, 1991], could provide hundreds of profiles at high vertical resolution and near-global coverage each day. The extinctive–refractive technique described here has the further advantage of the ability to probe the atmosphere down into the upper troposphere (a region that is under-sampled by other satellite techniques and is vital to understanding climate change).

Chapter 6

Optical Effects of Polar Stratospheric Clouds on Photolysis and Ozone Loss in the Arctic Lower Stratosphere

In section 4.5.2, comparisons with clear-sky j-value calculations indicated that j-values measured in the lower stratosphere during the NASA SAGE III Ozone Loss and Validation Experiment (SOLVE) were episodically attenuated at high solar zenith angles (SZAs). It was proposed that this attenuation was the result of optical effects of polar stratospheric clouds (PSCs) blocking the Sun. This chapter contains an exploratory study of how the optical effects of PSCs might impact photolysis and ozone loss in the Arctic stratosphere, based on the limited dataset obtained during SOLVE.

6.1 Introduction

Human activities have led to profound changes in stratospheric ozone concentrations over the past several decades. A quantitative understanding of the physical–chemical mechanisms of ozone loss and recovery [e.g., *Solomon*, 1999] is essential to the prediction of the evolution of stratospheric ozone in the future. PSCs, which are prevalent in the Antarctic winter and similarly occur intermittently in the Arctic, play a pivotal role in seasonal ozone loss by providing surfaces upon which heterogeneous chemical processes occur that are the prerequisites for rapid, halogen-catalyzed ozone loss. However, while PSCs act in a chemical sense to promote rapid ozone loss, the optical properties of PSCs also attenuate the weak actinic flux in polar twilight and slow the photochemical cycles that lead to ozone loss. In order to adequately quantify the photochemical processes controlling ozone and radical species concentrations, a realistic, quantitative estimate of photolysis rate coefficients (*j*-values) for photochemical processes in the stratosphere is needed.

6.1.1 Effects of Clouds on Photolysis

In the stratosphere, there are a number of geophysical factors that modulate *j*-values, including overhead ozone amount, surface albedo, surface height, and the albedo and altitude of tropospheric clouds. The effects of these variables on both measured and modeled summertime *j*-values have been studied in the context of the NASA Photochemistry of Ozone Loss in the Arctic Region in Summer (POLARIS) campaign by *Swartz et al.* [1999, see also chapter 3], and the sensitivity of *j*-values to these environmental forcings is now generally well understood.

Nack and Green [1974] first explained how clouds can both attenuate and enhance UV radiation at the surface of the Earth, depending on atmospheric conditions, and this phenomenon and its effect on photolysis have been considered numerous times since [e.g., *Thompson*, 1984; *Madronich*, 1987b; *Tsay and Stamnes*, 1992; *Kylling et al.*, 1995; *Los et al.*, 1997]. An extensive comparison of ground-based spectroradiometer data and radiative transfer model calculations from the International Photolysis Frequency Measurement and Modeling Intercomparison (IPMMI) near Boulder, Colorado in June

1998, has yielded a semi-quantitative assessment of spectral cloud effects at the surface [*Crawford et al.*, 2002]. Optical cloud effects have also been observed from aircraft in the lower [e.g., *Dickerson et al.*, 1982; *Kelley et al.*, 1995; *Crawford et al.*, 1999; *Shetter and Müller*, 1999; *Früh et al.*, 2000] and upper [e.g., *Crawford et al.*, 1999; *Shetter and Müller*, 1999] troposphere. During the SOLVE campaign, actinic flux and j-values in the presence of PSCs at high SZAs were observed in the Arctic lower stratosphere, providing a unique dataset for the study of the optical effects of PSCs on photolysis.

Modeling of the impacts of aerosols and clouds on photolysis and photochemistry in the troposphere has been the subject of extensive investigation [*Liao et al.*, 1999; *Früh et al.*, 2000; *Brasseur et al.*, 2002, and references therein]. The photolysis effects of aerosols and clouds in the stratosphere have also been modeled [*Anderson and Lloyd*, 1990; *Tsay and Stamnes*, 1992; *Anderson et al.*, 1995], and the resultant impact of volcanic stratospheric aerosols on ozone has been further investigated with chemistry–transport models [*Rosenfield et al.*, 1997; *Tie et al.*, 1994]. The impacts of the optical properties of PSCs on stratospheric heating rates [*Hicke and Tuck*, 2001, and references therein] and the Total Ozone Mapping Spectrometer (TOMS) total ozone retrieval [*Torres et al.*, 1992] have also been considered. However, while heterogeneous chemical processes on PSCs have been the subject of extensive modeling, measurement, and laboratory efforts, the impact of the optical effects of PSCs on photolysis and ozone loss is less well understood. The goal of this chapter is an estimate of the impact of the optical effects of PSCs on stratospheric photolysis and ozone loss during the 1999/2000 Arctic winter.

Recent studies [e.g., *Shindell et al.*, 1998] have predicted that, with the increase of greenhouse gases in the atmosphere and consequently a radiative cooling of the stratosphere, ozone depletion will be exacerbated in coming decades, slowing the recovery of stratospheric ozone following reductions in anthropogenic emissions of CFCs. *Pitari et al.* [2002] suggest that global change will lead to PSCs with increased frequency and optical depth (by a factor of 5 in the Arctic by 2030). In this context, it is vital to understand how the optical impacts of PSCs are affecting ozone loss now so that responses to changes in climate (decreasing temperature trends in the lower stratosphere [*Ramaswamy et al.*, 2001]) and the chemical composition of the atmosphere (increasing trends in stratospheric water vapor and nitric acid [*Isaksen and Jackman*, 1999, and references therein]) may be more fully understood. This understanding of optical PSC forcing could improve models predicting the future evolution and variability of stratospheric ozone.

6.1.2 SOLVE

The SOLVE campaign, based in Kiruna, Sweden (68°N, 20°E), from November 1999 through March 2000, provided an excellent opportunity for the extensive comparison of *j*-values in polar twilight, both measured with state-of-the-art in situ instruments and calculated with radiative transfer models. The winter 1999/2000 Arctic polar vortex was particularly stable over a long period of time [*Manney and Sabutis*, 2000], with cold temperatures, extensive PSCs, and significant photochemical ozone loss [*Newman et al.*, 2002].

Two tools were used in this preliminary study of the direct, optical impact of PSCs on photolysis rates during SOLVE: the APL radiative transfer model and NCAR's Scanning Actinic Flux Spectroradiometer (SAFS) [*Shetter and Müller*, 1999], both of which were used to derive photolysis rate coefficients. The analysis approach used in this chapter is outlined in Figure 6.1. This roadmap indicates how the different elements discussed fit together to provide an estimate of the optical effects of PSCs on ozone loss.

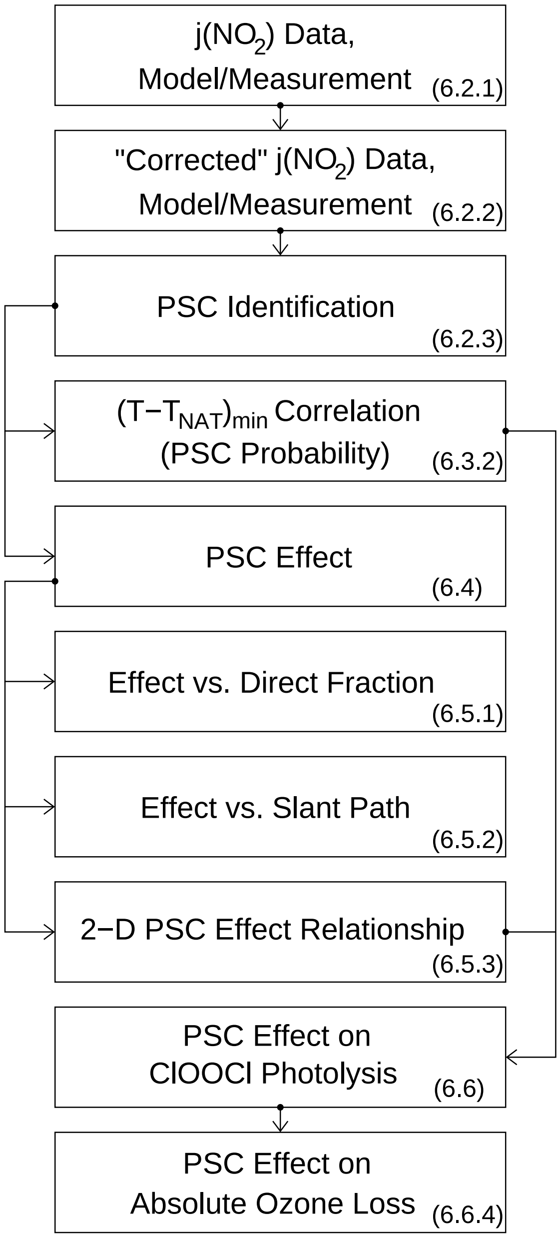

Figure 6.1. PSC optical effect analysis roadmap (with corresponding section numbers indicated in parentheses).

6.1.3 Model Description

The specific application of the APL model (described in section 1.3, with ancillary information in appendix A) during SOLVE was discussed in detail in chapter 4, but it is also summarized as follows. The APL model has been developed over a period of nearly two decades specifically for the calculation of twilight *j*-values (175–850 nm) in the lower stratosphere and troposphere. The model solves the integral equation of radiative transfer, in which direct solar deposition and reflection from a Lambertian reflecting surface are calculated in a spherical, refracting atmosphere, and isotropic multiple scattering is calculated using a plane-parallel approximation. Calculated *j*-values, particularly for NO_2, O_3, and $ClONO_2$ photolysis, have been compared extensively with those obtained from ultraviolet (UV)/visible spectroradiometers aboard aircraft, from other models, and *j*-values calculated from observed species concentrations, most recently during POLARIS [*Swartz et al.*, 1999; *Del Negro et al.*, 1999; *Stimpfle et al.*, 1999; *Gao et al.*, 2001; see chapter 3] and SOLVE (R. E. Shetter et al., manuscript in preparation, 2002; see chapter 4). Though the modeling of *j*-values at large SZAs has traditionally posed a challenge, the APL model has proved highly accurate in twilight, up to 95° [*Anderson*, 1983; *Dahlback and Stamnes*, 1991; *Gao et al.*, 2001].

6.1.4 SAFS Instrument

The SAFS instrument, described in section 4.5.1, provided *j*-values derived from in situ measurements of the 4π-sr actinic flux from the DC-8 (see *Shetter and Müller* [1999]). SAFS is composed of two independent double-pass spectroradiometer systems, mounted on the top and bottom of the DC-8, sampling the downwelling and upwelling hemispheres of the radiation field, respectively, including the direct solar beam, over

280–420 nm[1] with a FWHM resolution of 1 nm.

6.2 Identification of PSC Effects Using Modeled/Measured j_{NO_2}

An analysis of PSC effects on *j*-values begins with the identification of *j*-value measurements from SOLVE that were potentially affected by the optical properties of PSCs. Detailed comparisons of the APL model and SAFS during SOLVE were shown in section 4.5, with section 4.5.2 suggesting the influence of PSCs. For the present, more detailed analysis of the optical effects of PSCs, APL_{POAM} (clear-sky) model calculations where employed, using ozone profiles based on POAM III O_3–potential vorticity (PV)[2] reconstruction data [*Randall et al.*, 2002] and TOMS surface reflectivity [*McPeters et al.*, 1998]. When POAM and TOMS data were unavailable (e.g., at the largest SZAs), climatological data were used (APL_{clim}). Data from altitudes less than 8 km were not considered.

6.2.1 j_{NO_2} Model–Measurement Comparison

A comparison of j_{NO_2} as determined by SAFS and clear-sky APL model calculations at high SZAs is shown in Figure 6.2 for the SOLVE science flights (see section D.1 for a summary of SOLVE DC-8 flights). Each data point represents a 300-s average of 10-s interpolated data along the flight tracks. This analysis uses APL/SAFS *j*-value ratios (Figure 6.2a), but the reciprocal plot, SAFS/APL in Figure 6.2b, is also included for

[1]Extended to 280–535 nm during the January and February–March 2000 SOLVE intensives.

[2]See section F.2 for the definition of PV.

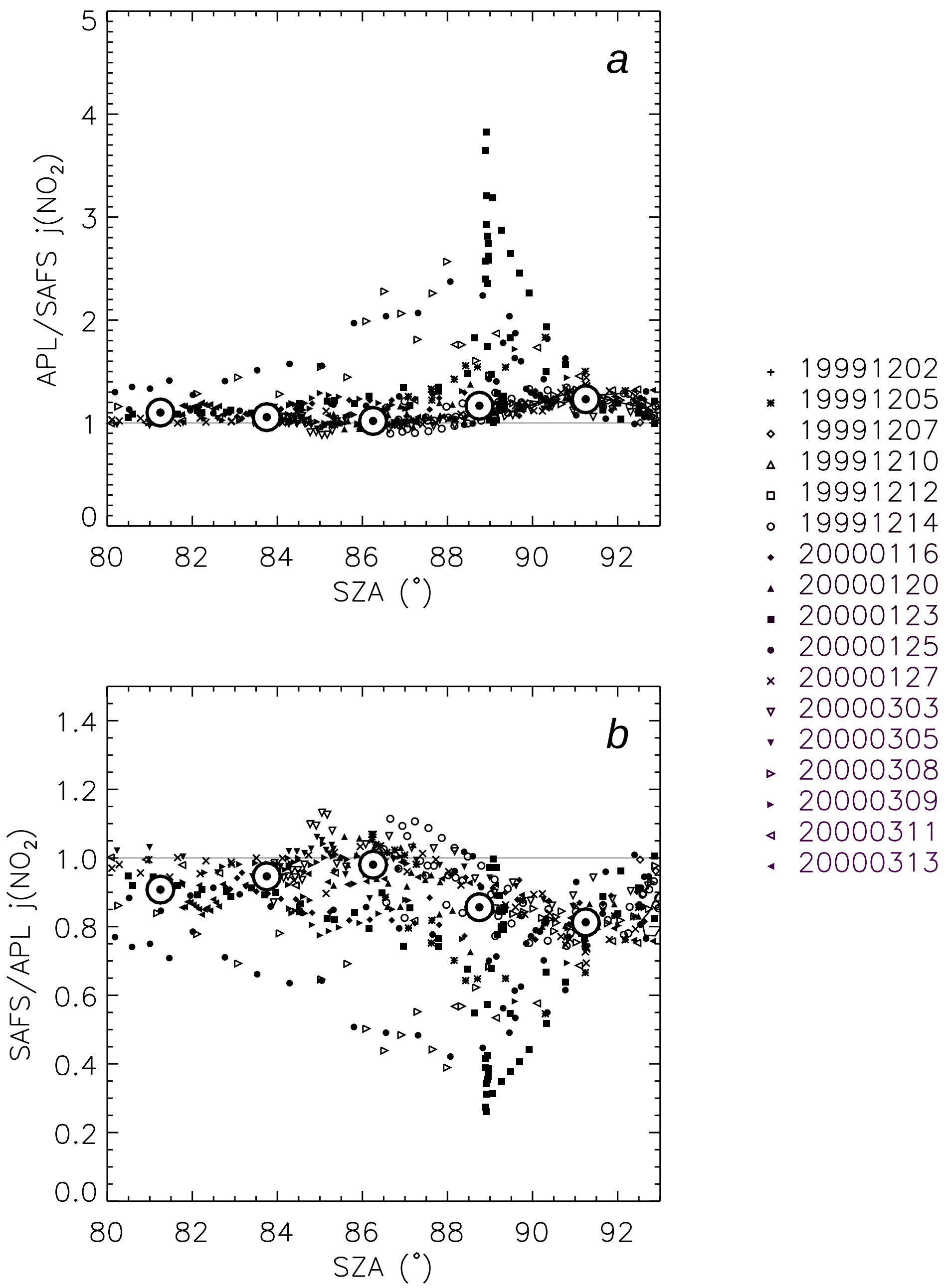

Figure 6.2. Ratios of (a) APL model (APL_{POAM})/SAFS measured and (b) SAFS/APL j_{NO_2} (reciprocal of (a)) for SZA$\geq$80° along DC-8 flight tracks during SOLVE. Each science flight is identified by a unique symbol, as keyed at right. All data points above 8 km altitude are considered, with no other data filtering. The bull's-eyes ($\odot$) along the baseline are the median values (excluding points outside 2-σ standard deviations of the medians of all of the points) centered in 2.5° SZA bins.

reference. The SAFS/APL ratios are useful when viewing the problem in terms of attenuation relative to clear-sky (APL) *j*-values. Points where the SAFS measurements were noticeably smaller than the clear-sky model are from flights where PSCs were prevalent (e.g., 20000123,[3] 20000125). Extensive PSCs were found during SOLVE, particularly near the end of January 2000 [*Bevilacqua et al.*, 2002, and references therein]. The smaller measured j_{NO_2} is consistent with attenuation of the solar flux by PSCs.

The j_{NO_2} ratios in Figure 6.2 are used here as evidence of the presence of PSCs along the line of sight (LOS) to the Sun. NO_2 photolysis is well suited for this purpose because it occurs at relatively long wavelengths (<424 nm)—at large SZAs, the shortest wavelengths of the solar flux succumb to long–path length extinction. j_{NO_2} is also insensitive to the overhead ozone column and the surface albedo when the Sun is close to the horizon [see chapter 3; *Swartz et al.*, 1999], which eliminates typical sources of error in the modeling of *j*-values.

6.2.2 j_{NO_2} "Corrected" Model–Measurement Comparison

While there are significant deviations from exact model–measurement agreement, most points in Figure 6.2 cluster near the 1-to-1 line, with a SZA-dependent bias. To derive a j_{NO_2} PSC metric, model–measurement biases were removed by subtracting a baseline "correction" from the ratio data points. An objective characterization of the underlying biases (not affected by PSCs) was obtained by binning the data in 2.5° SZA bins, then calculating the median value in each bin, excluding points lying outside 2-σ standard deviations of the medians of all of the points (thus rejecting attenuated *j*-value points in the correction). The baseline is indicated in Figure 6.2 with bull's-eyes ($\odot$). The

[3] Dates are represented in YYYYMMDD format. 20000123 denotes January 23, 2000.

“corrected” j_{NO_2} ratios are shown in Figure 6.3.

6.2.3 Identification of PSCs Using j_{NO_2} Comparison

A ratio threshold of $\pm 18\%$ was chosen to define a region outside of which something other than clear-sky noise was the cause of model–measurement discrepancy.[4] APL/SAFS points that exceed 1.18 were assumed influenced by PSCs. Unlike lidar techniques used on the DC-8 during SOLVE (LASE [*Browell*, 1997], UV-DIAL [*Browell et al.*, 1998], AROTEL [*Burris et al.*, 1998]), which measured aerosols in the vertical column above the DC-8 during SOLVE, the *j*-value effect does not readily yield information about PSC type or proximity. It does, however, provide a direct measure of PSC *j*-value attenuation of photolysis, by definition, which is the purpose of this analysis.

The results of the PSC criterion are demonstrated in Figure 6.4 for all DC-8 science flights during SOLVE, from December 1999 to March 2000. The presence of PSC effects are indicated, based on the PSC j_{NO_2} threshold criterion. *Bevilacqua et al.* [2002] observed PSCs between 13 and 25 km during SOLVE. The geometries of the light paths through the atmosphere were determined, and the geographic locations of the putative PSCs are included in Figure 6.4, assuming they lay along the solar LOS within the 13–25-km layer of the atmosphere.

[4]The choice of $\pm 18\%$ was somewhat arbitrary, but it contained most of the data scatter close to the 1-to-1 line, and the subsequent analysis is largely insensitive to small changes in the threshold.

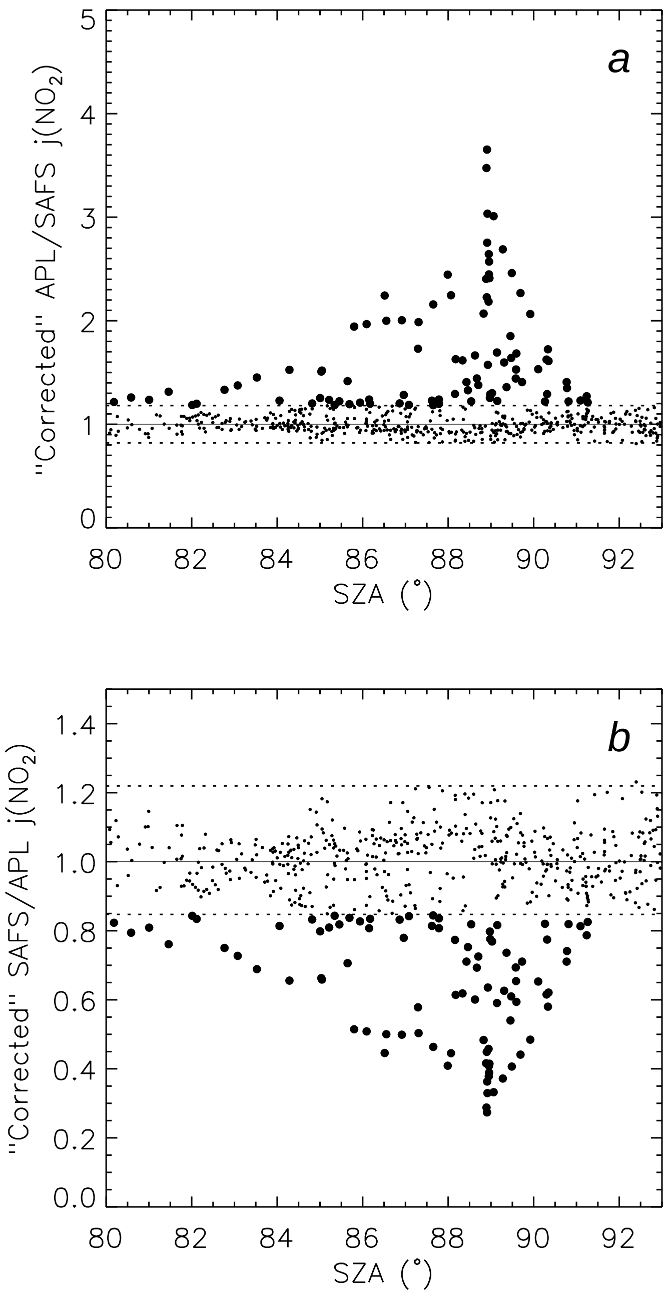

Figure 6.3. "Corrected" ratios of (a) APL/SAFS and (b) SAFS/APL j_{NO_2} for SZA$\geq$80° along DC-8 flight tracks during SOLVE. The points correspond to those from Figure 6.2, after the differences between the median ratios (represented there with bull's-eyes, $\odot$) and unity have been subtracted from the ratios, effectively removing model–measurement bias. The dotted lines, at 1 ± 0.18 in (a), represent a threshold beyond which the ratios are considered affected by PSCs (PSCs attenuated the measured j_{NO_2}). The points affected by PSCs are represented with larger dots (•).

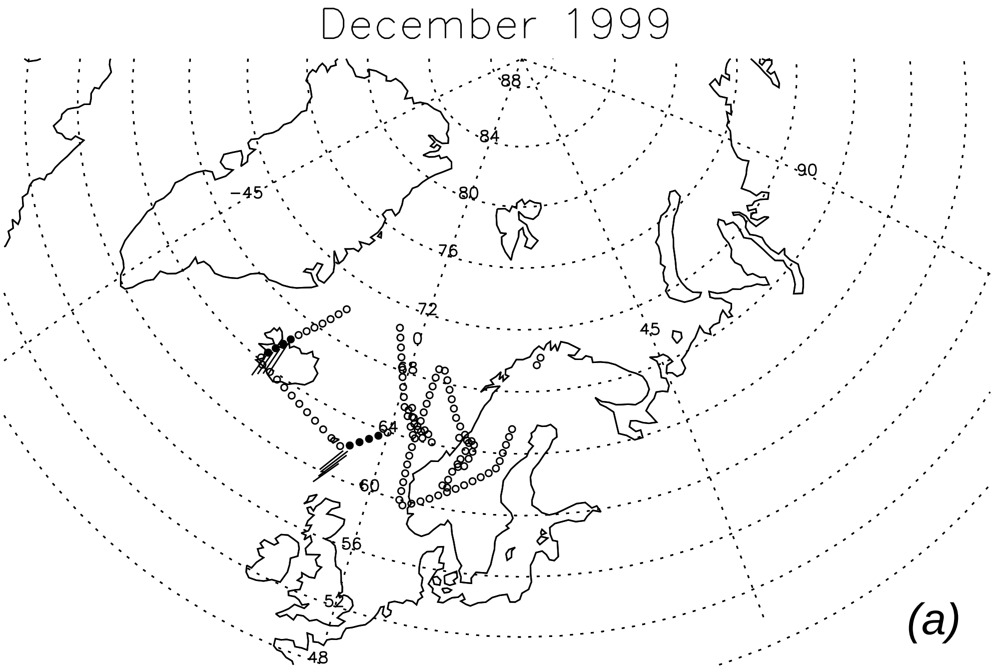

Figure 6.4. Maps of DC-8 flight tracks during (a) December 1999, (b) January 2000, and (c) February–March 2000, at SZA$\geq$80°. The filled (•) and open (○) circles represent points corresponding to the large and small dots in Figure 6.3, indicating the presence and absence of *j*-value attenuation, respectively. The lines radiating from the affected points show where the line of sight to the Sun intersected the 13–25-km PSC layer of the atmosphere at that moment, considering the solar zenith and azimuth angles.

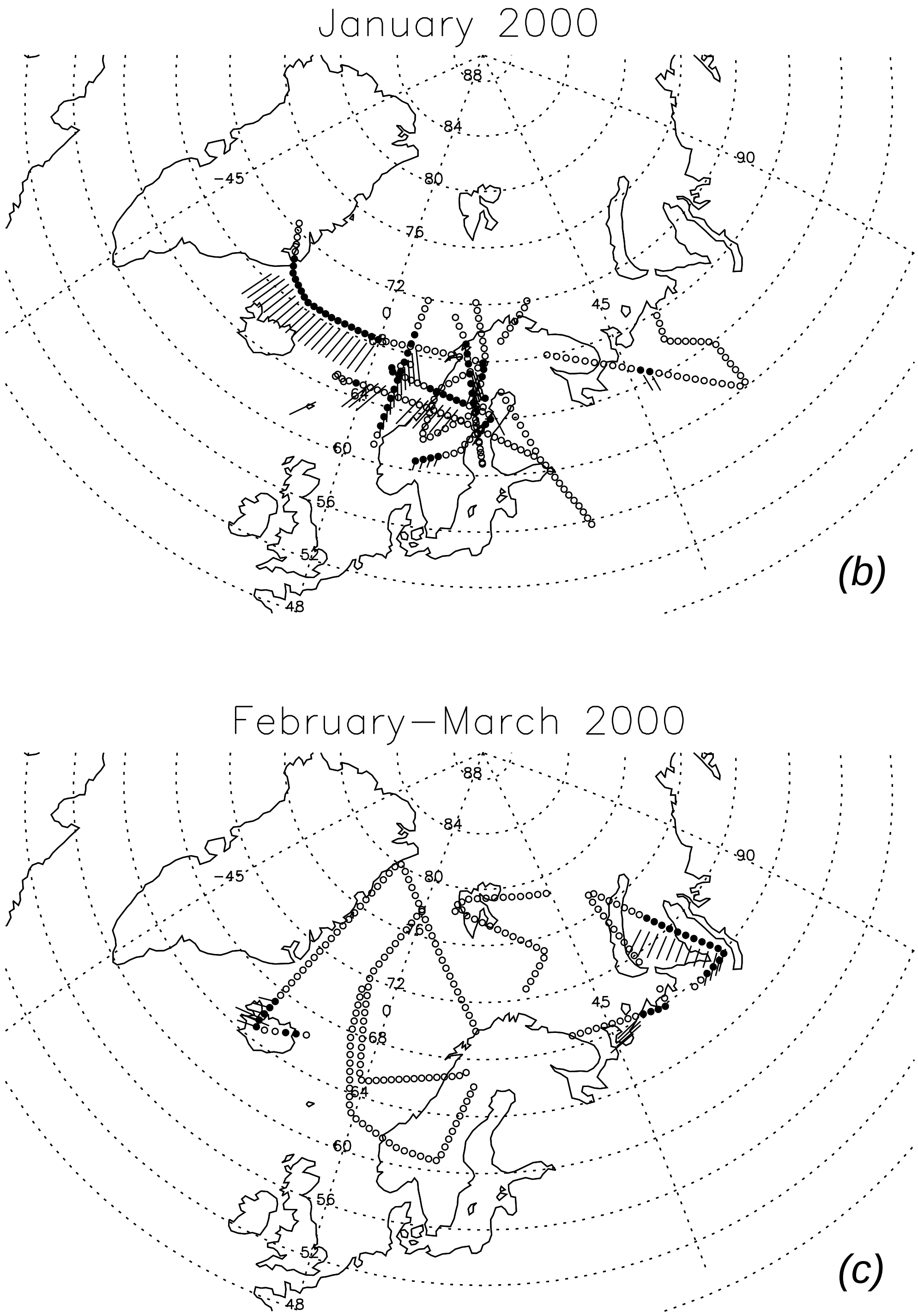

Figure 6.4. Maps of DC-8 flight tracks (continued).

6.3 Relationship of PSC Effects with Temperature

Since PSCs generally form when the in situ temperature drops below the saturation temperature of nitric acid trihydrate, T_{NAT} [*Hanson and Mauersberger*, 1988],[5] it would be expected that the locations of PSCs affecting $j_{\mathrm{NO_2}}$ along the DC-8 flight tracks would coincide with cold temperatures, below T_{NAT}. This assertion is tested in Figure 6.5 for the 20000308 SOLVE flight. T_{NAT} was computed [*Hanson and Mauersberger*, 1988] using United Kingdom Meteorological Office (UKMO) meteorological data [*Swinbank and O'Neill*, 1994] and assuming 10 ppbv HNO_3 and 5 ppmv H_2O,[6] and the minimum in situ temperature difference with T_{NAT}, $(T - T_{\mathrm{NAT}})_{\mathrm{min}}$, was determined in the vertical column between 13 and 25 km. The coincidence of cold temperatures and the inference of PSCs using modeled/measured $j_{\mathrm{NO_2}}$ is apparent for this flight.

6.3.1 Altitude Extent of Sub-T_{NAT} Temperatures

The $(T - T_{\mathrm{NAT}})_{\mathrm{min}}$ temperatures along solar LOSs from DC-8 flights were computed during SOLVE. The vertical extent (within the 13–25-km layer) of sub-T_{NAT} temperatures and the average altitude of $(T - T_{\mathrm{NAT}})_{\mathrm{min}}$ for each flight is shown in Figure 6.6. Sub-T_{NAT} temperatures sank within the vortex, as the figure shows, along with the air-

---

[5] T_{NAT} was determined by solving the *Hanson and Mauersberger* [1988] equation for the behavior of vapor over NAT, as follows.

$$T_{\mathrm{NAT}} = \frac{-b + \sqrt{b^2 - 4c}}{2},$$

$$b = \frac{38.9855 - 2.7836\log(p_{\mathrm{H_2O}}) - \log(p_{\mathrm{HNO_3}})}{0.009179 - 0.00088\log(p_{\mathrm{H_2O}})},$$

$$c = -\frac{11397}{0.009179 - 0.00088\log(p_{\mathrm{H_2O}})},$$

for $180 < T_{\mathrm{NAT}} < 200$ K and partial pressure p in Torr.

[6] Under these conditions, T_{NAT} ranges from 203 K at 13 km to 192 K at 25 km.

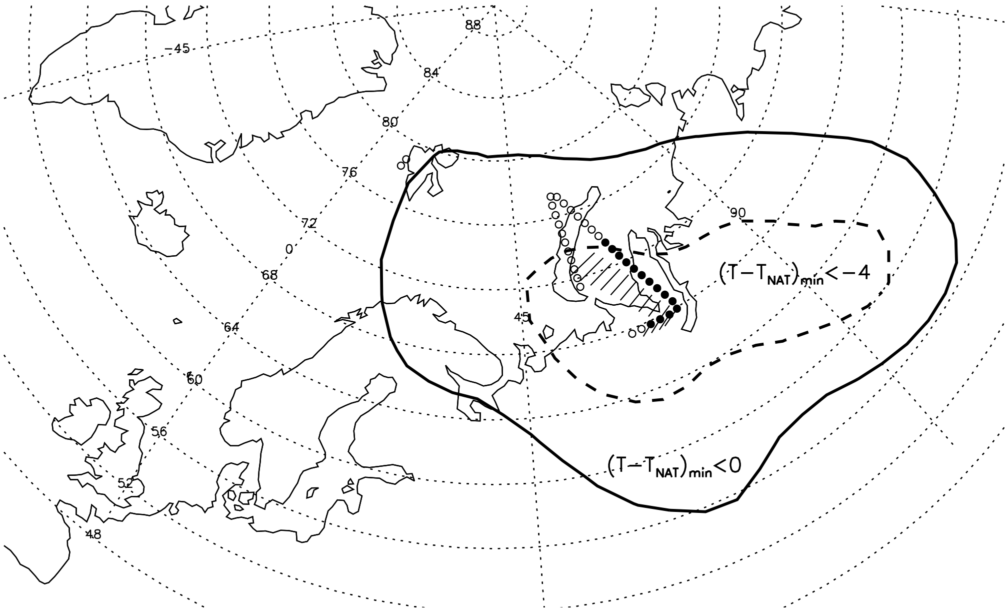

Figure 6.5. Map of 20000308 DC-8 flight track. The flight is represented as in Figure 6.4c, with the *j*-value attenuation (•/○) and putative locations of PSCs indicated. Also included are the regions with $(T - T_{\mathrm{NAT}})_{\mathrm{min}} < 0$ K and $(T - T_{\mathrm{NAT}})_{\mathrm{min}} < -4$ K in the vertical column overhead between 13 and 25 km, as derived from UKMO analyzed meteorological data, enclosed within solid and dashed lines, respectively.

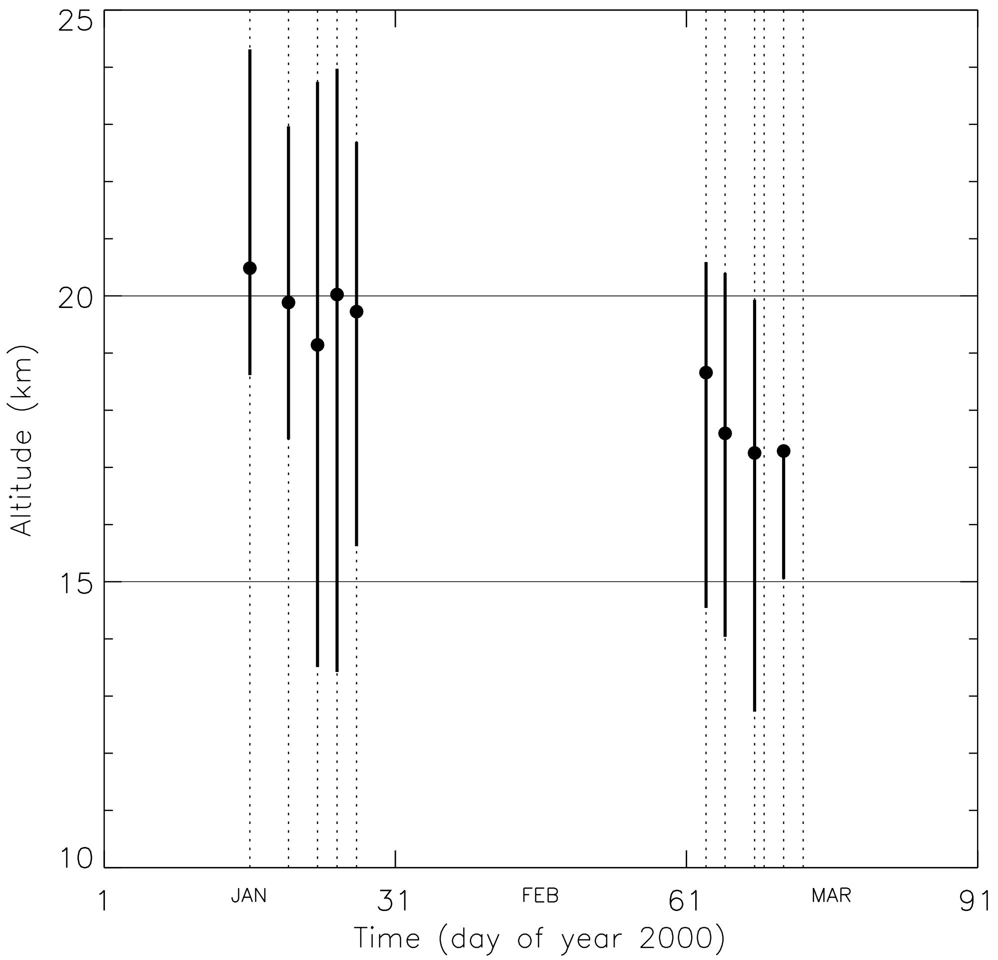

Figure 6.6. Vertical extents of $(T - T_{\mathrm{NAT}})_{\mathrm{min}} < 0$ K regions along solar LOSs for DC-8 flights during SOLVE. The vertical dotted lines mark the dates of each flight during January–March 2000 (the December 1999 flights did not experience $(T - T_{\mathrm{NAT}})_{\mathrm{min}}$ below 0 K). The range of altitudes along the LOSs to the Sun (between 13 and 25 km) with $(T - T_{\mathrm{NAT}})_{\mathrm{min}} < 0$ K, derived from UKMO meteorological data, for each flight is represented with a thick solid line. The average altitude of $(T - T_{\mathrm{NAT}})_{\mathrm{min}}$ is shown with a filled circle (●).

mass in general (air at 20 km sank about 1 km from late-January to early-March).[7] Two of the March 2000 and all of the early December 1999 flights never experienced sub-T_{NAT} temperatures along the solar LOS. Figure 6.4a shows j_{NO_2}-attenuated points, however. These suggested PSCs forming at temperatures that were "warm" according to the UKMO analysis may actually have resulted from orographically forced atmospheric waves. Such waves cause positive and negative adiabatic perturbations in the stratospheric temperature fields, thus creating sporadic conditions favorable for PSC formation not captured in the meteorological analyses [e.g., *Carslaw et al.*, 1998].

6.3.2 Statistical Correlation of PSCs with $(T - T_{NAT})_{min}$

While the coincidence of *j*-value attenuation with $(T - T_{NAT})_{min}$ in Figure 6.5 is compelling, a statistical correlation with temperature would be anticipated if the model/measurement ratio effects were indeed due to PSCs. With $(T - T_{NAT})_{min}$ along the solar LOSs through 13–25 km determined for each of the data points from Figure 6.2, the data were binned in 1-K intervals according to $(T - T_{NAT})_{min}$, and the probability of *j*-value attenuation (PSC occurrence), P_{PSC}, was defined simply as the ratio of the number of PSC-affected points to the total number of observations in each bin. The results are shown in Figure 6.7, with statistics of the data in Table 6.1. The figure shows a trend of increasing P_{PSC} as temperatures dropped below T_{NAT}, similar to findings from the POAM III satellite [*Bevilacqua et al.*, 2002]. At a $T - T_{NAT}$ of -5 K, POAM reported probabilities of observing a PSC of nearly unity under some conditions.[8] This

[7] The polar vortex and diabatic subsidence therein are described briefly in section F.4.

[8] An exponential fit to the correlation (rather than linear) is also consistent with the data. Such a fit reaches unity PSC probability at a warmer $(T - T_{NAT})_{min}$ and is similar to POAM PSC temperature dependencies. The linear–exponential differences in the temperature range considered here would be relatively minor.

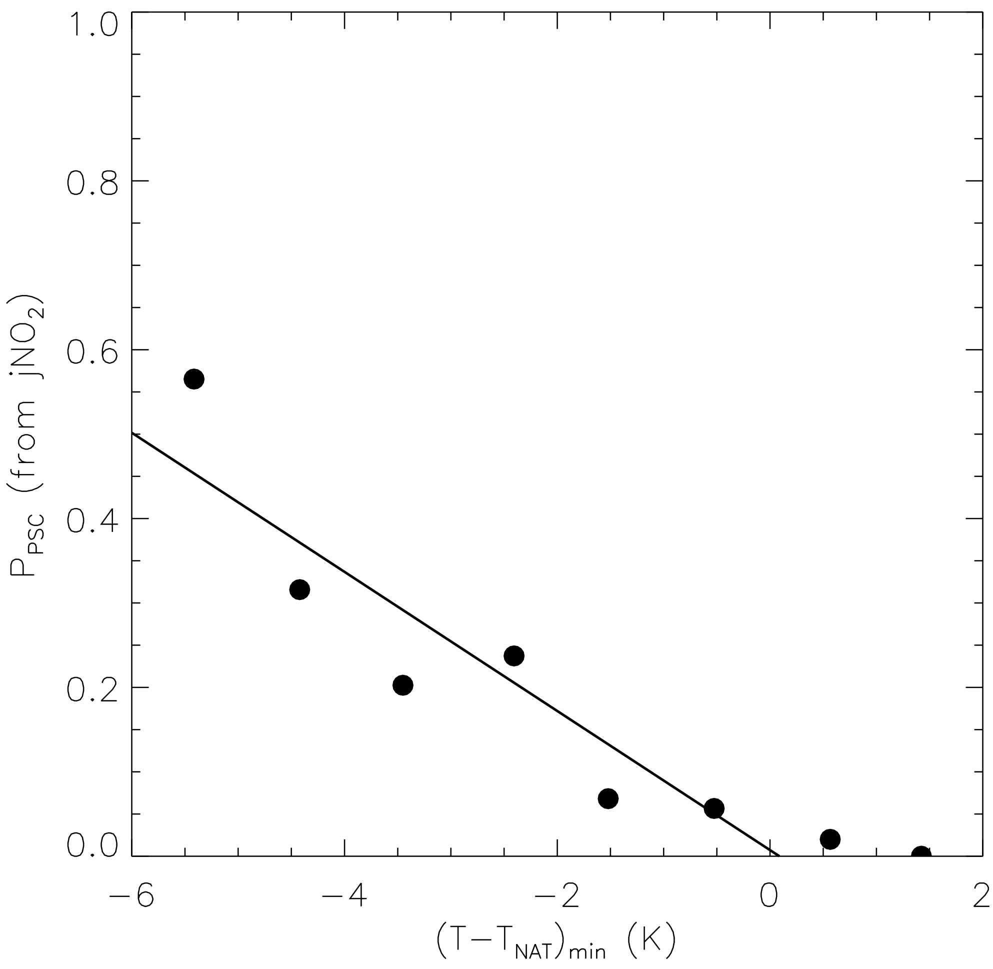

Figure 6.7. PSC probability as a function of $(T - T_{\mathrm{NAT}})_{\mathrm{min}}$ derived from modeled/measured $j_{\mathrm{NO_2}}$ from SOLVE DC-8 flights. The (corrected) APL/SAFS $j_{\mathrm{NO_2}}$ ratios were binned by $(T - T_{\mathrm{NAT}})_{\mathrm{min}}$ along the solar LOS in 1-K intervals. The probability of PSC occurrence, defined as the number of APL/SAFS points exceeding the 1.18 threshold relative to the total number of points in the interval, is plotted versus the average $(T - T_{\mathrm{NAT}})_{\mathrm{min}}$ within each temperature bin. The line is the linear fit to the data: $P_{\mathrm{PSC}} = -0.0824(T - T_{\mathrm{NAT}})_{\mathrm{min}} + 0.0072$. The statistics for the relationship are shown in Table 6.1.

Table 6.1. PSC probability–$(T - T_{NAT})_{min}$ correlation statistics

Mean[a] $(T - T_{NAT})_{min}$ (K)	Mean[a] SZA (°)	Mean[a] Altitude (km)	No. of PSC-affected/ Total No. Points
−5.4	85.2	10.4	13/ 23
−4.4	89.7	10.4	6/ 19
−3.5	89.4	10.4	16/ 79
−2.4	86.7	9.7	28/118
−1.5	87.4	9.7	6/ 88
−0.5	87.8	10.2	6/106
0.6	85.5	9.6	2/100
1.4	90.3	8.8	0/ 83

Each line in the table corresponds to a 1-K bin from Figure 6.7.

[a]Of all points in bin. SZA and altitude at the DC-8.

greater sensitivity of POAM could be attributed to the relatively longer wavelength of the POAM measurement (near 1 μm as opposed to the j_{NO_2} centroid wavelength of approximately 380 nm at large SZAs), which is not as readily scattered as the wavelengths effecting NO_2 photolysis. Denitrification of the vortex may have also led to an overestimation of T_{NAT} used in this analysis [*Bevilacqua et al.*, 2002].

The relationship of PSC probability with $(T - T_{NAT})_{min}$ shown in Figure 6.7 is based entirely on the comparison of clear-sky modeled and in situ measured j_{NO_2} near 11 km. The correlation with $(T - T_{NAT})_{min}$ along the solar LOS provides substantial support to the hypothesis that the model–measurement differences are the result of attenuation of light by PSCs occulting the Sun.

6.4 Impact of PSCs on *j*-Values at 11 km

The mere existence of the optical influence of PSCs on *j*-values has thus far been considered. Next, the magnitude of the PSC effect on *j*-values is assessed. The PSC-affected

Figure 6.8. Average optical effect of PSCs on the ratio of clear-sky–modeled to PSC-affected, SAFS-measured j-values along DC-8 flight tracks during SOLVE (see figure on page 176), for SZAs of (a) 80°, (b) 87°, and (c) 89°, in 1° bins about the labeled SZAs. The symbols represent the average model/measurement (corrected) ratios for 12 photolysis processes (excluding j_{ClOOCl}) as keyed, as a function of the APL model–calculated fractions of the clear-sky j-values due to the direct attenuated solar beam. The error bars are the 2-σ standard deviations of the means of the points in each SZA bin. The direct fraction calculation for each process was based on the average altitudes and SZAs of the PSC-affected points within the bin. The curves through the points are polynomial fits of the data, forced through the origin. Though j_{ClOOCl} was not reported from SAFS measurements, the effect on its clear-sky/PSC-affected j-value ratio is inferred from the j_{ClOOCl} direct fraction and the curve fits. The centroid wavelengths of photolysis for four of the processes at each SZA are noted (in nm) above the corresponding points for reference (replacing the upper half of the error bars for those points). The statistics for each SZA bin over 80°–91° are reported in Table 6.2.

points from this analysis (identified in section 6.2) are considered in Figure 6.8. The j-values for 12 photolysis processes are shown. Other j-values were reported by SAFS, but these were either computed differently than the APL model (e.g., using dissimilar molecular data) or photolyzed at the shortest wavelengths, where scattering dominated (thus producing little PSC attenuation effect). The PSC effect (APL/SAFS ratio) is plotted as a function of the fraction of the clear-sky j-values due to the direct solar beam, $f_{\mathrm{dir}} \equiv j_{\mathrm{dir}}/j_{\mathrm{total}}$, as calculated with the APL model (e.g., f_{dir}=0.2 for a j-value for which 80% of the actinic flux is from the scattered radiation field). Because PSCs affect the direct and scattered radiation fields differently, f_{dir} proves a useful coordinate relating the different species.

The j-value direct fraction is a function of altitude and SZA for each of the species (most of the PSC-affected data were observed near 11 km). The PSC-affected points have thus been separated into 1° SZA bins. The photolysis rate coefficient for ClOOCl photolysis, j_{ClOOCl}, was not reported by SAFS, so it has been added to the curve fits in Figure 6.8 according to its modeled f_{dir}. This analysis could similarly be performed on

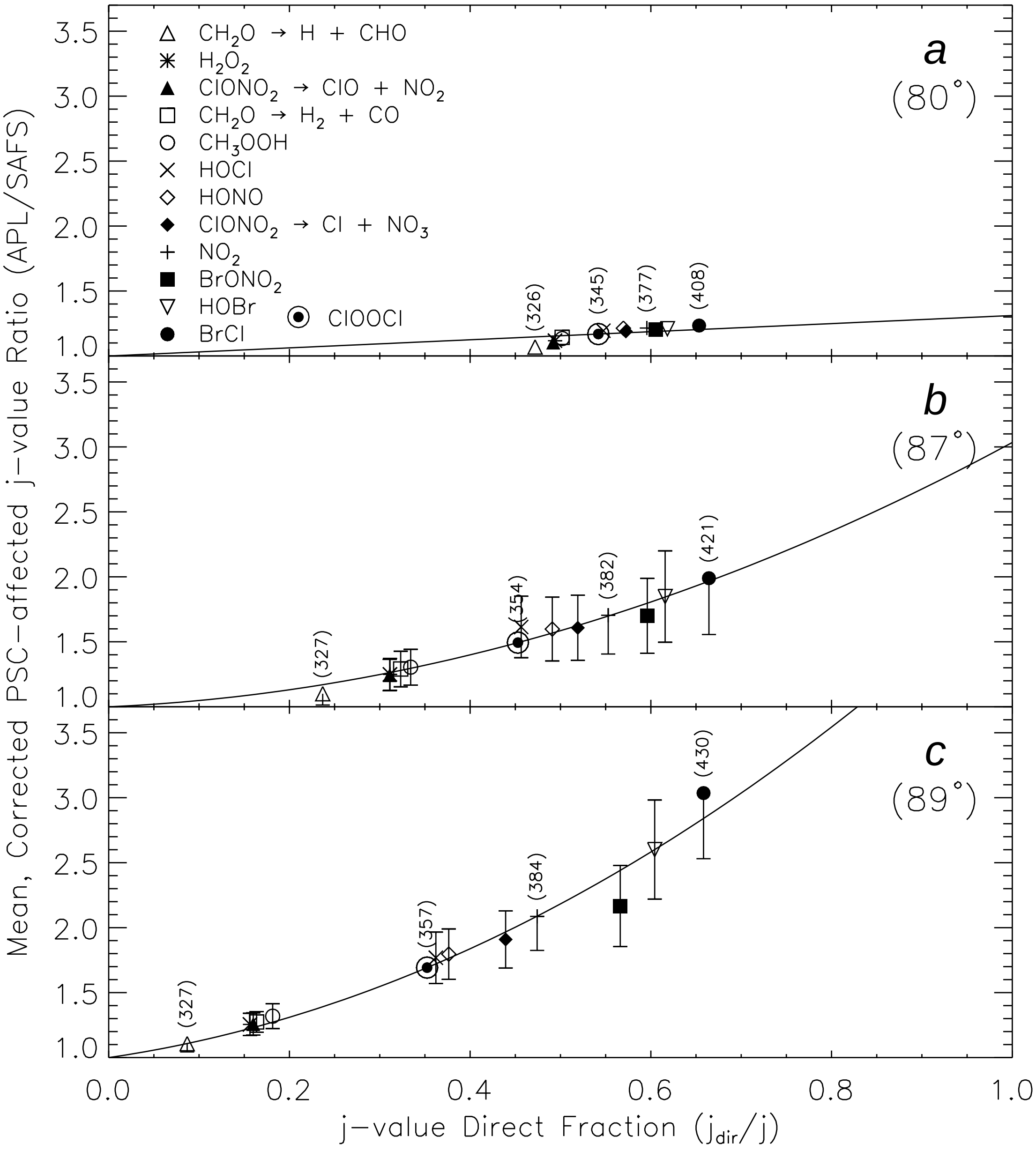

Figure 6.8. Average optical effect of PSCs on the ratio of clear-sky–modeled to PSC-affected, SAFS-measured *j*-values along DC-8 flight tracks during SOLVE (see caption on page 175).

Table 6.2. Average optical effect of PSCs on *j*-values statistics

Mean[a] SZA (°)	Mean[a] Altitude (km)	Minimum[a] Altitude (km)	Maximum[a] Altitude (km)	No. of Data Points
80.2	11.2	11.2	11.2	1
81.0	11.5	11.3	11.7	3
82.1	10.9	10.5	11.2	2
82.9	10.9	10.6	11.2	2
84.0	11.0	10.6	11.2	3
85.1	10.9	10.6	11.1	7
85.9	10.3	9.4	11.1	7
86.9	10.6	9.1	11.4	8
88.0	10.8	10.0	11.5	12
89.0	11.3	8.4	12.4	29
90.0	11.5	10.1	12.4	12
91.0	11.3	10.3	12.3	6

Each line in the table corresponds to a 1° bin from Figure 6.8.

[a]Of all PSC-affected points in bin. SZA and altitude at the DC-8.

the modeled and measured spectral actinic flux, but SAFS flux measurements have not been reported.

The magnitude of the PSC effect (the slope of the curves in Figure 6.8) was largest when the Sun was close to the horizon and the slant path throught the PSC layer was greatest. The statistics for the data in Figure 6.8 are reported in Table 6.2. The effect of PSCs beyond 91.5° SZA was not detected during SOLVE and would be expected to disappear as scattering dominates the radiation field at large SZAs.

6.5 Extension of PSC Analysis throughout the Lower Stratosphere

Figures 6.2 and 6.8 show that PSCs can have a huge impact on *j*-values at DC-8 altitudes. The extension of this effect to the photochemistry of the entire Arctic stratosphere polar vortex is desirable in order to assess its impact on ozone loss. In the troposphere, the radiation field is often enhanced in and above clouds by scattering. It is assumed here, however, that PSCs only attenuate the scattered radiation field. *Anderson and Lloyd* [1990] modeled the effects of a uniform PSC layer ($\tau = 0.1$) and found that scattered radiation was attenuated above, below, and within the layer at high SZAs (>86°). Combined with the reduction of direct solar radiation, it is expected that PSCs at large SZAs would result in reduced *j*-values in the stratosphere.

6.5.1 Direct Fraction–Altitude Dependence of the PSC Effect

The dependence of the PSC optical effect on the *j*-value direct fraction, f_{dir}, provides a physical basis for an extension of the effect observed at 11 km throughout the lower stratosphere. At any SZA, f_{dir} for a *j*-value is a function of altitude. Figure 6.9 shows the modeled clear-sky altitude dependence of several *j*-values of interest at 89° SZA. The PSC effect curves in Figure 6.8 can therefore be used to infer the magnitude of the PSC *j*-value effect at other altitudes, based on f_{dir}. This assumes that the relative magnitude of the PSC effect on the direct and scattered radiation fields is independent of altitude. *Anderson and Lloyd* [1990] have shown that the modeled impact on multiple scattering is sensitive to altitude relative to a PSC layer, but since the direct component was principally affected, the PSC effect curves still provide a good first-order estimate of the effect at other altitudes.

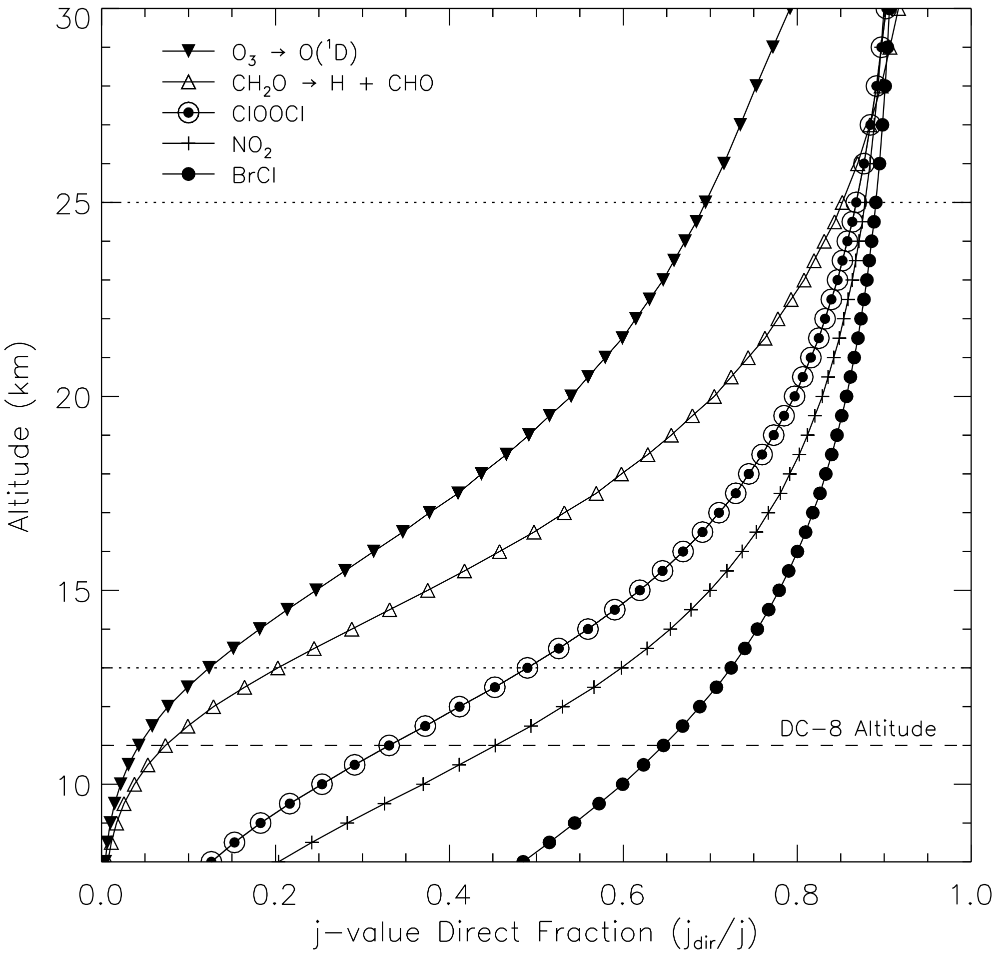

Figure 6.9. Altitude profiles of the direct solar contribution to *j*-values, from 8 to 30 km, for the five photolysis processes shown, calculated with the APL model at 89° SZA. The dashed line shows the average DC-8 altitude and the dotted lines represent the altitude range over which PSCs were observed during SOLVE.

Direct Evidence of Altitude Dependence

Observations were made during SOLVE over a relatively small range of altitudes. For each of the SZA bins in Figure 6.8, the altitude range of the data is shown in Table 6.2. The individual PSC-affected $j_{\mathrm{NO_2}}$ points from two of the SZA bins, which had a significant number of points, are shown in Figure 6.10. The data are consistent with the f_{dir}-dependence derived from the bin-averages of all the j-values, over a range of 2–4 km, providing support (though limited in altitude) for the inference of the PSC effect at higher altitudes by virtue of the j-value direct fraction.

6.5.2 Slant Path Dependence of the PSC Effect

The variation in the steepness of the curve fits (i.e., the magnitude of the PSC effect) with SZA in Figure 6.8 is shown in Figure 6.11. Since the sensitivity of any particular j-value varies with both f_{dir} and SZA, the f_{dir}=0.5 values of the PSC effect curves are plotted so that SZA-dependent scattering is not a factor. The SZA-dependence of these points is analogous to that of $j_{\mathrm{NO_2}}$ shown in Figures 6.2 and 6.3, except that the effect on $j_{\mathrm{NO_2}}$ beyond 90° rapidly diminishes, along with f_{dir}. Also plotted in Figure 6.11 is the geometric LOS slant path through the observed PSC layer (13–25 km). The variation in the slant path of the LOS through the PSC layer is proportional to the magnitude of the PSC effect. As the slant path through the PSC layer increased, so too did the opportunity for attenuation. Slant path and SZA can thus be used interchangeably to describe the magnitude of the PSC effect when a PSC was present. An exponential function derived from the Beer–Lambert law (1.5) is also shown in Figure 6.11:

$$\frac{F_0}{F_{\mathrm{PSC}}} = e^{\kappa s}, \tag{6.2}$$

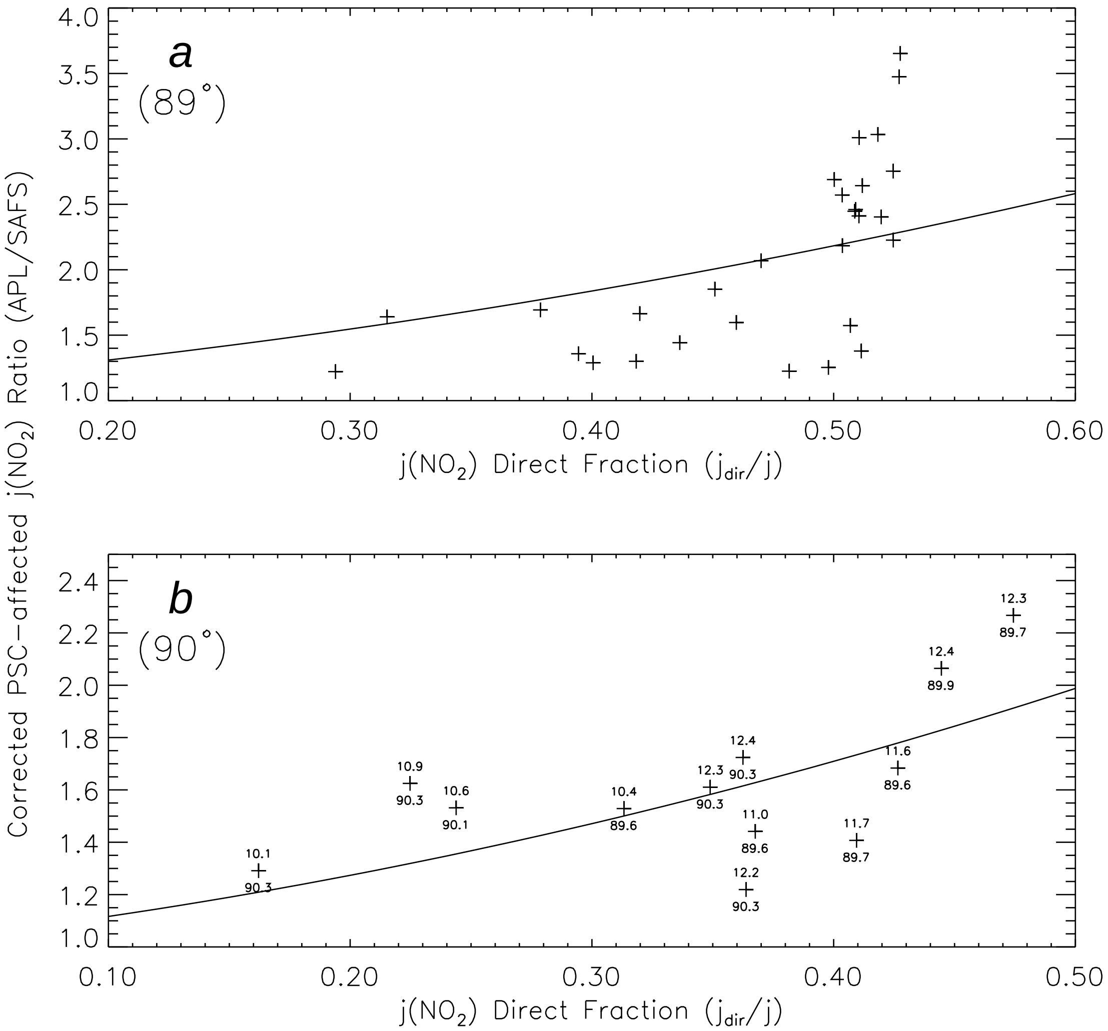

Figure 6.10. Optical effect of PSCs on the ratio of clear-sky–modeled to PSC-affected, SAFS-measured j_{NO_2} along DC-8 flight tracks during SOLVE, for SZAs of (a) 89° and (b) 90° in 1° bins about the labeled SZAs. The points represent the individual model/measurement (corrected) ratios for j_{NO_2} as a function of the APL model–calculated fractions of the j-values due to the direct, attenuated solar beam. The points in (a), for example, were averaged to generate the single j_{NO_2} point in Figure 6.8c. The curves shown are the fits to the averages of all the j-values shown in Figure 6.8 (i.e., the curve in (a) is the same as that in Figure 6.8c; the averaged data corresponding to (b) for 90° are not shown in Figure 6.8). The points in (b) are also annotated with the altitude (above, in km) and the SZA (below, in °).

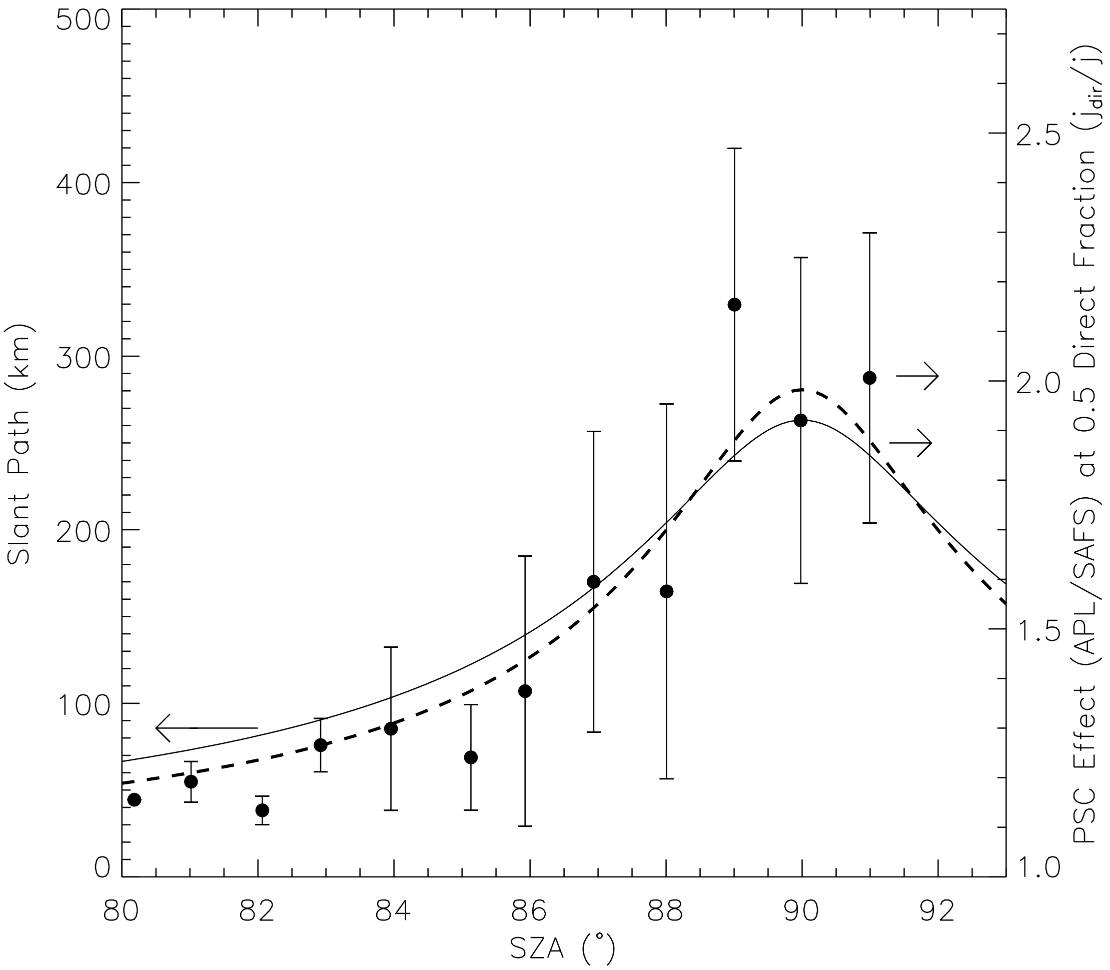

Figure 6.11. Relationship of slant path to the magnitude of the PSC optical effect. The solid curve shows the SZA-dependence of the slant path through the 13–25-km layer of the atmosphere, where PSCs have been observed, viewed from 11 km. Overlaid are the values of the curve fits of the PSC effect (sampled in Figure 6.8) at a direct fraction of 0.5. The values have been adjusted slightly to take into account variation in average altitude in each SZA bin, with a maximum correction of $\sim$3%, at 90°. The error bars are the relative 2-σ standard deviations of the means of PSC-affected APL/SAFS j_{HOBr}, which contributed to the PSC effect curves and has a direct fraction close to 0.5 out to 91° SZA. The dashed line is an exponential expression as a function of slant path (see (6.2) and explanation in text).

where s in the slant path and κ is a constant derived empirically from the data shown and is equivalent to kn in (1.5). This representation does not take into account the impact of PSCs on scattered radiation explicitly, but since PSCs affect principally the direct beam, this simple expression captures well the slant path (or SZA) dependence of the PSC attenuation. Variations in the atmospheric distribution and optical properties of PSCs, which are largely unknown in this case, are also not explicitly accounted for, so κ is essentially a composite average. In a statistical sense, the PSC altitude distribution and optical properties are homogeneous.

Slant path is a function of both the SZA and the altitude of the observer. Slant paths at a series of altitudes in the lower stratosphere are shown in Figure 6.12. The PSC effect at each altitude and SZA is expected to be related to the resultant slant path by (6.2).

6.5.3 Two-Dimensional PSC Effect Relationship

The slant path dependence of the PSC effect, coupled with that on j-value direct fraction, allows for the combination of the family of curves sampled in Figure 6.8 to form a two-dimensional fit, shown in Figure 6.13, as functions of slant path and f_{dir} and does not depend on altitude or SZA. The slant path determines the LOS thickness of the PSC layer (and thus the magnitude of PSC attenuation) and the j-value direct fraction relates to the sensitivity of a particular j-value to the reduction of the actinic flux, which primarily affects the direct solar beam. This PSC j-value effect relationship,

$$\varepsilon_{\text{PSC}}(s, f_{\text{dir}}) \equiv \frac{j_{\text{clear-sky}}}{j_{\text{PSC}}}, \tag{6.3}$$

is a function of the slant path s and the j-value direct fraction f_{dir}. The f_{dir} dependence of the relationship is from the normalized PSC effect curve in the 90° SZA bin (not shown in Figure 6.8). The slant path dependence is from the exponential function for

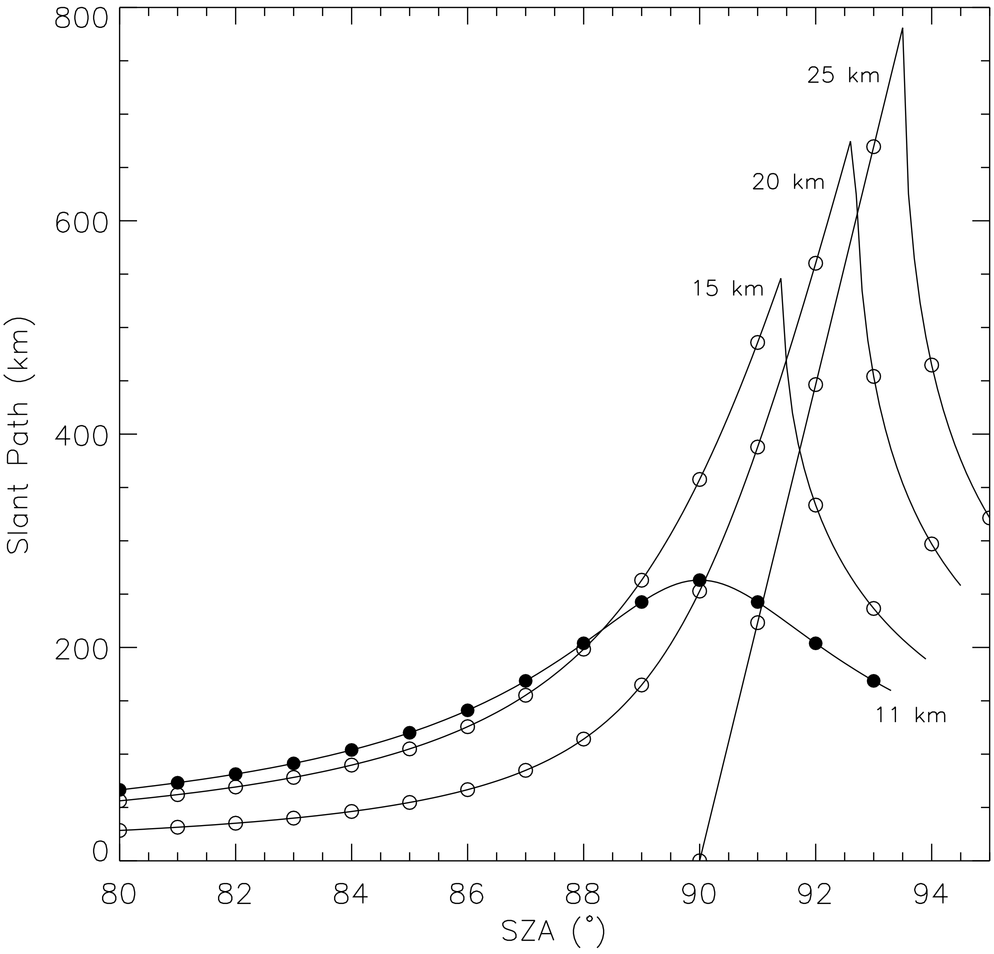

Figure 6.12. SZA dependence of slant path at 11, 15, 20, and 25 km. Similar to Figure 6.11, the curves show the slant path through the 13–25-km layer of the atmosphere, where PSCs have been observed, viewed from four altitudes, including within the layer itself. The curves terminate beyond 93° SZA as the Sun sets below the hard Earth horizon.

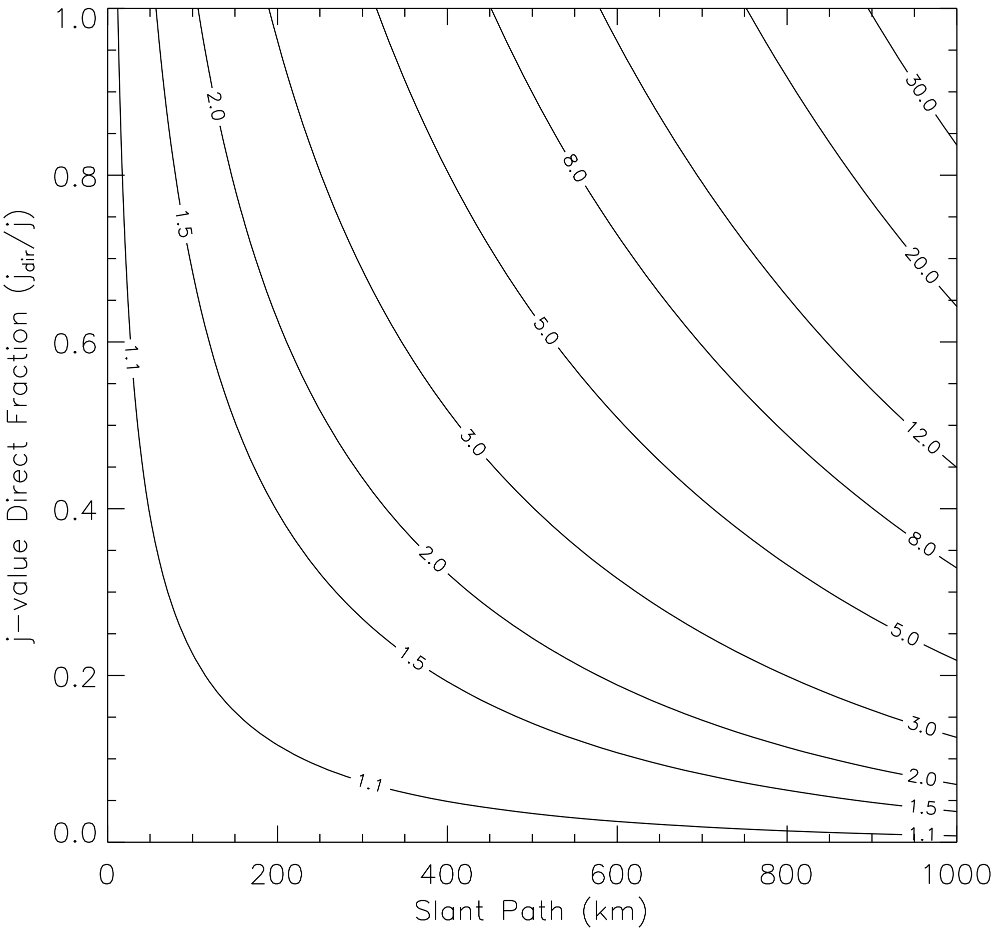

Figure 6.13. Clear-sky/PSC-affected *j*-value ratio relationship, fit to APL/SAFS *j*-value data as functions of slant path (through 13–25-km PSC layer) and *j*-value direct fraction.

$f_{\rm dir}$=0.5, shown in Figure 6.11. The 2-D surface $\varepsilon_{\rm PSC}(s, f_{\rm dir})$, derived from APL clear-sky modeling/SAFS measurement of PSC-affected *j*-values during SOLVE, represents the SOLVE *j*-value data well over their range of slant paths and $f_{\rm dir}$ and is a first approximation of the influence of PSCs on *j*-values in the lower stratosphere. Further, $\varepsilon_{\rm PSC}$ has been derived in a statistical sense and represents the average *j*-value effect experienced during SOLVE when a PSC was present. The PSC optical properties, thickness, history, and persistence were thus averaged over all of the SOLVE science DC-8 flights. For a given point in the atmosphere in the shadow of a PSC, $\varepsilon_{\rm PSC}$ describes the average impact on any given photolysis process.

6.6 Implications for ClOOCl Photolysis and Ozone Loss: Putting It Together

The measurement and modeling of ozone loss rates in the Arctic stratosphere during SOLVE have been the subject of numerous studies [see chapter 5; *Newman et al.*, 2002, and references therein]. Chlorine chemistry is responsible for the majority of ozone loss in the lower stratosphere inside the polar vortex [*Solomon*, 1999], and a key step limiting the rate of the ClO dimer ozone destruction cycle is the photolysis of ClOOCl (see section 1.1.4 and Figure 1.1). Any attenuation of $j_{\rm ClOOCl}$ will lead to a proportional reduction in the rate at which the cycle proceeds and hence the ozone loss rate.

The PSC-"influenced" (i.e., PSCs are only sometimes present) ozone loss rate is related to the clear-sky rate by

$$\left(\frac{d[\mathrm{O_3}]}{dt}\right)_{\rm PSC} \approx \left(\frac{d[\mathrm{O_3}]}{dt}\right)_{\rm clear\text{-}sky}\left(\frac{j_{\rm ClOOCl,PSC}}{j_{\rm ClOOCl,clear\text{-}sky}}\right). \tag{6.4}$$

If a chemical model assumes clear-sky *j*-values in the calculation of ozone loss rates, it will overestimate ozone loss when PSCs are present. The sensitivity of $j_{\rm ClOOCl}$ to

PSCs inferred from Figure 6.8 is significant. The preceding analysis of the optical effect of PSCs on j-values during SOLVE provides empirical data for the calculation of the PSC effect on polar ClOOCl photolysis and ozone loss. The attenuation of the radiation field by PSCs would also affect many other j-values, but j_{ClOOCl} limits the predominant ozone loss cycle.

6.6.1 Time-Dependent Calculation

Every component of this analysis is a function of position $\mathbf{x}$ in the atmosphere and time t: $(T-T_{\mathrm{NAT}})_{\mathrm{min}}$ (i.e., P_{PSC}), slant path, j_{ClOOCl}, j_{ClOOCl} direct fraction f_{dir}, and ozone loss rate. Therefore, to assess the impact of PSCs on ClOOCl photolysis, a position- and time-dependent calculation is required, which can be summarized as

$$\frac{\Delta[\mathrm{O_3}]_{\text{clear-sky}}}{\Delta[\mathrm{O_3}]_{\mathrm{PSC}}}(\mathbf{x}) \approx \frac{\mathscr{P}_{\text{ClOOCl,clear-sky}}}{\mathscr{P}_{\text{ClOOCl,PSC}}}(\mathbf{x}) = \frac{\int j_{\text{ClOOCl,clear-sky}}(\mathbf{x},t)\,dt}{\int \left[j_{\text{ClOOCl,clear-sky}}(\mathbf{x},t)\right]\chi^{-1}\,dt}, \tag{6.5}$$

$$\chi = \left[P_{\mathrm{PSC}}\big((T-T_{\mathrm{NAT}})_{\mathrm{min}}(\mathbf{x},t)\big)\right]\left[\varepsilon_{\mathrm{PSC}}\big(s(\mathbf{x},t), f_{\mathrm{dir}}(\mathbf{x},t)\big)-1\right]+1,$$

where $\mathscr{P}_{\mathrm{ClOOCl}}$ is the time-integrated j_{ClOOCl} (total ClOOCl photolysis), P_{PSC} is derived from $(T-T_{\mathrm{NAT}})_{\mathrm{min}}$ along the solar LOS, and f_{dir} is the j_{ClOOCl} direct fraction. It was necessary in this analysis to separate the probability of PSC occurrence and the average j-value effect for a PSC (rather than correlating the j-value effect directly with $(T-T_{\mathrm{NAT}})_{\mathrm{min}}$) because the j-value effect is a function of both $(T-T_{\mathrm{NAT}})_{\mathrm{min}}$ *and* SZA (slant path), and there were insufficient SOLVE data to simultaneously bin by $(T-T_{\mathrm{NAT}})_{\mathrm{min}}$ and SZA. With (6.5), the ratio of clear-sky to PSC-influenced ClOOCl photolysis may be calculated, integrated over an arbitrary time period.

An Example: 20000125

Integrated photolysis is first examined for a single day during SOLVE: 20000125. ClOOCl photolysis was considered in this analysis from 50°N to the pole on the UKMO grid (2.5° latitude × 3.75° longitude) at eight pressure levels from 146.8 to 10.0 mb. For each grid point, the solar ephemeris was computed every 10 minutes throughout the day, and T and T_{NAT} (and thus P_{PSC}) were interpolated to the resultant solar LOSs. Diurnal averages of $(T - T_{\mathrm{NAT}})_{\mathrm{min}}$ and P_{PSC} at 68.1 mb for 20000125 are shown in Figure 6.14. North of 75°N, the Sun never climbed above the horizon. Equatorward of polar night, the probability of the existence of PSCs vanished at temperatures above T_{NAT}, as suggested in Figure 6.7.

The diurnal effect of PSCs ($j_{\mathrm{ClOOCl,clear\text{-}sky}}/j_{\mathrm{ClOOCl,PSC}}$), if a PSC were present, is shown in Figure 6.15 on four of the UKMO pressure levels at two latitudes on the Prime Meridian. The effect was greatest when the Sun was near the horizon and slant paths were large and diminished in the middle of the day. The differences in behavior at the different pressure levels resulted from unique slant paths and f_{dir} as functions of time. The PSC effect scaled by P_{PSC} (see diurnal average at 68.1 mb in Figure 6.14b) is shown in Figure 6.16. This is the actual $j_{\mathrm{ClOOCl,clear\text{-}sky}}/j_{\mathrm{ClOOCl,PSC}}$.

Finally, the total photolysis ratio (clear-sky/PSC) was obtained after integrating $j_{\mathrm{ClOOCl,clear\text{-}sky}}$ and $j_{\mathrm{ClOOCl,PSC}}$. The result is shown at 68.1 mb in Figure 6.17. The effect was limited to the region where temperatures were cold and the slant paths to the Sun were large (and excluding polar night). The edge of the polar vortex is also denoted, as defined by *Nash et al.* [1996] (see section F.5). Chlorine-catalyzed ozone loss occurred at latitudes north of this boundary. While the instantaneous PSC effect was large during the day (>2), the effect on the integrated photolysis peaked at near 1.7 on 20000125 (at 70°N, 0°E, 68.1 mb).

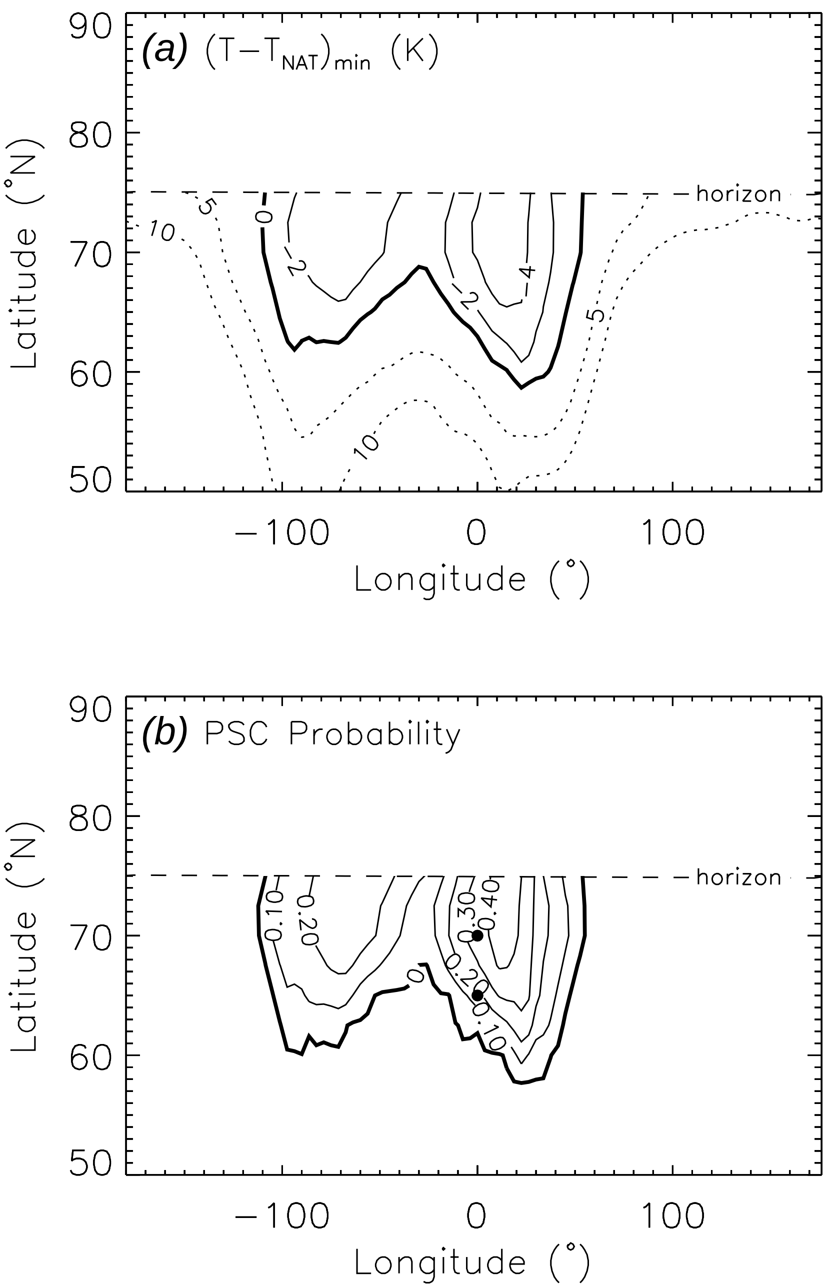

Figure 6.14. Diurnal averages of (a) $(T - T_{\mathrm{NAT}})_{\mathrm{min}}$ and (b) corresponding P_{PSC} along the solar LOS, at 68.1 mb (near 18 km at Kiruna) for 20000125 at high northern latitudes. In both panels, a high-latitude limit is denoted with a dashed line and marked "horizon," north of which was in polar night (SZA$>$ 94°). In (b), filled circles (•) mark 65° and 70°N latitude on the Prime Meridian, which are referenced in Figure 6.15.

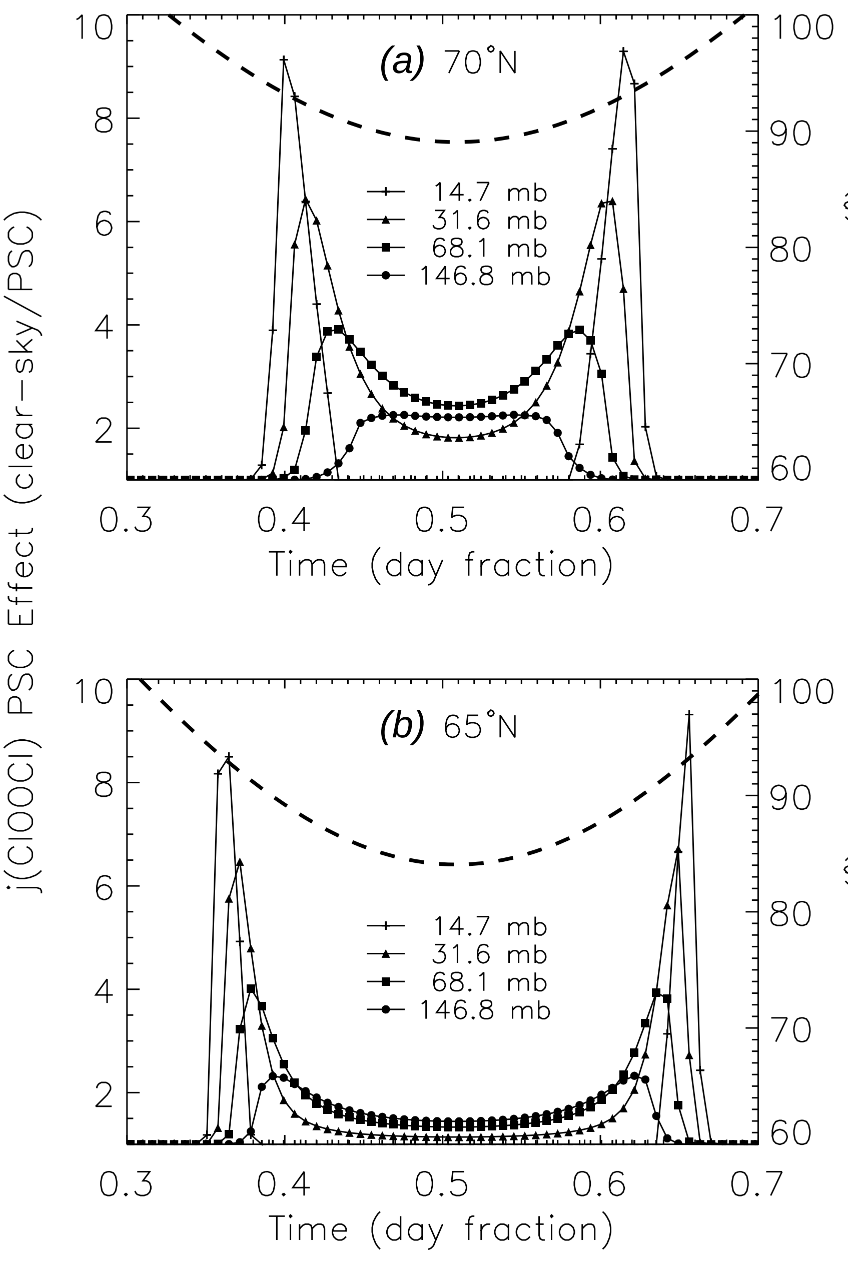

Figure 6.15. Diurnal dependence of the PSC effect (assuming a PSC were present) on j_{ClOOCl} at four pressure levels at (a) 70° and (b) 65°N latitude along the Prime Meridian (noted in Figure 6.14b) for 20000125. The SZA is also noted, with a dashed line.

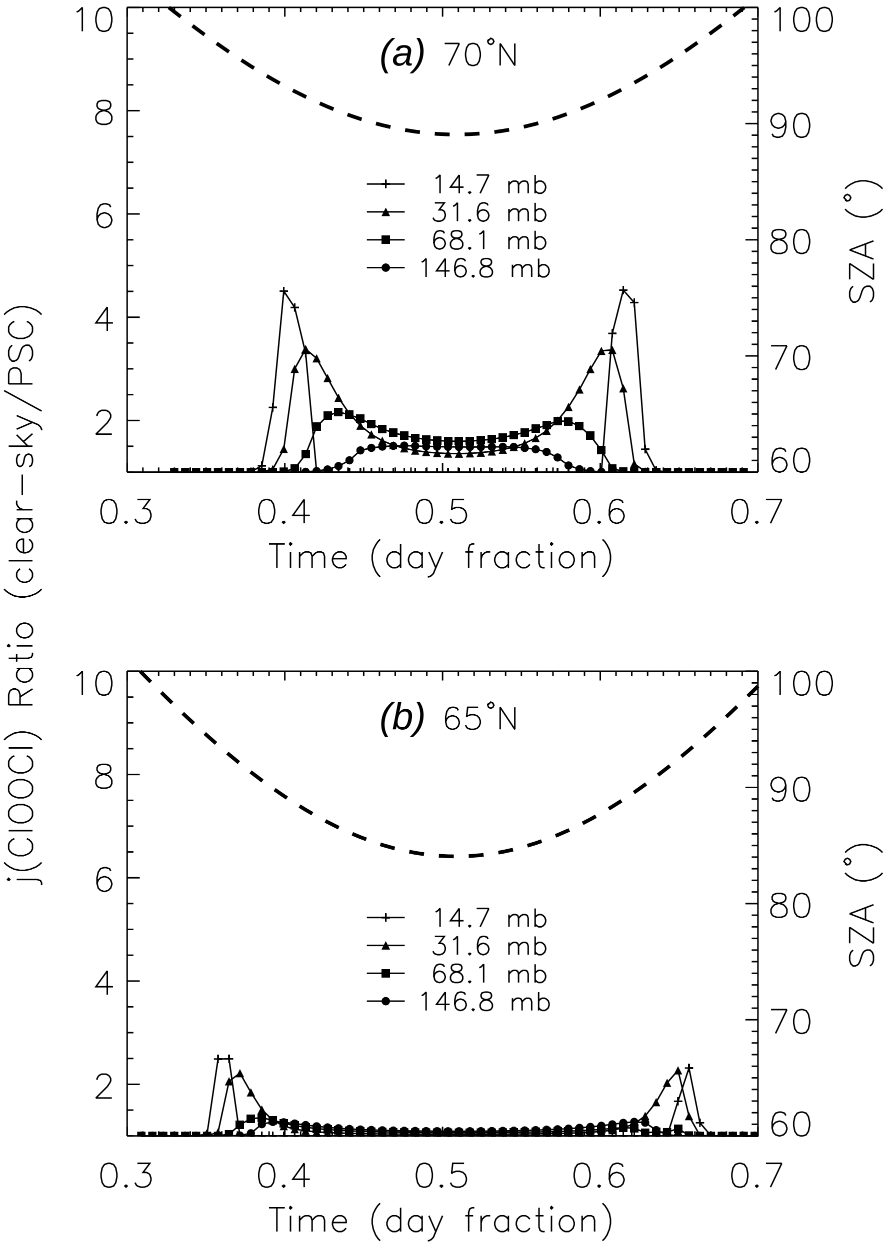

Figure 6.16. Diurnal dependence of the PSC effect $(\varepsilon_{PSC})\times P_{PSC}$ on j_{ClOOCl} at four pressure levels at (a) 70° and (b) 65°N latitude along the Prime Meridian for 20000125. The SZA is also noted, with a dashed line.

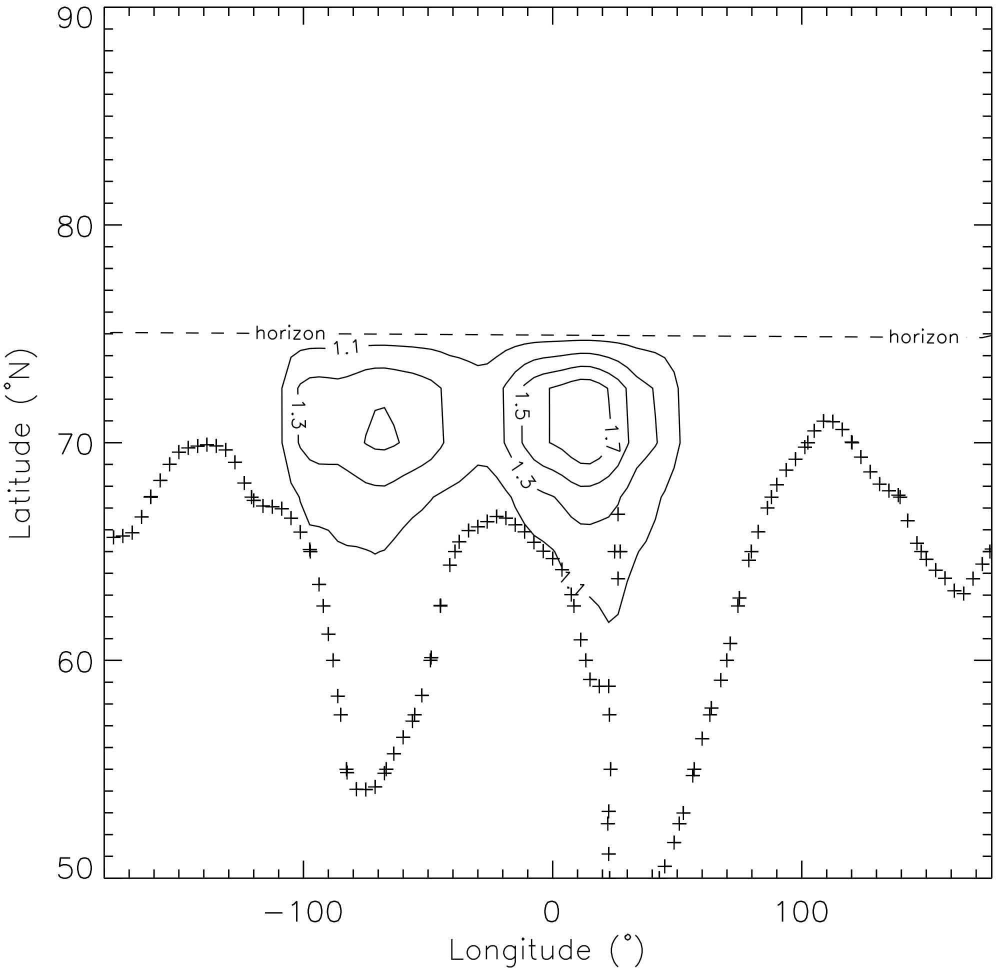

Figure 6.17. Cumulative PSC effect (clear-sky/PSC-influenced) on diurnally integrated j_{ClOOCl} (i.e., total photolysis) at 68.1 mb for 20000125. The edge of the polar vortex is represented with pluses (+). The polar night boundary is denoted with the dashed line marked “horizon.”

6.6.2 Effect on Integrated ClOOCl Photolysis throughout SOLVE

The ratio of all-day clear-sky to PSC-influenced photolysis (6.5) is shown for 20000125 in Figure 6.18 on all eight levels of the analysis, spanning roughly 13–30 km. The region of the hemisphere cold enough to support j_{ClOOCl}-attenuating PSC formation extends from Canada to Scandinavia. At lower latitudes, the temperatures were too high and the SZAs (slant paths) too small for a significant PSC effect; at higher latitudes, the Sun never reached above the horizon. The effect of PSCs on photolysis also diminished at the lower levels of the atmosphere as scattering in the atmosphere increased (as f_{dir} decreased); at the highest levels, less of the PSC layer lay along the solar LOS (the slant path decreased)—both of these conditions thus reducing the PSC effect (see Figure 6.13). In the middle pressure levels of the analysis, however, photolysis of ClOOCl was reduced by a factor of up to more than 2. Note that this was not simply a transient effect as a PSC blocked the Sun momentarily, but the total impact on photolysis integrated over the course of the entire day. Ozone loss in that region would also have been reduced by a similar factor (and it is at the middle levels of the analysis where most of the ozone loss occurred).

Figures 6.19–6.25 show the PSC optical effect on ClOOCl photolysis ($\mathscr{P}_{\mathrm{ClOOCl,clear\text{-}sky}}/\mathscr{P}_{\mathrm{ClOOCl,PSC}}$) integrated over two-week periods, from December 1999 through mid-March 2000, when the vortex began to break up (see *Piani et al.* [2002] for a discussion of the vortex breakup). These maps give a comprehensive picture of the optical effects of PSCs on ClOOCl photolysis (and ozone loss) throughout the SOLVE ozone loss season. The region of impact stretched zonally (i.e., parallel with latitude), biased toward $-90°$–$(+90)°$E longitude, consistent with the asymmetry of the vortex and cold temperatures. As time progressed from winter solstice toward the vernal equinox, the latitude of the effect advanced poleward, following twilight conditions.

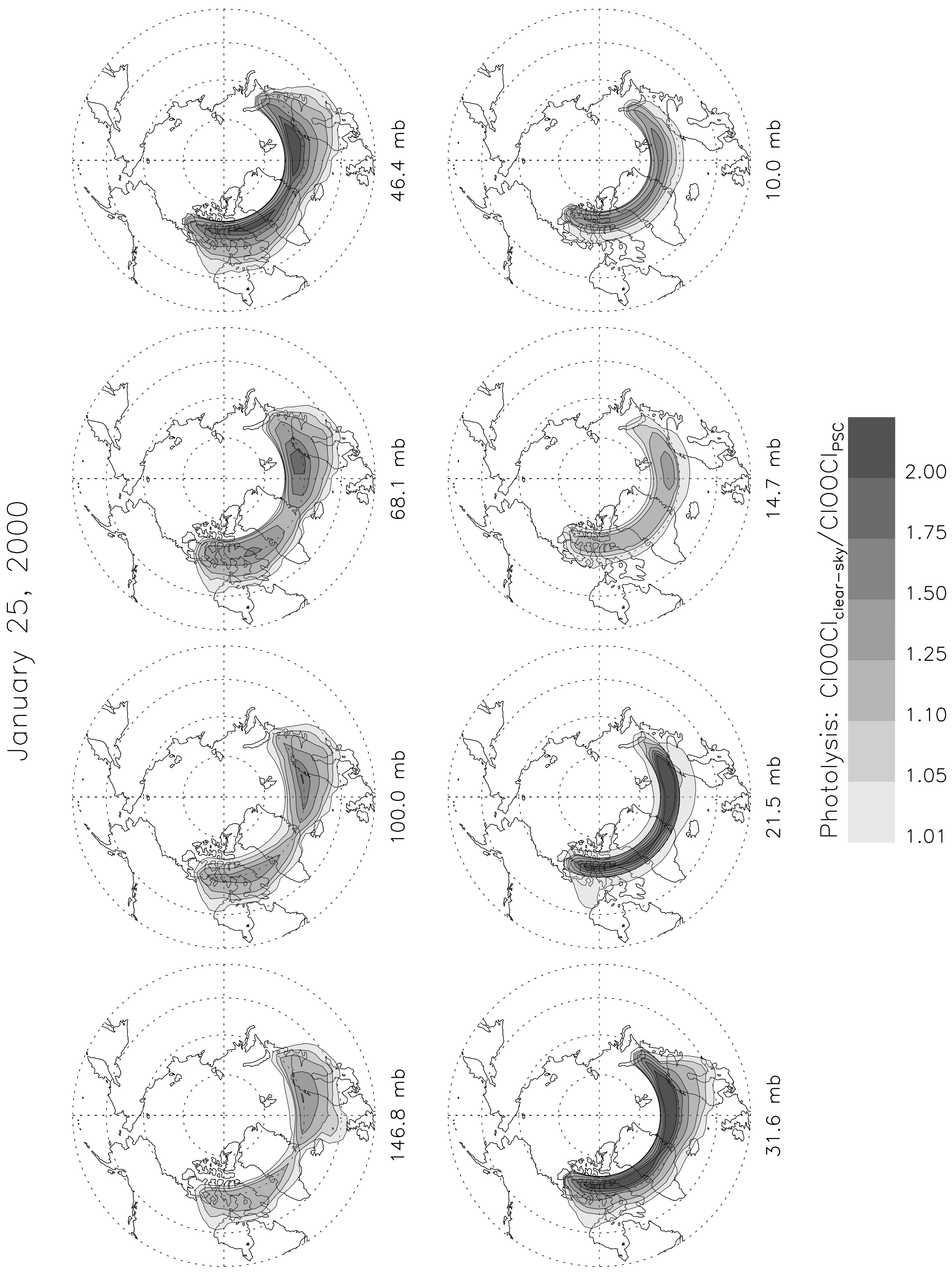

Figure 6.18. Clear-sky/PSC-influenced ClOOCl photolysis at eight pressure levels for 20000125 over the Northern Hemisphere, 50°N–North Pole.

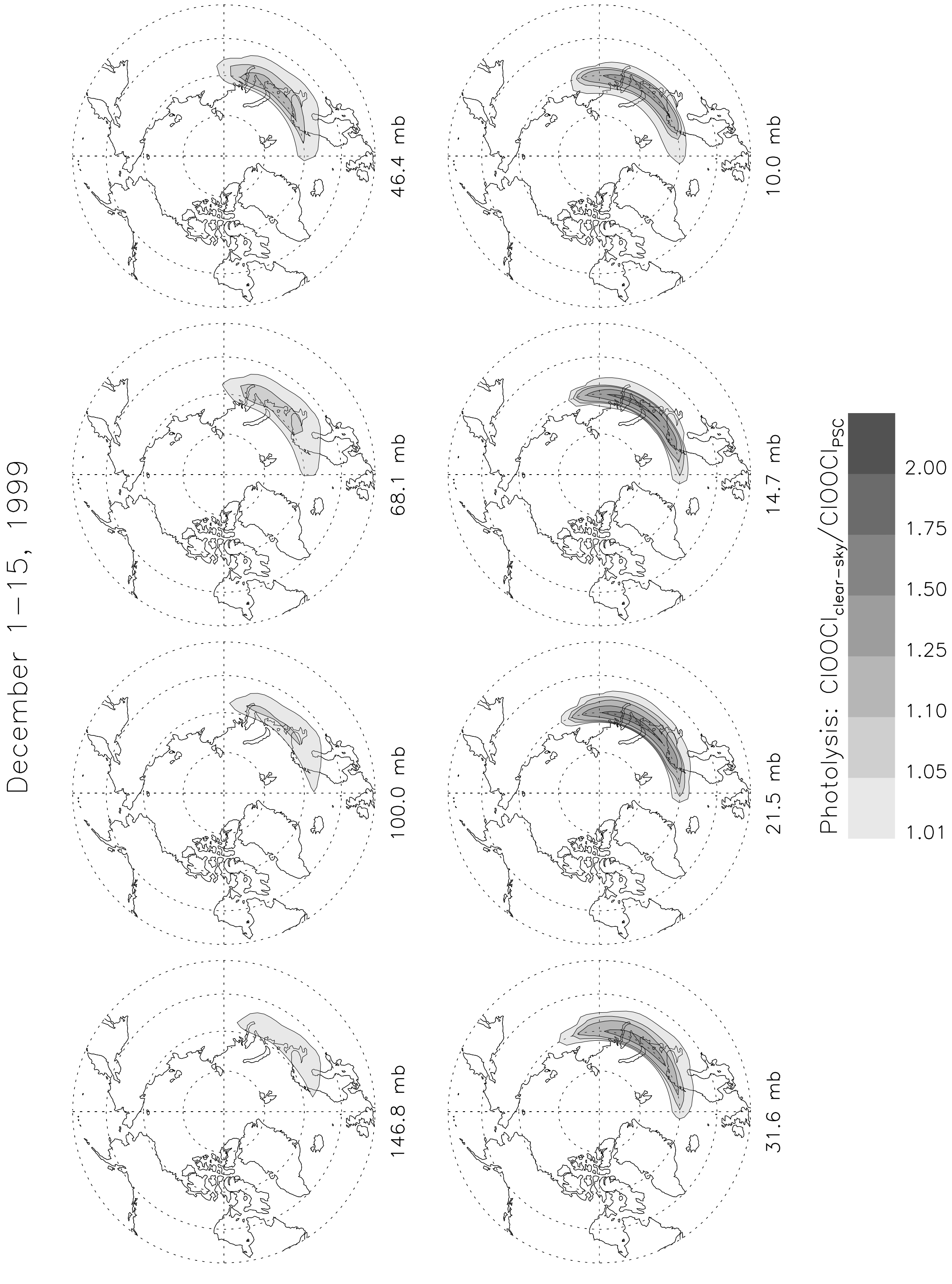

Figure 6.19. Clear-sky/PSC-influenced ClOOCl photolysis at eight pressure levels for 19991201–19991215 over the Northern Hemisphere, 50°N–North Pole.

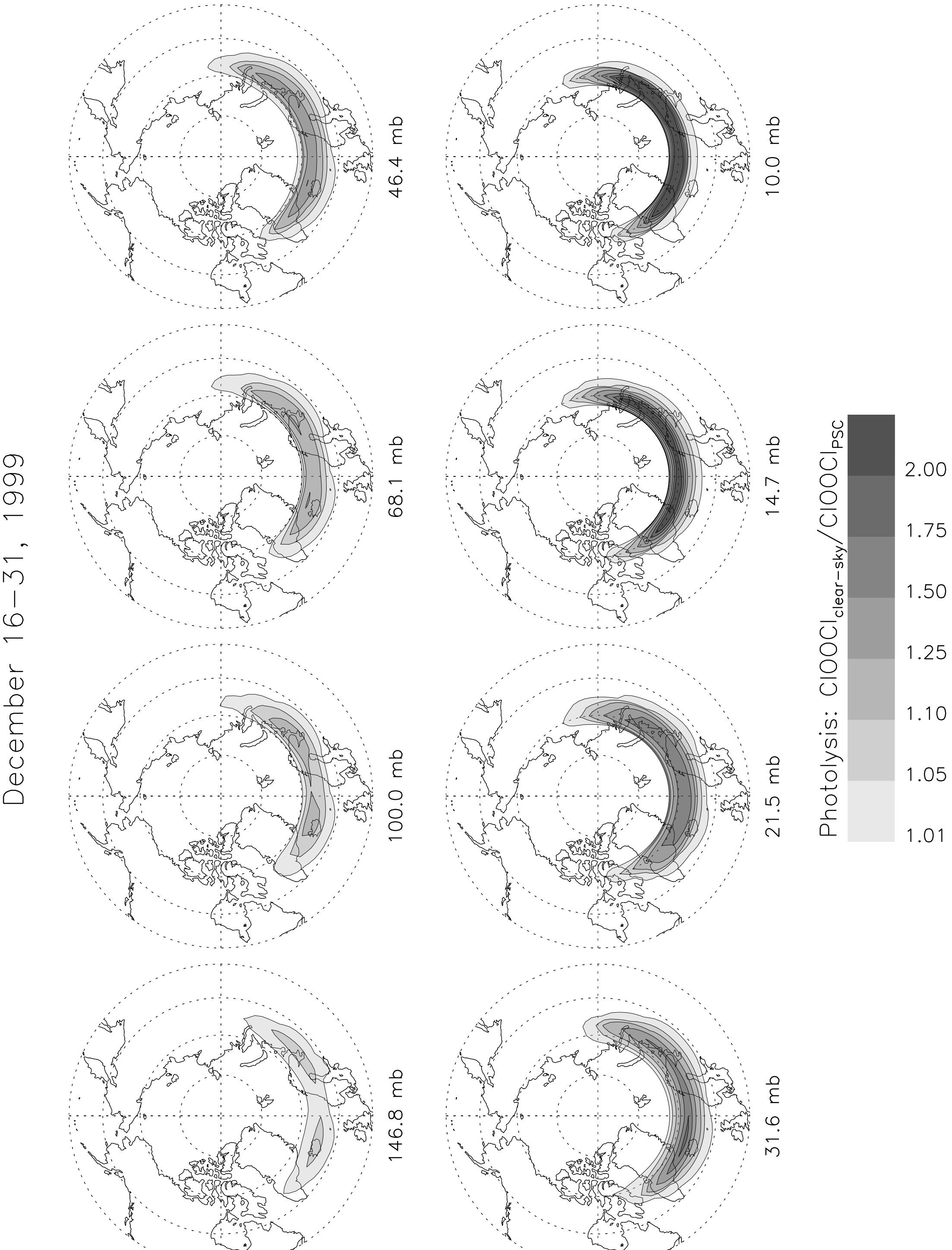

Figure 6.20. Clear-sky/PSC-influenced ClOOCl photolysis at eight pressure levels for 19991216–19991231 over the Northern Hemisphere, 50°N–North Pole.

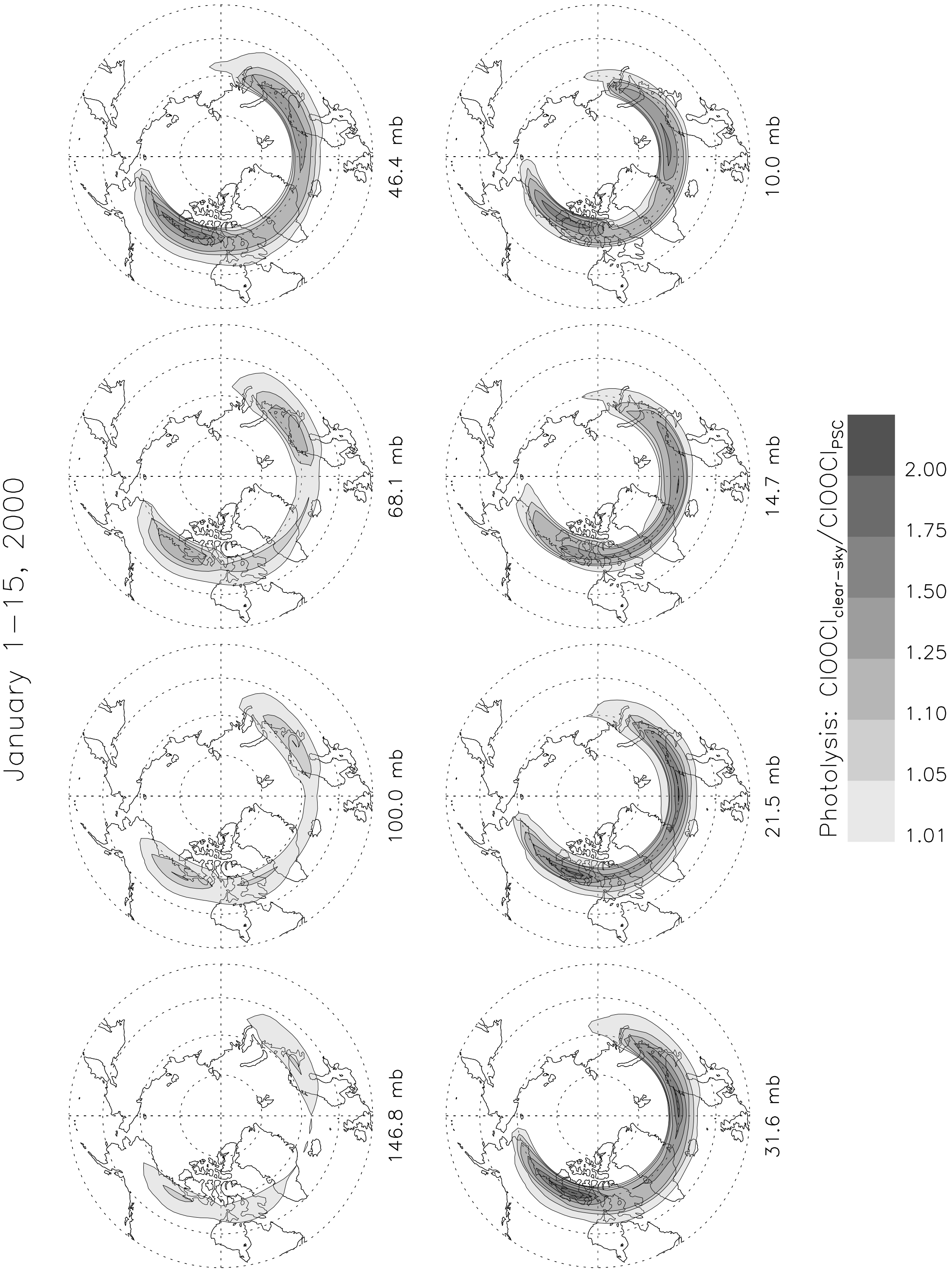

Figure 6.21. Clear-sky/PSC-influenced ClOOCl photolysis at eight pressure levels for 20000101–20000115 over the Northern Hemisphere, 50°N–North Pole.

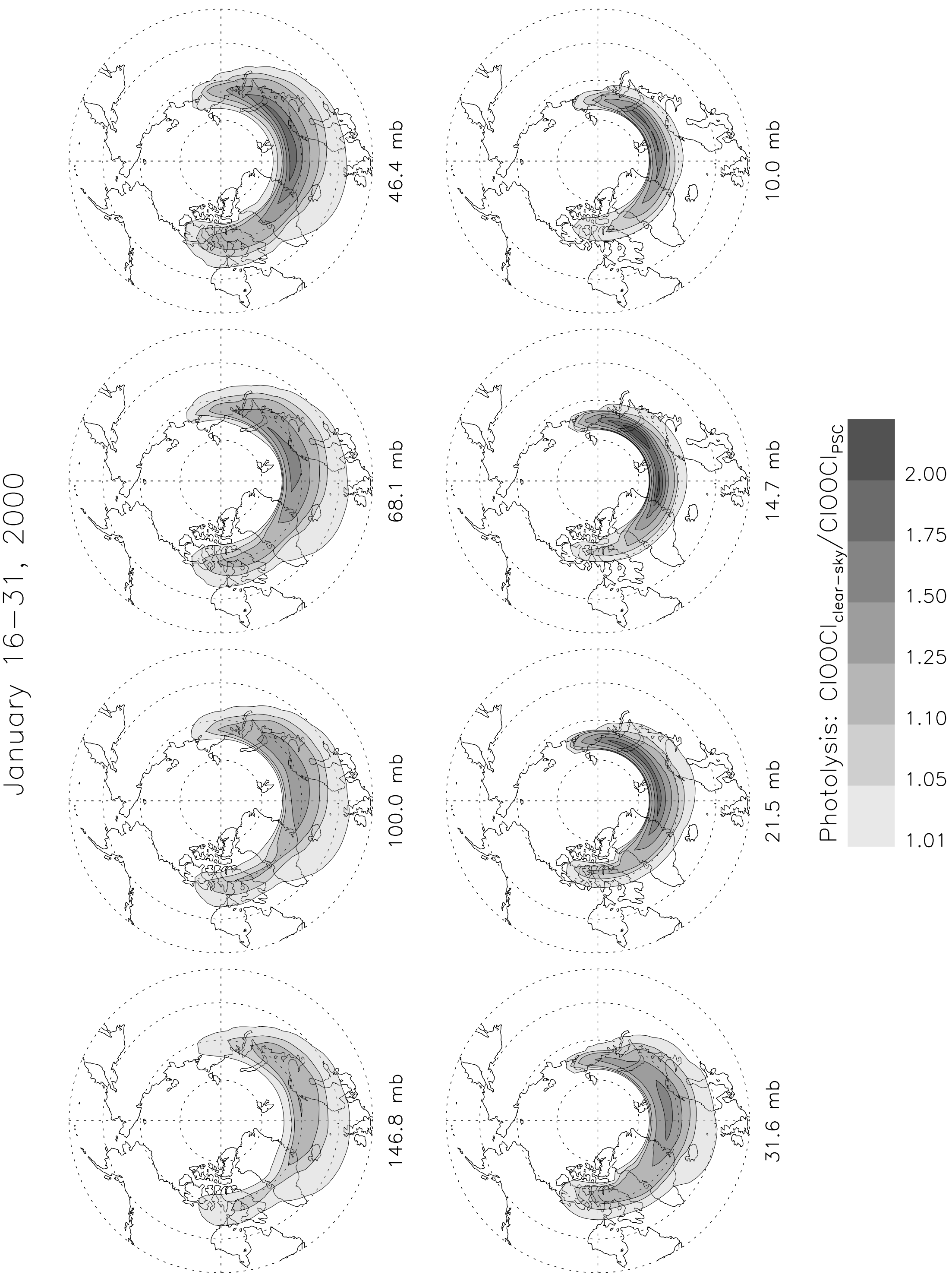

Figure 6.22. Clear-sky/PSC-influenced ClOOCl photolysis at eight pressure levels for 20000116–20000131 over the Northern Hemisphere, 50°N–North Pole.

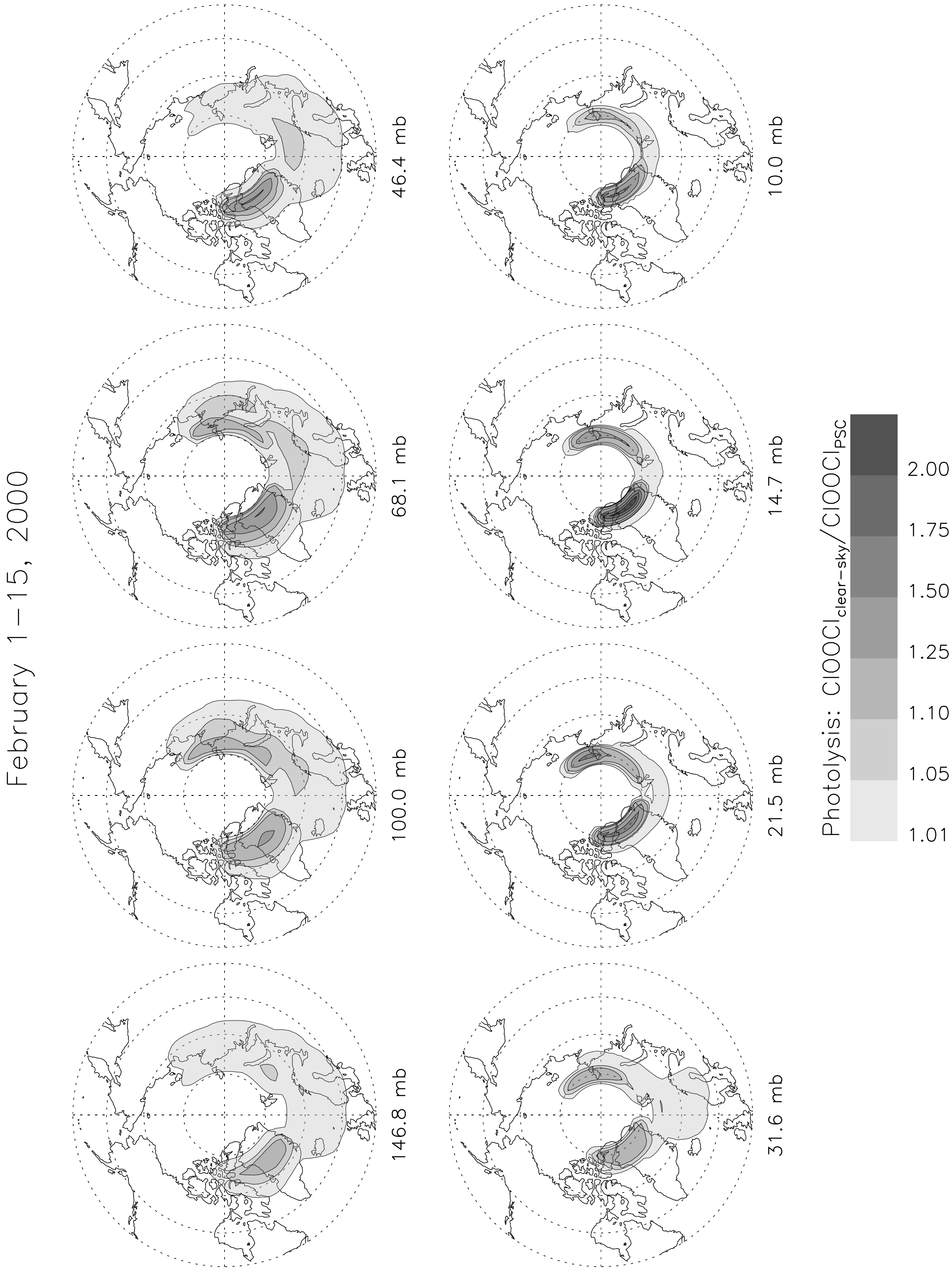

Figure 6.23. Clear-sky/PSC-influenced ClOOCl photolysis at eight pressure levels for 20000201–20000215 over the Northern Hemisphere, 50°N–North Pole.

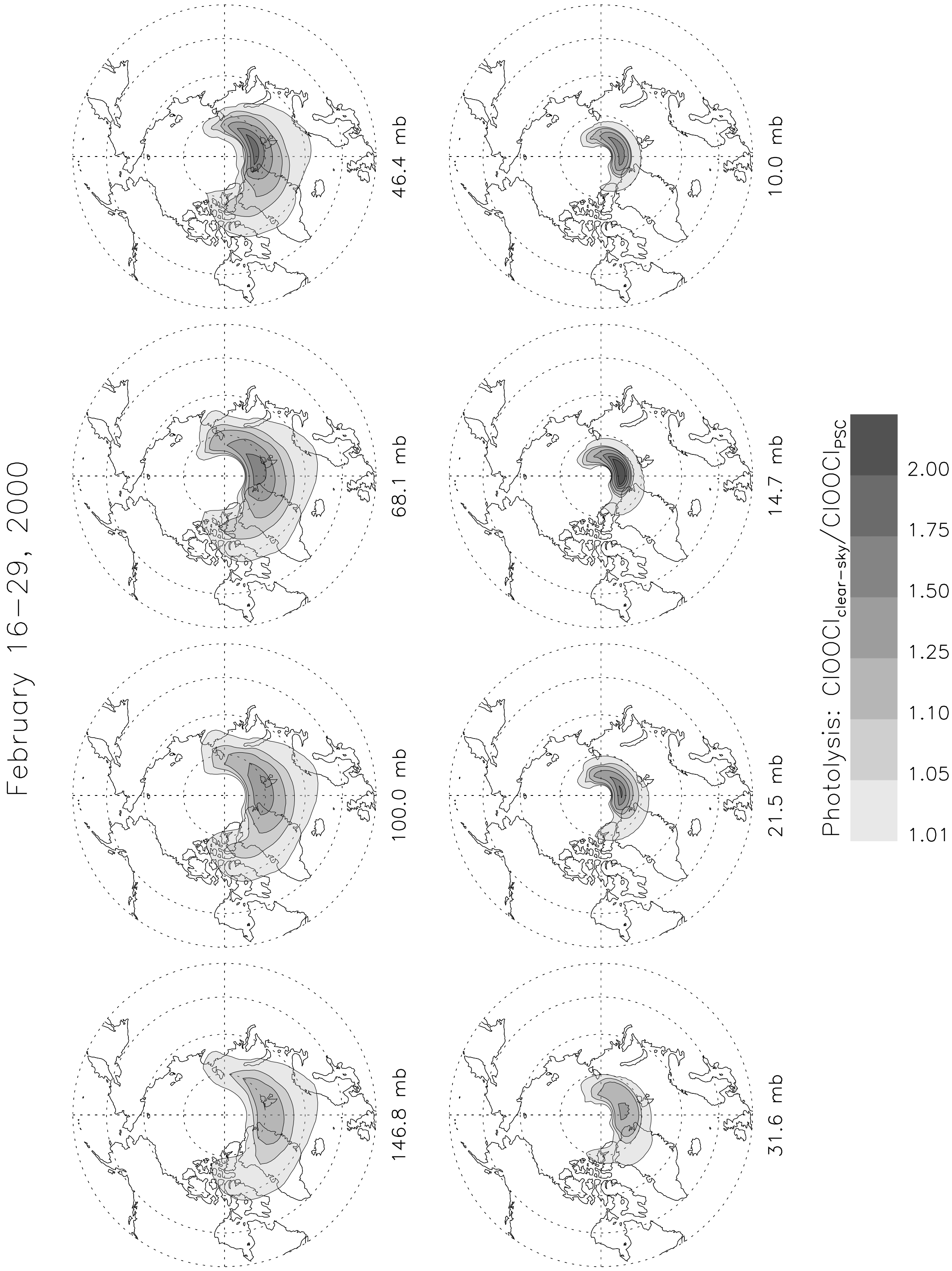

Figure 6.24. Clear-sky/PSC-influenced ClOOCl photolysis at eight pressure levels for 20000216–20000229 over the Northern Hemisphere, 50°N–North Pole.

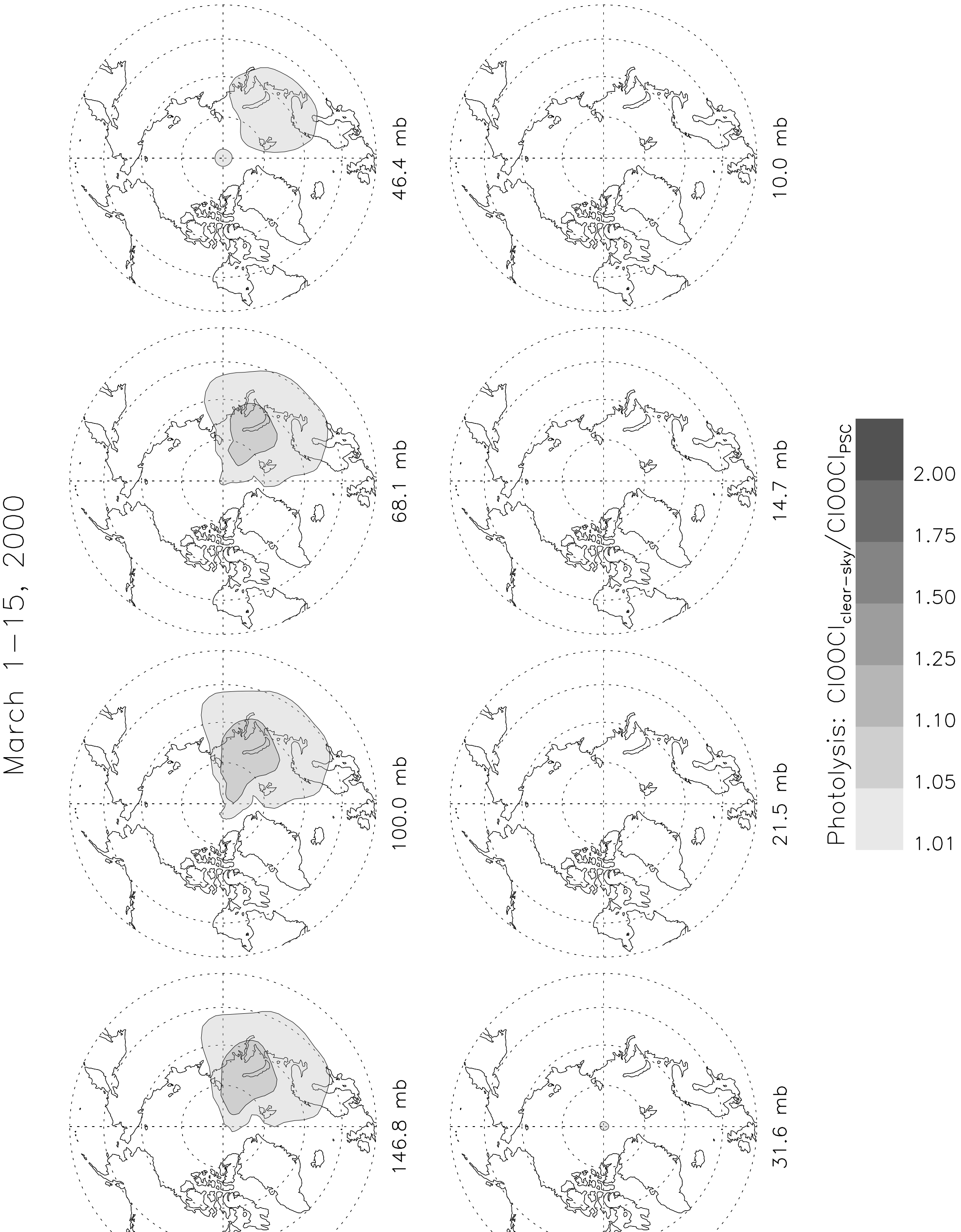

Figure 6.25. Clear-sky/PSC-influenced ClOOCl photolysis at eight pressure levels for 20000301–20000315 over the Northern Hemisphere, 50°N–North Pole.

6.6.3 Polar Vortex–Averaged Impact on ClOOCl Photolysis

With ozone loss related to j_{ClOOCl} (6.5), integration of ClOOCl photolysis throughout the polar region during SOLVE leads to an inferred impact on ozone loss rates. Cold temperatures, PSCs, chlorine activation, and subsequent ozone loss occur within the polar vortex (see chapter 5). Throughout the winter, the meteorological conditions of the atmosphere that make PSC formation favorable, as well as the radiative transfer of the polar vortex, change a great deal. To assess the impact on ozone loss throughout the vortex as a whole during the ozone loss season, clear-sky and PSC-influenced daily ClOOCl photolysis were integrated over the geographical extent of the vortex, such that

$$\left(\frac{\Delta[\mathrm{O_3}]_{\text{clear-sky}}}{\Delta[\mathrm{O_3}]_{\text{PSC}}}\right)_{\text{vortex}}(\theta) \approx \frac{\iint_{\text{vortex}} \mathscr{P}_{\text{ClOOCl,clear-sky}}(lat, lon, \theta)\, dA}{\iint_{\text{vortex}} \mathscr{P}_{\text{ClOOCl,PSC}}(lat, lon, \theta)\, dA}, \qquad (6.6)$$

where the $\mathscr{P}_{\text{ClOOCl}}(\mathbf{x})$ was considered as a function of latitude, longitude, and potential temperature θ and integrated over vortex area A. The results of (6.6) for December 1999–March 2000 are shown in Figure 6.26. The edge of the polar vortex was defined using the technique of *Nash et al.* [1996] at 480 K and used at all altitudes. The area-weighted clear-sky and PSC-influenced inside-vortex j_{ClOOCl} was then integrated over each day at each of the eight UKMO pressure levels. The evolution of the PSC effect on ClOOCl photolysis roughly followed that of the temperature structure of the vortex, following the diabatic descent throughout the period. Temperatures were relatively warm in the first half of December, but the effect reached daily vortex averages of nearly 10% at the lower altitudes by late January, when PSCs were most prevalent, and it disappeared by mid-March, due to both stratospheric warming and decreasing SZAs. The altitudes of maximum PSC effect roughly coincide with the maximum ozone loss [e.g., chapter 5; *Swartz et al.*, 2002]

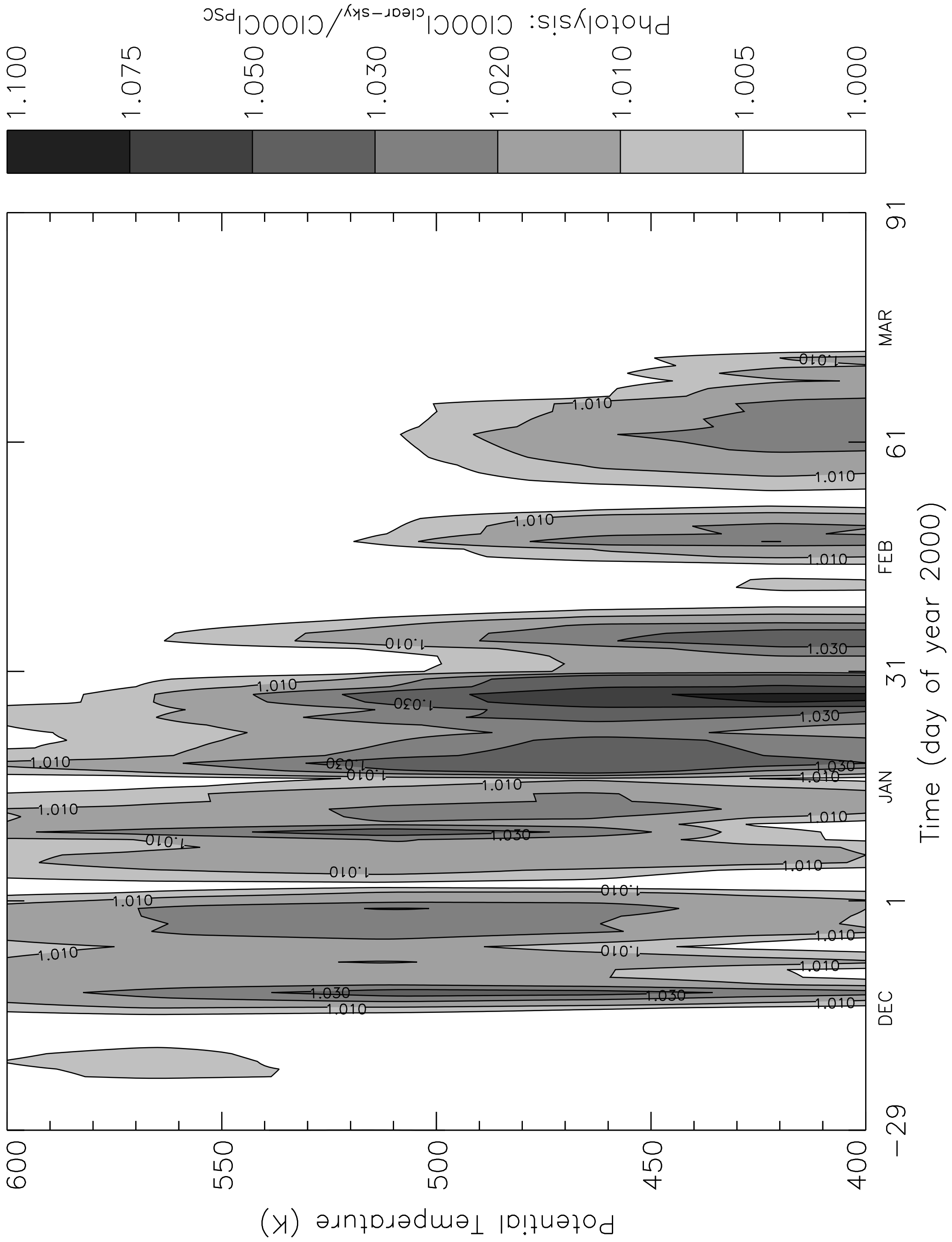

Figure 6.26. Clear-sky/PSC-influenced ClOOCl photolysis within the Arctic during SOLVE, integrated daily across the whole of the vortex for December 1999–March 2000 as a function of potential temperature.

6.6.4 Absolute Effect on Arctic Ozone Loss

To this point, the relative clear-sky/PSC effect on ClOOCl photolysis has been considered. Now the absolute difference in the clear-sky and PSC-influenced vortex is addressed. Eq. (6.6) relates clear-sky and PSC-influenced ozone loss. If the absolute value of either is known, the other can be computed simply.

The SOLVE 20000123–20000304 period is examined here, using vortex-averaged (PSC-influenced) ozone loss as measured using space-based stellar occultation [see chapter 5; *Swartz et al.*, 2002]. The photochemical ozone loss determined using average diabatic descent within the vortex (shown in Figure 5.12 as a function of potential temperature on 20000304) was mapped daily onto the vortex using the diabatic descent from the stellar occultation analysis (see sloped curves in Figure 5.4). The absolute differences in the clear-sky and PSC-influenced loss rates were computed. These absolute differences were then integrated following diabatic descent and are shown in Figure 6.27. With a nearly 1-ppmv maximum ozone loss near 425 K (referenced to 20000304; see Figure 5.12) for this period, the corresponding absolute impact of the optical effects of PSCs are on the order of 0.021 ppmv (2%). It was assumed here that all photochemical ozone destruction resulted from ClO_x chemistry and that only the modulation of ClOOCl photolysis had a significant effect on ozone loss.

The absolute ozone loss in Figure 5.12 between 400 and 575 K (referenced to March 4) during January 23–March 4 corresponds to a reduction of the total ozone column of 35.0 Dobson units (DU). It is estimated (see Figure 6.27) that under clear-sky j_{ClOOCl} conditions, the loss would be 35.5 DU (a 1.5% total difference due to the optical effects of PSCs).

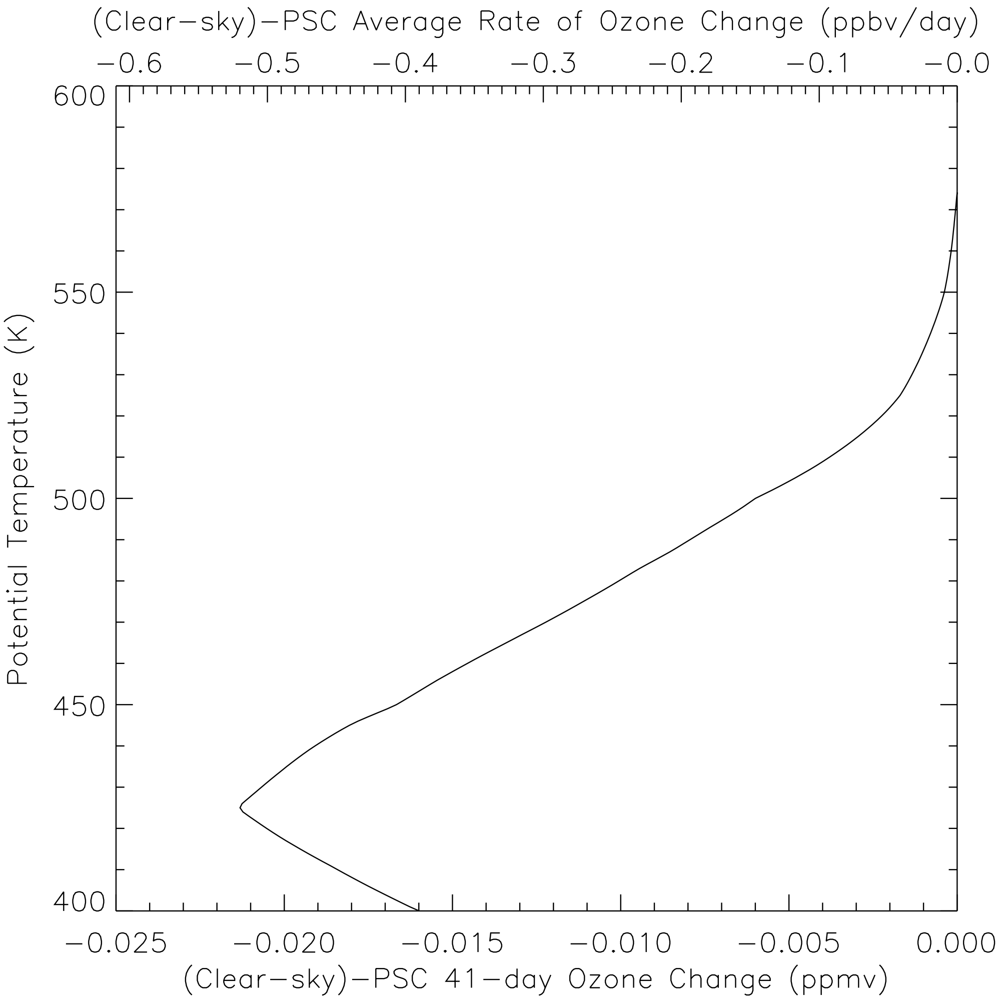

Figure 6.27. Absolute optical effect of PSCs on Arctic ozone loss for 20000123–20000304. Shown here is the absolute difference (clear-sky−PSC-influenced ClOOCl photolysis) in ozone change inferred from the loss rates derived from MSX/UVISI stellar occultations during SOLVE (in the presence of PSCs) (compare Figure 5.12). This result uses the average daily ozone loss rates derived from the stellar occultations and ensemble average diabatic descent described in chapter 5. The profile is referenced to potential temperature on 20000304.

6.7 Potential Influence of High-Altitude Cirrus

In this analysis, the *j*-value attenuation discussed has been attributed entirely to PSCs. The DC-8 also occasionally encountered high-altitude cirrus, however [*Kondo et al.*, 2002]. Three independent pieces of evidence suggest that cirrus did not have a significant impact on the ultraviolet radiation field at DC-8 altitudes during SOLVE or the present analysis. First, the time periods during the flights that experienced significant cirrus clouds at the DC-8 were noted by *Kondo et al.* [2002] and also inferred in data from upward- and downward-looking visible lidar instruments (LASE [*Browell*, 1997] and UV-DIAL [*Browell et al.*, 1998]) on-board the aircraft. While these time periods overlapped segments of the flights where *j*-values were attenuated, *j*-values were also modulated when no cirrus were present and vice versa. Second, *j*-value attenuation was well correlated with $(T - T_{\mathrm{NAT}})_{\mathrm{min}}$ along the solar LOS at 13–25 km (see Figure 6.7), well above the DC-8 flight altitude and potential cirrus interference. Finally, the SZA dependence of the *j*-value effect was proportional to an exponential Beer–Lambert function of slant path through the PSC layer (13–25 km, see Figure 6.11), not the observed cirrus layer (8–12 km). The SZA dependence of *j*-value attenuation by the cirrus layer would have led to a smaller effect at 80° SZA relative to 90°, with much greater attenuation beyond 90° (not shown). Thus, while contamination of some of the present data by cirrus cannot be entirely ruled out, the overall features of the analysis are more consistent with *j*-value attenuation by PSCs rather than cirrus.

6.8 Summary and Conclusions

By comparing in situ measurements of *j*-values with clear-sky model calculations during SOLVE, the direct, optical effect of PSCs on photolysis has been estimated. Significant attenuation of j-values (up to 75% for j_{NO_2}) was observed at DC-8 altitudes, near 11 km. This j-value attenuation, attributed to PSCs, was well correlated with cold temperatures (and presumably PSC occurrence) along the solar line of sight. The present analysis demonstrated how the magnitude of the inferred PSC effect on j-values was related to the slant path of the solar flux through the PSC layer in the atmosphere and the modeled j-value direct fraction. Empirical relationships of j-value attenuation with temperature, light path, and the local radiative transfer environment were developed, allowing for estimation of the PSC effect on j_{ClOOCl} throughout the lower stratosphere. PSCs were shown to have a significant (up to 10%) impact on daily polar vortex–averaged ClOOCl photolysis, especially in late January 2000, which has implications for the modeling of ozone loss during this period. For example, *Sinnhuber et al.* [2000] have shown a delay in observed ozone destruction in January 2000 relative to their model calculations. The PSC effect may in part be responsible for this discrepancy, leading to an overestimate of clear-sky model photolysis. Finally, when combined with ozone loss rates measured by MSX/UVISI stellar occultation, a total impact on ozone loss for 20000123–20000304 of up to 0.021 ppmv (2%) was determined.

While the total impact of the suggested optical effects of PSCs on ozone loss is presently relatively small in the Arctic, global change is expected to increase the occurrence of PSCs in the Arctic dramatically over the next several decades [*Pitari et al.*, 2002]. An understanding of how the optical properties of PSCs are affecting ozone loss now and how they will respond to changes in climate (stratospheric cooling) and the chemical composition of the atmosphere (trends in water vapor and nitric acid) is vital. Application of this analysis of PSC optical forcing could improve models predicting the future evolution and variability of stratospheric ozone.

Chapter 7

Concluding Remarks

7.1 Summary

State-of-the-art instruments and models have been used to quantify photolysis rate coefficients in the troposphere and stratosphere, in the context of the IPMMI, POLARIS, and SOLVE campaigns, at Earth's surface and also on aircraft in the lower stratosphere (see Table 7.1 and the individual conclusions of chapters 2–6). The physical parameters controlling j-values, including the extraterrestrial solar irradiance, molecular parameters (e.g., absorption cross sections and quantum yields), altitude, surface altitude, surface albedo, ozone column and profile, and aerosol properties, during these field missions have been considered. Model–measurement agreement under clear-sky conditions was excellent, roughly on the order of 5% or less for $j_{\mathrm{NO_2}}$ and 10% or less for $j_{\mathrm{O_3}}$, even at high ($>85°$) solar zenith angles (SZAs).

Satellite-based stellar occultation observations during SOLVE, coupled with diabatic trajectory analyses of subsidence within the polar vortex, have determined photochemical ozone loss in the Arctic stratosphere (a maximum of $\sim$1 ppmv ozone loss in the lower stratosphere during January 23–March 4, 2000). This analysis demonstrated the utility of the technique and also set the stage for the quantification of the optical effects

Table 7.1. Summary of j_{NO_2} and j_{O_3} model–measurement agreement

j_{NO_2} (%)^{a,b}	j_{O_3} (%)^{a}	Solar Zenith Angle	Altitude (km)	Instrument	Platform	Campaign	Chapter
14^{c}	$<$1	16°–75°	1.8 (surface)	actinometer	—	IPMMI	2
2	1	16°–75°	1.8 (surface)	spectroradiometer	—	IPMMI	2
6–9	1–7	27°–85°	15–22	spectroradiometer	ER-2	POLARIS	3
2–4^{d}	0–13^{d}	68°–85°	8–13	spectroradiometer	DC-8	SOLVE	4
4–6^{d}	3–15^{d}	85°–93°	8–13	spectroradiometer	DC-8	SOLVE	4

[a]Ranges for comparisons using different model inputs.

[b]Model and spectroradiometer calculations using *DeMore et al.* [1997] NO_2 cross sections.

[c]This 14% agreement would improve to 7% with the use of the *Harder et al.* [1997] NO_2 cross sections in the modeling calculations. The use of the larger *Harder et al.* [1997] NO_2 cross sections during POLARIS would reduce the steady-state [NO_2] inferred from modeled j_{NO_2} (see chapter 3) and in situ species concentrations by *Del Negro et al.* [1999], improving agreement with measured [NO_2].

[d]Not including model calculations using simple climatology.

of polar stratospheric clouds (PSCs) on absolute ozone loss.

Excellent clear-sky j-value model–measurement agreement has allowed for a preliminary assessment of PSC optical effects when comparing clear-sky model j-values with in situ measurements in the presence of PSCs. These comparisons (with attenuation of j_{NO_2} at 11 km up to 75%, attributed to PSCs) formed the basis for an estimate of the impact of PSCs on ozone loss rates. Inferred PSCs were shown to have a significant (up to 10%) impact on daily polar vortex–averaged ClOOCl photolysis in late January, with implications for the modeling of ozone loss in polar spring. Combined with ozone loss in the Arctic determined by satellite stellar occultation measurements, the absolute impact of PSC optical effects on ozone loss has been estimated over January 23–March 4, 2000 to be up to 0.021 ppmv (about 2% of the maximum loss). While this suggests that the impact on the integrated seasonal ozone loss is currently modest in the Arctic, the increased prevalence of PSCs due to global change could amplify the effect.

7.2 Future Work

Under clear-sky conditions, our ability to model j_{NO_2} and j_{O_3} at relatively low SZAs has improved to a level of agreement of just a few percent (chapters 2–3). The persistent spectroradiometer– and model–actinometer (negative) discrepancies for j_{NO_2} using currently accepted molecular data [*DeMore et al.*, 1997] call for a re-evaluation of the NO_2 absorption cross section. Use of more recent cross section measurements [e.g., *Harder et al.*, 1997] produces better consistency with actinometry and j-values derived from in situ chemical measurements. For highly accurate tropospheric j-value modeling, detailed optical characterization of aerosols, in addition to ancillary measurements of altitude, ozone profile, albedo, and temperature, is needed. While measured and modeled high-SZA j-values are also in reasonable agreement, polar ozone climatologies can be far from reality, markedly impacting j_{O_3} (chapter 4). Further model–measurement j-value intercomparisons at high SZAs could lead to better treatment of the geophysical environment (e.g., the overhead ozone profile and total vertical column have less relevance as the Sun approaches the horizon and its light traverses hundreds of horizontal kilometers through the inhomogeneous atmosphere).

Clouds complicate the tropospheric radiation field significantly, and their effects on surface j-values were beyond the scope of this dissertation. Three-dimensional radiative transfer models and/or robust parameterizations of cloud effects are needed when in situ measurements are not available. Estimations based on global satellite data could also hold promise in elucidating cloud effects on large-scale atmospheric photochemistry. The optical effects of clouds in the stratosphere on spectral actinic flux and j-values at high SZAs also need more investigation. The preliminary empirical analysis presented in chapter 6 relies on a number of assumptions that could be refined with further modeling of actinic flux. Modeling should also be conducted based on a thorough analysis of the available aerosol and cloud data collected during SOLVE from aircraft (in situ and lidar), balloons, and satellites. The PSC optical effects need to be confirmed at higher altitudes in the stratosphere with in situ flux measurements and then tested in a full chemistry–transport model.

The efficacy of a dedicated stellar occultation spacecraft instrument will soon be tested with the European GOMOS mission. As we enter an era of diminishing stratospheric chlorine loadings, the detection of the turnaround and eventual reversal of ozone trends will be subtle and altitude-dependent. A satellite mission that combines extinctive–refractive stellar occultation (demonstrated in chapter 5) and solar nadir- or limb-scatter instruments could provide hundreds of high–altitude resolution nighttime and daytime profiles of ozone (and other species) in the stratosphere and upper troposphere per day, virtually free of accuracy degradation. Long-term remote sensing observations of this type could detect trends signaling ozone recovery and global change.

Appendix A

APL Radiative Transfer Model

This appendix presents details of the APL radiative transfer model introduced in section 1.3, including the algorithm derivation, model input data, and general implementation used in the current, SOLVE version of the model code (see chapter 4). It also makes note of some differences in the inputs that were used in the earlier IPMMI (chapter 2) and POLARIS (chapter 3) campaigns. In appendix G, the model has been used to create a "photolysis atlas" of *j*-values, as functions of wavelength, throughout the troposphere and stratosphere.

A.1 Model Description

The APL radiative transfer model has proved a useful and accurate tool for computing photolysis rate coefficients from the surface of the Earth through the stratosphere. The model has been developed and utilized primarily for the calculation of *j*-values [e.g., *Anderson and Meier*, 1979; *Meier et al.*, 1982; *Anderson*, 1983; *Anderson and Lloyd*, 1990; *Anderson et al.*, 1995; *DeMajistre et al.*, 1995; *Swartz et al.*, 1999, and R. E. Shetter et al. (manuscript in preparation, 2002)], especially in twilight during stratospheric aircraft campaigns (see summary in section 1.4.2), over the past two decades. The model solves the integral equation of radiative transfer, with the direct solar deposition and reflection from a Lambertian reflecting surface calculated in a spherical, refracting atmosphere, and isotropic multiple scattering calculated using a plane-parallel approximation. Extensive comparisons have shown that this technique provides reliable estimates of the radiation field for solar zenith angles (SZAs) of up to 95° for all but extreme volcanic conditions [*Anderson*, 1983; *Dahlback and Stamnes*, 1991].

A.2 Model Algorithm Derivation

The source function formalism used in an early version of the model has been described by *Meier et al.* [1982], but it is also useful to recapitulate their basic derivation of the model and particularly the physical basis for the algorithm. A familiarity with the physical model not only improves understanding of the mathematics used but also creates an intuitive framework for considering radiative transfer in general.

The actinic flux into a volume element at wavelength λ at point $\mathbf{r}$ in the atmosphere is given by

$$F_\lambda(\mathbf{r}) = \iint I_\lambda(\mathbf{r},\Omega)d\Omega, \tag{A.1}$$

equivalent to (1.3). The total actinic flux is the integral of I_λ over all 4π steradians of solid angle. We may consider the different contributions to the radiation field by writing the actinic flux F (with the subscript λ dropped for clarity) as

$$F(\mathbf{r}) = \underbrace{F_0\mathscr{T}(\mathbf{r}-\mathbf{r_0})}_{\text{direct attenuated flux}} + \underbrace{\iint \varepsilon(\mathbf{r}',\Omega)\mathscr{T}(\mathbf{r}-\mathbf{r}')d|\mathbf{r}-\mathbf{r}'|d\Omega}_{\text{multiply scattered flux}}, \tag{A.2}$$

equivalent to (1.12), where F_0 is the actinic flux at the top of the atmosphere $\mathbf{r_0}$ (equivalent to the solar irradiance), $\mathscr{T}$ is the transmissivity or transmission probability along the path of the incident light beam, and ε is the volume scattering rate in the direction given by Ω (photons s^{-1} cm^{-3} sr^{-1} nm^{-1}). The first term in (A.2) represents the direct attenuated flux into a volume element and the second term is the diffuse flux multiply scattered from all other points in the atmosphere $\mathbf{r}'$. Reflection from Earth's surface is not yet considered.

The model algorithm calculates direct solar deposition and reflection from a Lambertian reflecting surface in a spherical, refracting atmosphere. The scattering calculation, however, benefits from making several simplifying assumptions. The first is that the atmosphere is considered plane-parallel (i.e., flat-Earth). Extensive comparisons have shown that this approach provides reliable estimates of the radiation field for SZAs of up to 95° for all but extreme volcanic conditions [*Anderson*, 1983; *Dahlback and Stamnes*, 1991]. For the current discussion, we shall adopt the plane-parallel formalism everywhere. The scattering distance $d|\mathbf{r}-\mathbf{r}'|$ is equivalent to $|dz\sec\gamma|$, where γ is the scattering zenith angle (angle from vertical) and dz is the altitude separation of $\mathbf{r}$ and $\mathbf{r}'$ (see Figure A.1). The transmission probabilities are therefore

$$\mathscr{T}(\mathbf{r}-\mathbf{r}') = \exp[(-|\tau_\mathrm{s}-\tau_\mathrm{s}'|-|\tau_\mathrm{a}-\tau_\mathrm{a}'|)\sec\gamma], \tag{A.3}$$

where $|\tau-\tau'|$ is the vertical optical depth between altitudes z and z'. The subscripts 's' and 'a' represent attenuation due to scattering and absorption, respectively, caused by gases and particles. The second assumption is that the (vertical) differential scattering optical depth can be represented as

$$d\tau_\mathrm{s} = [\sigma_\mathrm{R} n_\mathrm{R} + (1-g)\sigma_\mathrm{M} n_\mathrm{M}]dz, \tag{A.4}$$

where σ and n are the scattering cross section (cm^2) and number density of scatterers (cm^{-3}) for Rayleigh (R) and Mie (M) particles. In the formulation of (A.4), a third important assumption has been used. Scattering is assumed to be isotropic (independent of angle). This has been justified by *Anderson and Meier* [1979]. The isotropic as-

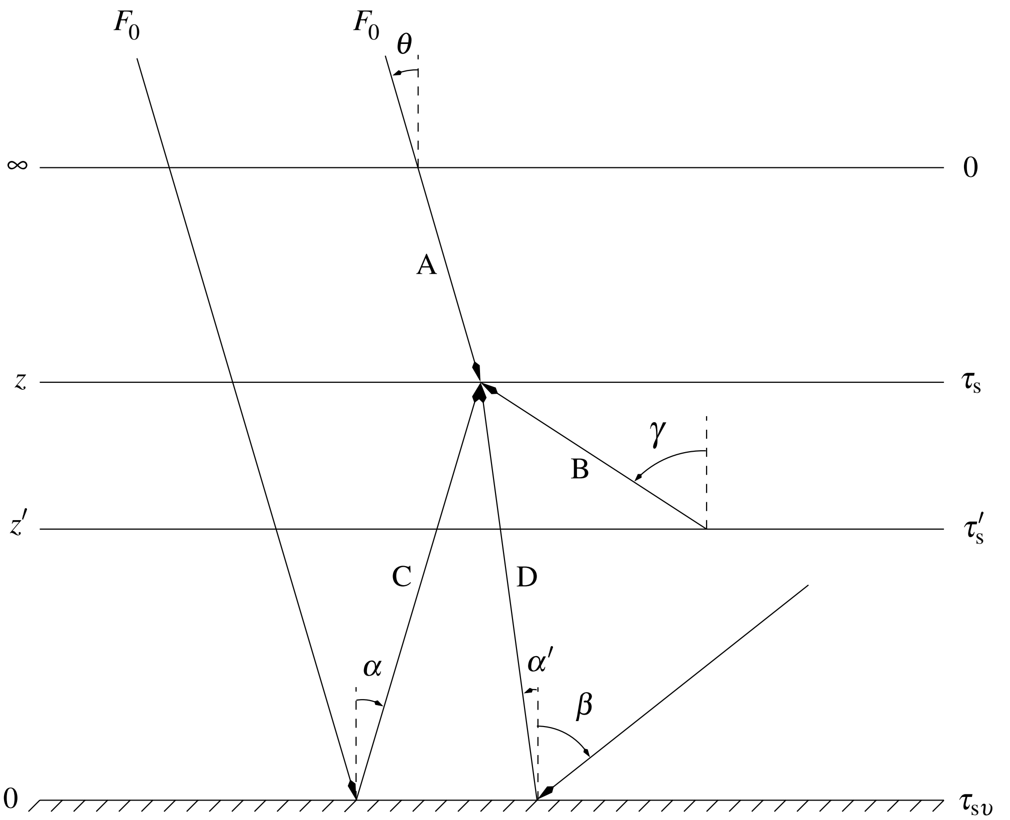

Figure A.1. Source function contributions to the radiation field (and thus actinic flux) at altitude z, as described by the APL model. The vertical coordinate is shown both as a function of altitude (left) and vertical scattering optical depth τ_s (right). The individual contributions are (A) direct attenuated solar flux, (B) multiply scattered flux, (C) ground reflection of the direct attenuated solar flux, and (D) ground reflection of the multiply scattered flux (adapted from *Meier et al.* [1982]).

sumption is excellent for Rayleigh (molecular) scattering. Aerosol scattering, however, may be highly anisotropic, and the effect on the scattering field may be significant at high aerosol loadings. Therefore, the correction term $1 - g$, where g is the asymmetry factor—a parameter representing the anisotropicity of scattering [e.g., *Jursa*, 1985]—modifies Mie (large-particle) scattering in (A.4), which greatly reduces the error associated with the isotropic assumption for aerosol scattering [*Anderson et al.*, 1980]. If the aerosol is highly forward-scattering (the change in direction of light propagation due to scattering is small), g is close to 1, and the contribution of Mie scattering to $d\tau_\mathrm{s}$ is small. The g for molecular scattering is 0.

For isotropic, conservative scattering (i.e., pure scattering, single-scattering albedo $\omega_0 = 1$), note the volume scattering rate

$$\varepsilon = F[\sigma_\mathrm{R} n_\mathrm{R} + (1-g)\sigma_\mathrm{M} n_\mathrm{M}]/4\pi. \tag{A.5}$$

Substituting (A.5) into (A.2) and integrating over $d\Omega = 2\pi\, d\cos\gamma$, a plane-parallel form of the actinic flux is

$$F(z) = F_0 \mathscr{T}(\Delta\tau_0) + \frac{1}{2}\int F(z)[\sigma_\mathrm{R} n_\mathrm{R} + (1-g)\sigma_\mathrm{M} n_\mathrm{M}]E_1(\Delta\tau')dz', \tag{A.6}$$

where $\Delta\tau' = |\tau_\mathrm{s} - \tau'_\mathrm{s}| + |\tau_\mathrm{a} - \tau'_\mathrm{a}|$, $\Delta\tau_0$ is the total optical depth to the Sun, and E_n is the nth exponential integral. Now, by changing the independent, vertical variable to the *scattering* optical depth τ_s, and by defining the source function,[1] the normalized actinic flux, as

$$S = F/F_0, \tag{A.7}$$

(A.6) becomes

$$S(\tau_\mathrm{s}) = S_0(\tau_\mathrm{s}) + \frac{1}{2}\int S(\tau'_\mathrm{s})E_1(\Delta\tau')d\tau'_\mathrm{s}. \tag{A.8}$$

[1]The "source function" defined here should not be confused with the source function discussed by *Chandrasekhar* [1960] or the source function coefficient in the equation of transfer (1.4).

This equation defines the source function, which is a scalar, unitless quantity, independent of F_0, the top-of-the-atmosphere flux. The actinic flux at an altitude z (or optical depth τ_s) is simply the product of the source function S and F_0. S_0 is the source function for the direct attenuated flux.

As in (A.2), (A.8) does not include reflection from the surface. Two additional terms must be added to account for the ground albedo, one for the direct solar beam and the other for the diffuse, multiply scattered flux. The component of the actinic flux due to the surface reflection of the direct solar beam is

$$F_{0g} = \iint I_{0g} d\Omega = 2\pi \int I_{0g} d\cos\alpha, \tag{A.9}$$

where I_{0g} is the radiance due to the reflection of the direct beam and α is the zenith angle of the reflection. Assuming a Lambertian reflecting surface of albedo R ($0 \leq R \leq 1$),

$$I_{0g} = \frac{R}{\pi} F_0 \cos\theta \mathscr{T}(\tau_\upsilon \sec\theta) \exp(-\Delta\tau_g \sec\alpha), \tag{A.10}$$

where θ is the solar zenith angle and τ_υ is the total optical depth to the surface, $F_0 \cos\theta \mathscr{T}(\tau_\upsilon \sec\theta)$ is the solar flux reaching the surface, followed by a fraction R (the surface albedo) reflected upward into 2π steradians. The exponential factor accounts for further attenuation between the surface and altitude z, where $\Delta\tau_g = |\tau_{s\upsilon} - \tau_s + \tau_{a\upsilon} - \tau_a|$. Substitution of (A.10) into (A.9) and integration of the result yields

$$S_{0g}(\tau_s) = \frac{F_{0g}}{F_0} = 2R\cos\theta \exp(-\tau_\upsilon \sec\theta) E_2(\Delta\tau_g). \tag{A.11}$$

This contribution to the total actinic flux is labeled “C” in Figure A.1.

A similar procedure yields an expression for the ground reflection of the multiply scattered actinic flux:

$$F_g = 2\pi \int I_g d\cos\alpha', \tag{A.12}$$

where

$$I_{\mathrm{g}} = \frac{R}{\pi}\left[2\pi \int I_{\mathrm{ms}} \cos\beta d\cos\beta\right] \exp(-\Delta\tau_{\mathrm{g}} \sec\alpha'). \tag{A.13}$$

The integration over $\cos\beta$ includes all multiply scattered radiation reaching the ground, and the integration over $\cos\alpha'$ is for all surface elements visible to the volume element. The multiply scattered radiance is given by

$$I_{\mathrm{ms}} = \int S(\tau_{\mathrm{s}}') \exp(-|\tau_{\upsilon} - \tau'| \sec\beta) d\tau_{\mathrm{s}}' \sec\beta. \tag{A.14}$$

Substitution of (A.14) and (A.13) into (A.12) and integration over $\cos\beta$ and $\cos\alpha'$ yields

$$S_{\mathrm{g}}(\tau_{\mathrm{s}}) = \frac{F_{\mathrm{g}}}{F_0} = RE_2(\Delta\tau_{\mathrm{g}}) \int S(\tau_{\mathrm{s}}') E_2(\Delta\tau_{\mathrm{g}}') d\tau_{\mathrm{s}}'. \tag{A.15}$$

This contribution to the total actinic flux is labeled "D" in Figure A.1.

The equation for the total source function is found by combining (A.8), (A.11), and (A.15):

$$\begin{aligned} S(\tau_{\mathrm{s}}) = {} & \overbrace{\exp(-\tau \sec\theta)}^{\mathrm{A}} + \overbrace{2R\cos\theta \exp(-\tau_{\upsilon} \sec\theta) E_2(\Delta\tau_{\mathrm{g}})}^{\mathrm{C}} \\ & + \int \Big[\underbrace{S(\tau_{\mathrm{s}}') \frac{E_1(\Delta\tau')}{2}}_{\mathrm{B}} + \underbrace{RE_2(\Delta\tau_{\mathrm{g}}) E_2(\Delta\tau_{\mathrm{g}}')}_{\mathrm{D}}\Big] d\tau_{\mathrm{s}}'. \end{aligned} \tag{A.16}$$

The labeled components of (A.16) correspond to the labels in Figure A.1, and the mathematical description of the physical contributions to the actinic flux is complete.

Eq. (A.16) is solved after dividing the model atmosphere into finite layers. The altitude resolution is sufficiently fine such that the source function does not vary significantly over each layer (75 layers over 0–120 km is typical, with finer resolution close to the surface) and is therefore assumed constant. A wavelength–altitude matrix of atmospheric optical depths, which is a function only of atmospheric properties, namely profiles of absorbers and scatterers (e.g., density, O_2, O_3, aerosols), is constructed and inverted to solve for the scattered radiation field throughout the entire atmosphere. The product of the inverted matrix and S_0 is the total source function S, which when multiplied by the top-of-the-atmosphere solar irradiance F_0 gives the actinic flux directly. Note that the scattering matrix is determined for all layers of the atmosphere at once, so the actinic fluxes at all altitudes are calculated simultaneously.

A.3 Model Inputs

A.3.1 Molecular Data

SOLVE

The photodissociation processes for which the APL model is currently equipped to calculate photolysis rate coefficients are shown in Table A.1. References for the molecular absorption cross sections and quantum yields are also listed. Perhaps the best single source for molecular data for species of interest in the stratosphere (and troposphere) is the Jet Propulsion Laboratory "Chemical Kinetics and Photochemical Data for Use in Stratospheric Modeling" (JPL97) [*DeMore et al.*, 1997] and its more recent supplement (JPL00) [*Sander et al.*, 2000]. For nearly every process listed in Table A.1, *DeMore et al.* [1997] and *Sander et al.* [2000] have reviewed the literature and have made recommendations as to which data (often combinations of laboratory measurements) should be used for photochemical modeling. With few exceptions, these recommendations have been adopted here (note that for most processes, ϕ is assumed to be unity). These data that were used in the SOLVE analysis (chapter 4), unless otherwise noted in Table A.1.

In all the variants of the APL model used in this dissertation, the absorption cross sections used for the calculation of the j-values for O_2, O_3, and NO_2 photolysis were also used when computing the attenuation of the solar flux (though NO_2 absorption is insignificant for all of the cases considered).

Table A.1. APL radiative transfer model input molecular data

Photolysis Process	Cross Section	Quantum Yield
O_2 $-h\nu(partial)\rightarrow$ $O(^3P) + O(^3P)$		
Partial j-value, Schumann–Runge Bands, 175–204 nm	DeMajistre/Minschwaner[a]	1
O_2 $-h\nu(partial)\rightarrow$ $O(^3P) + O(^3P)$		
Partial j-value, Herzberg continuum, 205–240 nm	*DeMore et al.* [1997]	1
O_2 $-h\nu\rightarrow$ $O(^3P) + O(^3P)$ Total j-value		
O_3 $-h\nu\rightarrow$ $O_2 + O(^3P)$	*Paur and Bass* [1985]; *Molina and Molina* [1986]; *WMO* [1986][b]	*Sander et al.* [2000]
O_3 $-h\nu\rightarrow$ $O_2 + O(^1D)$	*Paur and Bass* [1985]; *Molina and Molina* [1986]; *WMO* [1986][b]	*Sander et al.* [2000]
HO_2 $-h\nu\rightarrow$ OH + H	*DeMore et al.* [1997]	1
H_2O $-h\nu\rightarrow$ H + OH	*DeMore et al.* [1997]	1
H_2O_2 $-h\nu\rightarrow$ OH + OH	*DeMore et al.* [1997]	1
NO_2 $-h\nu\rightarrow$ NO + $O(^3P)$	*DeMore et al.* [1997]	*DeMore et al.* [1997]
NO_3 $-h\nu\rightarrow$ NO + O_2	*Graham and Johnston* [1978]	*Johnston et al.* [1996]
NO_3 $-h\nu\rightarrow$ $NO_2 + O(^3P)$	*Graham and Johnston* [1978]	*Johnston et al.* [1996]
N_2O $-h\nu\rightarrow$ $N_2 + O(^1D)$	*DeMore et al.* [1997]	1
N_2O_5 $-h\nu\rightarrow$ NO_3 + Products	*DeMore et al.* [1997]	1
HONO $-h\nu\rightarrow$ OH + NO	*DeMore et al.* [1997]	1
$HONO_2$ $-h\nu\rightarrow$ Products	*DeMore et al.* [1997]	1

[a]Parameterization of the solar transmission through the O_2 Schumann–Runge bands (175–204 nm) by R. DeMajistre (JHU/APL) was based on the work of *Minschwaner et al.* [1993].

[b]Ozone cross sections from three sources were used over different wavelength ranges: 175.4–185.2 nm (*WMO* [1986]), 185.2–245.0 nm (*Molina and Molina* [1986]), 245.0–342.0 nm (*Paur and Bass* [1985]), 342.0–345.0 nm (*Molina and Molina* [1986]), and 407.0–850.0 nm (*WMO* [1986]).

Table A.1. APL radiative transfer model input molecular data (continued)

Photolysis Process	Cross Section	Quantum Yield
HO_2NO_2 $-h\nu\rightarrow$ Products	*DeMore et al.* [1997]	1
CH_2O $-h\nu\rightarrow$ H + CHO	*DeMore et al.* [1997]	*DeMore et al.* [1997]
CH_2O $-h\nu\rightarrow$ H_2 + CO	*DeMore et al.* [1997]	*DeMore et al.* [1997]
$CH_3C(O)CH_3$ $-h\nu\rightarrow$ Products	*Martinez et al.* [1992]	*McKeen et al.* [1997]
CH_3ONO_2 $-h\nu\rightarrow$ CH_3O + NO_2	*Talukdar et al.* [1997]	1
$CH_3CH_2ONO_2$ $-h\nu\rightarrow$ Products	*Talukdar et al.* [1997]	1
CH_3O_2 $-h\nu\rightarrow$ Products	*DeMore et al.* [1997]	1
$C_2H_5O_2$ $-h\nu\rightarrow$ Products	*DeMore et al.* [1997]	1
CH_3OOH $-h\nu\rightarrow$ CH_3O + OH	*DeMore et al.* [1997]	1
$CH_3C(O)O_2NO_2$ $-h\nu\rightarrow$ Products	*DeMore et al.* [1997]	1
Cl_2 $-h\nu\rightarrow$ Cl + Cl	*DeMore et al.* [1997]	1
ClO $-h\nu\rightarrow$ Cl + $O(^3P)$	*DeMore et al.* [1997][c]	1
ClOO $-h\nu\rightarrow$ ClO + $O(^3P)$	*DeMore et al.* [1997]	1
OClO $-h\nu\rightarrow$ ClO + $O(^3P)$	*DeMore et al.* [1997][d]	1
Cl_2O $-h\nu\rightarrow$ Products	*DeMore et al.* [1997]	1
ClOOCl $-h\nu\rightarrow$ Cl + ClOO	*DeMore et al.* [1997]	1
Cl_2O_3 $-h\nu\rightarrow$ Products	*DeMore et al.* [1997]	1
Cl_2O_4 $-h\nu\rightarrow$ Products	*DeMore et al.* [1997]	1
Cl_2O_6 $-h\nu\rightarrow$ Products	*DeMore et al.* [1997]	1
HCl $-h\nu\rightarrow$ H + Cl	*DeMore et al.* [1997]	1
HOCl $-h\nu\rightarrow$ OH + Cl	*Sander et al.* [2000]	1
FNO $-h\nu\rightarrow$ F + NO	*DeMore et al.* [1997]	1
ClNO $-h\nu\rightarrow$ Cl + NO	*DeMore et al.* [1997]	1

[c] JPL97-derived analytic cross sections, 215-330 nm.
[d] Data digitized and binned from A. R. Ravishankara (NOAA/Aeronomy Laboratory, personal communication).

Table A.1. APL radiative transfer model input molecular data (continued)

Photolysis Process	Cross Section	Quantum Yield
$ClNO_2$ $-h\nu\rightarrow$ $Cl + NO_2$	*DeMore et al.* [1997]	1
$ClONO$ $-h\nu\rightarrow$ $Cl + NO_2$	*DeMore et al.* [1997]	1
$ClONO_2$ $-h\nu\rightarrow$ $Cl + NO_3$	*DeMore et al.* [1997]	*DeMore et al.* [1997]
$ClONO_2$ $-h\nu\rightarrow$ $ClO + NO_2$	*DeMore et al.* [1997]	*DeMore et al.* [1997]
CCl_4 $-h\nu\rightarrow$ Products	*DeMore et al.* [1997]	1
CCl_3F $-h\nu\rightarrow$ Products	*DeMore et al.* [1997]	1
CCl_2F_2 $-h\nu\rightarrow$ Products	*DeMore et al.* [1997]	1
$CF_2ClCFCl_2$ $-h\nu\rightarrow$ Products	*DeMore et al.* [1997]	1
CF_2ClCF_2Cl $-h\nu\rightarrow$ Products	*DeMore et al.* [1997]	1
CF_3CF_2Cl $-h\nu\rightarrow$ Products	*DeMore et al.* [1997]	1
CCl_2O $-h\nu\rightarrow$ Products	*DeMore et al.* [1997]	1
$CClFO$ $-h\nu\rightarrow$ Products	*DeMore et al.* [1997]	1
CF_2O $-h\nu\rightarrow$ Products	*DeMore et al.* [1997]	1
CH_3Cl $-h\nu\rightarrow$ Products	*DeMore et al.* [1997]	1
CH_3CCl_3 $-h\nu\rightarrow$ Products	*DeMore et al.* [1997]	1
$CHClF_2$ $-h\nu\rightarrow$ Products	*DeMore et al.* [1997]	1
CH_3CF_2Cl $-h\nu\rightarrow$ Products	*DeMore et al.* [1997]	1
CF_3CHCl_2 $-h\nu\rightarrow$ Products	*DeMore et al.* [1997]	1
CF_3CHFCl $-h\nu\rightarrow$ Cl + Products	*DeMore et al.* [1997]	1
CH_3CFCl_2 $-h\nu\rightarrow$ Products	*DeMore et al.* [1997]	1
$CF_3CF_2CHCl_2$ $-h\nu\rightarrow$ Products	*DeMore et al.* [1997]	1
CF_2ClCF_2CHFCl $-h\nu\rightarrow$ Products	*DeMore et al.* [1997]	1
CH_3OCl $-h\nu\rightarrow$ Products	*DeMore et al.* [1997]	1
Br_2 $-h\nu\rightarrow$ $Br + Br$	*Maric et al.* [1994]	1
BrO $-h\nu\rightarrow$ $Br + O(^3P)$	*DeMore et al.* [1997]	1

Table A.1. APL radiative transfer model input molecular data (continued)

Photolysis Process	Cross Section	Quantum Yield
$HOBr \xrightarrow{h\nu} OH + Br$	*Sander et al.* [2000]	1
$BrONO_2 \xrightarrow{h\nu} BrO + NO_2$	*DeMore et al.* [1997]	*DeMore et al.* [1997]
$BrONO_2 \xrightarrow{h\nu} Br + NO_3$	*DeMore et al.* [1997]	*DeMore et al.* [1997]
$BrCl \xrightarrow{h\nu} Br + Cl$	*DeMore et al.* [1997]	1
$CH_3Br \xrightarrow{h\nu}$ Products	*DeMore et al.* [1997]	1
$CHBr_3 \xrightarrow{h\nu}$ Products	*DeMore et al.* [1997]	1
$CF_3Br \xrightarrow{h\nu}$ Products	*DeMore et al.* [1997]	1
$CF_2Br_2 \xrightarrow{h\nu}$ Products	*DeMore et al.* [1997]	1
$CF_2BrCF_2Br \xrightarrow{h\nu}$ Products	*DeMore et al.* [1997]	1
$CF_2ClBr \xrightarrow{h\nu}$ Products	*DeMore et al.* [1997]	1
$CF_3I \xrightarrow{h\nu} CF_3 + I$	*DeMore et al.* [1997]	1
$SO_2 \xrightarrow{h\nu}$ Products	MODTRAN[e]	1
$OCS \xrightarrow{h\nu} CO + S$	*DeMore et al.* [1997]	1

[e]Derived from the MODTRAN radiative transfer model [*Berk et al.*, 1989].

POLARIS and IPMMI

During POLARIS and IPMMI, the ozone cross sections of *Molina and Molina* [1986] were used over 185.2–345.0 nm, with those of *WMO* [1986] at shorter and longer wavelengths. Since the JPL00 supplement had not been released before the these campaigns, the quantum yield for $O_3 \rightarrow O(^1D)$ was that recommended in JPL97.

A.3.2 Extraterrestrial Flux

The starting point for any radiative transfer model in Earth's atmosphere is the solar irradiance incident on the top of the atmosphere.

SOLVE

The APL model derives its extraterrestrial flux from a number of sources: 175.4–200.0 nm (*WMO* [1986]), 200.0–407.8 nm (ATLAS-3[2]), 407.8–419.9 nm (ATLAS-2[2]), 419.9–800.0 nm (MODTRAN[2]), and 800–850 nm (MODTRAN[3]).

As Earth's orbit is not exactly circular, the Earth–Sun distance varies over the course of a year, resulting is a solar flux variation of $\pm 3.5\%$. The model scales the flux to account for the day of year [*Madronich*, 1993].

POLARIS and IPMMI

The solar flux from MODTRAN[3] was used for the entire wavelength range during POLARIS and IPMMI.

[2]From B. Mayer (German Aerospace Center), in the `atlas_plus_modtran` file in A. Kylling's (Norwegian Institute for Air Research) LibRadtran v0.14 model. For a current version of the model, see `http://www.libradtran.org`.

[3]From the high-resolution `sun2` file in the MODTRAN3 distribution [*Berk et al.*, 1989]. See also `http://www2.bc.edu/~sullivab/soft/modtran4.html`.

A.3.3 Atmospheric Profiles

The model utilizes the 1976 U. S. Standard Atmosphere [*COESA*, 1976] profiles of temperature and pressure as a basic atmosphere. In most instances, however, application-specific profiles are known and substituted (see individual chapters for profiles used in IPMMI, POLARIS, and SOLVE).

A.3.4 Wavelength Binning

The model considers photons in individual wavelength bins.

SOLVE

The SOLVE version of the model divides the spectrum into: 175–295 nm (500-cm^{-1} bins), 295–330 nm (0.5-nm bins), 330–347.5 nm (2.5-nm bins), 347.5–427.5 nm (5-nm bins), and 427.5–852.5 nm (10-nm bins) wavelength regimes. This approach allows for fine resolution where the magnitudes of the solar flux and key cross sections are changing rapidly with wavelength [*Madronich and Weller*, 1990], while limiting the total number of wavelength bins that must be calculated.

POLARIS

The POLARIS version of the model used the following wavelength regimes: 175–298 nm (500-cm^{-1} bins),[4] 298–320 nm (0.5-nm bins), and 320–850 nm (5-nm).

[4] *Swartz et al.* [1999] erroneously reported 50-cm^{-1} bins at 175–295 nm.

Table A.2. Geophysical thresholds triggering scattering matrix recalculation along flight tracks

Geophysical Parameter	Threshold
In situ temperature (°C)	5.0°
Total column ozone (Dobson units)	5.0
Cloud top height (km)	0.5
Cloud fraction (%)	5.0
Terrain height (km)	0.5
Surface reflectivity (%)	2.0
Solar zenith angle	0.5° (SZA>90°)–20° (SZA=0°)
Maximum number of steps without recalculation	100

IPMMI

The IPMMI version of the model, since spectral flux comparisons were to be made at 1-nm resolution, was run at: 175–204 nm (500-cm^{-1} bins) and 204–852.5 nm (0.5-nm bins). Adjacent bins were summed to produce flux on a 1-nm grid.

A.4 *j*-Values along Flight Tracks

The direct component of the attenuated solar flux always uses measured geophysical conditions at every point along the flight track. Geophysical conditions continuously change along aircraft flight tracks, but since it is computationally expensive to recalculate the scattering properties of the atmosphere, the model attempts to strike a balance between speed and accuracy. Along the flight track, the model reports *j*-values at any time resolution, but the scattering matrix (see section A.2) is recalculated only if conditions change by more than certain threshold amounts, shown in Table A.2. The scattering matrix is recalculated after at most 100 *j*-value calculations. The scattering properties are then interpolated between each recalculation for each of the intervening *j*-value computations.

Appendix B

Supplemental IPMMI Information

This appendix supplements the IPMMI material in chapter 2.

B.1 $j_{\mathbf{NO_2}}$

Figures B.1–B.3 show comparisons of the UMD and NCAR j_{NO_2} chemical actinometers for June 15, 18, and 19, 1998.

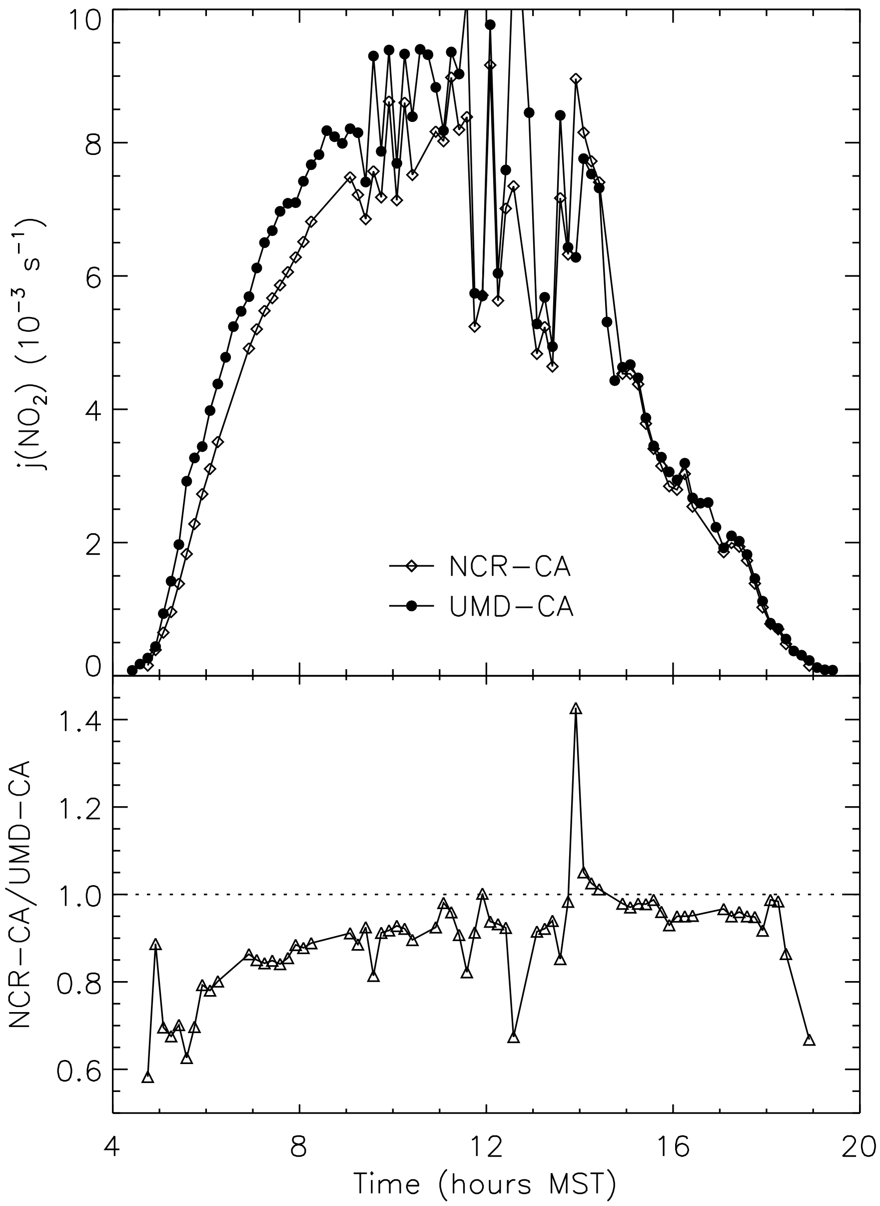

Figure B.1. Comparison of UMD and NCAR actinometer measurements of j_{NO_2} for June 15 (10-min data).

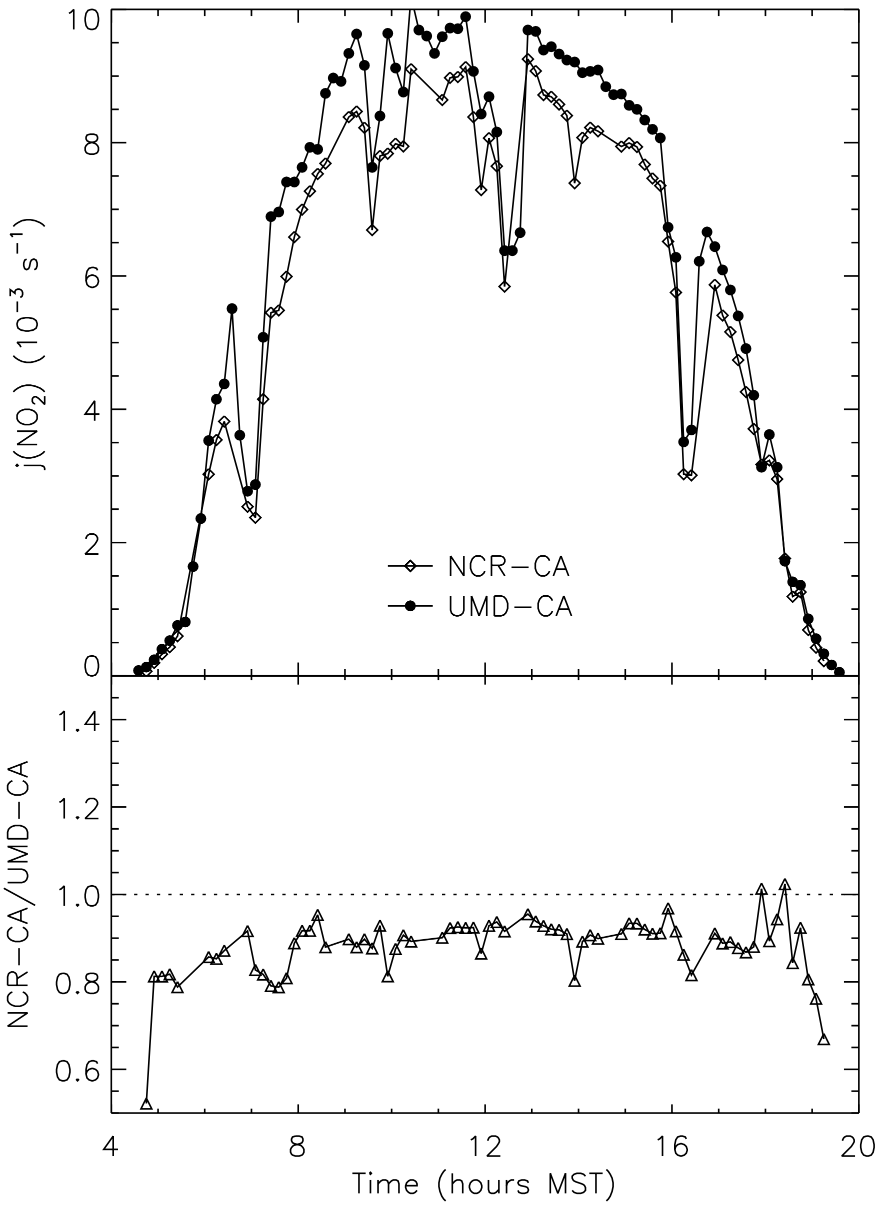

Figure B.2. Comparison of UMD and NCAR actinometer measurements of j_{NO_2} for June 18 (10-min data).

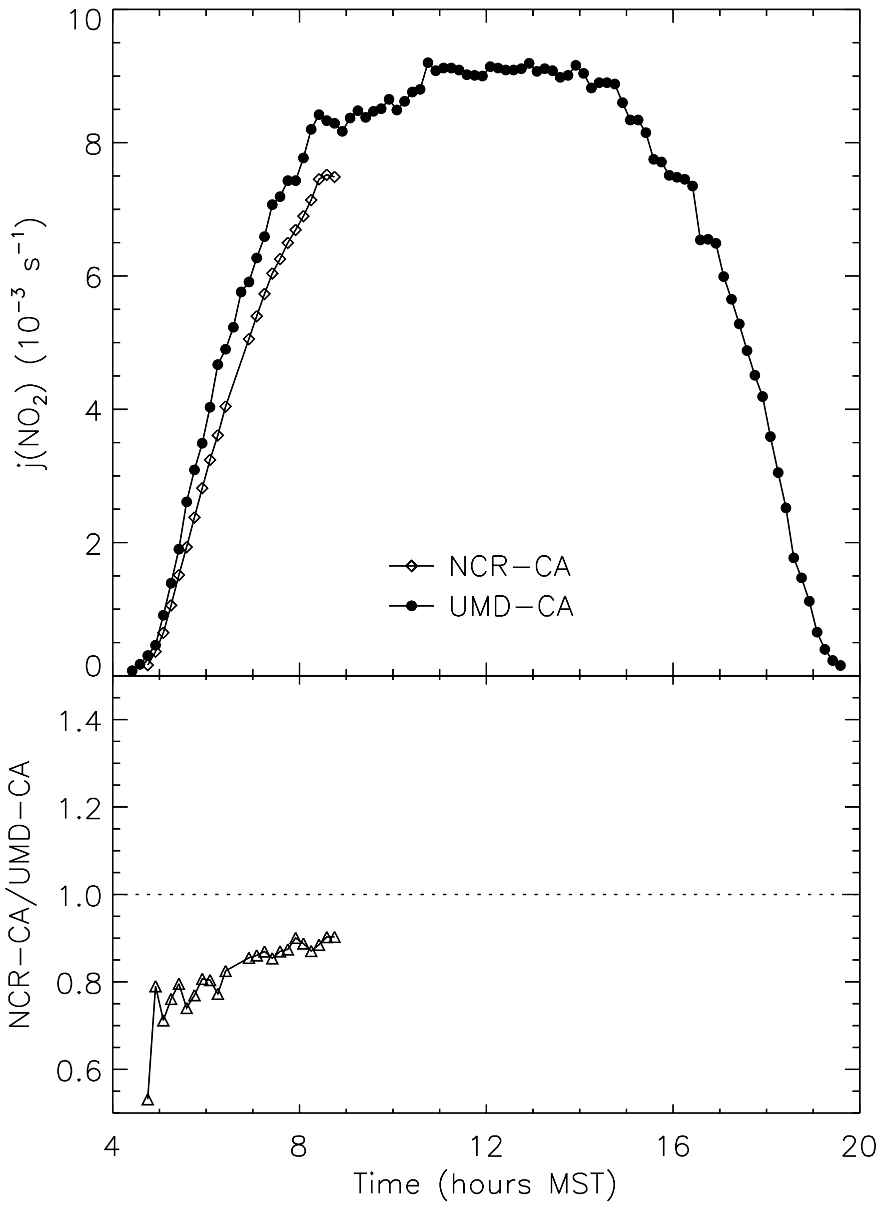

Figure B.3. Comparison of UMD and NCAR actinometer measurements of j_{NO_2} for June 19 (10-min data).

B.2 j_{O_3}

Table B.1 summarizes the j_{O_3} instruments used during IPMMI.

Figure B.4 shows the modeled temperature dependence of j_{O_3} on the surface temperature, at 1.8 km, reflecting the combined effects of the temperature dependencies of the ozone cross sections [*Molina and Molina*, 1986] and quantum yields [*DeMore et al.*, 1997]. Two solar zenith angles (SZAs) were chosen: 16.5° (noon on June 19) and 65°. The wavelength dependence of O_3 photolysis shifts to longer wavelengths at greater SZAs (see Figure 1.2). *Blackburn et al.* [1992] and *Dickerson et al.* [1982] measured the temperature dependence of j_{O_3} actinometrically at 19° and 65° SZA, respectively. Their results are consistent with that in Figure B.4.

Table B.1. j_{O_3} instruments participating in IPMMI[a]

Instrument/Institution	Technique[b]	Determination	IPMMI ID
Chemical Actinometer			
National Center for Atmospheric Research	Flow tube/$HNO_{3(aq)}$ detection	j_{O_3}	NCAR
Spectroradiometers			
Institut für Atmosphärische Chemie, Forschungszentrum, Jülich (Germany)	Double MC/PMT	Actinic flux	FZJ
Meteorologie Consult, Glashütten (Germany)	Double MC/PMT	Actinic flux	MET1
Meteorologie Consult, Glashütten (Germany)	Single MC/PDA	Actinic flux	MET2
National Center for Atmospheric Research	Double MC/PMT	Actinic flux	NCAR
University of Leicester (United Kingdom)	Single MC/PDA	Actinic flux	ULI
National Institute of Water and Atmospheric Research, Lauder (New Zealand)	Double MC/PMT	Irradiance	NIWA
Filter Radiometers			
Institut für Atmosphärische Chemie, Forschungszentrum, Jülich (Germany)	Filter/PMT	Broadband j_{O_3}	FZJ
Fraunhofer Institut für Atmosphärische Umweltforschung, Garmisch-Partenkirchen (Germany)	Filter/PMT	Broadband j_{O_3}	IFU
Meteorologie Consult, Glashütten (Germany)	Filter/PMT	Broadband j_{O_3}	MET
University of Leicester (United Kingdom)	Filter/PMT	Broadband j_{O_3}	ULI

[a]Other instrument details reported by *Cantrell et al.* [2002], *Bais et al.* [2002], *Shetter et al.* [2002], and *Hofzumahaus et al.* [2002].

[b]MC = monochromator, PDA = photodiode array, PMT = photomultiplier tube.

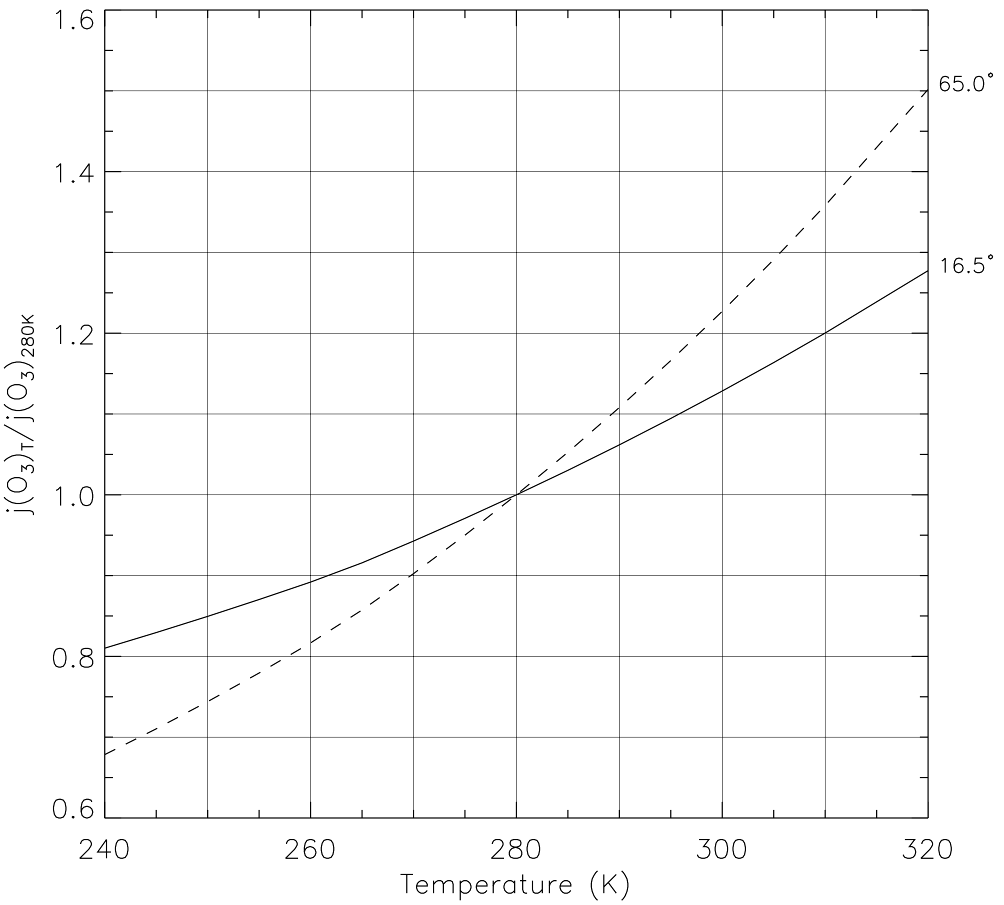

Figure B.4. Temperature dependence of j_{O_3} at the surface (1.8 km). Two solar zenith angles are shown: 16.5° (noon on June 19) and 65°.

B.3 IPMMI: Epilogue

While the execution of IPMMI in general went very smoothly, there were a number of shortcomings (mostly minor) that organizers of future intercomparisons should consider.

Communication. The misunderstandings surrounding the specification of the aerosol parameters used in the modeling effort highlight a fundamental deficiency in the communication before, during, and after the intercomparison. Information was distributed in hardcopy, by e-mail, by e-mail attachment, and by website not entirely consistently (and differently between the measurement and modeling portions of the campaign). Some data were stored on the website, others were not, some were in different forms in different places.

Having an agreed-upon and strictly enforced standard for data handling in effect during all phases of the intercomparison would improve communication. For example, in addition to the referees, there should be an individual that maintains a website/ftp site with all of the data, protocols, meetings notes, plans for publications, etc. E-mails could still be used for discussion and to remind participants of new information on the website, but the website itself should be the only authorized source of intercomparison information.

Measurement–modeling standardization. The author was the only IPMMI participant who was officially involved in both the measurement and modeling portions of the intercomparison and thus had perhaps a unique view on both exercises. While it was necessary for the measurement and modeling analyses to be separate (especially with two independent referees), greater coordination and standardization would have been helpful. For example, the measurement campaign was done completely in Mountain

Daylight Time, while the modeling was done in Mountain Standard Time. Further, the measurements were reported in time intervals referenced to the beginning of the interval (e.g., 1-min at 10:00, 10:00–10:01; 10-min at 10:00, 10:00–10:10; 30-min at 10:00, 10:00–10:30); the modeling data were referenced to what was in essence the middle of the intervals (e.g., 10:05, 11:05). When modelers incorporated ancillary measurement data, some care had to be taken to be sure exactly what the timescale meant.

Data format. All the primary IPMMI data were collected and distributed as Microsoft Excel files. This meant that in order to submit or use IPMMI results, the participant had to use MSExcel. Simple ASCII text files would be far superior, allowing rapid incorporation into just about any data analysis program, including MSExcel (and would be more readily archived). For those using software other than MSExcel, each individual data file had to be translated manually, which was laborious, with many MSExcel files containing many different datasets, and more error-prone.

Degrees of blindness and independence. A fundamental element of IPMMI was that it was a *blind* intercomparison, meaning that the experimentalists and modelers submitted data independently and with no knowledge of what other participants were finding and submitting. In some respects, this was not always strictly the case. For example, the author participated in both the measurement and modeling efforts. Also, the organizers, one of the referees, and key participants were all from NCAR and thus enjoyed something of a home court advantage. The NCAR j_{NO_2} and j_{O_3} actinometers and spectroradiometer were operated by the same group and had been operating side-by-side together at the Marshall Field Site for some time prior to the start of IPMMI. This should not be construed as a criticism in any way. The community should be grateful that the NCAR researchers were willing and able to create and coordinate IPMMI in the first place. It should be borne in mind, however, that others of the participants had to ship their instruments long distances, even from Europe and Australia, and had a limited amount of time to assemble and stabilize their instruments, which created additional challenges that the native instruments avoided.

In the modeling portion of IPMMI, several of the models used were the same or essentially the same. Some modelers submitted multiple datasets using related packages. The different modeling results should therefore not be viewed as entirely independent either.

Appendix C

Supplemental POLARIS Information

This appendix supplements the POLARIS material in chapter 3.

There were 19 ER-2 science flights during three deployments in Fairbanks, Alaska (65°N, 148°W), in April–May, June–July, and September 1997 and one aborted science flight, plus seven transit flights both to and from NASA/Ames in California and to Barber's Point, Hawaii, and a survey flight south from Hawaii. These 28 flights are summarized in Table C.1. Figure C.1 illustrates the actual flight tracks taken in each flight.

Table C.1. POLARIS ER-2 flight summary

Flight Date	Latitude (°N)	Solar Zenith Angle (°)	Temperature (K)
19970424[a]	37.7–66.3	40.9–53.4	208.4–227.4
19970426	65.1–89.9	55.4–76.3	215.0–228.7
19970430[b]	63.7–65.3	74.4–101.1	218.6–230.9
19970502	65.3–70.9	54.7–65.8	225.8–230.9
19970506	64.9–78.6	53.0–62.2	225.0–234.5
19970509	64.1–64.8	78.4–97.8	222.7–231.0
19970511[c]	61.6–64.3	44.1–54.7	222.9–233.5
19970513	65.3–84.9	54.5–67.1	225.5–234.2
19970515[a]	36.7–65.2	32.1–58.3	208.3–261.6
19970623[a]	37.8–64.5	27.9–41.3	210.7–227.8
19970626	54.9–77.1	40.8–56.3	211.7–230.3
19970629	48.4–64.5	33.4–56.4	212.7–227.0
19970630	62.6–67.1	39.8–47.3	213.8–228.0
19970704	47.7–71.1	26.7–56.6	217.3–229.8
19970707	64.9–89.9	53.4–67.4	220.2–232.7
19970710	63.2–66.5	41.1–49.0	219.9–229.3
19970712[a]	36.7–66.0	31.9–58.4	209.5–296.5
19970902[a]	37.4–65.0	32.4–58.0	210.0–292.0
19970908	65.3–86.0	67.7–83.9	218.3–228.3
19970910[d]	64.4–64.8	77.6–83.5	216.9–227.0
19970911	64.3–64.8	77.7–99.9	216.9–226.7
19970914	64.2–64.8	68.5–102.6	213.6–221.1
19970915	64.3–64.8	68.5–103.2	213.0–221.8
19970918	65.1–89.9	72.8–88.4	218.8–227.4
19970919	64.3–64.8	63.1–81.7	221.4–228.1
19970921[e]	22.3–64.1	35.6–72.9	200.9–231.0
19970923[f]	-3.4–20.9	0.2–65.3	194.1–234.3
19970925[g]	21.4–36.7	30.8–68.2	196.1–235.4

[a]Transit flight.

[b]CPFM data not available, so only APL_{TOMS} was calculated.

[c]Excluded from model–measurement comparison in Figure 3.10, for consistency with those of *Del Negro et al.* [1999].

[d]Flight aborted.

[e]Transit to Barber's Point, Hawaii.

[f]Survey flight south from Hawaii.

[g]Return transit from Hawaii to NASA/Ames.

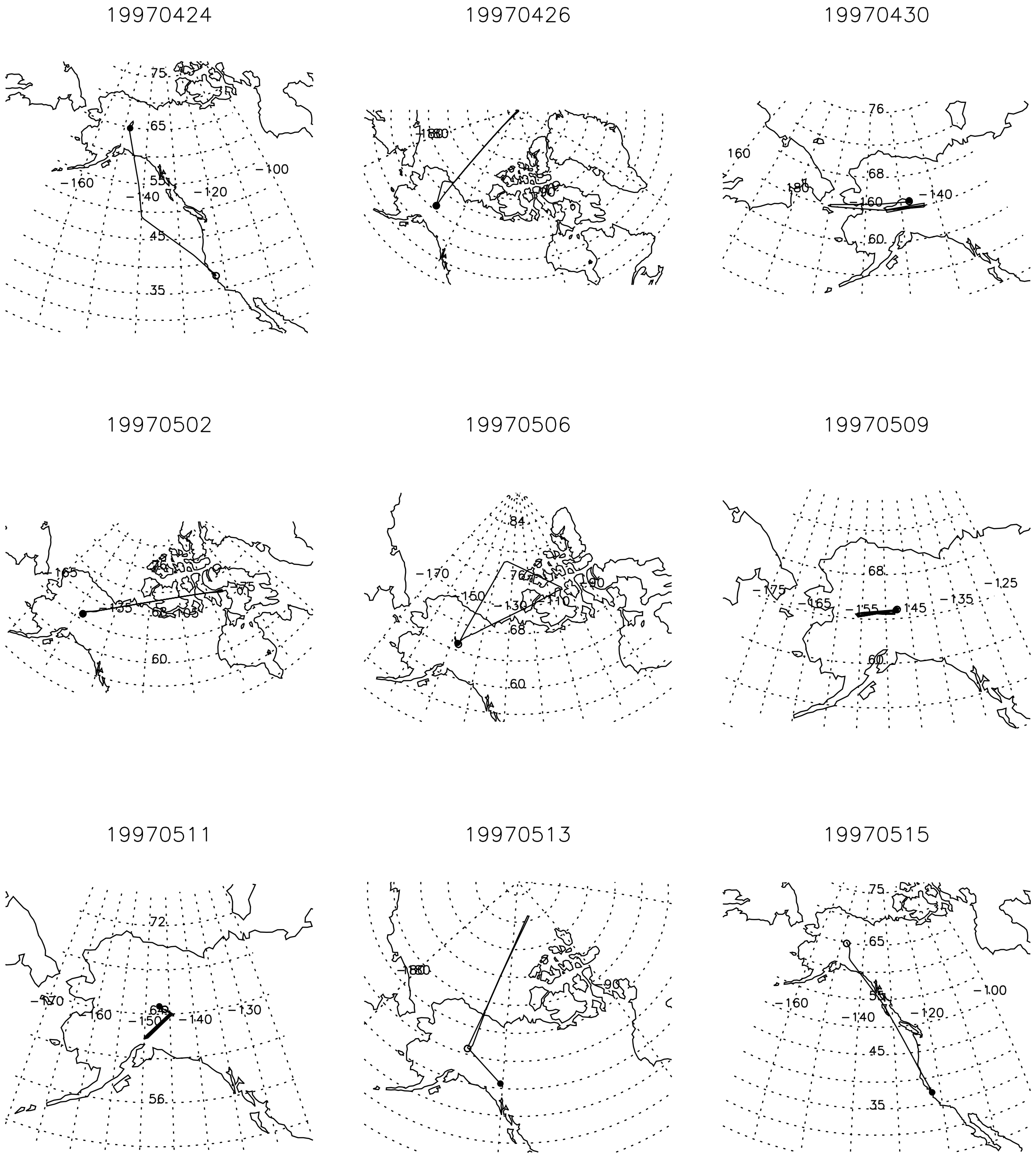

Figure C.1. POLARIS ER-2 flight tracks. The flight track from each ER-2 transit or science flight for the date indicated at the top of each map is shown. The open (○) and filled (•) circles indicate the beginning and end of each flight, respectively. For the science flights, both circles lie at the same place: Fairbanks, Alaska (65°N, 148°W).

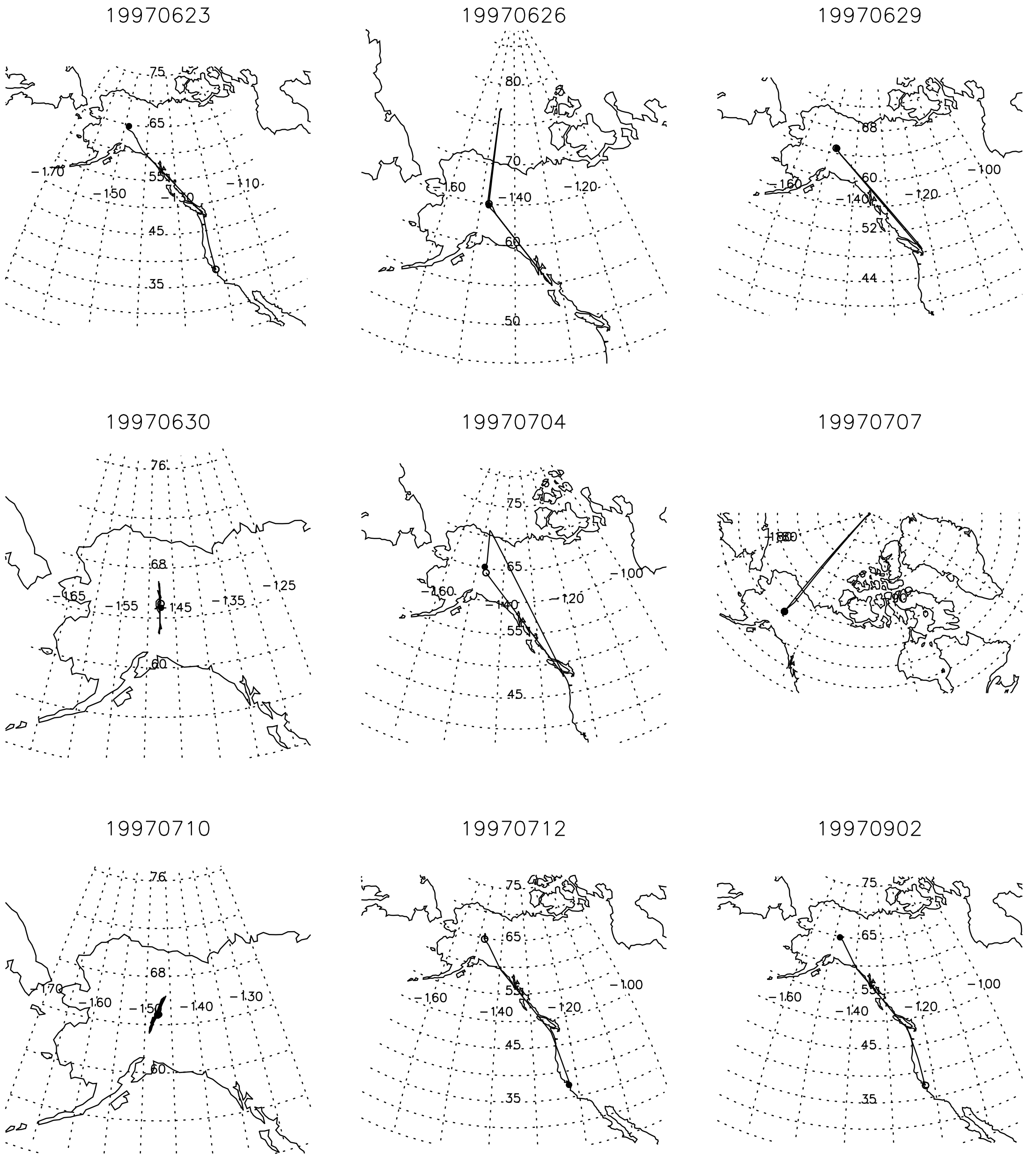

Figure C.1. POLARIS ER-2 flight tracks (continued).

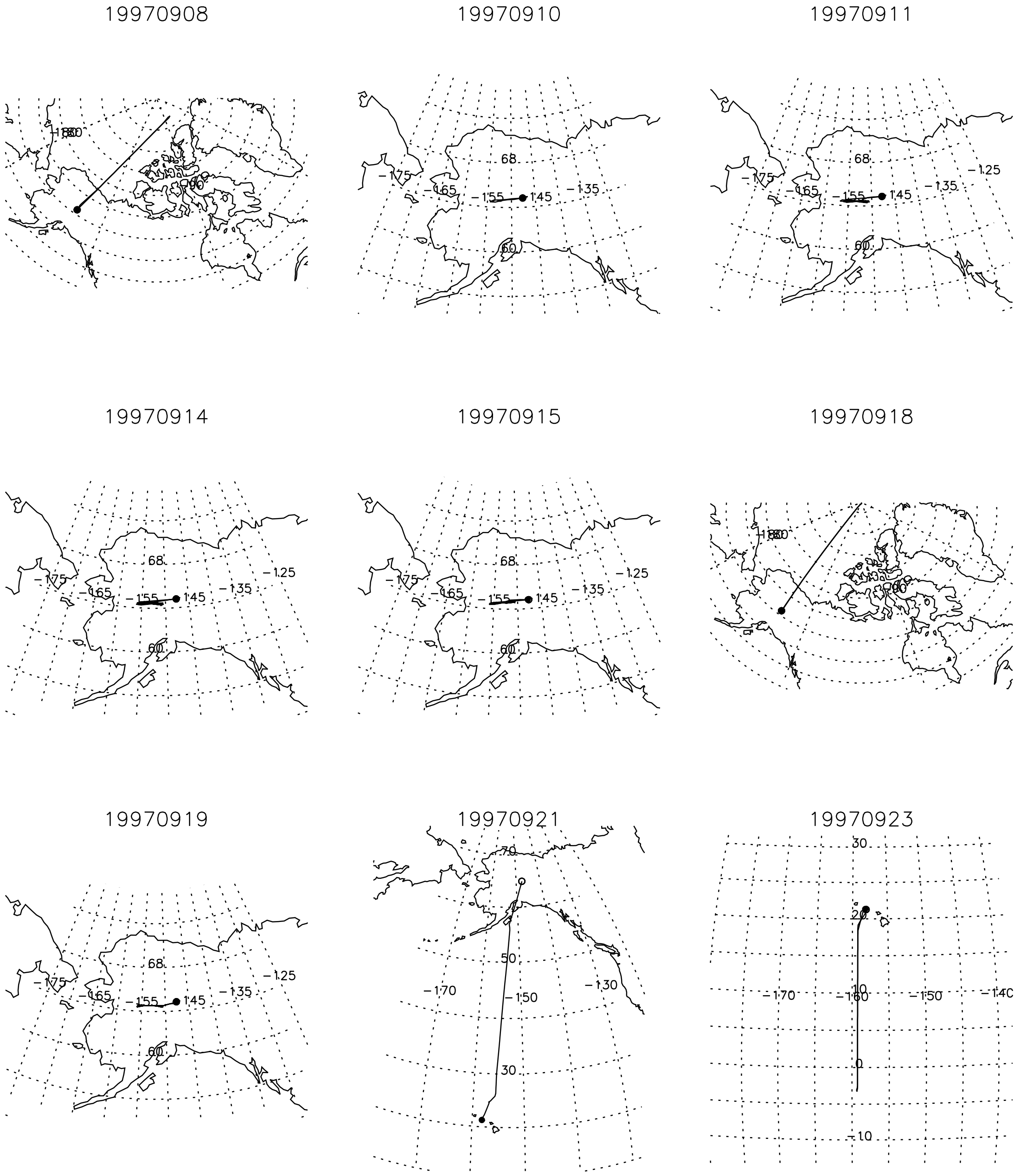

Figure C.1. POLARIS ER-2 flight tracks (continued).

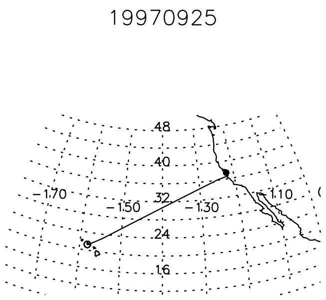

Figure C.1. POLARIS ER-2 flight tracks (continued).

Appendix D

Supplemental SOLVE Information

This appendix supplements the SOLVE material in chapters 4 and 6.

D.1 DC-8 Flight Track Information

There were 17 DC-8 science flights during three deployments in Kiruna, Sweden (68°N, 20°E), in November–December 1999, January 2000, and February–March 2000, the latter two coinciding with the ER-2 intensives. These, with a total of six transit flights, are listed in Table D.1. Figure D.1 shows the DC-8 flight tracks.

Table D.1. SOLVE DC-8 flight summary

Flight Date	Latitude (°N)	Solar Zenith Angle (°)	Temperature (K)
19991130[a]	35.8–78.1	89.3–132.5	206.9–266.0
19991202	63.1–79.6	89.2–108.7	213.1–236.0
19991205	62.0–80.7	86.2–108.6	209.1–232.3
19991207	68.5–85.7	91.7–122.5	205.1–234.6
19991210	67.5–82.8	92.8–114.8	210.6–235.0
19991212	67.9–81.3	91.4–125.5	205.4–234.3
19991214	59.6–69.0	86.3–107.7	210.7–233.0
19991216[a]	35.4–78.2	59.7–105.2	210.3–267.0
20000114[a]	35.6–78.2	83.3–130.0	206.9–263.1
20000116	60.2–82.0	82.8–109.3	201.2–243.9
20000120	62.2–89.3	85.3–113.8	206.5–227.7
20000123	58.6–73.8	78.1–111.7	199.0–242.5
20000125	59.4–75.9	78.5–111.2	199.1–247.6
20000127	51.5–67.1	74.1–118.1	207.1–230.6
20000129[a]	36.0–78.2	55.7–101.1	207.0–257.1
20000227[a]	35.4–78.2	46.8–111.2	200.0–255.3
20000303	60.7–86.5	83.9–117.4	202.9–237.9
20000305	63.8–79.4	74.3–115.0	203.7–229.5
20000308	63.1–80.2	68.0–101.6	196.1–234.9
20000309	57.4–80.1	80.3–118.4	201.4–237.3
20000311	67.6–80.1	73.3–111.1	198.6–234.5
20000313	65.1–83.9	81.7–114.0	206.0–243.5
20000315[a]	47.9–86.3	84.0–103.7	204.6–255.7

[a]Transit flight.

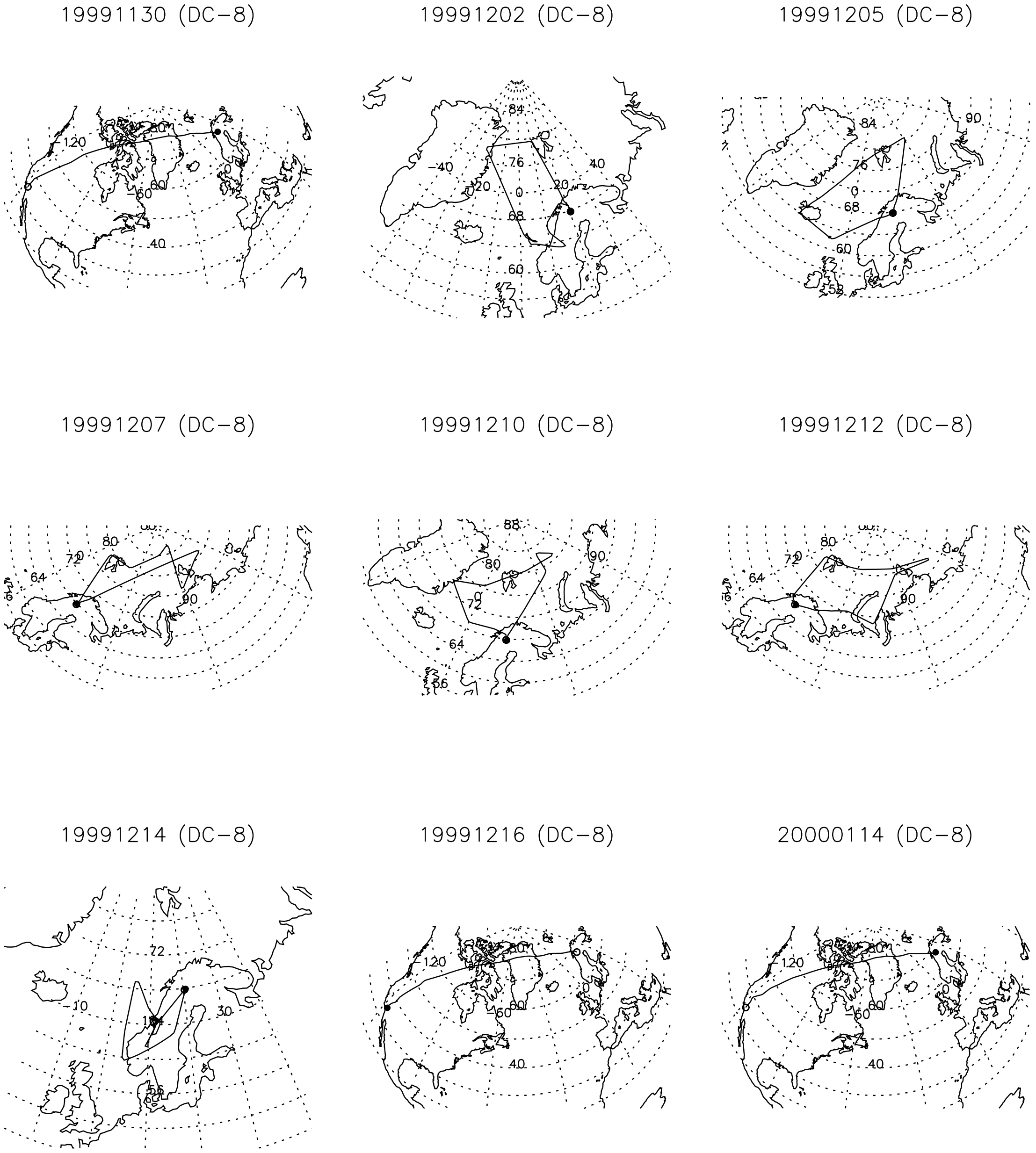

Figure D.1. SOLVE DC-8 flight tracks. The flight track from each DC-8 transit or science flight for the date indicated at the top of each map is shown. The open (○) and filled (•) circles indicate the beginning and end of each flight, respectively. For the science flights, both circles lie at the same place: Kiruna, Sweden (68°N, 20°E).

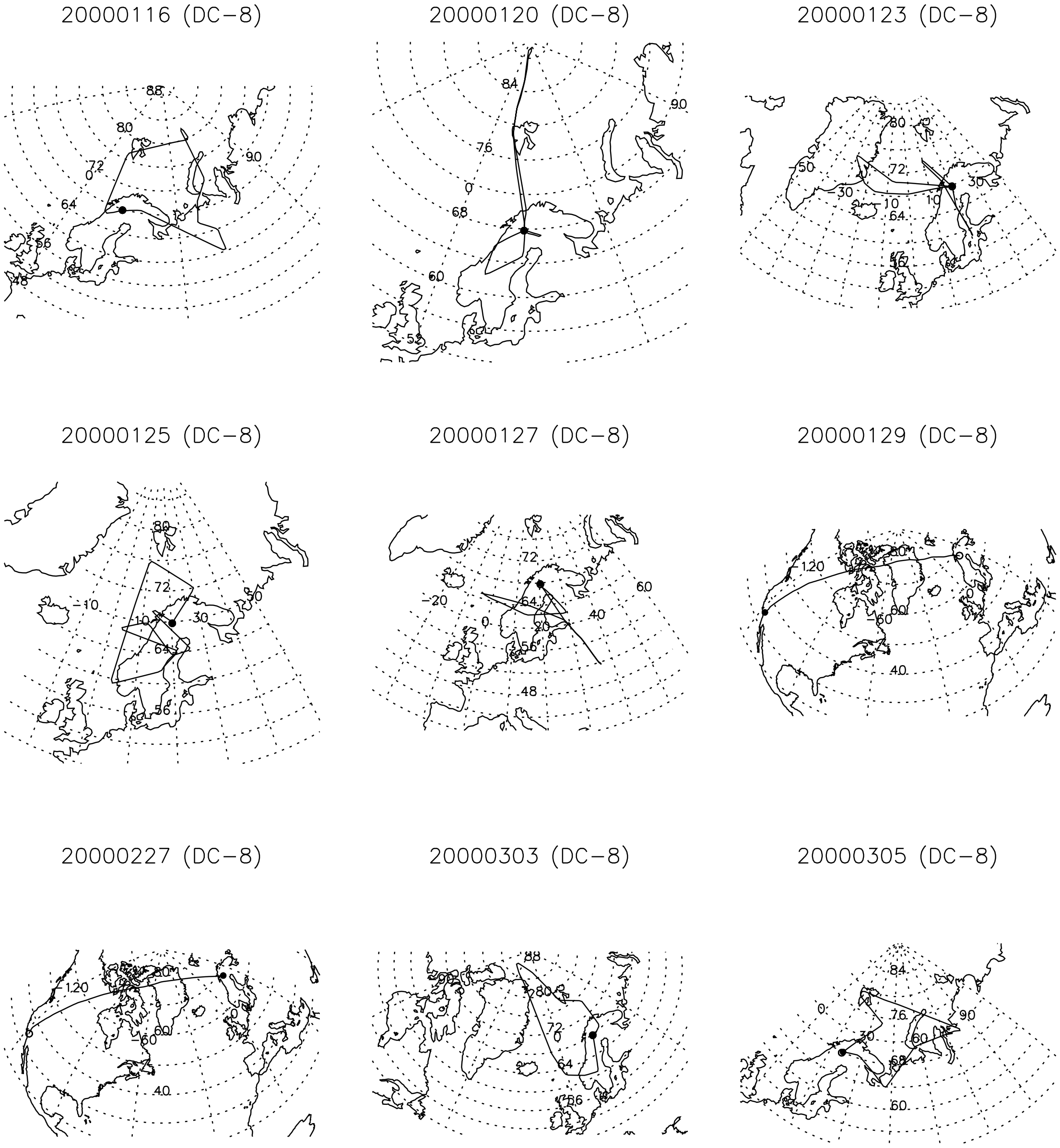

Figure D.1. SOLVE DC-8 flight tracks (continued).

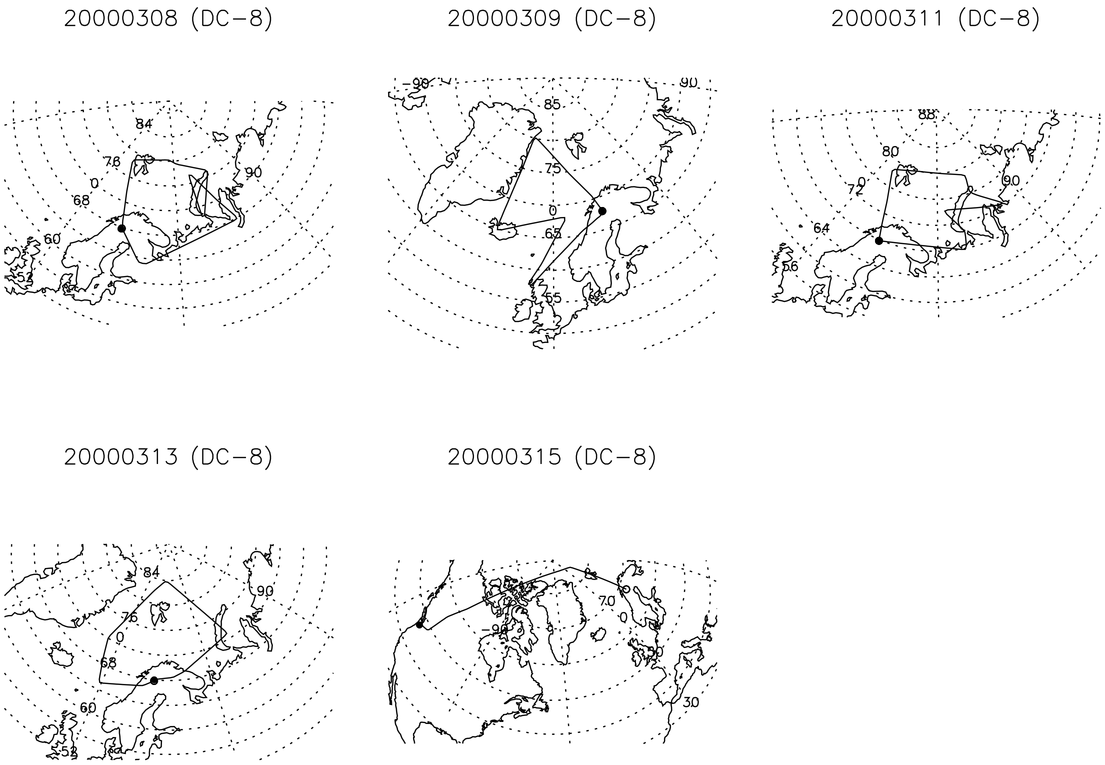

Figure D.1. SOLVE DC-8 flight tracks (continued).

D.2 ER-2 Flight Track Information

There were 11 ER-2 science flights spanning two deployments during SOLVE, in January–February and February–March 2000, plus two transit flights (with a stop-over in Westover, Massachusetts) both to and from NASA's Dryden Research Center in California. These 15 flights are summarized with descriptions of each flight in Table D.2. Figure D.2 illustrates the actual flight tracks taken in each flight.

Table D.2. SOLVE ER-2 flight summary

Flight Date	Latitude (°N)	Solar Zenith Angle (°)	Temperature (K)	Description[a]
20000109	34.9–42.0	63.7–86.9	208.0–226.1	Transit across U.S.
20000114	42.6–71.7	79.1–122.5	194.6–230.1	Transit from Westover, Massachusetts.
20000120	65.3–89.1	85.9–110.8	189.7–213.7	Sunset flight into dark vortex (to North Pole). Extensive PSCs north of Spitsbergen. Vortex well-mixed. Denitrification, but little dehydration. Active chlorine as ClO or ClOOCl.
20000123	58.8–73.8	78.3–97.7	191.0–204.3	Sunrise vortex flight over Scandinavia. PSCs north of Kiruna.
20000127	51.5–67.3	74.3–95.8	191.1–212.0	Russia flight. Flew through edge of vortex. Elevated ClO and ClOOCl inside, but not out.
20000131	68.2–79.0	86.1–96.6	191.0–214.6	Vortex survey (towards North Pole).
20000202	64.2–77.8	82.3–102.5	191.0–208.5	Sunset warm (no PSC)/cool (PSC) vortex flight to Russia then Spitsbergen.
20000203	68.0–73.2	118.0–127.9	191.3–206.6	"Stacked" vortex flight around Kiruna.
20000226	63.0–84.8	78.7–93.7	190.8–206.2	Vortex re-survey (daylight), near sunset. Very cold. PSCs noted on the horizon.
20000305	66.7–81.0	73.3–93.4	189.4–206.7	Russia flight. Vortex run toward sunset. Some PSCs. Chlorine activation and ozone loss.
20000307	67.9–82.9	77.8–88.9	192.7–209.0	Vortex survey. Ozone loss. Some PSCs. Midlatitude filament inside the vortex.
20000311	58.6–75.1	64.6–87.4	195.7–208.9	Scotland flight out of vortex. Ozone loss within.
20000312	65.3–79.5	71.2–91.4	194.8–211.0	Vortex survey, mostly above PSC temperature. Active chlorine. Ozone loss.
20000316	43.3–67.7	46.4–76.9	210.6–221.6	Transit to Westover.
20000318	35.1–42.2	36.0–57.5	205.6–227.0	Transit across U.S.

[a]Derived in part from the flight diary of SOLVE project scientist P. A. Newman (NASA/Goddard).

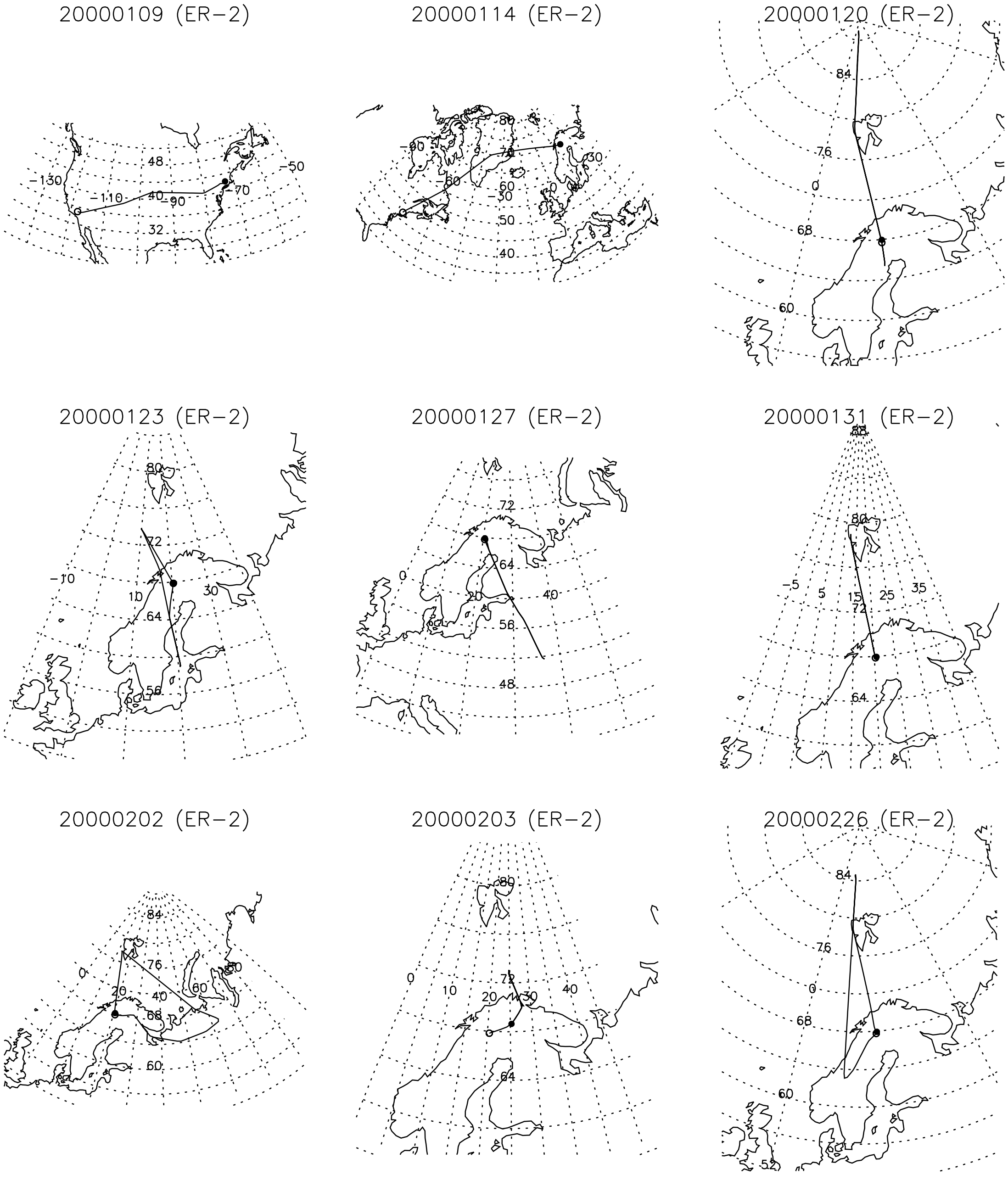

Figure D.2. SOLVE ER-2 flight tracks. Same as Figure D.1.

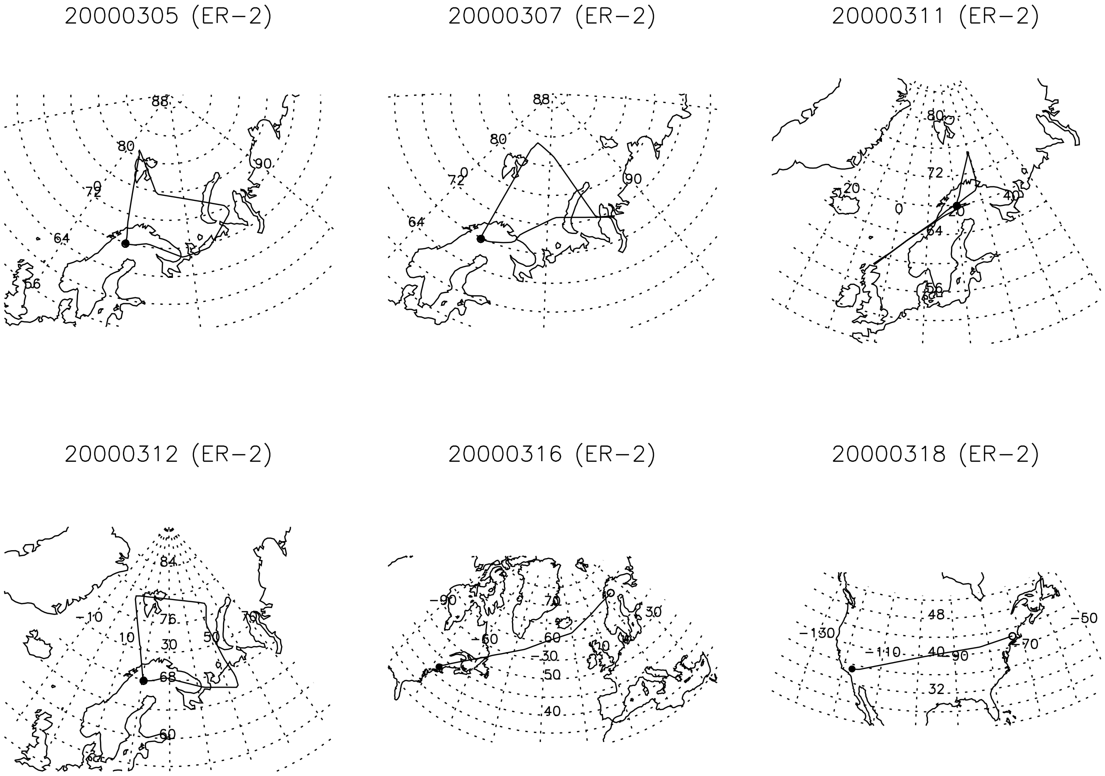

Figure D.2. SOLVE ER-2 flight tracks (continued).

Appendix E

SOLVE Detailed j-Value Modeling and Measurement Analysis

This appendix contains many of the details of how the APL model was applied during SOLVE (see chapters 4 and 6), but which lie outside the scope of the main body of the dissertation. A model–model comparison of j-values for the ER-2 is included, complementary to the DC-8 comparisons in section 4.5. There is also a series of tables of the correlations of the DC-8 and ER-2 j-value comparisons, as well as tables of comparisons and correlations of the model input data.

E.1 Detailed Description of the Application of the Model

The APL radiative transfer model was used in a number of different "modes" to simulate photolysis rate coefficients along the ER-2 and DC-8 flight tracks during SOLVE. The differences between the various j-value modes ($APL_{clim[*]}$, $APL_{TOMS[*]}$, $APL_{CPFM[*]}$, $APL_{POAM[*]}$) reflect how different model inputs were utilized.

E.1.1 Common Input Data and Climatologies, $APL_{clim[*]}$

Model inputs common to all the *j*-value modes include: (1) flight parameters, (2) in situ temperature, (3) initial ozone, pressure, and temperature profile climatologies, (4) terrain/cloud top heights, and (5) snow/ice climatology. APL_{clim} calculations relied on no additional or SOLVE-specific geophysical information.

Temperature and Pressure Climatologies

As a first-order estimate, temperature and pressure profile climatologies up to 60 km were compiled from National Centers for Environmental Prediction (NCEP) data [*Kalnay et al.*, 1996] from 1985 to 1999 in 10° latitude bands by month.[1] These profiles were supplemented with the U. S. Standard Atmosphere [*COESA*, 1976] above 60 km. Climatological profiles were interpolated to the exact date and location. Each temperature profile was then scaled so that the profile matched the observed in situ temperature at each point along the flight track and smoothly blended into the climatological (or POAM-modified) profile above and below the flight altitude.

Ozone Climatology

A climatology of ozone profiles covering 0–60 km altitude in 5° latitude bands by month was compiled using many years of SAGE II, HALOE, POAM II, and POAM III satellite data, supplemented with ozonesondes.[1] The U. S. Standard Atmosphere ozone profile was spliced onto the altitude layers above the climatology (60–120 km). Occasionally, data for the lowestmost altitude layers were estimated. Data is typically available for latitude bands from the North Pole to 75°S; however, climatological data are relatively

[1]Climatologies compiled by S. Hollandsworth Frith and G. Labow (NASA/Goddard).

sparse at the highest latitude bands. For the high latitudes encountered during SOLVE, the climatology was based mainly on POAM III data and ozonesondes. Climatological profiles were interpolated to the exact date and latitude.

Cloud Climatology

The climatology for cloud top pressure and fractional cloud cover was based on the International Satellite Cloud Climatology Project (ISCCP) dataset, and provided climatological monthly averages over a 2.5° latitude × 2.5° longitude grid. For consistency, the cloud climatology was the same as used in the TOMS version 7 retrieval algorithm (see *McPeters et al.* [1998]). No *j*-values were reported below the climatological cloud top height.

Terrain Data

The surface pressure for topography and terrain type were defined by a standard geographic terrain model from the NOAA/Geodetic Survey Division of Canada on a 0.5° latitude × 0.5° longitude grid. For consistency, the surface terrain data were the same as used in the TOMS version 7 retrieval algorithm [*McPeters et al.*, 1998]. Pressures were converted to equivalent geometric altitude using the climatological pressure profiles. Probabilities of snow/ice cover were collected by the Air Force Global Weather Center, as used by TOMS. These data provided a monthly snow/ice climatology on a 1° latitude × 1° longitude grid.

Composite Reflectivity

The surface, cloud, and "composite" or effective reflectivities (albedo) of the lower boundary of the atmosphere were all estimated. When only climatological reflectivity information was available, the following approach was adopted to handle surface reflectivity and cloud top/terrain heights. The surface reflectivity was determined by the terrain type: ocean (0.08), land (0.30), lowland (0.15), or snow/ice (0.80). The composite reflectivity, R, was then calculated as

$$R = R_{\mathrm{g}}(1 - CF) + 0.80CF, \tag{E.1}$$

where R_{g} is the reflectivity of the surface and CF is the climatological cloud fraction. The reflectivity of clouds was assumed to be 0.80. Two separate j-value calculations were then performed, one at the terrain height with a reflectivity R_{g} and another at the cloud top height with a reflectivity of 0.80. The cloud fraction was used to provide a weighted average of these two calculations, yielding total j-values. If the snow/ice climatology indicated that snow/ice was present, a modified surface reflectivity $R_{\mathrm{g}*}$,

$$R_{\mathrm{g}*} = R_{\mathrm{g}}(1 - SIF) + 0.80SIF, \tag{E.2}$$

where SIF is the snow/ice fraction, was used, consistent with the TOMS algorithm.

$\mathbf{APL_{clim*}}$

Like, $\mathrm{APL_{clim}}$, $\mathrm{APL_{clim*}}$ calculations were based on the various climatologies, but with the ozone profile scaled to match the in situ ozone and smoothly blending into the climatological profile above and below the aircraft altitude (see Figure E.1a).

E.1.2 $\mathbf{APL_{TOMS[*]}}$

The $\mathrm{APL_{TOMS[*]}}$ calculations utilized Earth Probe TOMS level 2 data for total column ozone and UV effective reflectivity as input.[2] Where Earth Probe TOMS level 2 data

[2] The author provided Earth Probe TOMS data along the flight track during SOLVE ("EP" files), including total column ozone and UV effective reflectivity, using TOMS data at NASA/Goddard. These

were available (when the SZA was $< 84°$ at the time of TOMS overpass near midday), the climatological ozone profile was scaled and the composite reflectivity and cloud fraction were replaced with the TOMS reflectivity and cloud fraction. TOMS model inputs specific to $APL_{TOMS[*]}$ include: (1) total ozone column, (2) cloud fraction, and (3) composite reflectivity (surface albedo).

Ozone Profile

In the case of APL_{TOMS*}, the climatological ozone profile was scaled so that the profile matched the observed in situ ozone concentration at each point along the flight track. The profile was scaled such that the local ozone blended smoothly into the climatological profile above and below the aircraft altitude. The APL_{TOMS} calculation did not incorporate in situ measurements.[3] The ozone profile was then scaled to also match TOMS total ozone (see Figure E.1b). The overhead and slant column ozone values were derived from the TOMS-scaled ozone profiles.

Composite Reflectivity

The TOMS UV effective reflectivity was taken as the composite reflectivity. If the composite reflectivity was less than or equal to 0.08, the baseheight was set to the terrain height with the observed reflectivity, assumed to be the surface reflectivity. If the reflectivity was greater than or equal to 0.80, the baseheight was set to the cloud top height, with the observed reflectivity, assumed to be the cloud reflectivity. If the reflectivity was between 0.08 and 0.80, two calculations were performed, one at the terrain height with a reflectivity of 0.08 and another at the cloud top height with a reflectivity of 0.80.

---

files are archived at `ftp://espoarchive.nasa.gov`.

[3]The "JT" files provided for SOLVE used the APL_{TOMS*} model mode.

The TOMS cloud fraction was used to provide a weighted average of these two calculations, yielding total *j*-values. If the snow/ice climatology used in the TOMS retrieval indicated that snow/ice was present, the reflectivities were recalculated accordingly (for more details, see *McPeters et al.* [1998]).

E.1.3 $\mathbf{APL_{CPFM[*]}}$

The $APL_{CPFM[*]}$ calculations (only along the ER-2 flight tracks) utilized CPFM data for partial column ozone above the ER-2 and 600-nm (575–625-nm mean) albedo as input. Where CPFM data were available, the climatological ozone profile was scaled and composite reflectivity replaced. CPFM-specific model inputs include: (1) partial ozone column above the ER-2 and (2) composite reflectivity (surface albedo).

Ozone Profile

In the case of APL_{CPFM*}, the climatological ozone profile was scaled so that the profile matched the observed in situ ozone concentration at each point along the flight track, using in situ ozone data. For APL_{CPFM}, no in situ scaling was performed.[4] Next, the ozone profile above the aircraft was scaled to match the CPFM overhead ozone column. Finally, the ozone profile was scaled to also match TOMS total ozone (if available) (see Figure E.1c). The slant column ozone values were derived from the CPFM/TOMS-scaled ozone profiles, with APL_{CPFM*} first scaled to match the in situ ozone.

[4]The “JU” files provided for SOLVE used the APL_{CPFM*} model mode.

Composite Reflectivity

The CPFM 600-nm albedo was taken as the composite reflectivity. If the composite reflectivity was less than or equal to 0.08, the cloud fraction was assumed to be 0 and the baseheight was set to the terrain height with the observed albedo, assumed to be the surface reflectivity. If the composite reflectivity was greater than or equal to 0.80, the cloud fraction was assumed to be 1 and the baseheight was set to the cloud top height with the observed albedo, assumed to be the cloud reflectivity. If the reflectivity was between 0.08 and 0.80, the cloud fraction, CF, defined as $CF = (\text{Composite Reflectivity} - 0.08)/0.72$, was computed and two calculations were performed, one at the terrain height with a reflectivity of 0.08 and another at the cloud-top height with a reflectivity of 0.80. The derived cloud fraction was used to provide a weighted average of these two calculations, yielding total j-values. If the snow/ice climatology used in the TOMS retrieval indicated that there was snow/ice present, the reflectivities were recalculated accordingly (for more details, see *McPeters et al.* [1998]).

E.1.4 $\mathbf{APL_{POAM[*]}}$

The $APL_{POAM[*]}$ calculations utilized POAM III satellite O_3–PV reconstructions [*Randall et al.*, 2002] of ozone profiles along the flight tracks as input. Pressure and temperature profiles were from the United Kingdom Meteorological Office (UKMO) analysis [*Swinbank and O'Neill*, 1994], as used in the ozone reconstruction.

Ozone Profile

The climatological ozone profile was replaced where POAM data were available (generally between 16 and 60 km). The APL_{POAM*} calculation was then scaled to match the in situ ozone (see Figure E.1d). For APL_{POAM}, no in situ scaling was performed.[5] The overhead and slant column ozone values were derived from the modified ozone profiles.

Composite Reflectivity

The composite reflectivity was based on TOMS data (where available) and treated exactly as in $APL_{TOMS[*]}$, described above.

E.2 Ozone Profile Scaling

The scaling of ozone profiles used as model input in this analysis was relatively complicated, so in order to make the process more transparent, an example is considered here, from the 20000311 ER-2 flight. The ozone profile changes continuously along the flight track, so we will focus on the profiles at 32757 s UT. Figure E.1 shows precisely how the ozone profiles were scaled in each of the model modes. In all cases, the climatological profile used by APL_{clim} was the basis for all subsequent manipulations. In Figure E.1a, this profile was scaled to match the in situ ozone measurement (APL_{clim*}), blending smoothly into the purely climatological profile. For APL_{TOMS} in Figure E.1b, the climatological profile was scaled to match the TOMS total ozone column. In the case of APL_{TOMS*}, this occurred after the profile was first scaled to match the in situ ozone. $APL_{CPFM[*]}$ in Figure E.1c benefited from the overhead ozone data derived from the CPFM.[6] APL_{CPFM*} was first scaled to the in situ ozone, then the overhead ozone of $APL_{CPFM[*]}$ were scaled to match the CPFM measurement. Since TOMS data were

[5] The "JP" files provided for SOLVE used the APL_{POAM} model mode.

[6] C. T. McElroy et al. retrieved the slant ozone column (or the integrated ozone density along the light path to the Sun) and then reported the overhead *vertical* ozone column along with an airmass factor based on an assumed ozone profile. The derived vertical column was used to adjust the climatological ozone profiles in the $APL_{CPFM[*]}$ modes.

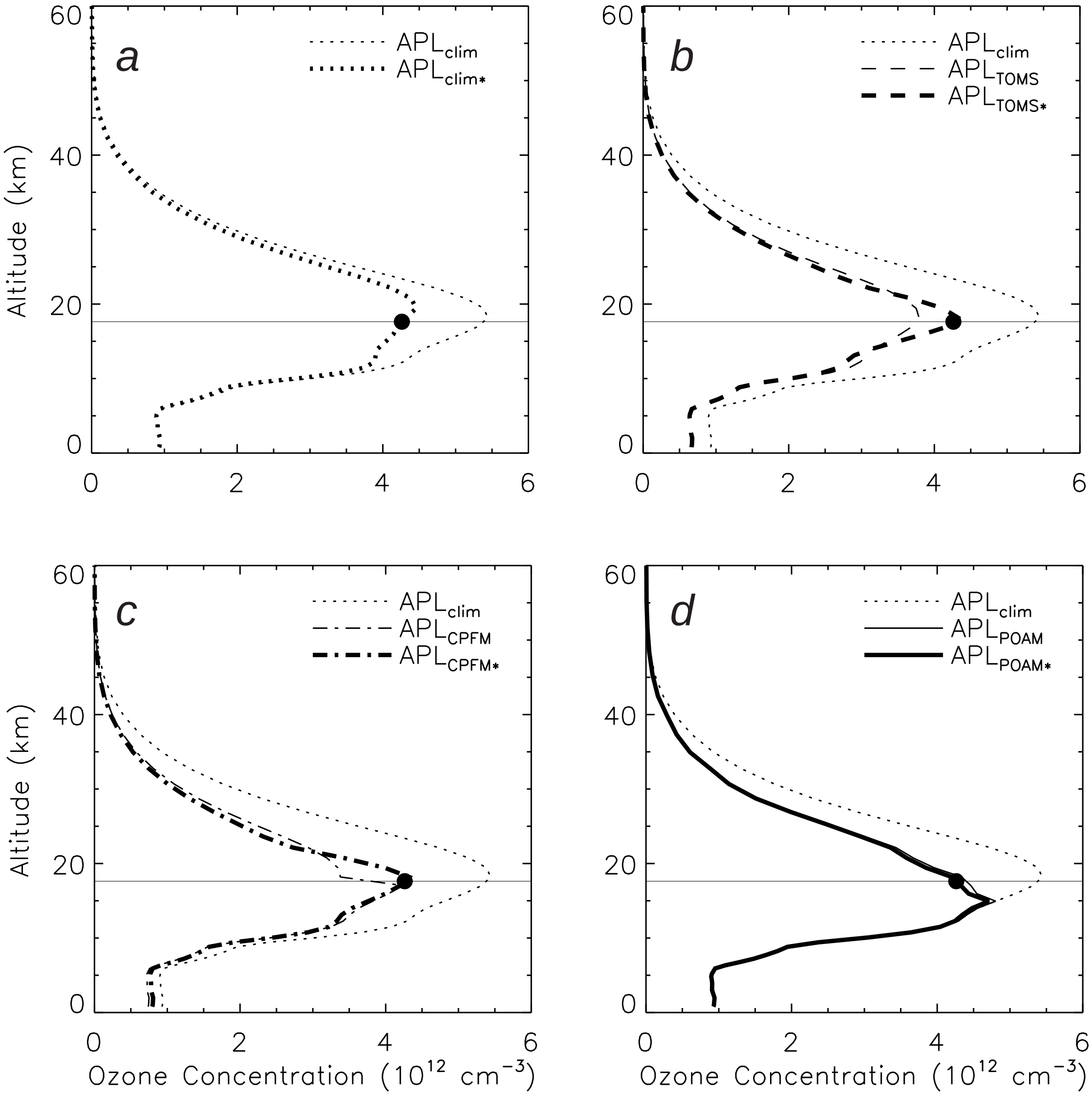

Figure E.1. Example of how the different model modes, (a) APL$_{clim[*]}$, (b) APL$_{TOMS[*]}$, (c) APL$_{CPFM[*]}$, and (d) APL$_{POAM[*]}$, scale the ozone profile based on various input data. The profiles are from the 20000311 ER-2 flight, at 32757 s UT. In each case, the climatological profile (APL$_{clim}$) is shown, along with the profiles as they were modified to account for ancillary data. The filled circle (•) in each panel indicates the measured in situ ozone concentration (4.3×10^{12} cm^{-3}) at the ER-2 altitude (17.6 km; shown with a thin horizontal line).

Table E.1. Overhead, slant, and total ozone for ozone scaling example (see Figure E.1)

Model Mode	Overhead (Vertical) Column Ozone[a] (DU)	Overhead Slant Column Ozone (DU)	Total Column Ozone[b] (DU)
APL_{CPFM*}	141.2	488.7	278.5
APL_{POAM*}	159.4	552.5	323.9
APL_{TOMS*}	156.7	542.2	278.5
APL_{clim*}	198.0	684.7	351.2
APL_{CPFM}	141.2	491.9	278.5
APL_{POAM}	163.0	564.9	329.9
APL_{TOMS}	158.3	547.8	278.5
APL_{clim}	227.4	786.7	400.0

[a]CPFM overhead ozone: 141.2 Dobson units (DU).
[b]TOMS total column ozone: 278.5 DU.

available in this particular case, the $APL_{CPFM[*]}$ profiles were also scaled to match the total ozone column. Finally, Figure E.1d shows how the climatological profile was modified where POAM III O_3–PV reconstruction data were available (above $\sim$16 km). The APL_{POAM*} profile was then scaled to the in situ ozone.

The final overhead (vertical), slant, and total ozone column results for each of the model modes for this 20000311 example are listed in Table E.1, corresponding to Figure E.1. Note that the overhead ozone for the APL_{CPFM} and APL_{CPFM*} match CPFM, despite the additional scaling to the in situ and total column ozone, but that the slant ozone columns in these cases are different, since the ozone is distributed slightly differently. Also, the total ozone for $APL_{TOMS[*]}$ and $APL_{CPFM[*]}$ all agree with the TOMS measurement.

E.3 ER-2: Model–Model *j*-Value Comparisons

Section 4.4 explains how the SOLVE *j*-value data were filtered for the comparisons. See section 4.5 for the analogous DC-8 comparisons.

Similar to the DC-8, Figure E.2 contains a comprehensive synopsis of each of the science flights, including input data availability for each of the different model modes, SZA, j_{NO_2}, j_{O_3}, albedo, overhead ozone, temperature, and flight altitude. Both TOMS and CPFM required sunlight to make their measurements, so the connection between sufficiently small SZAs and availability of TOMS and CPFM data can be seen when combining the bands at the top of the figure with SZA in the second panel.

Tables showing comparisons of ER-2 j_{NO_2} and j_{O_3} appear in this section. Tables of the corresponding correlation coefficients and comparisons/correlations of surface albedo and overhead and total ozone columns appear in the following sections. The CPFM instrument is described in section 3.4.1.[7]

E.3.1 j_{NO_2}

A matrix of comparisons of all the different model modes with each other is shown in Table E.2, divided into low- and high-SZA regimes. Albedo is much more important than the ozone column for j_{NO_2}, particularly at lower SZAs, so the various TOMS- and POAM-derived modes, which all utilized TOMS surface albedo, have slopes of nearly 1.00, as well as each mode with and without in situ ozone scaling (e.g., APL_{CPFM*}:APL_{CPFM} = 1.00). The corresponding comparisons of albedo are in Table E.14. Considering APL_{TOMS}:APL_{clim}, a ratio in albedo of 0.76 translates into a j_{NO_2} ratio of 0.97 at (relatively) low SZAs. There is a curious 3% disparity between

[7]CPFM performed quite well during POLARIS (see chapter 3). To accommodate the twilight conditions of SOLVE, C. T. McElroy et al. made significant modifications to the instrument, including the addition of a periscope that could observe the direct solar beam. The tracking mechanism, which had to anticipate the position of the Sun and compensate for the orientation of the ER-2, however, did not perform adequately. Thus, though overhead ozone and surface albedo measurements were available and used as inputs to the APL model, no meaningful actinic flux measurements could be derived from the CPFM data.

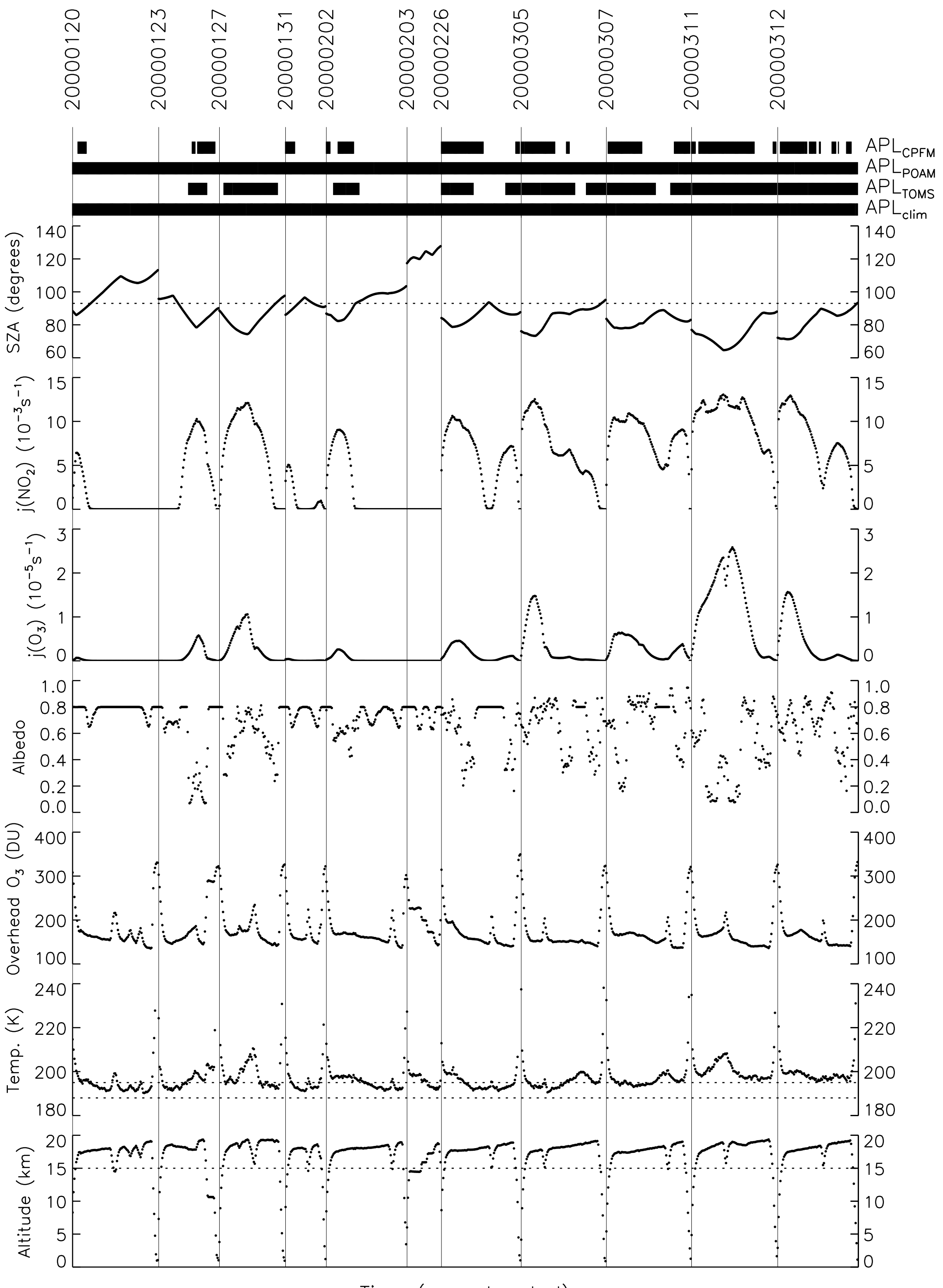

Figure E.2. Same as Figure 4.2, but for the ER-2.

Table E.2. SOLVE model–model ER-2 j_{NO_2} comparison matrix

	APL_{clim}	APL_{TOMS}	APL_{POAM}	APL_{CPFM}	APL_{clim*}	APL_{TOMS*}	APL_{POAM*}	APL_{CPFM*}
SZA $<$ 85°:								
APL_{CPFM*}	0.95	0.98	0.97	1.00	0.94	0.97	0.97	—
APL_{POAM*}	0.98	1.01	1.00	1.03	0.97	1.01	—	1.03
APL_{TOMS*}	0.97	1.00	1.00	1.03	0.97	—	0.99	1.03
APL_{clim*}	1.00	1.03	1.03	1.06	—	1.03	1.02	1.06
APL_{CPFM}	0.95	0.98	0.97	—	0.94	0.97	0.97	1.00
APL_{POAM}	0.98	1.01	—	1.03	0.97	1.00	1.00	1.03
APL_{TOMS}	0.97	—	0.99	1.03	0.97	1.00	0.99	1.02
APL_{clim}	—	1.03	1.02	1.06	1.00	1.03	1.02	1.06
SZA $\geq$ 85°:								
APL_{CPFM*}	0.99	1.00	0.98	1.00	0.99	1.00	0.97	—
APL_{POAM*}	1.03	1.03	1.00	1.03	1.02	1.03	—	1.03
APL_{TOMS*}	1.00	1.00	0.97	1.00	0.99	—	0.97	1.00
APL_{clim*}	1.01	1.01	0.98	1.01	—	1.01	0.98	1.01
APL_{CPFM}	0.99	1.00	0.98	—	0.99	1.00	0.97	1.00
APL_{POAM}	1.03	1.03	—	1.02	1.02	1.03	1.00	1.02
APL_{TOMS}	1.00	—	0.97	1.00	0.99	1.00	0.97	1.00
APL_{clim}	—	1.00	0.97	1.01	0.99	1.00	0.97	1.01

Numbers represent the slopes of the least squares fits (forced through the origin) of scatter plots of j-value data with the ordinates and abscissas indicated by the model mode labels along the corresponding edges of the matrix. The data have been separated into low- and high-SZA regimes and filtered as described in section 4.4. Table E.6 contains the corresponding matrix of correlation coefficients.

$APL_{POAM[*]}$ and $APL_{TOMS[*]}$ at high SZAs, which can be attributed to neither albedo (since they were same) nor the overhead ozone column (APL_{POAM}:APL_{TOMS} = 0.99 and APL_{POAM*}:APL_{TOMS} = 0.85; see Table E.16). This discrepancy reveals a subtle difference of the $APL_{POAM[*]}$ modes. $APL_{POAM[*]}$ used pressure and temperature profiles derived from UKMO analyses [*Swinbank and O'Neill*, 1994], whereas the other modes were based on climatologies. A bias in the $APL_{POAM[*]}$ pressure/temperature profiles translates into a bias in the airmass factor and local scattering environment near the ER-2. These biases cause the differences, albeit small, in $APL_{POAM[*]}$ j_{NO_2} compared to the other modes, particularly at higher SZAs.

APL_{TOMS} and APL_{CPFM} j_{NO_2} were well correlated with each other and, in general, with APL_{clim}, as shown in Figure E.3, with the exception of APL_{clim} from the 20000311 flight. The corresponding albedos are shown in Figure E.4. CPFM–climatology albedo deviations, combined with relatively small SZAs, led to the j_{NO_2} deviations on 20000311. It is also clear from Figure E.4a that the albedo climatology has a maximum of 0.8.

E.3.2 j_{O_3}

The model–model j_{O_3} comparison is shown in Table E.3. Compared with albedo and its effects on j_{NO_2}, large differences in overhead ozone (Table E.16) mean larger differences in j_{O_3}. The climatological overhead ozone is nearly 60% larger than that measured by CPFM, producing j_{O_3} smaller by a factor of 2 at SZAs $< 85°$, with larger discrepancies at larger SZAs.

ER-2 flight 20000311 deviates from the other flights in terms of ozone climatology, as can be seen in the comparisons of j_{O_3} and overhead ozone in Figures E.5a and E.5b. The in situ data from the 20000311 and 20000312 flights also differ from the other

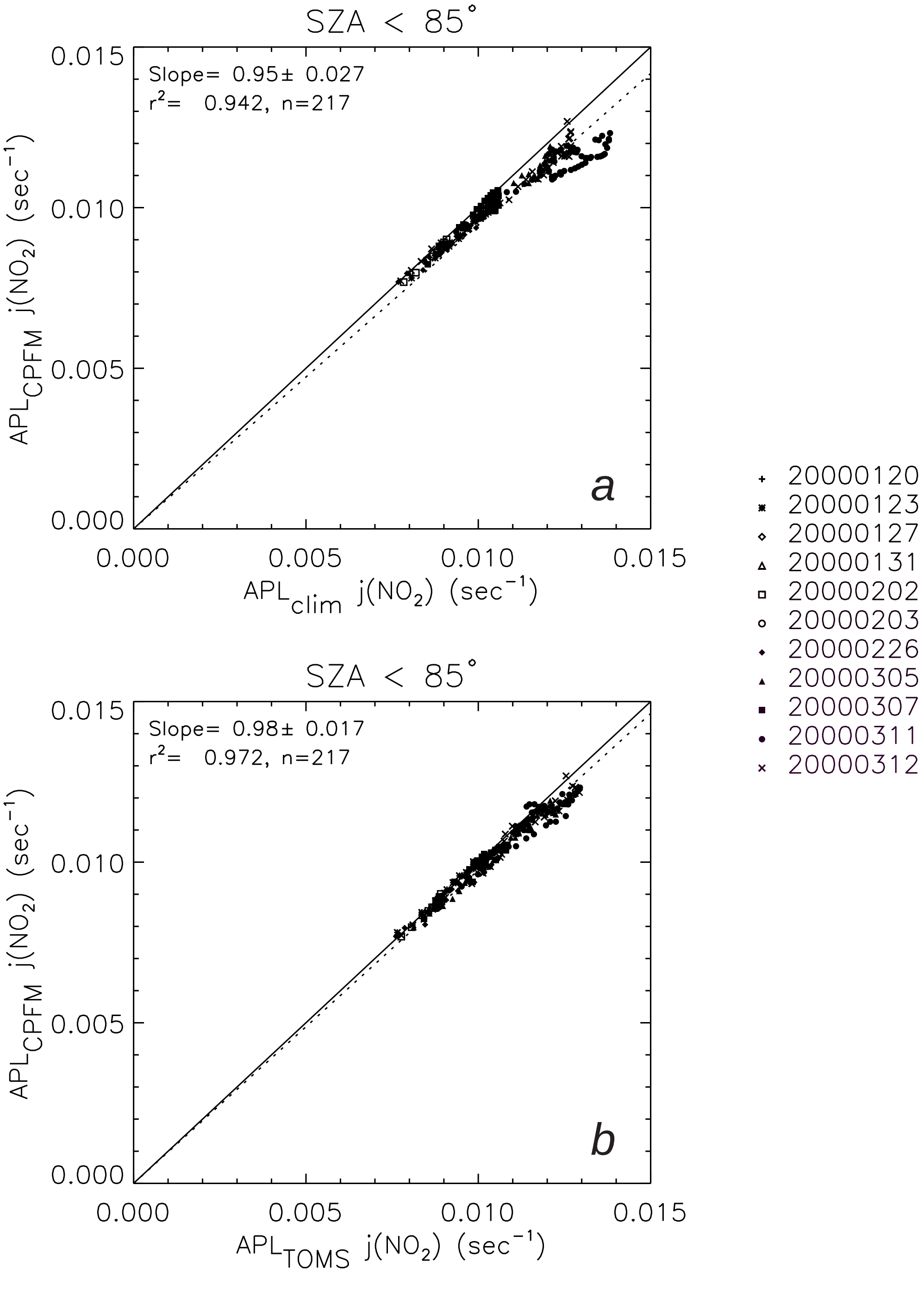

Figure E.3. Comparison of (a) APL_{CPFM} and APL_{clim} and (b) APL_{CPFM} and APL_{TOMS} j_{NO_2} calculations along the ER-2 flight tracks during SOLVE at SZAs $< 85°$. Each science flight is identified by a unique symbol, as keyed at right. The data were filtered as described in section 4.4. The slopes and correlation coefficients, r^2, are also indicated, corresponding to those recorded in, for example, Tables E.2 and E.6, respectively.

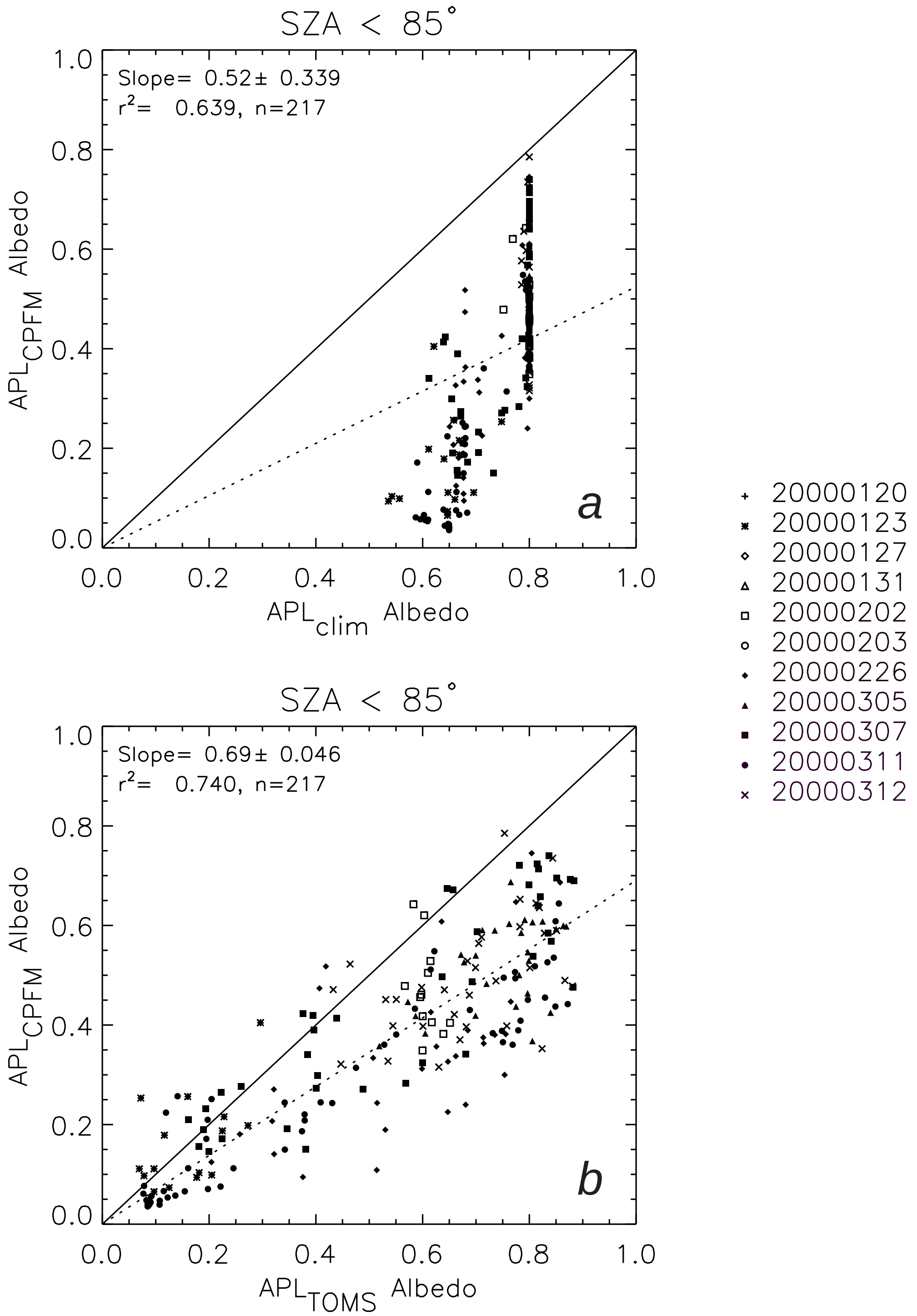

Figure E.4. Same as Figure E.3, with (a) APL_{CPFM}/APL_{clim} and (b) APL_{CPFM}/APL_{TOMS} surface reflectivity (albedo).

Table E.3. SOLVE model–model ER-2 j_{O_3} comparison matrix

	APL_{clim}	APL_{TOMS}	APL_{POAM}	APL_{CPFM}	APL_{clim*}	APL_{TOMS*}	APL_{POAM*}	APL_{CPFM*}
SZA $<$ 85°:								
APL_{CPFM*}	1.97	1.05	1.16	1.00	1.28	1.01	1.02	—
APL_{POAM*}	1.87	1.01	1.11	0.96	1.28	0.97	—	0.95
APL_{TOMS*}	1.92	1.04	1.12	0.96	1.25	—	0.96	0.95
APL_{clim*}	1.45	0.78	0.85	0.74	—	0.76	0.76	0.73
APL_{CPFM}	1.96	1.04	1.15	—	1.28	1.00	1.01	1.00
APL_{POAM}	1.70	0.91	—	0.85	1.10	0.88	0.85	0.85
APL_{TOMS}	1.85	—	1.08	0.92	1.20	0.96	0.92	0.92
APL_{clim}	—	0.54	0.58	0.49	0.64	0.51	0.49	0.49
SZA $\geq$ 85°:								
APL_{CPFM*}	2.45	1.68	1.67	1.04	1.32	1.52	1.29	—
APL_{POAM*}	1.98	1.40	1.33	0.78	1.04	1.24	—	0.74
APL_{TOMS*}	1.72	1.14	1.14	0.67	0.80	—	0.79	0.65
APL_{clim*}	1.80	1.32	1.21	0.70	—	1.18	0.94	0.67
APL_{CPFM}	2.35	1.62	1.60	—	1.28	1.47	1.25	0.96
APL_{POAM}	1.50	0.99	—	0.62	0.72	0.86	0.71	0.59
APL_{TOMS}	1.52	—	1.00	0.61	0.68	0.87	0.68	0.59
APL_{clim}	—	0.65	0.66	0.42	0.47	0.56	0.47	0.40

Same as Table E.2, but for j_{O_3}. Table E.7 contains the corresponding matrix of correlation coefficients.

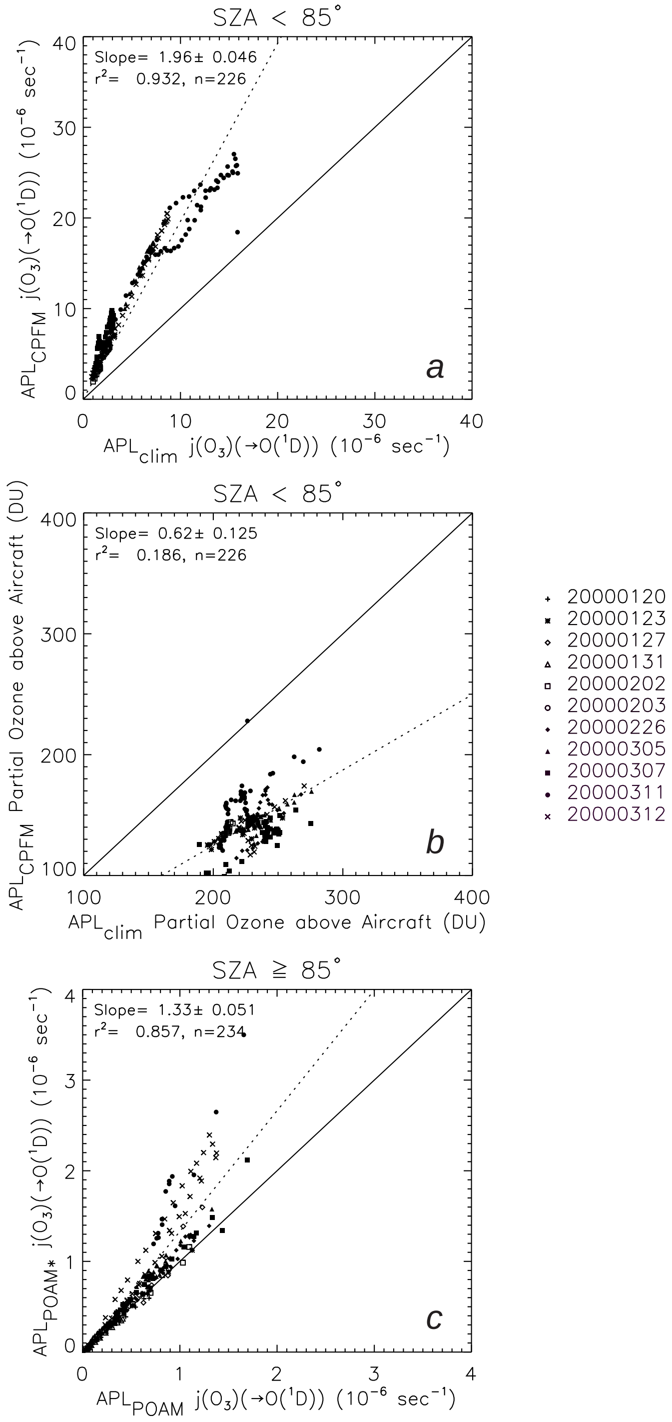

Figure E.5. Same as Figure E.3, with (a) APL_{CPFM}/APL_{clim} j_{O_3} and (b) APL_{CPFM}/APL_{clim} overhead ozone column (SZA $<$ 85°) and (c) APL_{POAM*}/APL_{POAM} j_{O_3} (SZA $\geq$ 85°).

flights, as shown in its effect on APL_{POAM} in Figure E.5c. These flights were near the end of the deployment, as the polar vortex was breaking up, which may explain some of the inhomogeneities (in fact, 20000311 flew completely out of the vortex for a large portion of the flight).

In Situ Ozone Scaling

The use of in situ ozone profile scaling had little effect on the correlation coefficients of the comparisons of j_{NO_2} (see Table E.6), but played a more important role for j_{O_3}. The incorporation of in situ data mostly improved the correlation of overhead ozone (Table E.17) and led to improved agreement with CPFM (Table E.16), especially in the case of APL_{clim}. But the correlation of j_{O_3} actually worsened somewhat overall (Table E.7). Figures E.6 and E.7 show the impact of including the in situ ozone data in comparisons of $APL_{TOMS[*]}$ and $APL_{clim[*]}$ in terms of overhead ozone and j_{O_3}, respectively.

E.4 SOLVE *j*-Value Correlations

Tables E.4–E.7 present *j*-value correlations corresponding to the comparisons in section 4.5 and in the previous section, for the DC-8 and ER-2, respectively.

E.5 SOLVE Input Data Comparisons/Correlations

Tables E.8–E.19 summarize the comparison and correlation of various inputs to the APL model during SOLVE.

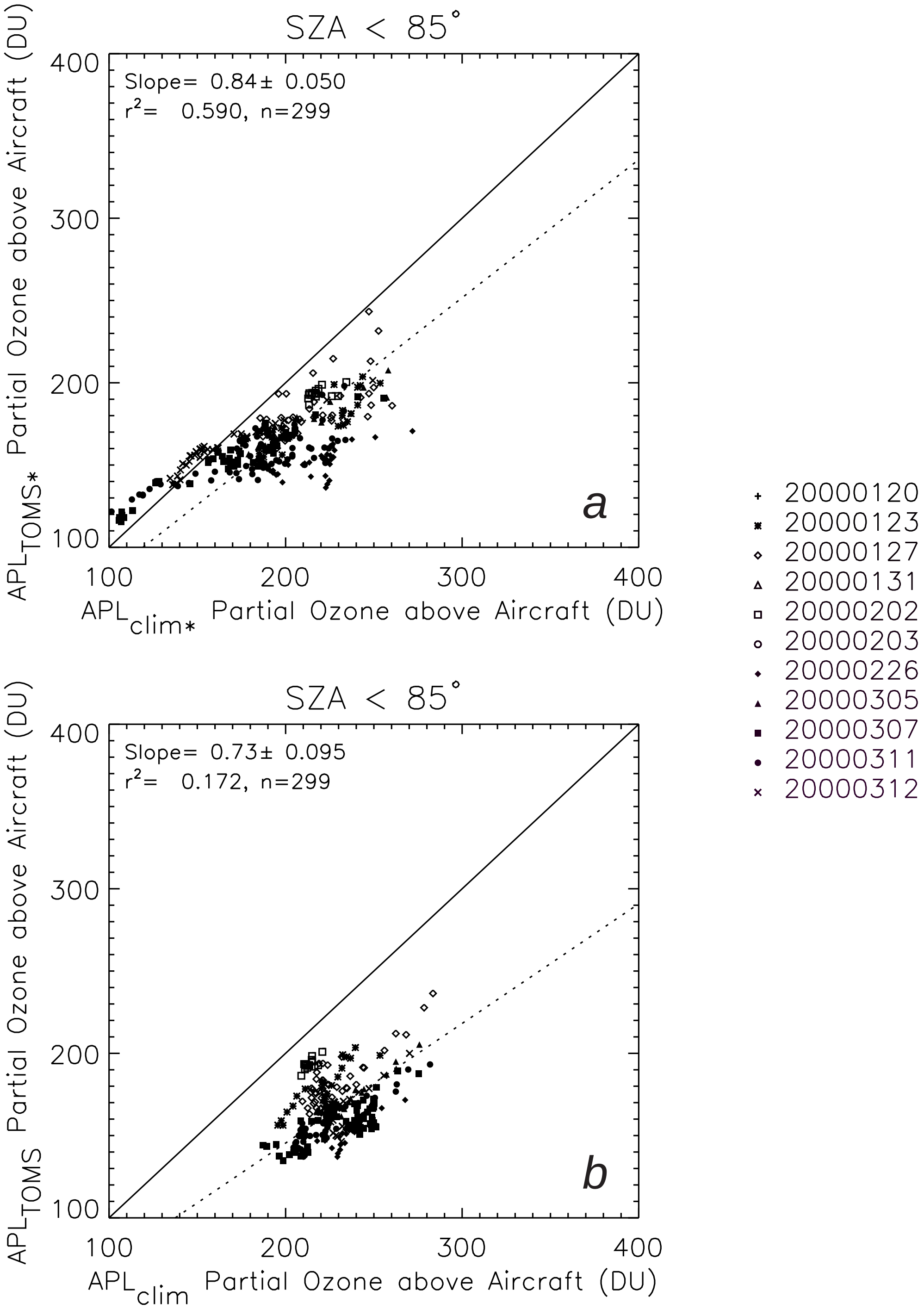

Figure E.6. Same as Figure E.3, with (a) APL_{TOMS*}/APL_{clim*} and (b) APL_{TOMS}/APL_{clim} overhead ozone column.

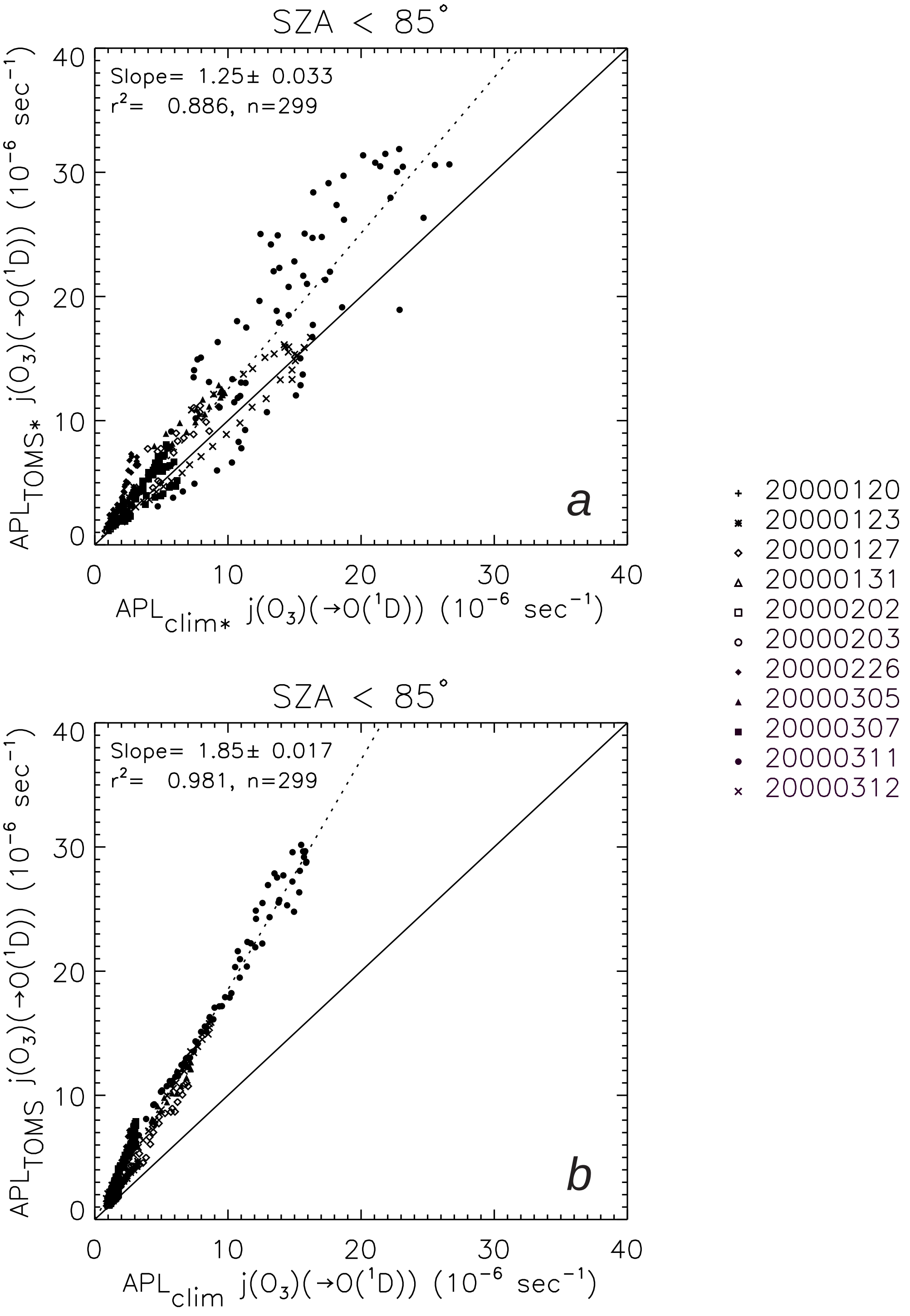

Figure E.7. Same as Figure E.3, with (a) APL_{TOMS*}/APL_{clim*} and (b) APL_{TOMS}/APL_{clim} j_{O_3}.

Table E.4. SOLVE model–model and model–SAFS DC-8 j_{NO_2} correlation matrix

	SAFS	APL_{clim}	APL_{TOMS}	APL_{POAM}	APL_{clim*}	APL_{TOMS*}	APL_{POAM*}
SZA $<$ 85°:							
APL_{POAM*}	0.976 (172)	0.989 (178)	0.999 (178)	1.000 (178)	0.990 (178)	0.999 (178)	— (178)
APL_{TOMS*}	0.942 (216)	0.989 (222)	1.000 (222)	0.998 (222)	0.989 (222)	— (222)	0.999 (178)
APL_{clim*}	0.929 (218)	1.000 (224)	0.989 (222)	0.986 (222)	— (224)	0.989 (222)	0.990 (178)
APL_{POAM}	0.958 (216)	0.986 (222)	0.998 (222)	— (222)	0.986 (222)	0.998 (222)	1.000 (178)
APL_{TOMS}	0.942 (216)	0.989 (222)	— (222)	0.998 (222)	0.989 (222)	1.000 (222)	0.999 (178)
APL_{clim}	0.931 (218)	— (224)	0.989 (222)	0.986 (222)	1.000 (224)	0.989 (222)	0.989 (178)
SAFS	— (218)	0.931 (218)	0.942 (216)	0.958 (216)	0.929 (218)	0.942 (216)	0.976 (172)
SZA $\geq$ 85°:							
APL_{POAM*}	0.940 (152)	0.997 (156)	0.999 (156)	1.000 (156)	0.997 (156)	0.999 (156)	— (156)
APL_{TOMS*}	0.934 (162)	0.997 (167)	1.000 (167)	0.999 (166)	0.997 (167)	— (167)	0.999 (156)
APL_{clim*}	0.918 (370)	1.000 (385)	0.997 (167)	0.995 (166)	— (385)	0.997 (167)	0.997 (156)
APL_{POAM}	0.940 (162)	0.995 (166)	0.999 (166)	— (166)	0.995 (166)	0.999 (166)	1.000 (156)
APL_{TOMS}	0.933 (162)	0.997 (167)	— (167)	0.999 (166)	0.997 (167)	1.000 (167)	0.999 (156)
APL_{clim}	0.919 (370)	— (385)	0.997 (167)	0.995 (166)	1.000 (385)	0.997 (167)	0.997 (156)
SAFS	— (373)	0.919 (370)	0.933 (162)	0.940 (162)	0.918 (370)	0.934 (162)	0.940 (152)

Numbers represent the correlation coefficients, r^2, (and number of data points n) of j-value data indicated by the model mode labels along the edges of the matrix. The data have been separated into low- and high-SZA regimes and filtered as described in section 4.4. Table 4.2 contains the corresponding comparison matrix.

Table E.5. SOLVE Model–model and model–SAFS DC-8 j_{O_3} correlation matrix

	SAFS	APL_{clim}	APL_{TOMS}	APL_{POAM}	APL_{clim*}	APL_{TOMS*}	APL_{POAM*}
SZA $<$ 85°:							
APL_{POAM*}	0.990 (174)	0.971 (180)	0.990 (178)	0.983 (180)	0.992 (180)	0.986 (178)	— (180)
APL_{TOMS*}	0.994 (216)	0.979 (222)	0.998 (222)	0.985 (222)	0.981 (222)	— (222)	0.986 (178)
APL_{clim*}	0.984 (218)	0.979 (224)	0.985 (222)	0.970 (224)	— (224)	0.981 (222)	0.992 (180)
APL_{POAM}	0.985 (218)	0.991 (224)	0.977 (222)	— (224)	0.970 (224)	0.985 (222)	0.983 (180)
APL_{TOMS}	0.993 (216)	0.971 (222)	— (222)	0.977 (222)	0.985 (222)	0.998 (222)	0.990 (178)
APL_{clim}	0.980 (218)	— (224)	0.971 (222)	0.991 (224)	0.979 (224)	0.979 (222)	0.971 (180)
SAFS	— (218)	0.980 (218)	0.993 (216)	0.985 (218)	0.984 (218)	0.994 (216)	0.990 (174)
SZA $\geq$ 85°:							
APL_{POAM*}	0.962 (226)	0.918 (221)	0.971 (124)	0.964 (242)	0.952 (222)	0.960 (123)	— (245)
APL_{TOMS*}	0.955 (129)	0.873 (122)	0.989 (138)	0.945 (135)	0.903 (123)	— (138)	0.960 (123)
APL_{clim*}	0.911 (290)	0.935 (288)	0.904 (123)	0.907 (295)	— (296)	0.903 (123)	0.952 (222)
APL_{POAM}	0.963 (299)	0.961 (289)	0.899 (135)	— (317)	0.907 (295)	0.945 (135)	0.964 (242)
APL_{TOMS}	0.935 (130)	0.823 (122)	— (139)	0.899 (135)	0.904 (123)	0.989 (138)	0.971 (124)
APL_{clim}	0.915 (284)	— (289)	0.823 (122)	0.961 (289)	0.935 (288)	0.873 (122)	0.918 (221)
SAFS	— (307)	0.915 (284)	0.935 (130)	0.963 (299)	0.911 (290)	0.955 (129)	0.962 (226)

Same as Table E.4, but for DC-8 j_{O_3}. Table 4.3 contains the corresponding comparison matrix.

Table E.6. SOLVE model–model ER-2 j_{NO_2} correlation matrix

	APL_{clim}	APL_{TOMS}	APL_{POAM}	APL_{CPFM}	APL_{clim*}	APL_{TOMS*}	APL_{POAM*}	APL_{CPFM*}
SZA < 85°:								
APL_{CPFM*}	0.941 (217)	0.972 (217)	0.971 (217)	1.000 (217)	0.944 (217)	0.971 (217)	0.968 (217)	— (217)
APL_{POAM*}	0.920 (299)	0.999 (299)	1.000 (299)	0.967 (217)	0.924 (299)	0.999 (299)	— (299)	0.968 (217)
APL_{TOMS*}	0.930 (299)	1.000 (299)	1.000 (299)	0.971 (217)	0.933 (299)	— (299)	0.999 (299)	0.971 (217)
APL_{clim*}	0.999 (301)	0.934 (299)	0.929 (299)	0.944 (217)	— (301)	0.933 (299)	0.924 (299)	0.944 (217)
APL_{CPFM}	0.942 (217)	0.972 (217)	0.970 (217)	— (217)	0.944 (217)	0.971 (217)	0.967 (217)	1.000 (217)
APL_{POAM}	0.925 (299)	0.999 (299)	— (299)	0.970 (217)	0.929 (299)	1.000 (299)	1.000 (299)	0.971 (217)
APL_{TOMS}	0.930 (299)	— (299)	0.999 (299)	0.972 (217)	0.934 (299)	1.000 (299)	0.999 (299)	0.972 (217)
APL_{clim}	— (301)	0.930 (299)	0.925 (299)	0.942 (217)	0.999 (301)	0.930 (299)	0.920 (299)	0.941 (217)
SZA ≥ 85°:								
APL_{CPFM*}	0.996 (25)	0.993 (14)	0.991 (14)	1.000 (25)	0.995 (25)	0.992 (14)	0.990 (14)	— (25)
APL_{POAM*}	0.998 (148)	0.999 (148)	1.000 (148)	0.990 (14)	0.998 (148)	0.999 (148)	— (148)	0.990 (14)
APL_{TOMS*}	0.999 (150)	1.000 (150)	0.999 (149)	0.992 (14)	0.999 (150)	— (150)	0.999 (148)	0.992 (14)
APL_{clim*}	1.000 (258)	0.999 (150)	0.998 (149)	0.995 (25)	— (258)	0.999 (150)	0.998 (148)	0.995 (25)
APL_{CPFM}	0.996 (25)	0.993 (14)	0.991 (14)	— (25)	0.995 (25)	0.992 (14)	0.990 (14)	1.000 (25)
APL_{POAM}	0.998 (149)	0.999 (149)	— (149)	0.991 (14)	0.998 (149)	0.999 (149)	1.000 (148)	0.991 (14)
APL_{TOMS}	0.999 (150)	— (150)	0.999 (149)	0.993 (14)	0.999 (150)	1.000 (150)	0.999 (148)	0.993 (14)
APL_{clim}	— (258)	0.999 (150)	0.998 (149)	0.996 (25)	1.000 (258)	0.999 (150)	0.998 (148)	0.996 (25)

Same as Table E.4, but for ER-2 j_{NO_2}, excluding SAFS measurements. Table E.2 contains the corresponding comparison matrix.

Table E.7. SOLVE model–model ER-2 j_{O_3} correlation matrix

	APL_{clim}	APL_{TOMS}	APL_{POAM}	APL_{CPFM}	APL_{clim*}	APL_{TOMS*}	APL_{POAM*}	APL_{CPFM*}
SZA $<$ 85°:								
APL_{CPFM*}	0.926 (226)	0.914 (226)	0.966 (226)	1.000 (226)	0.851 (226)	0.913 (226)	0.900 (226)	— (226)
APL_{POAM*}	0.807 (301)	0.814 (299)	0.853 (301)	0.896 (226)	0.941 (301)	0.840 (299)	— (301)	0.900 (226)
APL_{TOMS*}	0.973 (299)	0.994 (299)	0.957 (299)	0.918 (226)	0.886 (299)	— (299)	0.840 (299)	0.913 (226)
APL_{clim*}	0.832 (301)	0.845 (299)	0.831 (301)	0.851 (226)	— (301)	0.886 (299)	0.941 (301)	0.851 (226)
APL_{CPFM}	0.932 (226)	0.921 (226)	0.970 (226)	— (226)	0.851 (226)	0.918 (226)	0.896 (226)	1.000 (226)
APL_{POAM}	0.980 (301)	0.965 (299)	— (301)	0.970 (226)	0.831 (301)	0.957 (299)	0.853 (301)	0.966 (226)
APL_{TOMS}	0.981 (299)	— (299)	0.965 (299)	0.921 (226)	0.845 (299)	0.994 (299)	0.814 (299)	0.914 (226)
APL_{clim}	— (301)	0.981 (299)	0.980 (301)	0.932 (226)	0.832 (301)	0.973 (299)	0.807 (301)	0.926 (226)
SZA $\geq$ 85°:								
APL_{CPFM*}	0.920 (66)	0.969 (36)	0.961 (66)	0.999 (66)	0.722 (66)	0.932 (36)	0.884 (66)	— (66)
APL_{POAM*}	0.804 (223)	0.850 (143)	0.857 (234)	0.902 (66)	0.952 (226)	0.936 (143)	— (234)	0.884 (66)
APL_{TOMS*}	0.861 (140)	0.963 (143)	0.926 (143)	0.949 (36)	0.851 (143)	— (143)	0.936 (143)	0.932 (36)
APL_{clim*}	0.666 (223)	0.726 (143)	0.702 (226)	0.746 (66)	— (226)	0.851 (143)	0.952 (226)	0.722 (66)
APL_{CPFM}	0.923 (66)	0.977 (36)	0.966 (66)	— (66)	0.746 (66)	0.949 (36)	0.902 (66)	0.999 (66)
APL_{POAM}	0.976 (223)	0.977 (143)	— (236)	0.966 (66)	0.702 (226)	0.926 (143)	0.857 (234)	0.961 (66)
APL_{TOMS}	0.929 (140)	— (143)	0.977 (143)	0.977 (36)	0.726 (143)	0.963 (143)	0.850 (143)	0.969 (36)
APL_{clim}	— (223)	0.929 (140)	0.976 (223)	0.923 (66)	0.666 (223)	0.861 (140)	0.804 (223)	0.920 (66)

Same as Table E.4, but for ER-2 j_{O_3}, excluding SAFS measurements. Table E.3 contains the corresponding comparison matrix.

Table E.8. SOLVE model–model DC-8 surface reflectivity comparison matrix

	APL_{clim}	APL_{TOMS}	APL_{POAM}	APL_{clim*}	APL_{TOMS*}	APL_{POAM*}
SZA $<$ 85°:						
APL_{POAM*}	0.80	—	—	0.80	—	—
APL_{TOMS*}	0.75	—	—	0.75	—	—
APL_{clim*}	—	1.21	1.21	—	1.21	1.18
APL_{POAM}	0.75	—	—	0.75	—	—
APL_{TOMS}	0.75	—	—	0.75	—	—
APL_{clim}	—	1.21	1.21	—	1.21	1.18
SZA $\geq$ 85°:						
APL_{POAM*}	0.81	—	—	0.81	—	—
APL_{TOMS*}	0.79	—	—	0.79	—	—
APL_{clim*}	—	1.13	1.13	—	1.13	1.11
APL_{POAM}	0.79	—	—	0.79	—	—
APL_{TOMS}	0.79	—	—	0.79	—	—
APL_{clim}	—	1.13	1.13	—	1.13	1.11

Same as Table E.2, but for DC-8 albedo. Table E.9 contains the corresponding correlation matrix.

Table E.9. SOLVE model–model DC-8 surface reflectivity correlation matrix

	APL_{clim}	APL_{TOMS}	APL_{POAM}	APL_{clim*}	APL_{TOMS*}	APL_{POAM*}
SZA $<$ 85°:						
APL_{POAM*}	0.300 (178)	— (178)	— (178)	0.300 (178)	— (178)	— (178)
APL_{TOMS*}	0.362 (222)	— (222)	— (222)	0.362 (222)	— (222)	— (178)
APL_{clim*}	— (224)	0.362 (222)	0.362 (222)	— (224)	0.362 (222)	0.300 (178)
APL_{POAM}	0.362 (222)	— (222)	— (222)	0.362 (222)	— (222)	— (178)
APL_{TOMS}	0.362 (222)	— (222)	— (222)	0.362 (222)	— (222)	— (178)
APL_{clim}	— (224)	0.362 (222)	0.362 (222)	— (224)	0.362 (222)	0.300 (178)
SZA $\geq$ 85°:						
APL_{POAM*}	0.358 (156)	— (156)	— (156)	0.358 (156)	— (156)	— (156)
APL_{TOMS*}	0.303 (167)	— (167)	— (166)	0.303 (167)	— (167)	— (156)
APL_{clim*}	— (385)	0.303 (167)	0.300 (166)	— (385)	0.303 (167)	0.358 (156)
APL_{POAM}	0.300 (166)	— (166)	— (166)	0.300 (166)	— (166)	— (156)
APL_{TOMS}	0.303 (167)	— (167)	— (166)	0.303 (167)	— (167)	— (156)
APL_{clim}	— (385)	0.303 (167)	0.300 (166)	— (385)	0.303 (167)	0.358 (156)

Same as Table E.4, but for DC-8 albedo. Table E.8 contains the corresponding comparison matrix.

Table E.10. SOLVE model–model DC-8 overhead ozone comparison matrix

	APL_{clim}	APL_{TOMS}	APL_{POAM}	APL_{clim*}	APL_{TOMS*}	APL_{POAM*}
SZA $<$ 85°:						
APL_{POAM*}	0.81	1.06	0.98	0.82	1.05	—
APL_{TOMS*}	0.77	1.02	0.92	0.79	—	0.95
APL_{clim*}	0.97	1.27	1.15	—	1.25	1.21
APL_{POAM}	0.83	1.10	—	0.86	1.08	1.02
APL_{TOMS}	0.75	—	0.90	0.78	0.98	0.94
APL_{clim}	—	1.31	1.19	1.03	1.29	1.23
SZA $\geq$ 85°:						
APL_{POAM*}	0.88	1.05	0.99	0.89	1.04	—
APL_{TOMS*}	0.81	1.01	0.94	0.83	—	0.96
APL_{clim*}	0.95	1.20	1.06	—	1.19	1.11
APL_{POAM}	0.89	1.07	—	0.93	1.06	1.01
APL_{TOMS}	0.80	—	0.92	0.82	0.99	0.95
APL_{clim}	—	1.23	1.12	1.04	1.22	1.12

Same as Table E.2, but for DC-8 overhead ozone. Table E.11 contains the corresponding correlation matrix.

Table E.11. SOLVE model–model DC-8 overhead ozone correlation matrix

	APL_{clim}	APL_{TOMS}	APL_{POAM}	APL_{clim*}	APL_{TOMS*}	APL_{POAM*}
SZA $<$ 85°:						
APL_{POAM*}	0.005 (180)	0.612 (178)	0.623 (180)	0.381 (180)	0.384 (178)	— (180)
APL_{TOMS*}	0.077 (222)	0.929 (222)	0.592 (222)	0.192 (222)	— (222)	0.384 (178)
APL_{clim*}	0.609 (224)	0.398 (222)	0.053 (224)	— (224)	0.192 (222)	0.381 (180)
APL_{POAM}	0.001 (224)	0.543 (222)	— (224)	0.053 (224)	0.592 (222)	0.623 (180)
APL_{TOMS}	0.129 (222)	— (222)	0.543 (222)	0.398 (222)	0.929 (222)	0.612 (178)
APL_{clim}	— (224)	0.129 (222)	0.001 (224)	0.609 (224)	0.077 (222)	0.005 (180)
SZA $\geq$ 85°:						
APL_{POAM*}	0.074 (221)	0.713 (124)	0.571 (242)	0.308 (222)	0.458 (123)	— (245)
APL_{TOMS*}	0.000 (122)	0.917 (138)	0.692 (135)	0.110 (123)	— (138)	0.458 (123)
APL_{clim*}	0.506 (288)	0.222 (123)	0.297 (295)	— (296)	0.110 (123)	0.308 (222)
APL_{POAM}	0.234 (289)	0.521 (135)	— (317)	0.297 (295)	0.692 (135)	0.571 (242)
APL_{TOMS}	0.001 (122)	— (139)	0.521 (135)	0.222 (123)	0.917 (138)	0.713 (124)
APL_{clim}	— (289)	0.001 (122)	0.234 (289)	0.506 (288)	0.000 (122)	0.074 (221)

Same as Table E.4, but for DC-8 overhead ozone. Table E.10 contains the corresponding comparison matrix.

Table E.12. SOLVE model–model DC-8 total ozone comparison matrix

	APL_{clim}	APL_{TOMS}	APL_{POAM}	APL_{clim*}	APL_{TOMS*}	APL_{POAM*}
SZA $< 85°$:						
APL_{POAM*}	0.82	1.07	0.97	0.84	1.07	—
APL_{TOMS*}	0.75	—	0.88	0.79	—	0.93
APL_{clim*}	0.95	1.25	1.11	—	1.25	1.18
APL_{POAM}	0.85	1.12	—	0.89	1.12	1.03
APL_{TOMS}	0.75	—	0.88	0.79	—	0.93
APL_{clim}	—	1.31	1.17	1.05	1.31	1.21
SZA $\geq 85°$:						
APL_{POAM*}	0.89	1.05	0.98	0.90	1.05	—
APL_{TOMS*}	0.80	—	0.91	0.83	—	0.94
APL_{clim*}	0.93	1.19	1.03	—	1.19	1.10
APL_{POAM}	0.90	1.09	—	0.96	1.09	1.01
APL_{TOMS}	0.80	—	0.91	0.83	—	0.95
APL_{clim}	—	1.23	1.11	1.06	1.23	1.11

Same as Table E.2, but for DC-8 total ozone. Table E.13 contains the corresponding correlation matrix.

Table E.13. SOLVE model–model DC-8 total ozone correlation matrix

	APL_{clim}	APL_{TOMS}	APL_{POAM}	APL_{clim*}	APL_{TOMS*}	APL_{POAM*}
SZA $<$ 85°:						
APL_{POAM*}	0.010 (180)	0.545 (178)	0.479 (180)	0.683 (180)	0.545 (178)	— (180)
APL_{TOMS*}	0.077 (222)	— (222)	0.398 (222)	0.381 (222)	— (222)	0.545 (178)
APL_{clim*}	0.291 (224)	0.381 (222)	0.014 (224)	— (224)	0.381 (222)	0.683 (180)
APL_{POAM}	0.026 (224)	0.398 (222)	— (224)	0.014 (224)	0.398 (222)	0.479 (180)
APL_{TOMS}	0.077 (222)	— (222)	0.398 (222)	0.381 (222)	— (222)	0.545 (178)
APL_{clim}	— (224)	0.077 (222)	0.026 (224)	0.291 (224)	0.077 (222)	0.010 (180)
SZA $\geq$ 85°:						
APL_{POAM*}	0.045 (221)	0.560 (124)	0.254 (242)	0.464 (222)	0.564 (123)	— (245)
APL_{TOMS*}	0.008 (122)	— (138)	0.338 (135)	0.264 (123)	— (138)	0.564 (123)
APL_{clim*}	0.202 (288)	0.264 (123)	0.075 (295)	— (296)	0.264 (123)	0.464 (222)
APL_{POAM}	0.405 (289)	0.338 (135)	— (317)	0.075 (295)	0.338 (135)	0.254 (242)
APL_{TOMS}	0.008 (122)	— (139)	0.338 (135)	0.264 (123)	— (138)	0.560 (124)
APL_{clim}	— (289)	0.008 (122)	0.405 (289)	0.202 (288)	0.008 (122)	0.045 (221)

Same as Table E.4, but for DC-8 total ozone. Table E.12 contains the corresponding comparison matrix.

Table E.14. SOLVE model–model ER-2 surface reflectivity comparison matrix

	APL_{clim}	APL_{TOMS}	APL_{POAM}	APL_{CPFM}	APL_{clim*}	APL_{TOMS*}	APL_{POAM*}	APL_{CPFM*}
SZA $< 85°$:								
APL_{CPFM*}	0.52	0.69	0.69	—	0.52	0.69	0.69	—
APL_{POAM*}	0.76	—	—	1.37	0.76	—	—	1.37
APL_{TOMS*}	0.76	—	—	1.37	0.76	—	—	1.37
APL_{clim*}	—	1.17	1.17	1.61	—	1.17	1.17	1.61
APL_{CPFM}	0.52	0.69	0.69	—	0.52	0.69	0.69	—
APL_{POAM}	0.76	—	—	1.37	0.76	—	—	1.37
APL_{TOMS}	0.76	—	—	1.37	0.76	—	—	1.37
APL_{clim}	—	1.17	1.17	1.61	—	1.17	1.17	1.61
SZA $\geq 85°$:								
APL_{CPFM*}	0.65	0.80	0.80	—	0.65	0.80	0.80	—
APL_{POAM*}	0.74	—	—	1.12	0.74	—	—	1.12
APL_{TOMS*}	0.74	—	—	1.12	0.74	—	—	1.12
APL_{clim*}	—	1.23	1.23	1.43	—	1.23	1.23	1.43
APL_{CPFM}	0.65	0.80	0.80	—	0.65	0.80	0.80	—
APL_{POAM}	0.74	—	—	1.12	0.74	—	—	1.12
APL_{TOMS}	0.74	—	—	1.12	0.74	—	—	1.12
APL_{clim}	—	1.23	1.23	1.43	—	1.23	1.23	1.43

Same as Table E.2, but for the ER-2 albedo. Table E.15 contains the corresponding correlation matrix.

Table E.15. SOLVE model–model ER-2 surface reflectivity correlation matrix

	APL_{clim}	APL_{TOMS}	APL_{POAM}	APL_{CPFM}	APL_{clim*}	APL_{TOMS*}	APL_{POAM*}	APL_{CPFM*}
SZA $<$ 85°:								
APL_{CPFM*}	0.639 (217)	0.740 (217)	0.740 (217)	1.000 (217)	0.639 (217)	0.740 (217)	0.740 (217)	— (217)
APL_{POAM*}	0.640 (299)	1.000 (299)	1.000 (299)	0.740 (217)	0.640 (299)	1.000 (299)	— (299)	0.740 (217)
APL_{TOMS*}	0.640 (299)	1.000 (299)	1.000 (299)	0.740 (217)	0.640 (299)	— (299)	1.000 (299)	0.740 (217)
APL_{clim*}	1.000 (301)	0.640 (299)	0.640 (299)	0.639 (217)	— (301)	0.640 (299)	0.640 (299)	0.639 (217)
APL_{CPFM}	0.639 (217)	0.740 (217)	0.740 (217)	— (217)	0.639 (217)	0.740 (217)	0.740 (217)	1.000 (217)
APL_{POAM}	0.640 (299)	1.000 (299)	— (299)	0.740 (217)	0.640 (299)	1.000 (299)	1.000 (299)	0.740 (217)
APL_{TOMS}	0.640 (299)	— (299)	1.000 (299)	0.740 (217)	0.640 (299)	1.000 (299)	1.000 (299)	0.740 (217)
APL_{clim}	— (301)	0.640 (299)	0.640 (299)	0.639 (217)	1.000 (301)	0.640 (299)	0.640 (299)	0.639 (217)
SZA $\geq$ 85°:								
APL_{CPFM*}	0.469 (25)	0.189 (14)	0.189 (14)	1.000 (25)	0.469 (25)	0.189 (14)	0.189 (14)	— (25)
APL_{POAM*}	0.218 (148)	1.000 (148)	1.000 (148)	0.189 (14)	0.218 (148)	1.000 (148)	— (148)	0.189 (14)
APL_{TOMS*}	0.209 (150)	1.000 (150)	1.000 (149)	0.189 (14)	0.209 (150)	— (150)	1.000 (148)	0.189 (14)
APL_{clim*}	1.000 (258)	0.209 (150)	0.219 (149)	0.469 (25)	— (258)	0.209 (150)	0.218 (148)	0.469 (25)
APL_{CPFM}	0.469 (25)	0.189 (14)	0.189 (14)	— (25)	0.469 (25)	0.189 (14)	0.189 (14)	1.000 (25)
APL_{POAM}	0.219 (149)	1.000 (149)	— (149)	0.189 (14)	0.219 (149)	1.000 (149)	1.000 (148)	0.189 (14)
APL_{TOMS}	0.209 (150)	— (150)	1.000 (149)	0.189 (14)	0.209 (150)	1.000 (150)	1.000 (148)	0.189 (14)
APL_{clim}	— (258)	0.209 (150)	0.219 (149)	0.469 (25)	1.000 (258)	0.209 (150)	0.218 (148)	0.469 (25)

Same as Table E.4, but for ER-2 albedo. Table E.14 contains the corresponding comparison matrix.

Table E.16. SOLVE model–model ER-2 overhead ozone comparison matrix

	APL_{clim}	APL_{TOMS}	APL_{POAM}	APL_{CPFM}	APL_{clim*}	APL_{TOMS*}	APL_{POAM*}	APL_{CPFM*}
SZA $<$ 85°:								
APL_{CPFM*}	0.62	0.88	0.86	—	0.75	0.89	0.94	—
APL_{POAM*}	0.67	0.92	0.92	1.06	0.80	0.94	—	1.06
APL_{TOMS*}	0.71	0.98	0.97	1.10	0.84	—	1.05	1.10
APL_{clim*}	0.84	1.15	1.14	1.31	—	1.17	1.25	1.31
APL_{CPFM}	0.62	0.88	0.86	—	0.75	0.89	0.94	—
APL_{POAM}	0.73	1.00	—	1.15	0.86	1.02	1.08	1.15
APL_{TOMS}	0.73	—	0.99	1.12	0.85	1.02	1.07	1.12
APL_{clim}	—	1.36	1.36	1.58	1.16	1.38	1.46	1.58
SZA $\geq$ 85°:								
APL_{CPFM*}	0.56	0.72	0.76	—	0.62	0.75	0.78	—
APL_{POAM*}	0.67	0.85	0.92	1.26	0.83	0.90	—	1.26
APL_{TOMS*}	0.69	0.95	0.96	1.31	0.95	—	1.11	1.31
APL_{clim*}	0.79	0.97	1.08	1.56	—	1.03	1.19	1.56
APL_{CPFM}	0.56	0.72	0.76	—	0.62	0.75	0.78	—
APL_{POAM}	0.74	0.99	—	1.30	0.89	1.04	1.07	1.30
APL_{TOMS}	0.74	—	1.01	1.38	0.99	1.05	1.16	1.38
APL_{clim}	—	1.35	1.35	1.75	1.20	1.42	1.45	1.75

Same as Table E.2, but for ER-2 overhead ozone. Table E.17 contains the corresponding correlation matrix.

Table E.17. SOLVE model–model ER-2 overhead ozone correlation matrix

	APL_{clim}	APL_{TOMS}	APL_{POAM}	APL_{CPFM}	APL_{clim*}	APL_{TOMS*}	APL_{POAM*}	APL_{CPFM*}
SZA $< 85°$:								
APL_{CPFM*}	0.186 (226)	0.119 (226)	0.529 (226)	— (226)	0.333 (226)	0.183 (226)	0.610 (226)	— (226)
APL_{POAM*}	0.185 (301)	0.278 (299)	0.549 (301)	0.610 (226)	0.812 (301)	0.397 (299)	— (301)	0.610 (226)
APL_{TOMS*}	0.216 (299)	0.948 (299)	0.476 (299)	0.183 (226)	0.590 (299)	— (299)	0.397 (299)	0.183 (226)
APL_{clim*}	0.236 (301)	0.424 (299)	0.474 (301)	0.333 (226)	— (301)	0.590 (299)	0.812 (301)	0.333 (226)
APL_{CPFM}	0.186 (226)	0.119 (226)	0.530 (226)	— (226)	0.333 (226)	0.183 (226)	0.610 (226)	— (226)
APL_{POAM}	0.573 (301)	0.431 (299)	— (301)	0.530 (226)	0.474 (301)	0.476 (299)	0.549 (301)	0.529 (226)
APL_{TOMS}	0.172 (299)	— (299)	0.431 (299)	0.119 (226)	0.424 (299)	0.948 (299)	0.278 (299)	0.119 (226)
APL_{clim}	— (301)	0.172 (299)	0.573 (301)	0.186 (226)	0.236 (301)	0.216 (299)	0.185 (301)	0.186 (226)
SZA $\geq 85°$:								
APL_{CPFM*}	0.283 (66)	0.500 (36)	0.558 (66)	— (66)	0.645 (66)	0.490 (36)	0.631 (66)	— (66)
APL_{POAM*}	0.455 (223)	0.690 (143)	0.779 (234)	0.632 (66)	0.933 (226)	0.821 (143)	— (234)	0.631 (66)
APL_{TOMS*}	0.220 (140)	0.928 (143)	0.718 (143)	0.491 (36)	0.839 (143)	— (143)	0.821 (143)	0.490 (36)
APL_{clim*}	0.514 (223)	0.736 (143)	0.728 (226)	0.646 (66)	— (226)	0.839 (143)	0.933 (226)	0.645 (66)
APL_{CPFM}	0.283 (66)	0.500 (36)	0.559 (66)	— (66)	0.646 (66)	0.491 (36)	0.632 (66)	— (66)
APL_{POAM}	0.643 (223)	0.743 (143)	— (236)	0.559 (66)	0.728 (226)	0.718 (143)	0.779 (234)	0.558 (66)
APL_{TOMS}	0.243 (140)	— (143)	0.743 (143)	0.500 (36)	0.736 (143)	0.928 (143)	0.690 (143)	0.500 (36)
APL_{clim}	— (223)	0.243 (140)	0.643 (223)	0.283 (66)	0.514 (223)	0.220 (140)	0.455 (223)	0.283 (66)

Same as Table E.4, but for ER-2 overhead ozone. Table E.16 contains the corresponding comparison matrix.

Table E.18. SOLVE model–model ER-2 total ozone comparison matrix

	APL_{clim}	APL_{TOMS}	APL_{POAM}	APL_{CPFM}	APL_{clim*}	APL_{TOMS*}	APL_{POAM*}	APL_{CPFM*}
SZA $< 85°$:								
APL_{CPFM*}	0.71	—	0.85	1.00	0.84	—	0.91	—
APL_{POAM*}	0.78	1.07	0.93	1.09	0.91	1.07	—	1.08
APL_{TOMS*}	0.73	—	0.87	—	0.85	—	0.92	—
APL_{clim*}	0.85	1.16	1.01	1.17	—	1.16	1.09	1.17
APL_{CPFM}	0.71	—	0.85	—	0.84	—	0.91	1.00
APL_{POAM}	0.84	1.15	—	1.17	0.97	1.15	1.07	1.17
APL_{TOMS}	0.73	—	0.87	—	0.85	—	0.92	—
APL_{clim}	—	1.37	1.19	1.40	1.15	1.37	1.27	1.40
SZA $\geq 85°$:								
APL_{CPFM*}	0.86	—	1.02	1.01	0.98	—	1.07	—
APL_{POAM*}	0.77	1.00	0.93	0.94	0.95	1.00	—	0.93
APL_{TOMS*}	0.73	—	0.89	—	0.97	—	0.99	—
APL_{clim*}	0.80	1.01	0.96	1.02	—	1.01	1.05	1.01
APL_{CPFM}	0.85	—	1.01	—	0.96	—	1.05	0.95
APL_{POAM}	0.84	1.13	—	0.97	1.01	1.13	1.06	0.95
APL_{TOMS}	0.73	—	0.89	—	0.97	—	0.99	—
APL_{clim}	—	1.35	1.19	1.15	1.20	1.35	1.27	1.13

Same as Table E.2, but for ER-2 total ozone. Table E.19 contains the corresponding correlation matrix.

Table E.19. SOLVE model–model ER-2 total ozone correlation matrix

SZA $<$ 85°:								
APL_{CPFM*}	0.266 (226)	— (226)	0.000 (226)	1.000 (226)	0.052 (226)	— (226)	0.032 (226)	— (226)
APL_{POAM*}	0.011 (301)	0.060 (299)	0.336 (301)	0.034 (226)	0.805 (301)	0.060 (299)	— (301)	0.032 (226)
APL_{TOMS*}	0.257 (299)	— (299)	0.017 (299)	— (226)	0.134 (299)	— (299)	0.060 (299)	— (226)
APL_{clim*}	0.014 (301)	0.134 (299)	0.213 (301)	0.053 (226)	— (301)	0.134 (299)	0.805 (301)	0.052 (226)
APL_{CPFM}	0.261 (226)	— (226)	0.000 (226)	— (226)	0.053 (226)	— (226)	0.034 (226)	1.000 (226)
APL_{POAM}	0.328 (301)	0.017 (299)	— (301)	0.000 (226)	0.213 (301)	0.017 (299)	0.336 (301)	0.000 (226)
APL_{TOMS}	0.257 (299)	— (299)	0.017 (299)	— (226)	0.134 (299)	— (299)	0.060 (299)	— (226)
APL_{clim}	— (301)	0.257 (299)	0.328 (301)	0.261 (226)	0.014 (301)	0.257 (299)	0.011 (301)	0.266 (226)
SZA $\geq$ 85°:								
APL_{CPFM*}	0.024 (66)	— (36)	0.055 (66)	0.855 (66)	0.697 (66)	— (36)	0.689 (66)	— (66)
APL_{POAM*}	0.000 (223)	0.151 (143)	0.244 (234)	0.603 (66)	0.904 (226)	0.151 (143)	— (234)	0.689 (66)
APL_{TOMS*}	0.009 (140)	— (143)	0.151 (143)	— (36)	0.224 (143)	— (143)	0.151 (143)	— (36)
APL_{clim*}	0.003 (223)	0.224 (143)	0.226 (226)	0.595 (66)	— (226)	0.224 (143)	0.904 (226)	0.697 (66)
APL_{CPFM}	0.030 (66)	— (36)	0.016 (66)	— (66)	0.595 (66)	— (36)	0.603 (66)	0.055 (66)
APL_{POAM}	0.479 (223)	0.151 (143)	— (236)	0.016 (66)	0.226 (226)	0.151 (143)	0.244 (234)	0.055 (66)
APL_{TOMS}	0.009 (140)	— (143)	0.151 (143)	— (36)	0.224 (143)	— (143)	0.151 (143)	— (36)
APL_{clim}	— (223)	0.009 (140)	0.479 (223)	0.030 (66)	0.003 (223)	0.009 (140)	0.000 (223)	0.024 (66)
	APL_{clim}	APL_{TOMS}	APL_{POAM}	APL_{CPFM}	APL_{clim*}	APL_{TOMS*}	APL_{POAM*}	APL_{CPFM*}

Same as Table E.4, but for ER-2 total ozone. Table E.18 contains the corresponding comparison matrix.

E.6 Summary and Conclusions

SOLVE presented a modeling (and measurement) challenge beyond POLARIS that required changes to the APL radiative transfer model. Based on the conclusions from IPMMI and POLARIS, several key pieces of input data were updated. New climatologies of ozone, pressure, temperature, and albedo were incorporated into the model, along with POAM III satellite and in situ ozone data, in order to more accurately capture the physical characteristics of the atmosphere. Many of the details and nuances of the data application were reported (see also chapter 4).

The CPFM instrument on board the ER-2, which formed the basis for the POLARIS model–measurement comparison, did not produce comparable in situ j-values, but extensive model–model comparisons were performed. For j_{NO_2}, even at high solar zenith angles the model consistency was within 5% and highly correlated between the various model modes. Larger differences were found for j_{O_3}, especially at larger SZAs, mainly due to differences in overhead ozone. The climatological overhead ozone was nearly 60% larger than that measured by CPFM (which did provide overhead ozone and surface reflectivity), leading to APL_{clim} j_{O_3} smaller than APL_{CPFM} by a factor of 2 at SZAs $< 85°$, with larger differences at larger SZAs. The in situ ozone scaling mostly improved overhead ozone correlation and improved agreement with CPFM, but the correlation of j_{O_3} model modes worsened somewhat overall. The use of POAM III potential vorticity reconstructions for ozone provided input data for SOLVE that were decidedly superior to climatologies.

Appendix F

Definitions of Meteorological Terms

This dissertation, chapters 5 and 6 in particular, relies on a number of concepts commonly used in meteorology and the study of atmospheric dynamics, including potential temperature, potential vorticity, streamfunction, and the polar vortex. In order to clarify how ozone loss using stellar occultation and the quantification of the optical effects of polar stratospheric clouds (PSCs) on ozone loss were computed, these terms will be briefly discussed here.

F.1 Potential Temperature

For an ideal gas undergoing adiabatic motions in the atmosphere, the first law of thermodynamics may be integrated from a state at pressure p and temperature T to Earth's surface at pressure p_s and temperature θ:

$$\theta = T(p_s/p)^{R/c_p}, \tag{F.1}$$

where R is the gas constant and c_p is the heat capacity at constant pressure of the gas. Eq. (F.1) defines *potential temperature*[1] θ, which is simply the temperature of an air parcel in the atmosphere if it were moved (compressed or expanded) adiabatically to the surface. Potential temperature generally increases with altitude as pressure drops and more compression is required to reach p_s. For reversible processes, fractional changes in θ are proportional to changes in entropy. Therefore, adiabatic (isentropic) motions in the atmosphere occur along constant–potential temperature surfaces, often making potential temperature an ideal vertical coordinate (analogous to altitude) for studying synoptic-scale atmospheric dynamics.

F.2 Potential Vorticity

Another important meteorological concept utilized in this work is that of vorticity, or the microscopic measure of the rotation of a fluid. The absolute vorticity $\boldsymbol{\omega}_\mathbf{a}$ of the atmosphere is the curl of the absolute velocity $\mathbf{U}_\mathrm{a}$ of its wind field. For large-scale motions, only the vertical component of the vorticity is important:

$$\eta \equiv \mathbf{k} \cdot (\boldsymbol{\nabla} \times \mathbf{U}_\mathrm{a}). \tag{F.2}$$

The absolute vorticity η is composed of the planetary vorticity f, due to the rotation of the Earth (i.e., via the Coriolis force), and the relative vorticity ζ, owing to the motions of the atmosphere relative to the Earth's surface.

It can be shown that for a closed loop defining an infinitesimal air parcel of area δA on a roughly horizontal isentropic (θ) surface, that $\delta A(\zeta_\theta + f)$ is constant. Further,

[1]For a more detailed derivation of potential temperature, see *Wallace and Hobbs* [1977] or *Holton* [1992].

for a parcel confined between two potential temperature surfaces, *potential vorticity*[2] (Ertel's potential vorticity, EPV, or simply PV) may be defined as follows:

$$\mathrm{PV} \equiv (\zeta_\theta + f)\left(-g\frac{\partial\theta}{\partial p}\right) = \text{constant}, \tag{F.3}$$

where g is the acceleration of gravity. PV has units of K kg^{-1} m^2 s^{-1}. Potential vorticity is conserved in a homogeneous, incompressible fluid and is a powerful constraint on large-scale atmospheric motions. The conservation of PV makes it useful as a "tracer" of the motion of air parcels, in some respects analogous to a chemical tracer.

Ertel's potential vorticity increases exponentially with altitude. "Modified" potential vorticity (MPV) [*Lait*, 1994], defined as

$$\mathrm{MPV} = \mathrm{EPV} \times \left(\frac{\theta}{420.0\ \mathrm{K}}\right)^{-\frac{9}{2}}, \tag{F.4}$$

is often more suitable when considering vertical profiles of PV, reducing its exponential gradient with altitude.

F.3 Streamfunction

Wind fields in the atmosphere are 3-dimensional, but the vertical component is often very small. As a result, quasi-nondivergent, horizontal wind fields are often considered in meteorological analyses. If the horizontal wind field **V** is defined as

$$\mathbf{V} \equiv \mathbf{i}u + \mathbf{j}v, \tag{F.5}$$

where **i** and **j** represent the zonal (east–west) and meridional (north–south) wind directions and u and v the corresponding wind speeds, respectively, then the velocity field

[2]For a more detailed description and derivation of Ertel's potential vorticity, see *Holton* [1992].

may be expressed in terms of *streamfunction*[3] ψ with

$$\mathbf{V} = \mathbf{k} \times \nabla \psi. \tag{F.6}$$

Likewise,

$$u = \partial \psi / \partial y, \;\; v = \partial \psi / \partial x, \tag{F.7}$$

where x and y are longitude and latitude, respectively.

Stream*lines*, connecting points of constant ψ, may be used in maps to indicate the instantaneous wind field, being everywhere parallel to **V** at a particular level. The spacing of the streamlines is inversely proportional to the wind speed. A wind jet, such as that defining the edge of the polar vortex [*Nash et al.*, 1996], may be identified by a region of closely spaced streamlines, a maximum of the streamfunction.

F.4 Polar Vortex

Net solar heating in the tropics and cooling at the poles causes large-scale ascent of air near the equator and large-scale descent, or subsidence, at the poles. These air motions, combined with wave-driven pumping, lead to the transport of low-latitude stratospheric air to the polar regions [*Holton et al.*, 1995]. Because of this poleward circulation and the rotation of the Earth, a pronounced circumpolar wind field forms each winter. The *polar vortex* is confined by a steep potential vorticity gradient and a jet of high winds that inhibit mixing with lower-latitude air, thus isolating vortex chemistry from the rest of the atmosphere. Radiative, diabatic cooling of the vortex during the Sunless winter leads to very cold temperatures ($<$200 K), subsidence, and the formation of polar stratospheric

[3]For a more detailed derivation of the streamfunction, see *Holton* [1992] and *Wallace and Hobbs* [1977].

clouds, which activate chlorine reservoirs (see section 1.1.4). The vortex remains intact until mid-spring, allowing reactive chlorine species at high concentrations to photolyze after the Sun returns, destroying ozone and forming the “ozone hole” when conditions are favorable. Though the Antarctic vortex is more stable, longer-lived, and colder than its Arctic counterpart, ozone depletion in the high-latitude Northern Hemisphere is worsening [*Newman et al.*, 1997].

F.5 Objective Determination of the Polar Vortex

The edge of the polar vortex is characterized by steep temperature and chemical gradients and strong westerly winds. *Nash et al.* [1996] developed an objective description of the polar vortex edge, which is used in chapter 6 as follows.

Using the UKMO meteorological analysis [*Swinbank and O'Neill*, 1994], Ertel's potential vorticity was computed throughout the Northern Hemisphere over 400–800 K potential temperature, for each day during the PSC analysis period. The EPV isolines were then represented in terms of *equivalent latitude*. The equivalent latitude corresponding to a given EPV isoline is simply the geographic latitude circle that encloses the same area on the Earth's surface. EPV increases from near zero at the equator to a maximum within the vortex, with a sigmoidal relationship.

The derivative of EPV was computed with respect to equivalent latitude (the maximum gradient is a simple definition of the vortex edge). The EPV gradient was then multiplied by the average wind speed along the EPV isolines. The EPV isoline corresponding to the maximum of this product, as a function of equivalent latitude, was taken to be the vortex edge.

Appendix G

Photolysis Atlas

The APL radiative transfer model (current, SOLVE version, described in appendix A) has been used to create a "photolysis atlas" of *j*-values, as functions of wavelength, throughout the troposphere and stratosphere. Figure G.1, on the following pages, contains wavelength-dependent calculations of *j*-values for the photochemical processes listed in Table A.1, over 0–40 km and at solar zenith angles (SZAs) of 0°, 60°, 85°, and 90°. The contours are drawn to maintain equal areas, so each row of plots has a different scale.

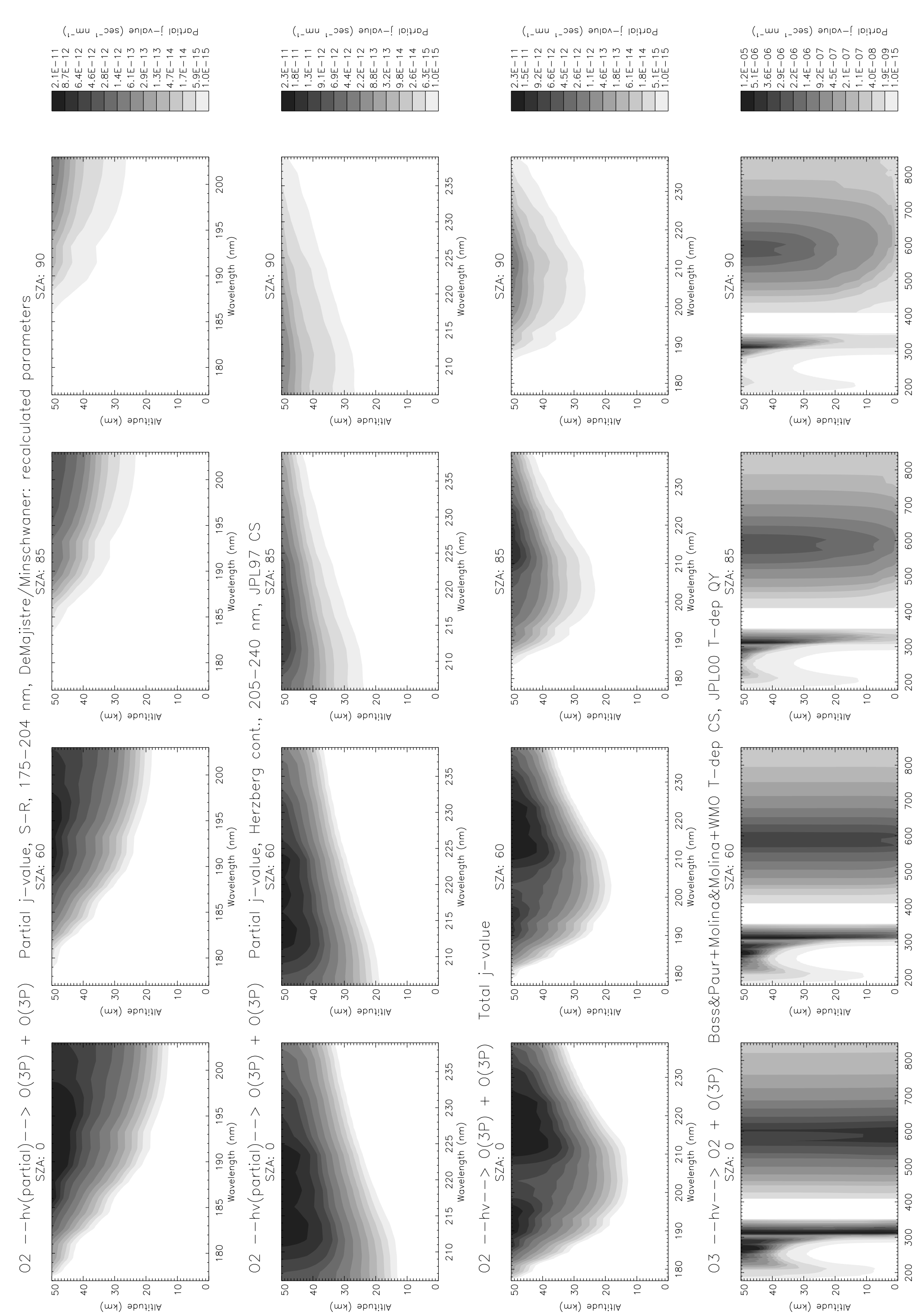

Figure G.1. Spectral *j*-value altitude profiles.

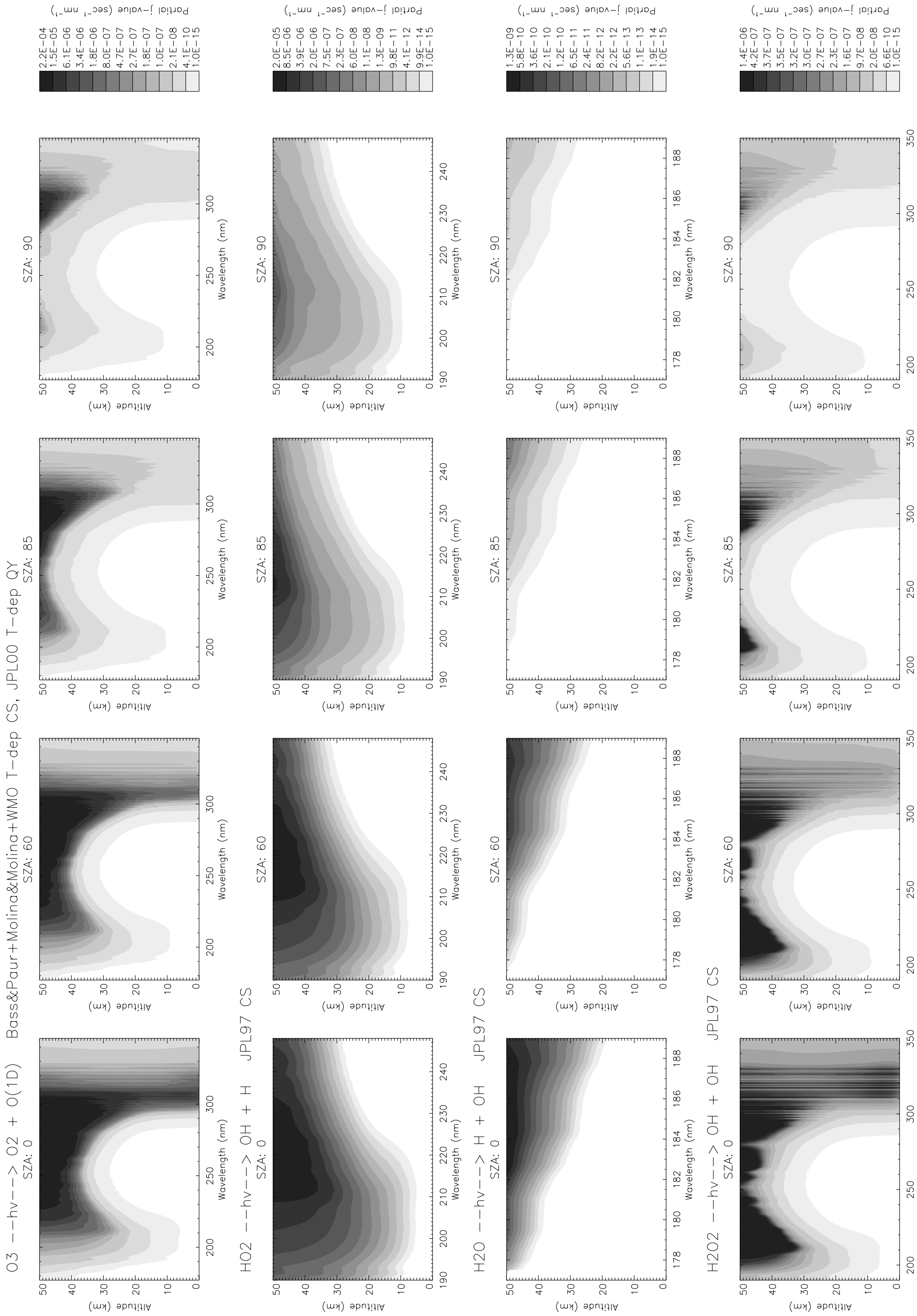

Figure G.1. Spectral j-value altitude profiles (continued).

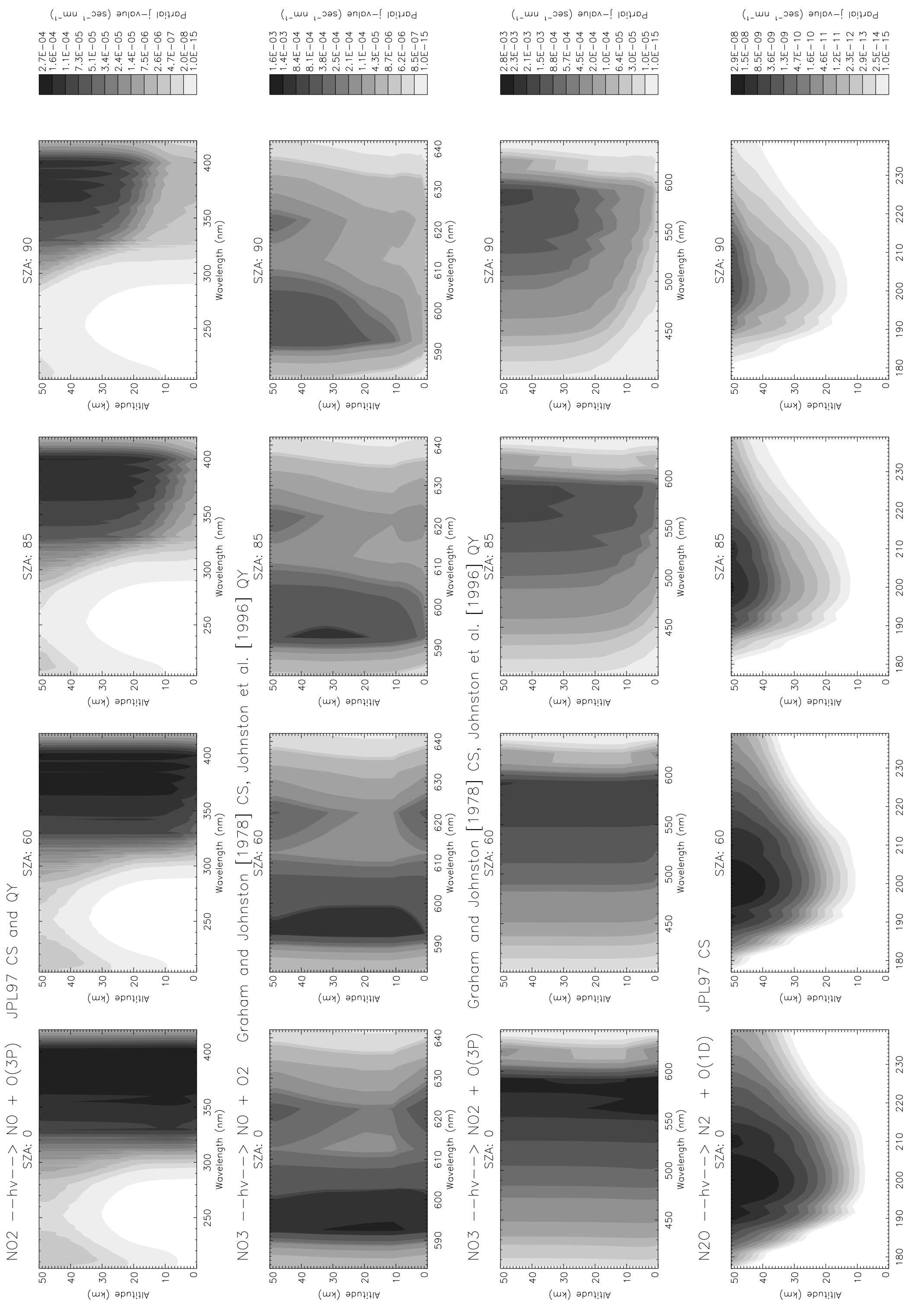

Figure G.1. Spectral *j*-value altitude profiles (continued).

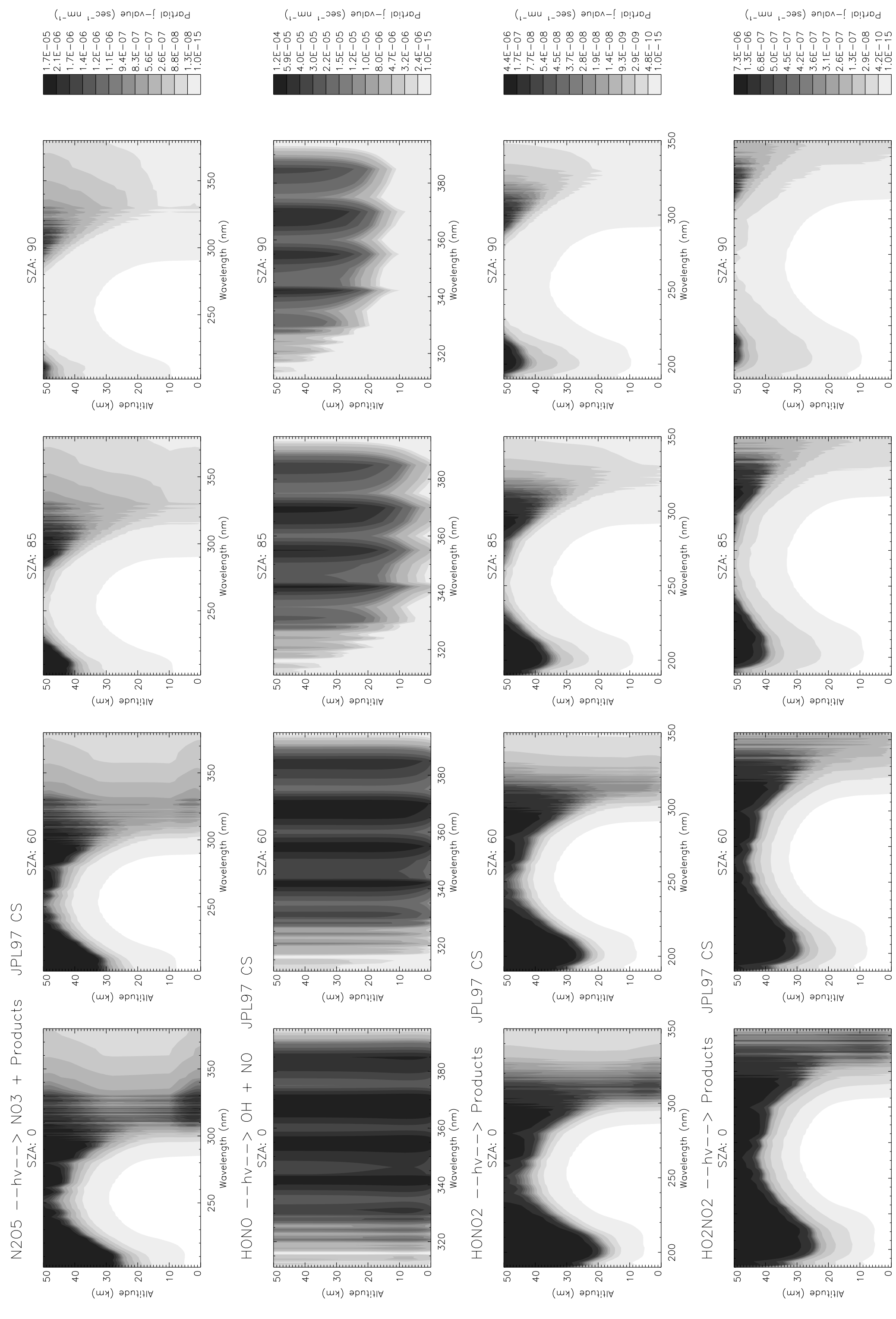

Figure G.1. Spectral *j*-value altitude profiles (continued).

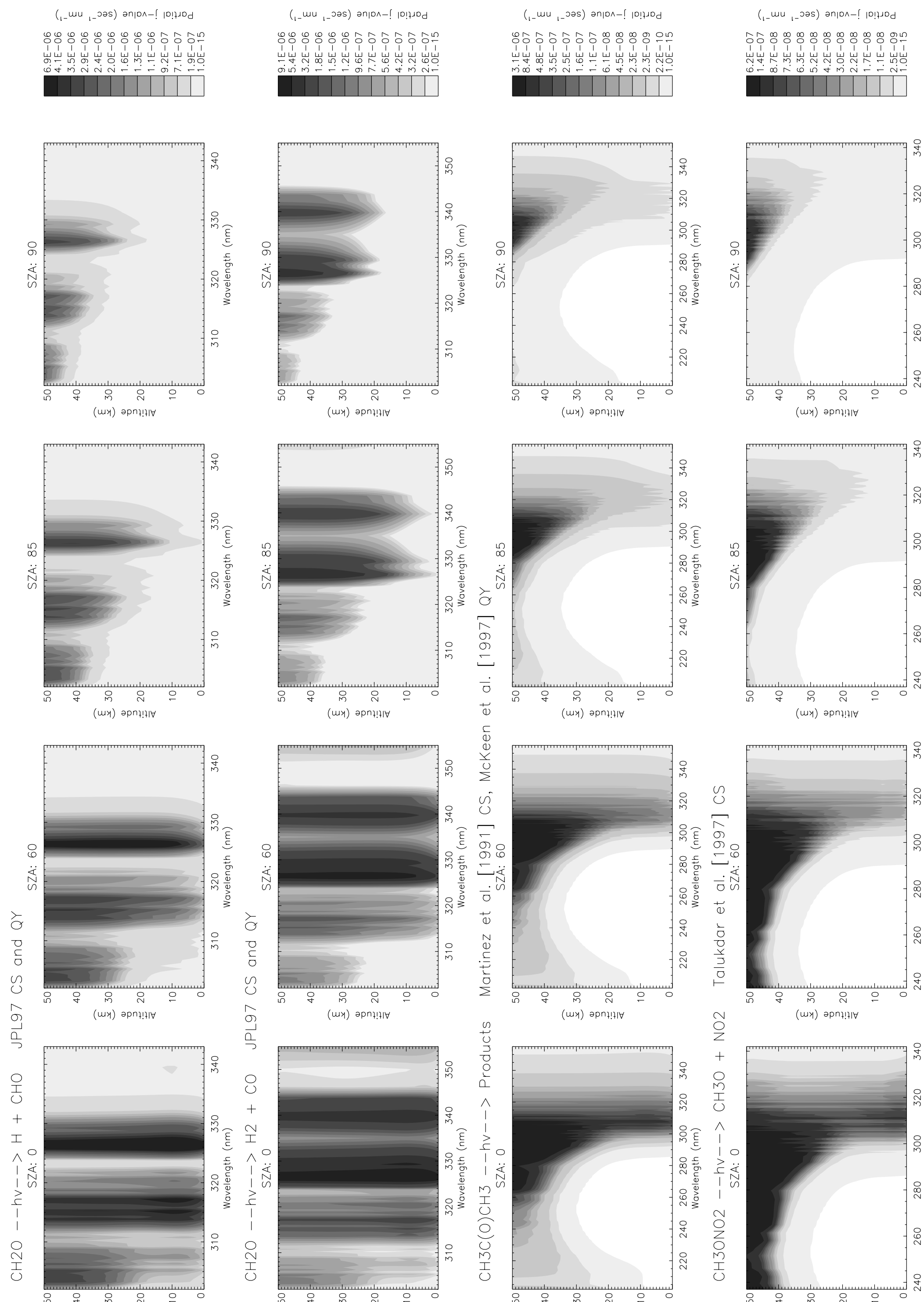

Figure G.1. Spectral *j*-value altitude profiles (continued).

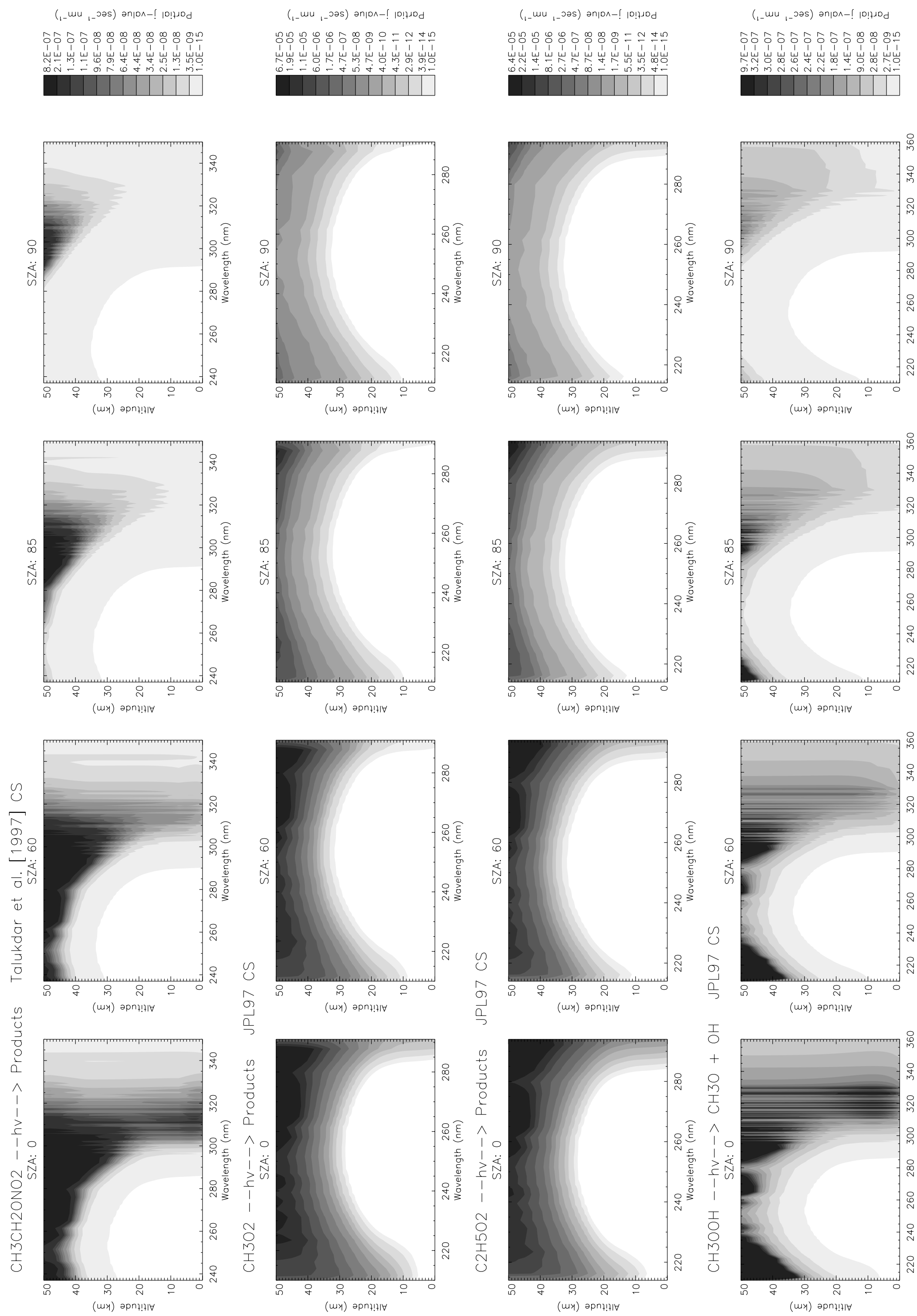

Figure G.1. Spectral *j*-value altitude profiles (continued).

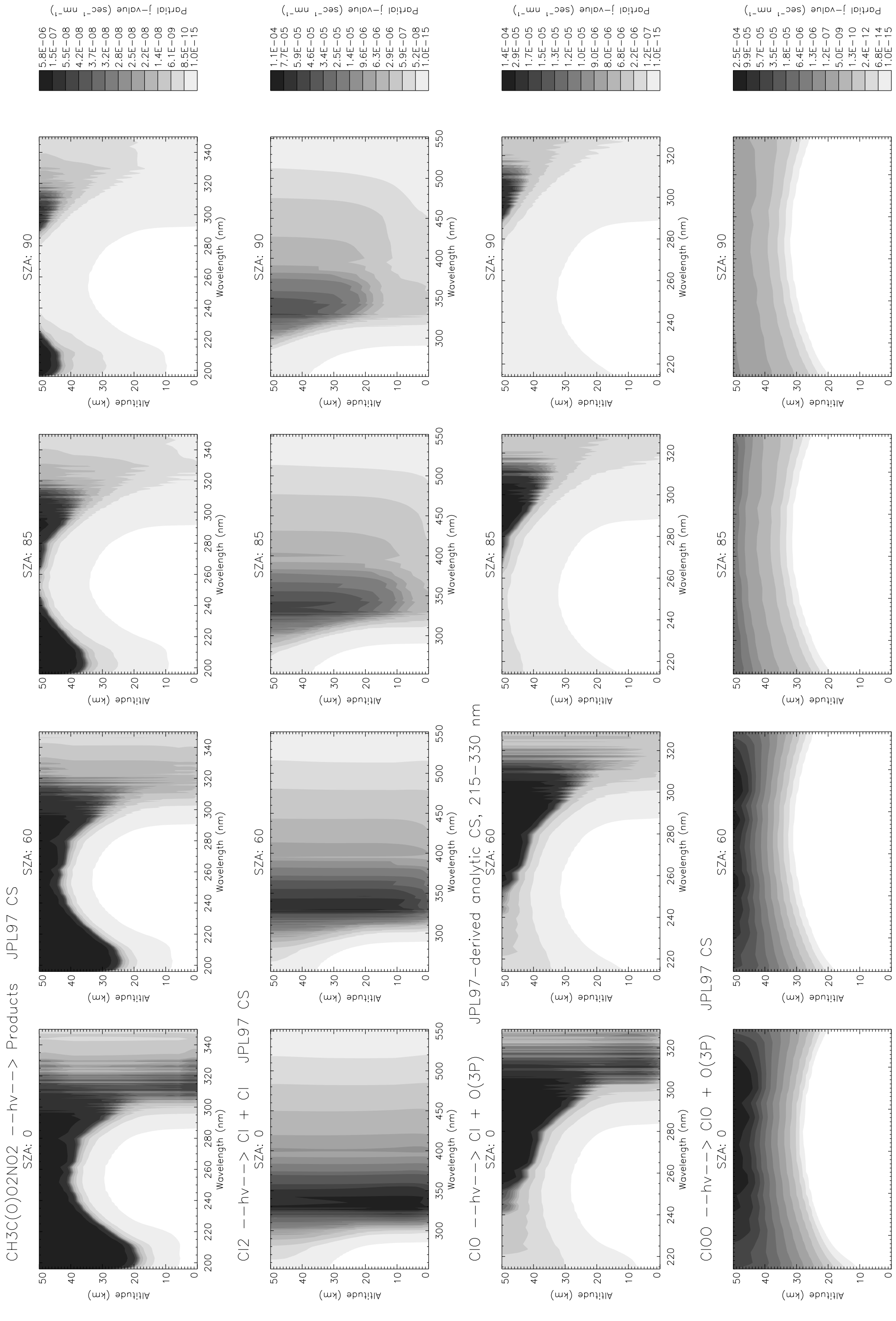

Figure G.1. Spectral j-value altitude profiles (continued).

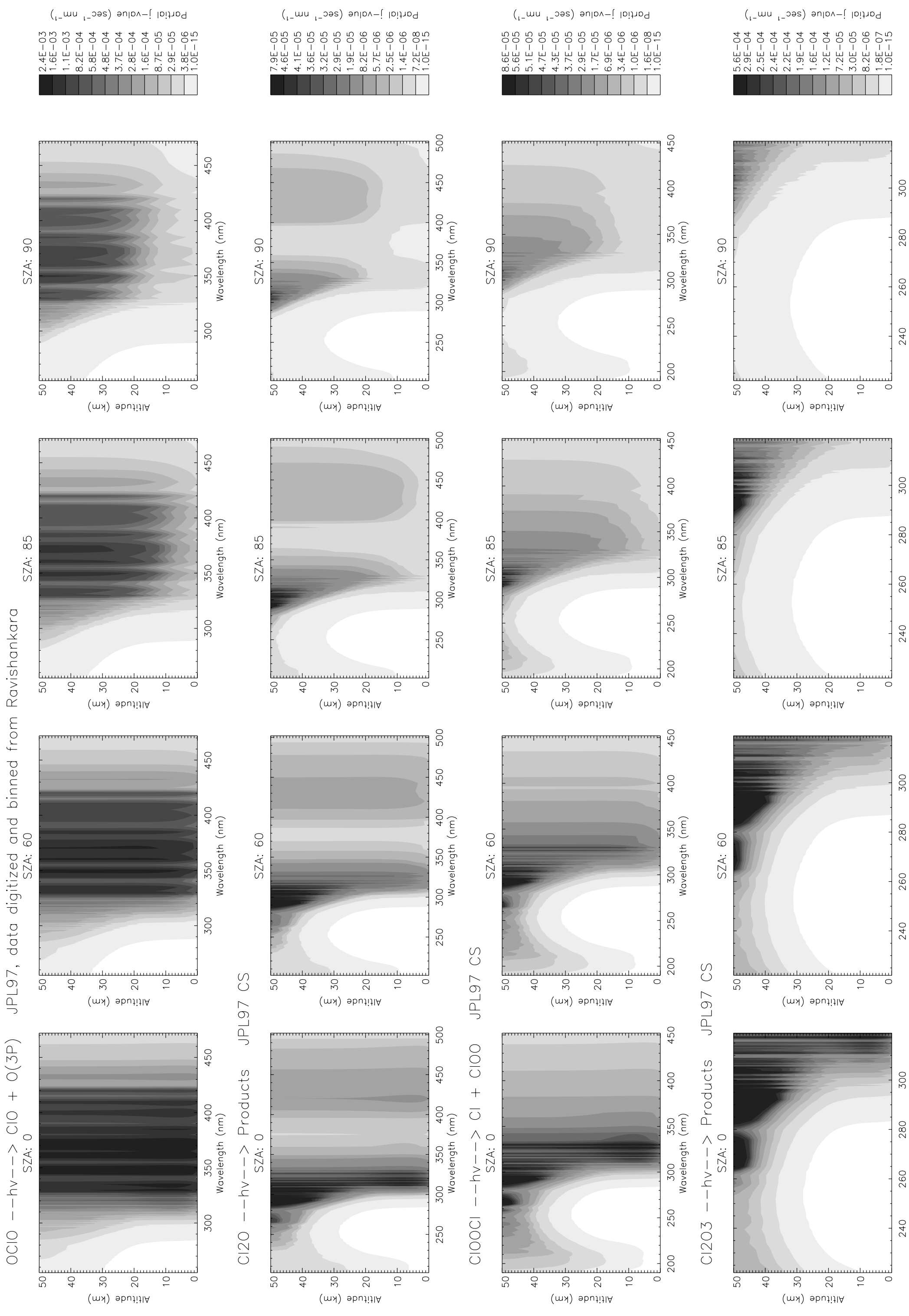

Figure G.1. Spectral *j*-value altitude profiles (continued).

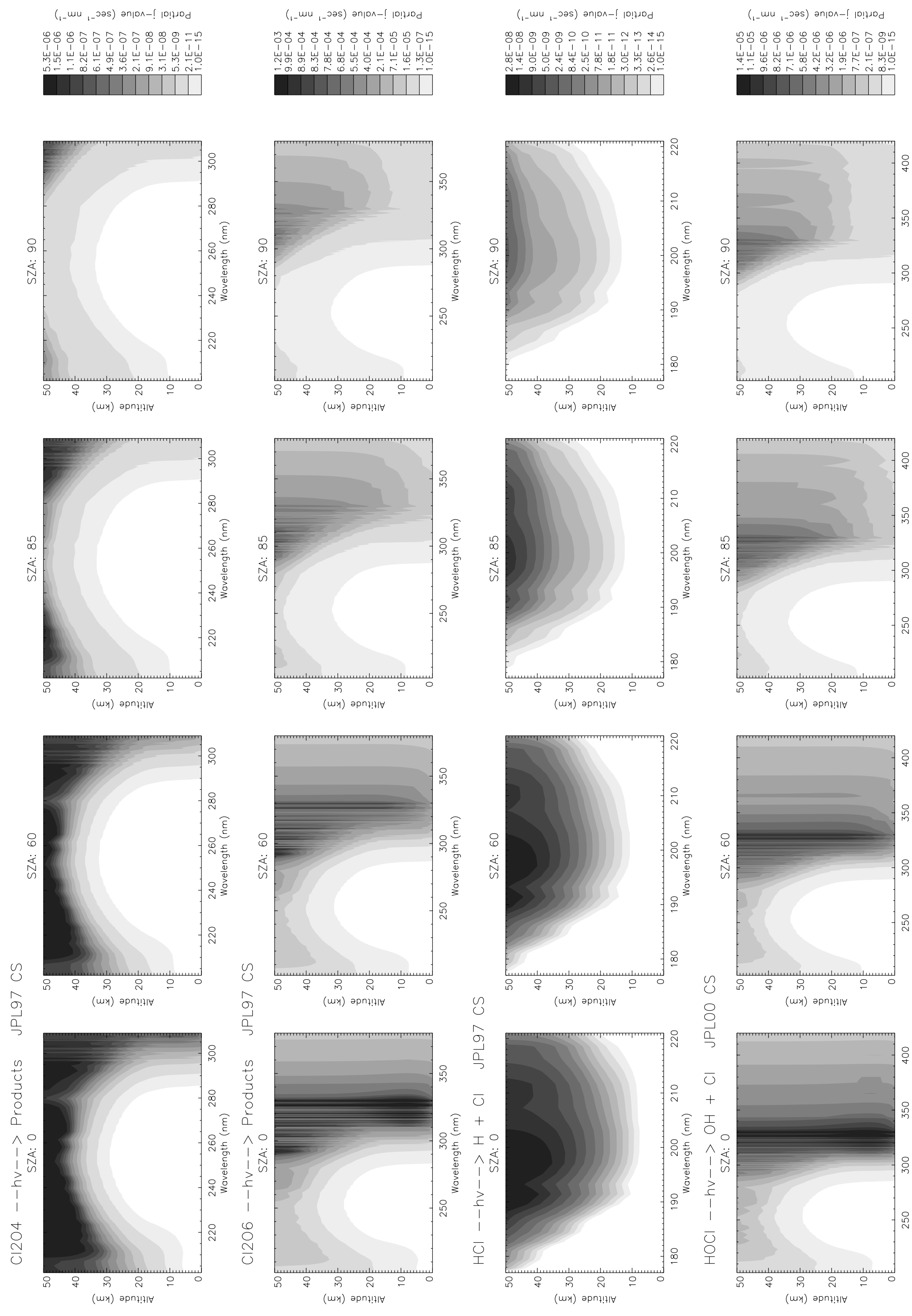

Figure G.1. Spectral *j*-value altitude profiles (continued).

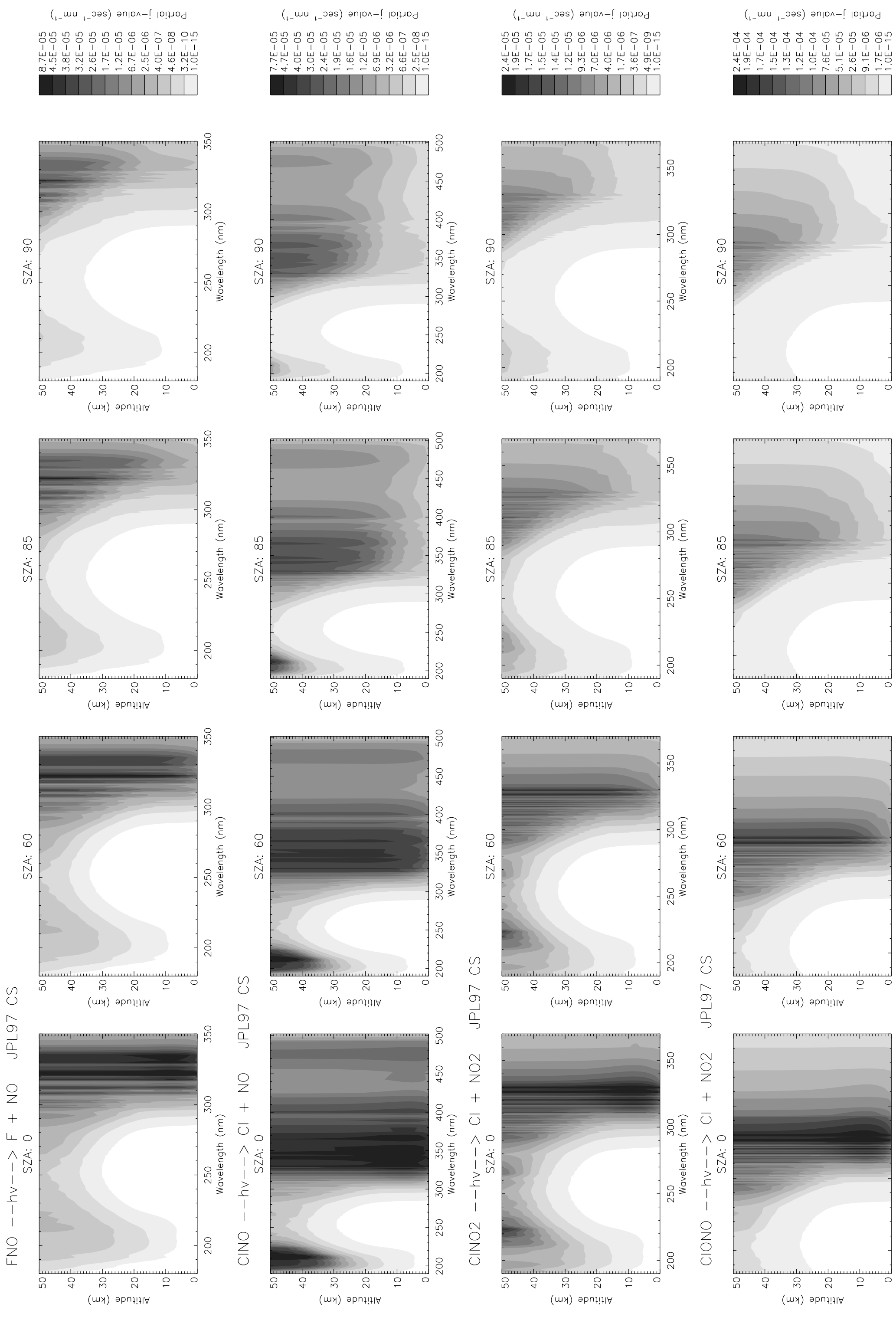

Figure G.1. Spectral *j*-value altitude profiles (continued).

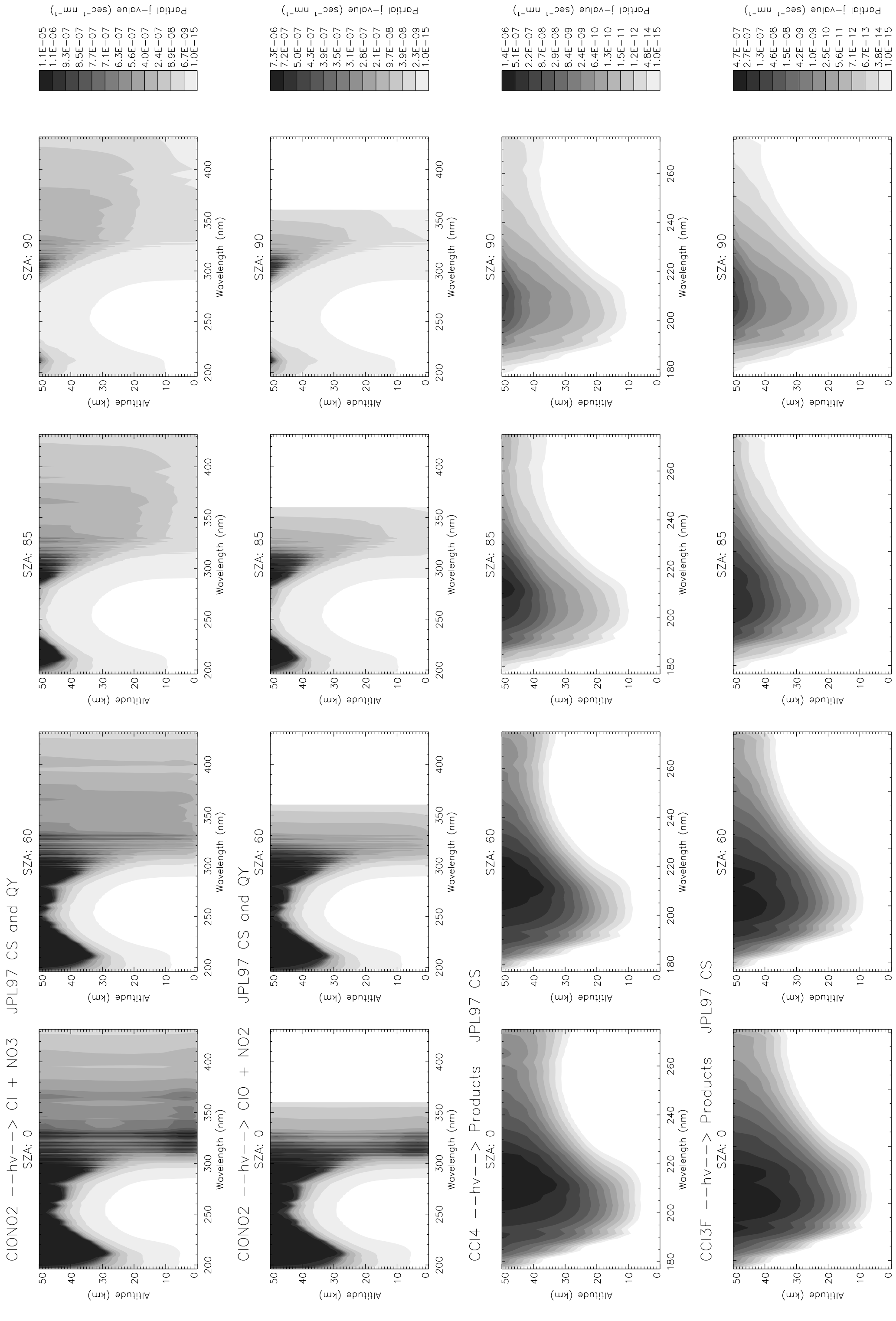

Figure G.1. Spectral *j*-value altitude profiles (continued).

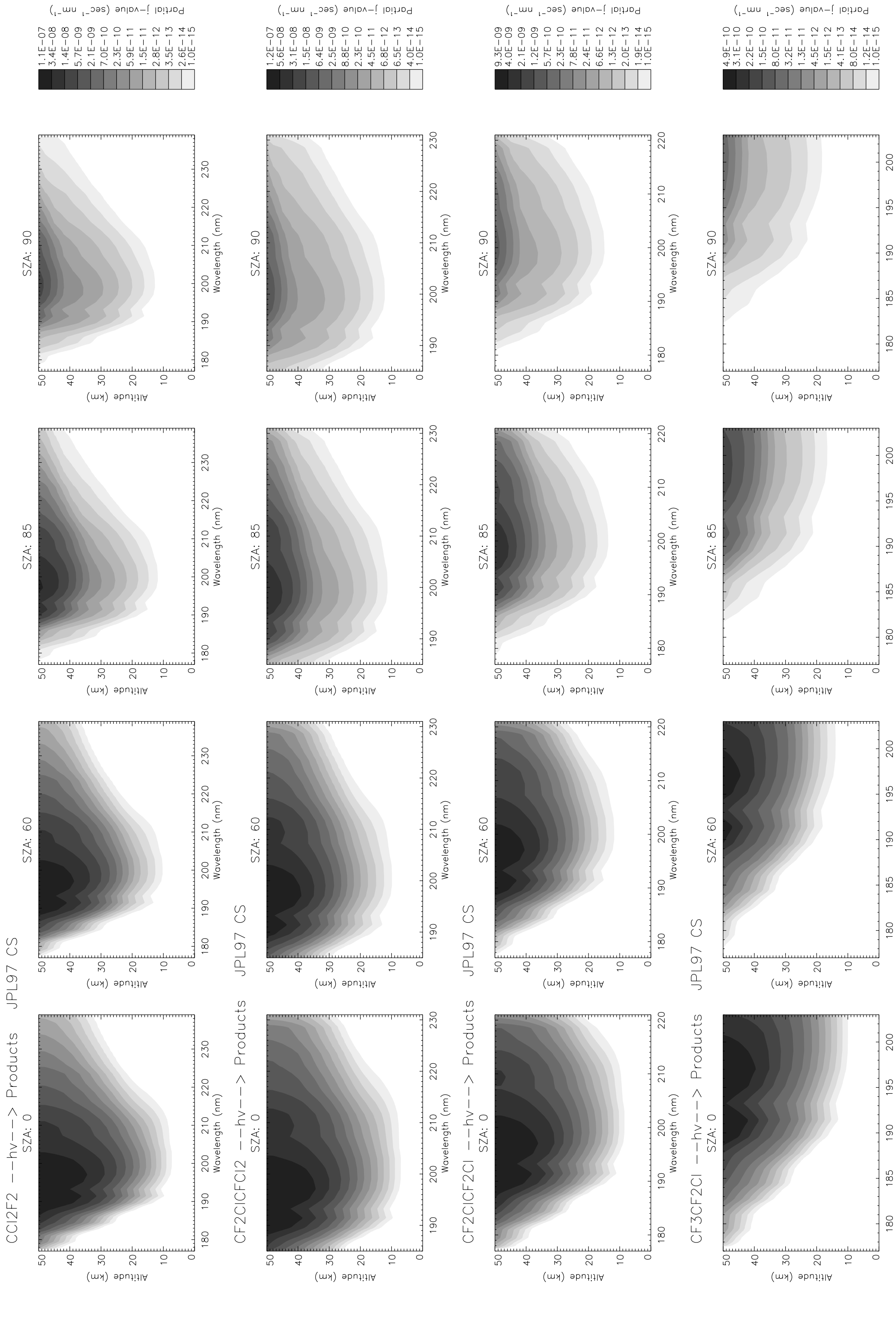

Figure G.1. Spectral *j*-value altitude profiles (continued).

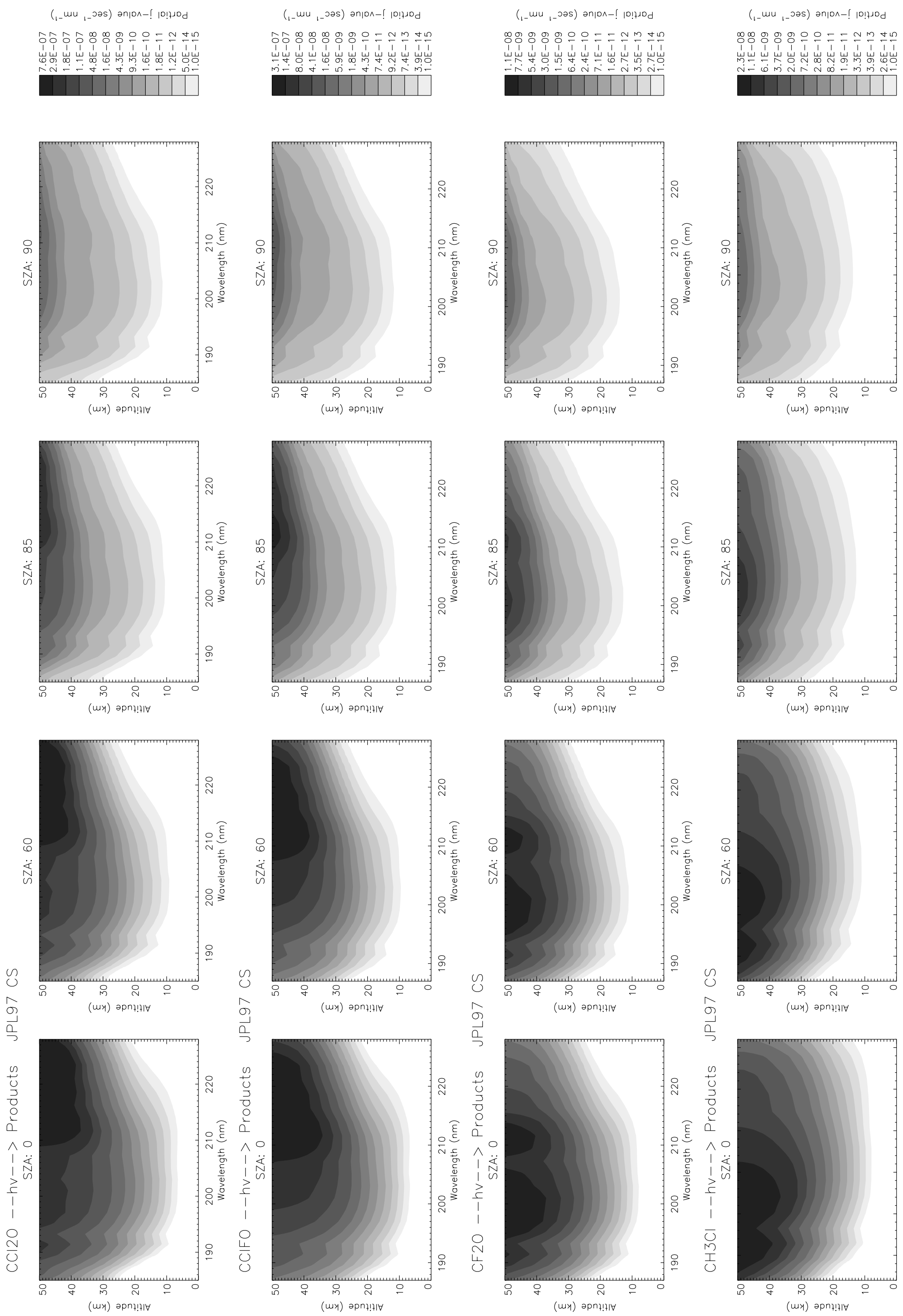

Figure G.1. Spectral *j*-value altitude profiles (continued).

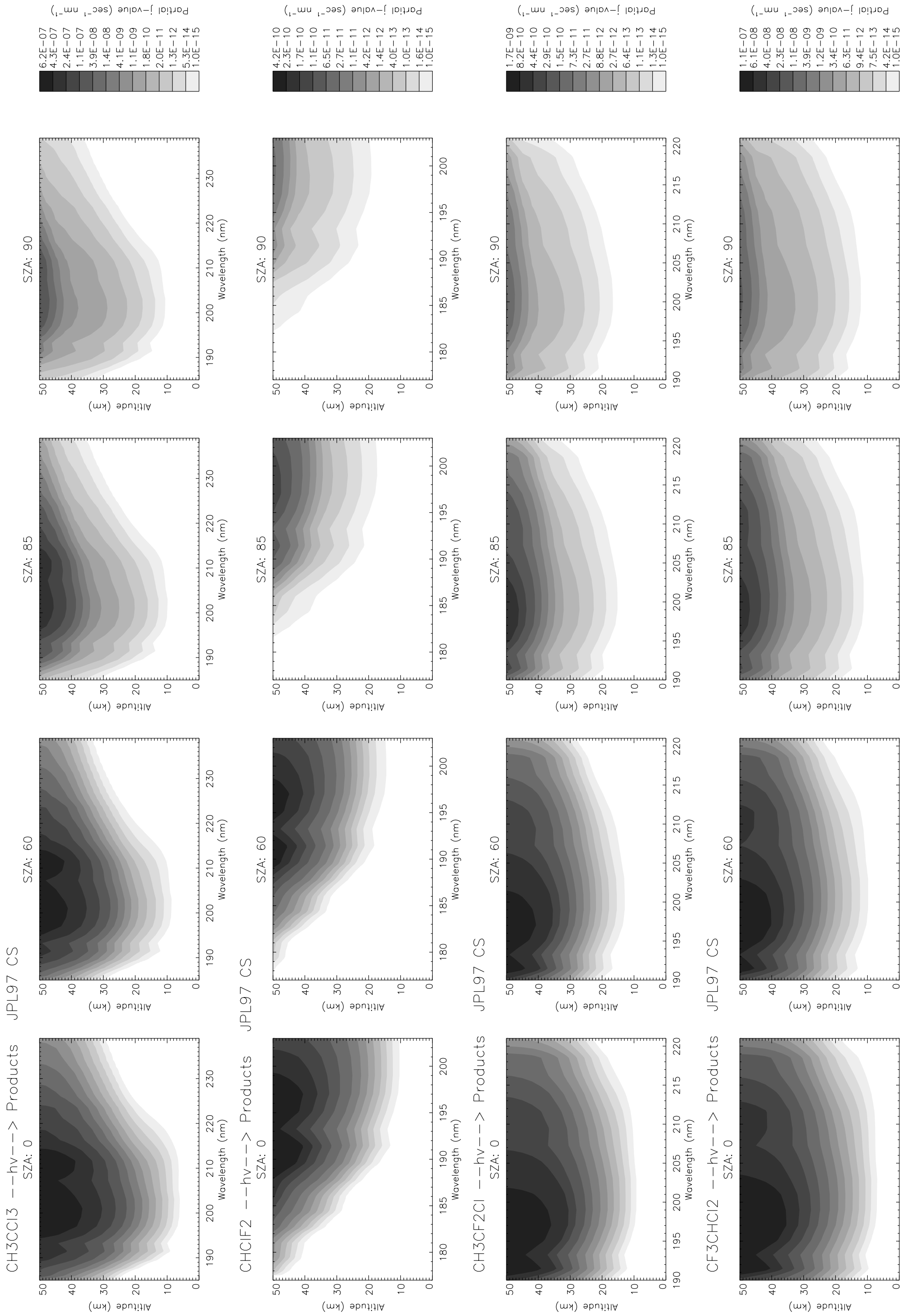

Figure G.1. Spectral *j*-value altitude profiles (continued).

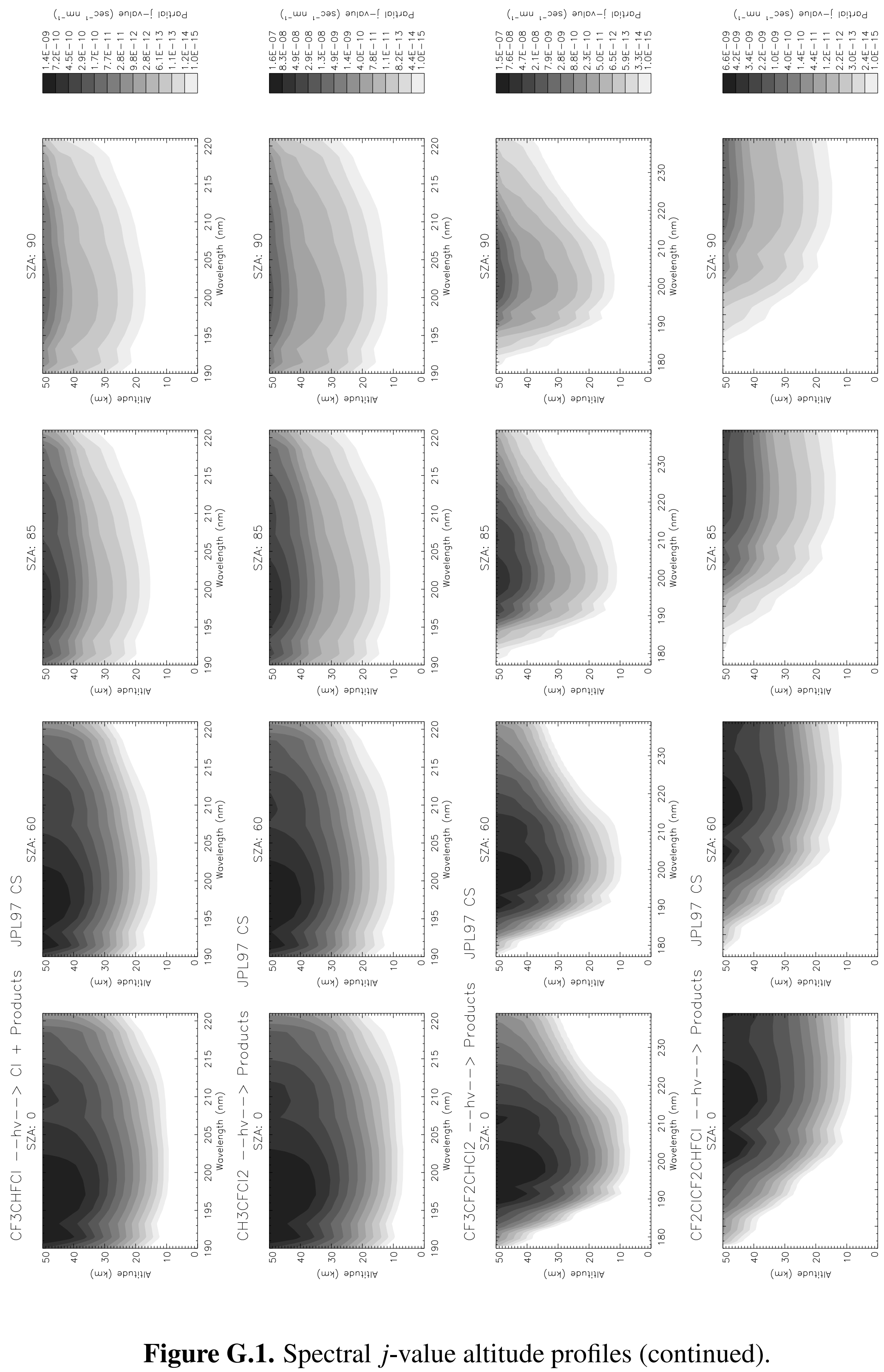

Figure G.1. Spectral *j*-value altitude profiles (continued).

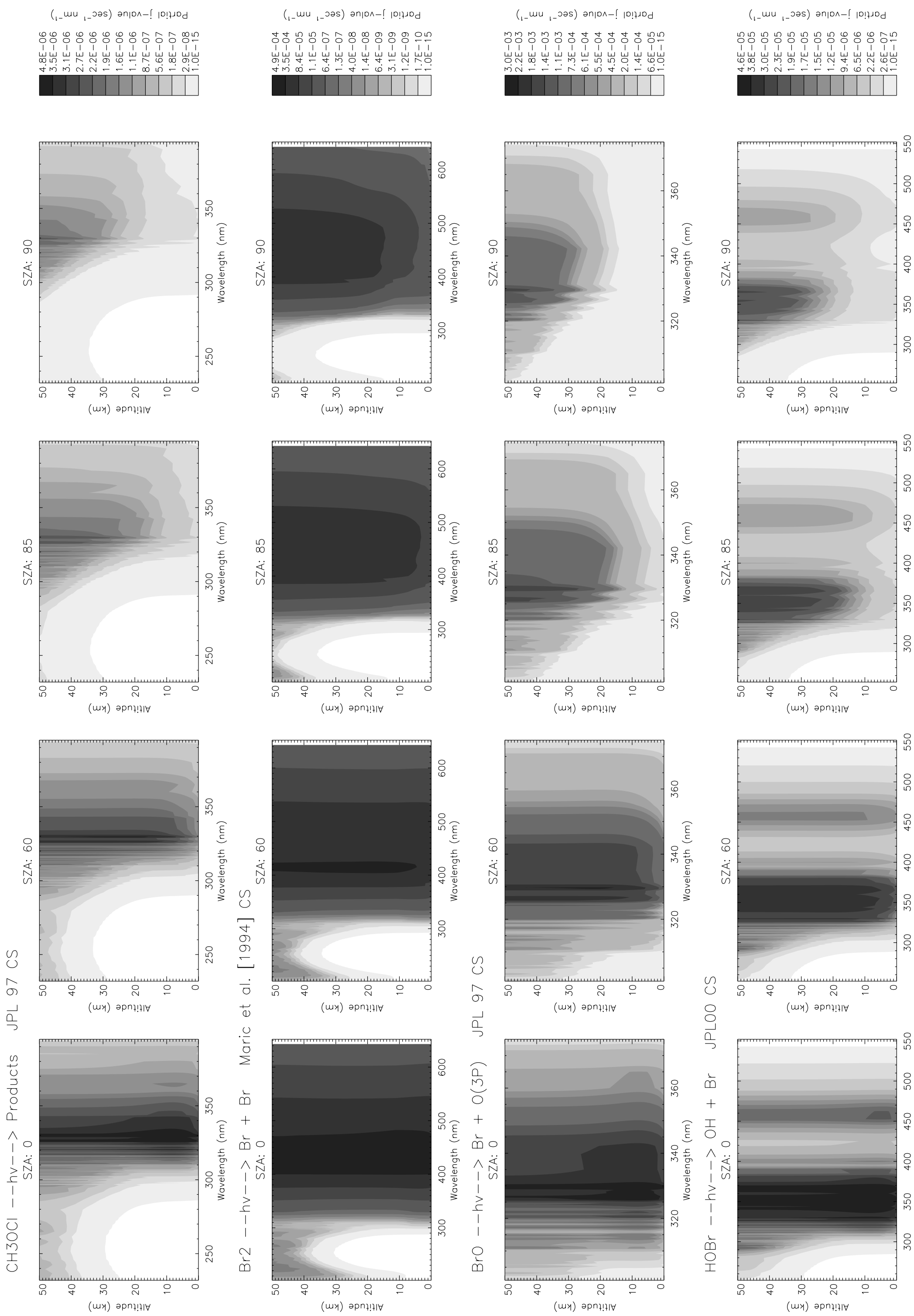

Figure G.1. Spectral *j*-value altitude profiles (continued).

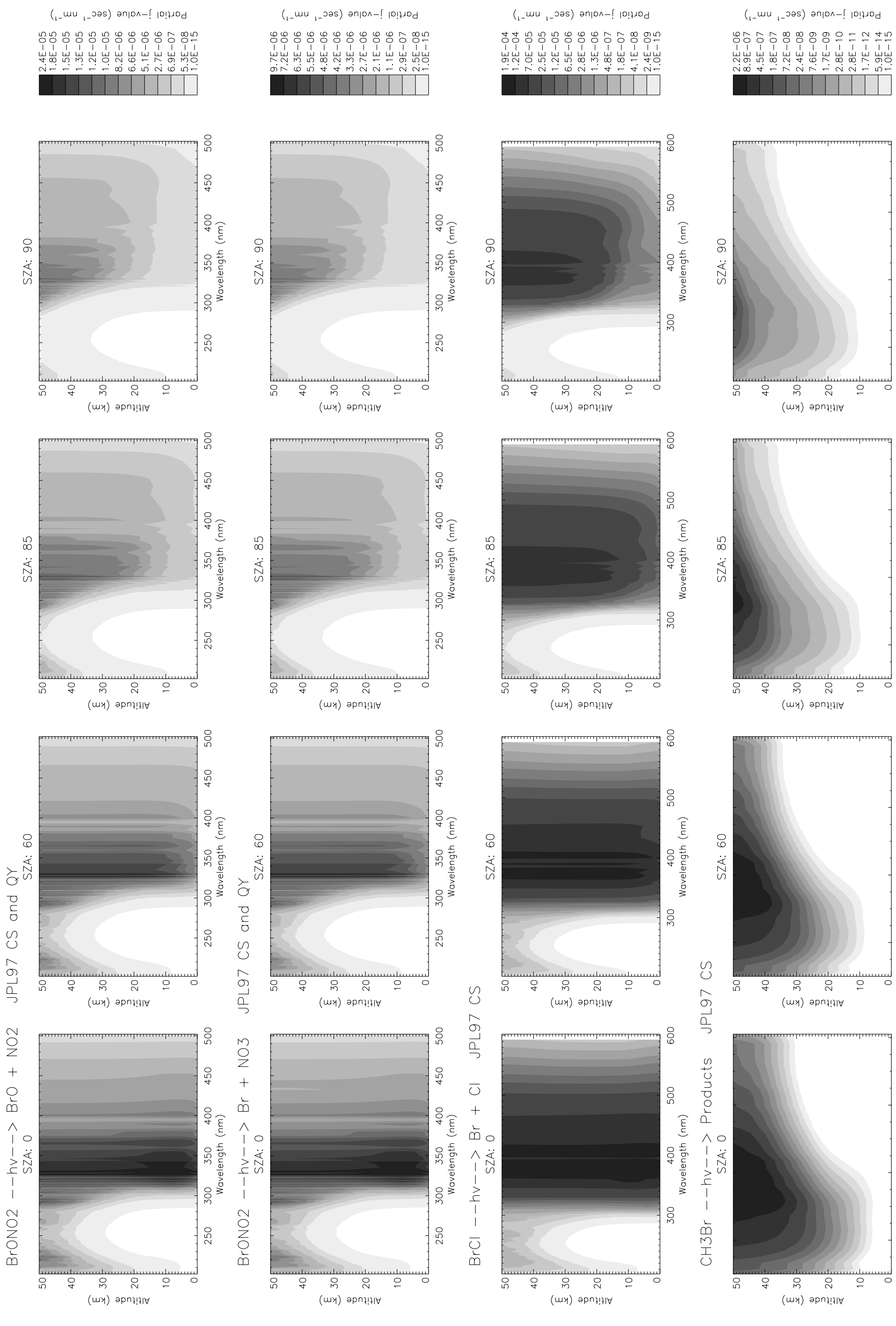

Figure G.1. Spectral *j*-value altitude profiles (continued).

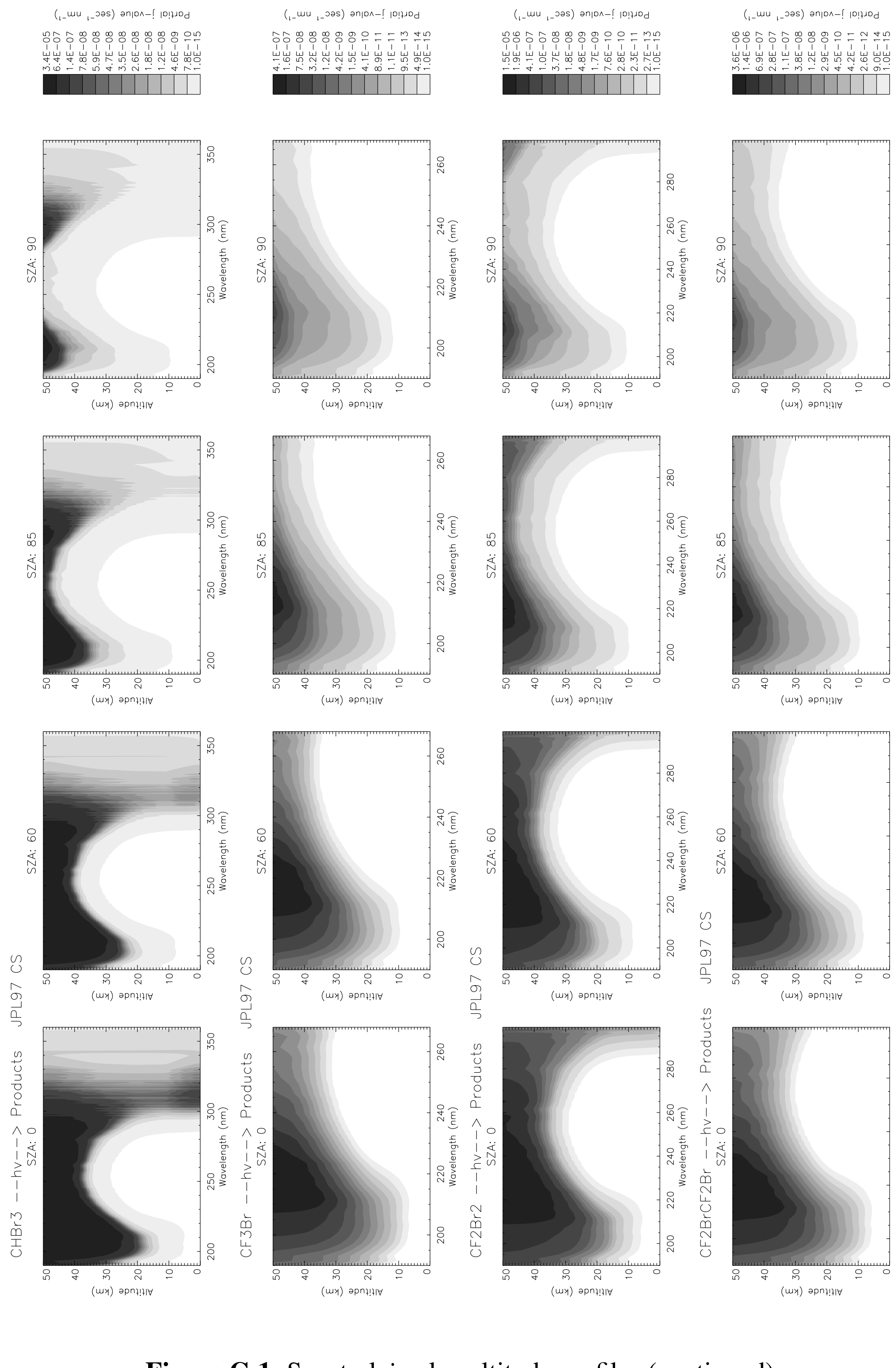

Figure G.1. Spectral j-value altitude profiles (continued).

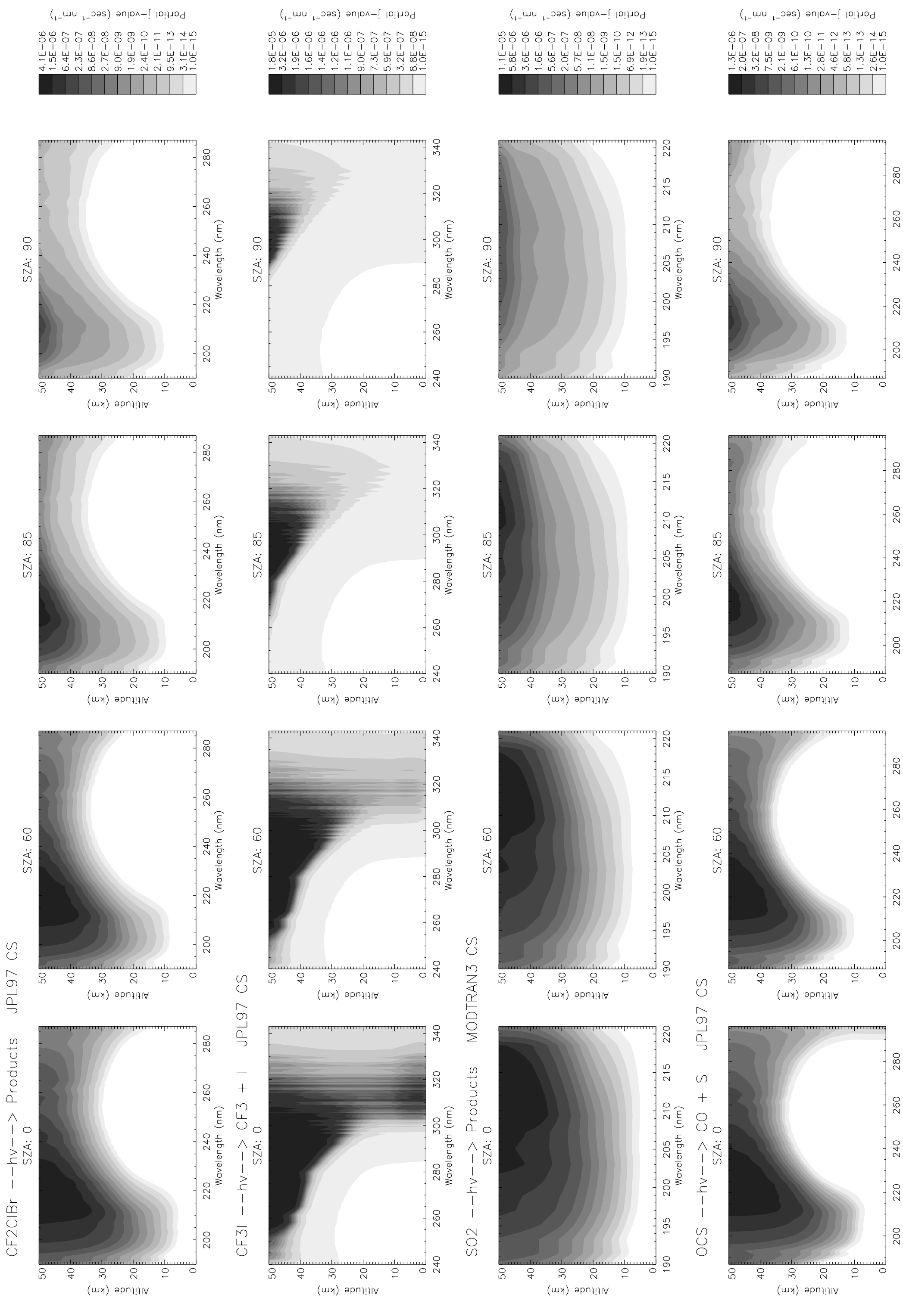

Figure G.1. Spectral *j*-value altitude profiles (continued).

REFERENCES

Albritton, D. L., F. C. Fehsenfeld, and A. F. Tuck, Instrumental requirements for global atmospheric chemistry, *Science*, *250*, 75–81, 1990.

Anderson, D. E., R. DeMajistre, S. A. Lloyd, and P. K. Swaminathan, Impact of aerosols and clouds on the troposphere and stratosphere radiation field with application to twilight photochemistry at 20 km, *J. Geophys. Res.*, *100*, 7135–7145, 1995.

Anderson, D. E., Jr., The troposphere–stratosphere radiation field at twilight: A spherical model, *Planet. Space Sci.*, *31*, 1517–1523, 1983.

Anderson, D. E., Jr., and S. A. Lloyd, Polar twilight UV-visible radiation field: Perturbations due to multiple scattering, ozone depletion, stratospheric clouds, and surface albedo, *J. Geophys. Res.*, *95*, 7429–7434, 1990.

Anderson, D. E., Jr., and R. R. Meier, Effects of anisotropic multiple scattering on solar radiation in the troposphere and stratosphere, *Appl. Opt.*, *18*, 1955–1960, 1979.

Anderson, D. E., Jr., R. R. Meier, and J. B. Kumer, Improved model of Mie scattering contribution to tropospheric and stratospheric photodissociation fluxes, *Appl. Opt.*, *19*, 1230–1231, 1980.

Anderson, J. G., W. H. Brune, and M. H. Proffitt, Ozone destruction by chlorine radicals within the Antarctic vortex: The spatial and temporal evolution of $ClO–O_3$ anticorrelations based on in situ ER-2 data, *J. Geophys. Res.*, *94*, 11,465–11,479, 1989.

Arvesen, J. C., R. N. Griffin, Jr., and B. D. Pearson, Jr., Determination of extraterrestrial solar spectral irradiance from a research aircraft, *Appl. Opt.*, *11*, 2215–2232, 1969.

Bahe, F. C., W. N. Marx, U. Schurath, and E. P. Röth, Determination of the absolute photolysis rate of ozone by sunlight, $O_3 + h\nu \rightarrow O(^1D) + O_2(^1\Delta_g)$, at ground level, *Atmos. Environ.*, *13*, 1515–1522, 1979.

Bahe, F. C., U. Schurath, and K. H. Becker, The frequency of NO_2 photolysis at ground level, as recorded by a continuous actinometer, *Atmos. Environ.*, *14*, 711–718, 1980.

Bairai, S. T., and D. H. Stedman, Actinometric measurement of j[O_3–O(^1D)] using a luminol detector, *Geophys. Res. Lett.*, *19*, 2047–2050, 1992.

Bais, A., S. Madronich, J. Crawford, S. R. Hall, B. Mayer, M. van Weele, J. Lenoble, J. G. Calvert, C. A. Cantrell, R. E. Shetter, A. Hofzumahaus, P. Koepke, P. S. Monks, G. Frost, R. McKenzie, N. Krotkov, A. Kylling, W. H. Swartz, S. A. Lloyd, G. Pfister, T. J. Martin, E. P. Röth, E. Griffioen, A. Ruggaber, M. Krol, A. Kraus, G. D. Edwards, M. Müller, B. L. Lefer, P. Johnston, H. Schwander, D. Flittner, B. G. Gardiner, J. Barrick, and R. Schmitt, International Photolysis Frequency Measurement and Model Intercomparison: Spectral actinic solar flux measurements and modeling, *J. Geophys. Res.*, submitted, 2002.

Bass, A. M., and R. J. Paur, The ultraviolet cross-sections of ozone, I, The measurements, in *Atmospheric Ozone: Proceedings of the Quadrennial Ozone Symposium*, edited by C. S. Zerefos and A. M. Ghazi, pp. 606–610, Reidel, Boston, 1985.

Bates, D. R., and M. Nicolet, Atmospheric hydrogen, *Publ. Astron. Soc. Pac.*, *62*, 106–110, 1950.

Berk, A., L. S. Bernstein, and D. C. Robertson, MODTRAN: A moderate resolution model for LOWTRAN 7, *Tech. Rep. GL-TR-89-0122*, Geophysics Laboratory, Air Force System Command, Hanscom AFB, Massachusetts, 1989.

Bertaux, J. L., G. Mégie, T. Widemann, E. Chassefière, R. Pellinen, E. Kyrola, S. Korpela, and P. Simon, Monitoring of ozone trend by stellar occultations: The GOMOS instrument, *Adv. Space Res.*, *11*, 237–242, 1991.

Bevilacqua, R. M., et al., Observations and analysis of polar stratospheric clouds detected by POAM III during the 1999/2000 Northern Hemisphere winter, *J. Geophys. Res.*, *107*(D20), 8281, doi:10.1029/2001JD000477, 2002.

Blackburn, T. E., S. T. Bairai, and D. H. Stedman, Solar photolysis of ozone to singlet *D* oxygen atoms, *J. Geophys. Res.*, *97*, 10,109–10,117, 1992.

Brasseur, A.-L., R. Ramaroson, A. Delannoy, W. Skamarock, and M. Barth, Three-dimensional calculation of photolysis frequencies in the presence of clouds and impact on photochemistry, *J. Atmos. Chem.*, *41*, 211–237, 2002.

Brauers, T., and A. Hofzumahaus, Latitudinal variation of measured NO_2 photolysis frequencies over the Atlantic Ocean between 50°N and 30°S, *J. Atmos. Chem.*, *15*, 269–282, 1992.

Bremer, H., et al., Ozone depletion observed by the Airborne Submillimeter Radiometer (ASUR) during the Arctic Winter 1999/2000, *J. Geophys. Res.*, *107*(D20), 8277, doi:10.1029/2001JD000546, 2002.

Browell, E. V., S. Ismail, and W. B. Grant, Differential absorption lidar (DIAL) measurements from air and space, *Appl. Phys. B*, *67*, 399–410, 1998.

Browell, E. V., et al., LASE validation experiment, in *Advances in Atmospheric Remote Sensing with Lidar*, edited by A. Ansmann, R. Neuber, P. Rairoux, and U. Wandinger, pp. 289–295, Springer, New York, 1997.

Burris, J., W. Heaps, B. Gary, W. Hoegy, L. Lait, T. McGee, M. Gross, and U. Singh, Lidar temperature measurements during the Tropical Ozone Transport Experiment (TOTE)/Vortex Ozone Transport Experiment (VOTE) mission, *J. Geophys. Res.*, *103*, 3505–3510, 1998.

Burris, J., et al., Validation of temperature measurements from the airborne Raman ozone temperature and aerosol lidar during SOLVE, *J. Geophys. Res.*, *107*(D20), 8286, doi:10.1029/2001JD001028, 2002.

Burrows, J. P., A. Richter, A. Dehn, B. Deters, S. Himmelmann, S. Voigt, and J. Orphal, Atmospheric remote-sensing reference data from GOME, 2, Temperature-dependent absorption cross sections of O_3 in the 231–794 nm range, *J. Quant. Spectrosc. Radiat. Transfer*, *61*, 509–517, 1999.

Cantrell, C. A., J. G. Calvert, A. Bais, R. E. Shetter, B. L. Lefer, and G. D. Edwards, Overview and conclusions of the International Photolysis Frequency Measurement and Modeling Intercomparison (IPMMI) study, *J. Geophys. Res.*, submitted, 2002.

Carbary, J. F., E. H. Darlington, T. J. Harris, P. J. McEvaddy, M. J. Mayr, K. Peacock, and C. I. Meng, Ultraviolet and visible imaging and spectrographic imaging instrument, *Appl. Opt.*, *33*, 4201–4213, 1994.

Carslaw, K. S., et al., Increased stratospheric ozone depletion due to mountain-induced atmospheric waves, *Nature*, *391*, 675–678, 1998.

Castro, T., S. Madronich, S. Rivale, A. Muhlia, and B. Mar, The influence of aerosols on photochemical smog in Mexico City, *Atmos. Environ.*, *35*, 1765–1772, 2001.

Chameides, W., and J. C. G. Walker, A photochemical theory of tropospheric ozone, *J. Geophys. Res.*, *78*, 8751–8760, 1973.

Chandrasekhar, S., *Radiative Transfer*, Dover, New York, 1960.

Chapman, S., On ozone and atomic oxygen in the upper atmosphere, *Philos. Mag., S. 7*, *10*, 369–383, 1930.

Chubachi, S., A special ozone observation at Syowa Station, Antarctica from February 1982 to January 1983, in *Atmospheric Ozone: Proc. of the Quadrennial Ozone Symp.*, edited by C. S. Zerefos and A. M. Ghazi, pp. 285–289, D. Reidel, Norwell, Mass., 1985.

COESA, *U. S. Standard Atmosphere, 1976*, U. S. Government Printing Office, Washington, D. C., 1976.

Cotte, H., C. Devaux, and P. Carlier, Transformation of irradiance measurements into spectral actinic flux for photolysis rates determination, *J. Atmos. Chem.*, *26*, 1–28, 1997.

Crawford, J., D. Davis, G. Chen, R. Shetter, M. Müller, J. Barrick, and J. Olson, An assessment of cloud effects on photolysis rate coefficients: Comparison of experimental and theoretical values, *J. Geophys. Res.*, *104*, 5725–5734, 1999.

Crawford, J., R. Shetter, B. Lefer, C. Cantrell, W. Junkermann, S. Madronich, and J. Calvert, Cloud impacts on UV spectral actinic flux observed during IPMMI, *J. Geophys. Res.*, submitted, 2002.

Crutzen, P. J., The influence of nitrogen oxides on the atmospheric ozone content, *Quart. J. Roy. Meteor. Soc.*, *96*, 320–325, 1970.

Dahlback, A., and K. Stamnes, A new spherical model for computing the radiation field available for photolysis and heating at twilight, *Planet. Space Sci.*, *39*, 671–683, 1991.

Davidson, J. A., C. A. Cantrell, A. H. McDaniel, R. E. Shetter, S. Madronich, and J. G. Calvert, Visible-ultraviolet absorption cross sections for NO_2 as a function of temperature, *J. Geophys. Res.*, *93*, 7105–7112, 1988.

de Zafra, R. L., M. Jaramillo, A. Parrish, P. Solomon, B. Connor, and J. Barrett, High concentrations of chlorine monoxide at low altitudes in the Antarctic spring stratosphere: Diurnal variation, *Nature*, *328*, 408–411, 1987.

de Zafra, R. L., M. Jaramillo, J. Barrett, L. K. Emmons, P. M. Solomon, and A. Parrish, New observations of a large concentration of ClO in the springtime lower stratosphere over Antarctica and its implications for ozone-depleting chemistry, *J. Geophys. Res.*, *94*, 11,423–11,428, 1989.

Del Negro, L. A., D. W. Fahey, R. S. Gao, S. G. Donnelly, E. R. Keim, J. A. Neuman, R. C. Cohen, K. K. Perkins, L. C. Koch, R. J. Salawitch, S. A. Lloyd, M. H. Proffitt, J. J. Margitan, R. M. Stimpfle, G. P. Bonne, P. B. Voss, P. O. Wennberg, C. T. McElroy, W. H. Swartz, T. L. Kusterer, D. E. Anderson, L. R. Lait, and T. P. Bui, Comparison of modeled and observed values of NO_2 and J_{NO_2} during the Photochemistry of Ozone Loss in the Arctic Region in Summer (POLARIS) mission, *J. Geophys. Res.*, *104*, 26,687–26,703, 1999.

DeMajistre, R., and J.-H. Yee, Atmospheric remote sensing using a combined extinctive and refractive stellar occultation technique, 2, Inversion method for extinction measurements, *J. Geophys. Res.*, *107*(D15), 4260, doi:10.1029/2001JD000795, 2002.

DeMajistre, R., D. E. Anderson, S. Lloyd, P. K. Swaminathan, and S. Zasadil, Effects of refraction on photochemical calculations, *J. Geophys. Res.*, *100*, 18,817–18,822, 1995.

Demerjian, K. L., K. L. Schere, and J. T. Peterson, Theoretical estimates of actinic (spherically integrated) flux and photolytic rate constants of atmospheric species in the lower troposphere, *Adv. Environ. Sci. Technol.*, *10*, 369–459, 1980.

DeMore, W. M., S. P. Sander, D. M. Golden, R. F. Hampson, M. J. Kurylo, C. J. Howard, A. R. Ravishankara, C. E. Kolb, and M. J. Molina, Chemical kinetics and photochemical data for use in stratospheric modeling, *Tech. Rep. JPL Publication 97-4*, Jet Propulsion Laboratory, California Institute of Technology, Pasadena, California, 1997.

Dickerson, R. R., Direct measurements of ozone and nitrogen dioxide photolysis rates in the atmosphere, Ph.D. thesis, University of Michigan, Ann Arbor, Michigan, 1980.

Dickerson, R. R., and D. H. Stedman, Precision of NO_2 photolysis rate measurements, *Environ. Sci. Technol.*, *14*, 1261–1262, 1980.

Dickerson, R. R., D. H. Stedman, W. L. Chameides, P. J. Crutzen, and J. Fishman, Actinometric measurements and theoretical calculations of $j(O_3)$, the rate of photolysis of ozone to $O(^1D)$, *Geophys. Res. Lett.*, *6*, 833–836, 1979.

Dickerson, R. R., D. H. Stedman, and A. C. Delany, Direct measurements of ozone and nitrogen dioxide photolysis rates in the troposphere, *J. Geophys. Res.*, *87*, 4933–4946, 1982.

Dickerson, R. R., S. Kondragunta, G. Stenchikov, K. L. Civerolo, B. G. Doddridge, and B. N. Holben, The impact of aerosols on solar ultraviolet radiation and photochemical smog, *Science*, *278*, 827–830, 1997.

Fahey, D. W., K. K. Kelly, S. R. Kawa, A. F. Tuck, M. Loewenstein, K. R. Chan, and L. E. Heidt, Observations of denitrification and dehydration in the winter polar stratospheres, *Nature*, *344*, 321–324, 1990.

Fahey, D. W., R. S. Gao, L. A. Del Negro, E. R. Keim, S. R. Kawa, R. J. Salawitch, P. O. Wennberg, T. F. Hanisco, E. J. Lanzendorf, K. K. Perkins, S. A. Lloyd, W. H. Swartz, M. H. Proffitt, J. J. Martigan, J. C. Wilson, R. M. Stimpfle, R. C. Cohen, C. T. McElroy, C. R. Webster, M. Loewenstein, J. W. Elkins, and T. P. Bui, Ozone destruction and production rates between spring and autumn in the Arctic stratosphere, *Geophys. Res. Lett.*, *27*, 2605–2608, 2000.

Farman, J. C., B. G. Gardiner, and J. D. Shanklin, Large losses of total ozone in Antarctica reveal seasonal ClO_x/NO_x interaction, *Nature*, *315*, 207–210, 1985.

Finlayson-Pitts, B. J., and J. N. Pitts, Jr., *Chemistry of the Upper and Lower Atmosphere: Theory, Experiments and Applications*, Academic Press, San Diego, 2000.

Fish, D. J., R. L. Jones, R. A. Freshwater, H. K. Roscoe, D. J. Oldham, and J. E. Harries, Total ozone measured during EASOE by a UV-visible spectrometer which observes stars, *Geophys. Res. Lett.*, *21*, 1387–1390, 1994.

Früh, B., T. Trautmann, M. Wendisch, and A. Keil, Comparison of observed and simulated NO_2 photodissociation frequencies in a cloudless atmosphere and in continental boundary layer clouds, *J. Geophys. Res.*, *105*, 9843–9857, 2000.

Gao, R. S., L. A. Del Negro, W. H. Swartz, R. J. Salawitch, S. A. Lloyd, M. H. Proffitt, D. W. Fahey, S. G. Donnelly, J. A. Neuman, R. M. Stimpfle, and T. P. Bui, J_{NO_2} at high solar zenith angles in the lower stratosphere, *Geophys. Res. Lett.*, *28*, 2405–2408, 2001.

Gardner, E. P., P. D. Sperry, and J. G. Calvert, Primary quantum yields of NO_2 photodissociation, *J. Geophys. Res.*, *92*, 6642–6652, 1987.

Graham, R. A., and H. S. Johnston, The photochemistry of NO_3 and the kinetics of the N_2O_5–O_3 system, *J. Phys. Chem.*, *82*, 254–268, 1978.

Grant, W. B., E. V. Browell, C. F. Butler, S. C. Gibson, S. A. Kooi, and P. von der Gathen, Use of ozone distributions, potential vorticity, and cooling rates to estimate Arctic polar vortex ozone loss during the winter of 1999/2000, *J. Geophys. Res.*, submitted, 2001.

Gröbner, J., and J. B. Kerr, Ground-based determination of the spectral ultraviolet extraterrestrial solar irradiance: Providing a link between space-based and ground-based solar UV measurements, *J. Geophys. Res.*, *106*, 7211–7217, 2001.

Gunson, M. R., et al., The Atmospheric Trace Molecule Spectroscopy (ATMOS) experiment: Deployment on the ATLAS Space Shuttle missions, *Geophys. Res. Lett.*, *23*, 2333–2336, 1996.

Hanson, D., and K. Mauersberger, Laboratory studies of the nitric acid trihydrate: Implications for the south polar stratosphere, *Geophys. Res. Lett.*, *15*, 855–858, 1988.

Harder, J. W., J. W. Brault, P. V. Johnston, and G. H. Mount, Temperature dependent NO_2 cross sections at high spectral resolution, *J. Geophys. Res.*, *102*, 3861–3879, 1997.

Harvey, R. B., D. H. Stedman, and W. Chameides, Determination of the absolute rate of solar photolysis of NO_2, *J. Air Pollut. Control Assoc.*, *27*, 663–666, 1977.

He, S., and G. R. Carmichael, Sensitivity of photolysis rates and ozone production in the troposphere to aerosol properties, *J. Geophys. Res.*, *104*, 26,307–26,324, 1999.

Hicke, J., and A. Tuck, Polar stratospheric cloud impacts on Antarctic stratospheric heating rates, *Q. J. R. Meteorol. Soc.*, *127*, 1645–1658, 2001.

Hildebrand, J. H., *Principles of Chemistry*, Macmillan, New York, 1919.

Hofzumahaus, A., T. Brauers, U. Platt, and J. Callies, Latitudinal variation of measured O_3 photolysis frequencies $J(O^1D)$ and the primary OH production rates over the Atlantic Ocean between 50°N and 30°S, *J. Atmos. Chem.*, *15*, 283–298, 1992.

Hofzumahaus, A., A. Kraus, and M. Müller, Solar actinic flux spectroradiometry: A technique for measuring photolysis frequencies in the atmosphere, *Appl. Opt.*, *38*, 4443–4460, 1999.

Hofzumahaus, A., B. L. Lefer, P. S. Monks, S. R. Hall, A. Kylling, B. Mayer, R. E. Shetter, W. Junkermann, B. Bohn, A. Bais, J. G. Calvert, C. A. Cantrell, S. Madronich, G. D. Edwards, A. Kraus, M. Müller, R. Schmitt, P. Johnston, R. McKenzie, G. Frost, E. Griffioen, M. Krol, T. Martin, G. Pfister, E. P. Röth, A. Ruggaber, W. H. Swartz, S. A. Lloyd, and M. van Weele, Photolysis of O_3 to $O(^1D)$: Measurements and modeling during the International Photolysis Measurement and Modeling Intercomparison 1998, *J. Geophys. Res.*, submitted, 2002.

Holton, J. R., *An Introduction to Dynamic Meteorology*, third ed., Academic Press, San Diego, 1992.

Holton, J. R., P. H. Haynes, M. E. McIntyre, A. R. Douglass, R. B. Rood, and L. Pfister, Stratosphere–troposphere exchange, *Rev. Geophys.*, *33*, 403–439, 1995.

Hoppel, K., et al., POAM III observations of Arctic ozone loss for the 1999/2000 winter, *J. Geophys. Res.*, *107*(D20), 8262, doi:10.1029/2001JD000476, 2002.

Isaksen, I., and C. Jackman, Modeling the chemical composition of the future atmosphere, in *Aviation and the Global Atmosphere*, edited by J. E. Penner, D. H. Lister, D. J. Griggs, D. J. Dokken, and M. McFarland, pp. 121–163, Cambridge University Press, New York, 1999.

Jackson, J. O., D. H. Stedman, R. G. Smith, L. H. Hecker, and P. O. Warner, Direct NO_2 photolysis rate monitor, *Rev. Sci. Inst.*, *46*, 376–378, 1975.

Johnston, H., Reduction of stratospheric ozone by nitrogen oxide catalysts from supersonic transport exhaust, *Science*, *173*, 517–522, 1971.

Johnston, H. S., H. F. Davis, and Y. T. Lee, NO_3 photolysis product channels: Quantum yields from observed energy thresholds, *J. Phys. Chem.*, *100*, 4713–4723, 1996.

Junkermann, W., U. Platt, and A. Volz-Thomas, A photoelectric detector for the measurement of photolysis frequencies of ozone and other atmospheric molecules, *J. Atmos. Chem.*, *8*, 203–227, 1989.

Jursa, A. S. (Ed.), *Handbook of Geophysics and the Space Environment*, Air Force Geophysics Laboratory, Hanscom AFB, Massachusetts, 1985.

Kalnay, E., et al., The NCEP/NCAR 40-year reanalysis project, *Bull. Amer. Meteor. Soc.*, *77*, 437–471, 1996.

Kaye, J. A., and T. L. Miller, The ATLAS series of Shuttle missions, *Geophys. Res. Lett.*, *23*, 2285–2288, 1996.

Kelley, P., R. R. Dickerson, W. T. Luke, and G. L. Kok, Rate of NO_2 photolysis from the surface to 7.6 km altitude in clear-sky and clouds, *Geophys. Res. Lett.*, *22*, 2621–2624, 1995.

Klein, U., I. Wohltmann, K. Lindner, and K. F. Künzi, Ozone depletion and chlorine activation in the Arctic winter 1999/2000 observed in Ny-Ålesund, *J. Geophys. Res.*, *107*(D20), 8288, doi:10.1029/2001JD000543, 2002.

Kondo, Y., et al., Uptake of nitric acid on cirrus cloud particles in the upper troposphere and lowermost stratosphere, *Science*, submitted, 2002.

Kondragunta, S., The impact of aerosols on urban photochemical ozone production, Ph.D. thesis, University of Maryland, College Park, Maryland, 1997.

Kopp, G., et al., Evolution of ozone and ozone related species over Kiruna during the THESEO/2000-SOLVE campaign retrieved from ground-based millimeter wave and infrared observations and modeled with KASIMA, *J. Geophys. Res.*, *107*, in press, 2002.

Kraus, A., and A. Hofzumahaus, Field measurements of atmospheric photolysis frequencies for O_3, NO_2, HCHO, CH_3CHO, H_2O_2, and HONO by UV spectroscopy, *J. Atmos. Chem.*, *31*, 161–180, 1998.

Kraus, A., F. Rohrer, and A. Hofzumahaus, Intercomparison of NO_2 photolysis frequency measurements by actinic flux spectroradiometry and chemical actinometry during JCOM97, *Geophys. Res. Lett.*, *27*, 1115–1118, 2000.

Kylling, A., K. Stamnes, and S.-C. Tsay, A reliable and efficient two-stream algorithm for spherical radiative transfer: Documentation of accuracy in realistic layered media, *J. Atmos. Chem.*, *21*, 115–150, 1995.

Lait, L. R., An alternative form for potential vorticity, *J. Atmos. Sci.*, *51*, 1754–1759, 1994.

Lait, L. R., et al., Ozone loss from quasi-conservative coordinate mapping during the 1999–2000 SOLVE/THESEO 2000 campaigns, *J. Geophys. Res.*, *107*(D20), 8274, doi:10.1029/2001JD000998, 2002.

Lantz, K. O., R. E. Shetter, C. A. Cantrell, S. J. Flocke, J. G. Calvert, and S. Madronich, Theoretical, actinometric, and radiometric determinations of the photolysis rate coefficient of NO_2 during the Mauna Loa Observatory Photochemistry Experiment 2, *J. Geophys. Res.*, *101*, 14,613–14,629, 1996.

Leighton, P. A., *Photochemistry of Air Pollution*, Academic Press, New York, 1961.

Levy, H., II, Normal atmosphere: Large radical and formaldehyde concentrations predicted, *Science*, *173*, 141–143, 1971.

Liao, H., Y. L. Yung, and J. H. Seinfeld, Effects of aerosols on tropospheric photolysis rates in clear and cloudy atmospheres, *J. Geophys. Res.*, *104*, 23,697–23,707, 1999.

Liou, K.-N., *An Introduction to Atmospheric Radiation*, Academic Press, San Diego, 1980.

Lloyd, S., W. H. Swartz, T. Kusterer, D. Anderson, C. T. McElroy, C. Midwinter, R. Hall, K. Nassim, D. Jaffe, W. Simpson, J. Kelley, D. Griffin, B. Johnson, R. Evans, D. Quincy, S. Oltmans, P. Newman, R. McPeters, G. Labow, L. Moy, C. Seftor, G. Toon, B. Sen, and J.-F. Blavier, Intercomparison of total ozone observations at Fairbanks, Alaska, during POLARIS, *J. Geophys. Res.*, *104*, 27,767–26,778, 1999.

Lloyd, S. A., Issues in stratospheric ozone depletion, Ph.D. thesis, Harvard University, Cambridge, Massachusetts, 1993.

Los, A., M. van Weele, and P. G. Duynkerke, Actinic fluxes in broken cloud fields, *J. Geophys. Res.*, *102*, 4257–4266, 1997.

Lucke, R. L., et al., The Polar Ozone and Aerosol Measurement (POAM) III instrument and early validation results, *J. Geophys. Res.*, *104*, 18,785–18,799, 1999.

Madronich, S., Intercomparison of NO_2 photodissociation and U. V. radiometer measurements, *Atmos. Environ.*, *21*, 569–578, 1987a.

Madronich, S., Photodissociation in the atmosphere, 1, Actinic flux and the effects of ground reflections and clouds, *J. Geophys. Res.*, *92*, 9740–9752, 1987b.

Madronich, S., UV radiation in the natural and perturbed atmosphere, in *UV-B: Radiation and Ozone Depletion*, edited by M. Tevini, pp. 17–69, Lewis, Boca Raton, 1993.

Madronich, S., and G. Weller, Numerical integration errors in calculated tropospheric photodissociation rate coefficients, *J. Atmos. Chem.*, *10*, 289–300, 1990.

Madronich, S., D. R. Hastie, B. A. Ridley, and H. I. Schiff, Measurement of the photodissociation coefficient of NO_2 in the atmosphere, I, Method and surface measurements, *J. Atmos. Chem.*, *1*, 3–25, 1983.

Malicet, J., D. Daumont, J. Charbonnier, C. Parisse, A. Chakir, and J. Brion, Ozone UV spectroscopy, II, Absorption cross-sections and temperature dependence, *J. Atmos. Chem.*, *15*, 263–273, 1995.

Manney, G. L., and J. L. Sabutis, Development of the polar vortex in the 1999–2000 Arctic winter, *Geophys. Res. Lett.*, *27*, 2589–2592, 2000.

Maric, D., J. P. Burrows, and G. K. Moortgat, A study of the UV-visible absorption spectra of Br_2 and BrCl, *J. Photochem. Photobiol. A: Chem.*, *83*, 179–192, 1994.

Martinez, R. D., A. A. Buitrago, N. W. Howell, C. H. Hearn, and J. A. Joens, The near U. V. absorption spectra of several aliphatic aldehydes and ketones at 300 K, *Atmos. Environ.*, *26A*, 785–792, 1992.

McCormick, M. P., H. M. Steele, P. Hamill, W. P. Chu, and T. J. Swissler, Polar stratospheric cloud sightings by SAM II, *J. Atmos. Sci.*, *39*, 1387–1397, 1982.

McCormick, M. P., J. M. Zawodny, R. E. Veiga, J. C. Larsen, and P. H. Wang, An overview of SAGE I and II ozone measurements, *Planet. Space Sci.*, *37*, 1567–1586, 1989.

McDonald, M. K., D. N. Turnbull, and D. P. Donovan, Steller Brewer, ozonesonde, and DIAL measurements of Arctic O_3 column over Eureka, N.W.T. during 1996 winter/spring, *Geophys. Res. Lett.*, *26*, 2383–2386, 1999.

McElroy, C. T., The determination of stratospheric nitrogen dioxide concentrations from limb brightness measurements made from a balloon platform, Ph.D. thesis, York University, Toronto, Ontario, Canada, 1984.

McElroy, C. T., A spectroradiometer for the measurement of direct and scattered solar irradiance from on-board the NASA ER-2 high-altitude research aircraft, *Geophys. Res. Lett.*, *22*, 1361–1364, 1995.

McElroy, C. T., C. Midwinter, D. V. Barton, and R. B. Hall, A comparison of J-values from the composition and photodissociative flux measurement with model calculations, *Geophys. Res. Lett.*, *22*, 1365–1368, 1995.

McKeen, S. A., et al., The photochemistry of acetone in the upper troposphere: A source of odd-hydrogen radicals, *Geophys. Res. Lett.*, *24*, 3177–3180, 1997.

McKenzie, R., P. Johnston, A. Hofzumahaus, A. Kraus, S. Madronich, C. Cantrell, J. Calvert, and R. Shetter, Relationship between photolysis frequencies derived from spectroscopic measurements of actinic fluxes and irradiance during the IPMMI campaign, *J. Geophys. Res.*, *107*(D5), 4042, doi:10.1029/2001JD000601, 2002.

McPeters, R., et al., Earth Probe Total Ozone Mapping Spectrometer (TOMS) data products user's guide, *Tech. Rep. NASA/TP-1998-206895*, NASA, Goddard Space Flight Center, Greenbelt, Maryland, 1998.

Meier, R. R., D. E. Anderson Jr., and M. Nicolet, Radiation field in the troposphere and stratosphere from 240–1000 nm, I, General analysis, *Planet. Space Sci.*, *30*, 923–933, 1982.

Meier, R. R., G. P. Anderson, C. A. Cantrell, L. A. Hall, J. Lean, K. Minschwaner, R. E. Shetter, E. P. Shettle, and K. Stamnes, Actinic radiation in the terrestrial atmosphere, *J. Atmos. Sol.-Terr. Phys.*, *59*, 2111–2157, 1997.

Mérienne, M. F., A. Jenouvrier, and B. Coquart, The NO_2 absorption spectrum. I. Absorption cross-sections at ambient temperature in the 300–500 nm region, *J. Atmos. Chem.*, *20*, 281–297, 1995.

Michelsen, H. A., R. J. Salawitch, P. O. Wennberg, and J. G. Anderson, Production of $O(^1D)$ from photolysis of O_3, *Geophys. Res. Lett.*, *21*, 2227–2230, 1994.

Mill, J. D., et al., Midcourse Space Experiment: Introduction to the spacecraft, instruments, and scientific objectives, *J. Spacecr. Roc.*, *31*, 900–907, 1994.

Minschwaner, K., R. J. Salawitch, and M. B. McElroy, Absorption of solar radiation by O_2: Implications for O_3 and lifetimes of N_2O, $CFCl_3$, and CF_2Cl_2, *J. Geophys. Res.*, *98*, 10,543–10,561, 1993.

Molina, L. T., and M. J. Molina, Absolute absorption cross sections of ozone in the 185- to 350-nm wavelength range, *J. Geophys. Res.*, *91*, 14,501–14,508, 1986.

Molina, L. T., and M. J. Molina, Production of Cl_2O_2 from the self-reaction of the ClO radical, *J. Phys. Chem.*, *91*, 433–436, 1987.

Molina, M. J., and F. S. Rowland, Stratospheric sink for chlorofluoromethanes: Chlorine atom-catalysed destruction of ozone, *Nature*, *249*, 810–812, 1974.

Müller, M., A. Kraus, and A. Hofzumahaus, $O_3 \rightarrow O(^1D)$ photolysis frequencies determined from spectroradiometric measurements of solar actinic UV-radiation: Comparison with chemical actinometer measurements, *Geophys. Res. Lett.*, *22*, 679–682, 1995.

Müller, R., S. Tilmes, J. Grooß D. S. McKenna, G. C. Toon, R. A. Stachnik, J. J. Margitan, J. W. Elkins, and J. M. Russell III, Chemical ozone loss and chlorine activation deduced from HALOE and OMS measurements in the Arctic winter 1999-2000, *J. Geophys. Res.*, submitted, 2001.

Nack, M. L., and A. E. S. Green, Influence of clouds, haze, and smog on the middle ultraviolet reaching the ground, *Appl. Opt.*, *13*, 2405–2415, 1974.

Nash, E. R., P. A. Newman, J. E. Rosenfield, and M. R. Schoeberl, An objective determination of the polar vortex using Ertel's potential vorticity, *J. Geophys. Res.*, *101*, 9471–9478, 1996.

Neckel, H., and D. Labs, The solar radiation between 3300 and 12500 Å, *Solar Phys.*, *90*, 205–258, 1984.

Newman, P. A., J. F. Gleason, R. D. McPeters, and R. S. Stolarski, Anomalously low ozone over the Arctic, *Geophys. Res. Lett.*, *24*, 2689–2692, 1997.

Newman, P. A., D. W. Fahey, W. H. Brune, M. J. Kurylo, and S. R. Kawa, Photochemistry of Ozone Loss in the Arctic Region in Summer (POLARIS): Preface, *J. Geophys. Res.*, *104*, 26,481–26,495, 1999.

Newman, P. A., et al., An overview of the SOLVE/THESEO 2000 campaign, *J. Geophys. Res.*, *107*(D20), 8259, doi:10.1029/2001JD001303, 2002.

Nicolet, M., R. R. Meier, and D. E. Anderson Jr., Radiation field in the troposphere and stratosphere, II, Numerical analysis, *Planet. Space Sci.*, *30*, 935–983, 1982.

Olson, J., et al., Results from the Intergovernmental Panel on Climate Change Photochemical Model Intercomparison (PhotoComp), *J. Geophys. Res.*, *102*, 5979–5991, 1997.

Parrish, D. D., P. C. Murphy, D. L. Albritton, and F. C. Fehsenfeld, The measurement of the photodissociation rate of NO_2 in the atmosphere, *Atmos. Environ.*, *17*, 1365–1379, 1983.

Paur, R. J., and A. M. Bass, The ultraviolet cross-sections of ozone, II, Results and temperature dependence, in *Atmospheric Ozone: Proceedings of the Quadrennial Ozone Symposium*, edited by C. S. Zerefos and A. M. Ghazi, pp. 611–616, Reidel, Boston, 1985.

Pawson, S., and B. Naujokat, The cold winters of the middle 1990s in the northern lower stratosphere, *J. Geophys. Res.*, *104*, 14,209–14,222, 1999.

Paxton, L. J., C.-I. Meng, D. E. Anderson, and G. J. Romick, MSX—A multiuse space experiment, *Johns Hopkins APL Tech. Dig.*, *17*, 19–34, 1996.

Payan, S., et al., Diurnal and nocturnal distribution of stratospheric NO_2 from solar and stellar occultation measurements in the Arctic vortex: Comparison with models and ILAS satellite measurements, *J. Geophys. Res.*, *104*, 21,585–21,593, 1999.

Peterson, J. T., Dependence of the NO_2 photodissociation rate constant on altitude, *Atmos. Environ.*, *11*, 689–695, 1977.

Piani, C., W. A. Norton, A. M. Iwi, E. A. Ray, and J. W. Elkins, Transport of ozone-depleted air on the breakup of the stratospheric polar vortex in spring/summer 2000, *J. Geophys. Res.*, *107*(D20), 8270, doi:10.1029/2001JD000488, 2002.

Pitari, G., E. Mancici, V. Rizi, and D. T. Shindell, Impact of future climate and emission changes on stratospheric aerosols and ozone, *J. Atmos. Sci.*, *59*, 414–440, 2002.

Poole, L. R., and M. C. Pitts, Polar stratospheric cloud climatology based on Stratospheric Aerosol Measurement II observations from 1978 to 1989, *J. Geophys. Res.*, *99*, 13,083–13,089, 1994.

Popp, P. J., et al., Severe and extensive denitrification in the 1999–2000 Arctic winter stratosphere, *Geophys. Res. Lett.*, *28*, 2875–2878, 2001.

Proffitt, M. H., and R. J. McLaughlin, Fast-response dual-beam UV-absorption ozone photometer suitable for use on stratospheric balloons, *Rev. Sci. Inst.*, *54*, 1719–1728, 1983.

Ramaswamy, V., et al., Stratospheric temperature trends: Observations and model simulations, *Rev. Geophys.*, *39*, 71–122, 2001.

Randall, C. E., J. D. Lumpe, R. M. Bevilacqua, K. W. Hoppel, M. D. Fromm, R. J. Salawitch, W. H. Swartz, S. A. Lloyd, E. Kyro, P. von der Gathen, H. Claude, J. Davies, H. DeBacker, H. Dier, M. J. Molyneux, and J. Sancho, Reconstruction of three-dimensional ozone fields using POAM III during SOLVE, *J. Geophys. Res.*, *107*(D20), 8299, doi:10.1029/2001JD000471, 2002.

Renard, J.-B., M. Pirre, C. Robert, G. Moreau, D. Huguenin, and J. M. Russell III, Nocturnal vertical distribution of stratospheric O_3, NO_2, and NO_3 from balloon measurements, *J. Geophys. Res.*, *101*, 28,793–28,804, 1996.

Rex, M., et al., Chemical depletion of Arctic ozone in winter 1999/2000, *J. Geophys. Res.*, *107*(D20), 8276, doi:10.1029/2001JD000533, 2002.

Rhoads, K. P., P. Kelley, R. R. Dickerson, T. P. Carsey, M. Farmer, D. L. Savoie, and J. M. Prospero, Composition of the troposphere over the Indian Ocean during the monsoonal transition, *J. Geophys. Res.*, *102*, 18,981–18,995, 1997.

Richard, E. C., et al., Severe chemical ozone loss inside the Arctic polar vortex during Winter 1999-2000 inferred from *in situ* airborne measurements, *Geophys. Res. Lett.*, *28*, 2197–2200, 2001.

Ritter, J. A., D. H. Stedman, and T. J. Kelley, Ground-level measurements of nitric oxide, nitrogen dioxide and ozone in rural air, in *Nitrogenous Air Pollutants: Chemical and Biological Implications*, edited by D. Grosjean, pp. 325–343, Ann Arbor Science, Ann Arbor, 1979.

Ritter, J. A., D. H. Stedman, R. R. Dickerson, and T. E. Blackburn, Dependence of $j[O_3–O(^1D)]$ on the choice of extraterrestrial solar irradiance data, *Environ. Sci. Technol.*, *21*, 505–508, 1987.

Robinson, A., et al., Ozone loss derived from balloon-borne tracer measurements and the SLIMCAT CTM, *J. Geophys. Res.*, submitted, 2001.

Roscoe, H. K., R. A. Freshwater, R. Wolfenden, R. L. Jones, D. J. Fish, J. E. Harries, A. M. South, and D. J. Oldham, Using stars for remote-sensing of the Earth's stratosphere, *Appl. Opt.*, *33*, 7126–7131, 1994.

Roscoe, H. K., W. H. Taylor, J. D. Evans, A. M. Tait, R. Freshwater, D. Fish, E. K. Strong, and R. L. Jones, Automated ground-based star-pointing UV-visible spectrometer for stratospheric measurements, *Appl. Opt.*, *36*, 6069–6075, 1997.

Rosenfield, J. E., D. B. Considine, P. E. Meade, J. T. Bacmeister, C. H. Jackman, and M. R. Schoeberl, Stratospheric effects of Mount Pinatubo aerosol studied with a coupled two-dimensional model, *J. Geophys. Res.*, *102*, 3649–3670, 1997.

Ruggaber, A., R. Forkel, and R. Dlugi, Spectral actinic flux and its ratio to spectral irradiance by radiation transfer calculations, *J. Geophys. Res.*, *98*, 1151–1162, 1993.

Russell, J. M., III, et al., The Halogen Occultation Experiment, *J. Geophys. Res.*, *98*, 10,777–10,797, 1993.

Ryerson, T. B., L. G. Huey, K. Knapp, J. A. Neuman, D. D. Parrish, D. T. Sueper, and F. C. Fehsenfeld, Design and initial characterization of an inlet for gas-phase NO_y measurements from aircraft, *J. Geophys. Res.*, *104*, 5483–5492, 1999.

Salawitch, R. J., et al., The distribution of hydrogen, nitrogen, and chlorine radicals in the lower stratosphere: Implications for changes in O_3 due to emission of NO_y from supersonic aircraft, *Geophys. Res. Lett.*, *21*, 2547–2550, 1994.

Salawitch, R. J., et al., Chemical loss of ozone during the Arctic winter of 1999/2000: An analysis based on balloon-borne observations, *J. Geophys. Res.*, *107*(D20), 8269, doi:10.1029/2001JD000620, 2002.

Sander, S. P., et al., Chemical kinetics and photochemical data for use in stratospheric modeling, *Tech. Rep. JPL Publication 00-3*, Jet Propulsion Laboratory, California Institute of Technology, Pasadena, California, 2000.

Santee, M. L., G. L. Manney, N. J. Livesey, and J. W. Waters, UARS Microwave Limb Sounder observations of denitrification and ozone loss in the 2000 Arctic late winter, *Geophys. Res. Lett.*, *27*, 3213–3216, 2000.

Schneider, W., G. K. Moortgat, G. S. Tyndall, and J. P. Burrows, Absorption cross-sections of NO_2 in the UV and visible region (200–700 nm) at 298 K, *J. Photochem. Photobiol. A: Chem.*, *40*, 195–217, 1987.

Schoeberl, M. R., and P. A. Newman, A multiple-level trajectory analysis of vortex filaments, *J. Geophys. Res.*, *100*, 25,801–25,815, 1995.

Schoeberl, M. R., L. R. Lait, P. A. Newman, and J. E. Rosenfield, The structure of the polar vortex, *J. Geophys. Res.*, *97*, 7859–7882, 1992.

Schoeberl, M. R., et al., An assessment of the ozone loss during the 1999–2000 SOLVE/THESEO 2000 Arctic campaign, *J. Geophys. Res.*, *107*(D20), 8261, doi:10.1029/2001JD000412, 2002.

Seinfeld, J. H., and S. N. Pandis, *Atmospheric Chemistry and Physics: From Air Pollution to Climate Change*, Wiley, New York, 1998.

Shetter, R. E., and M. Müller, Photolysis frequency measurements using actinic flux spectroradiometry during the PEM-Tropics mission: Instrumentation description and some results, *J. Geophys. Res.*, *104*, 5647–5661, 1999.

Shetter, R. E., A. H. McDaniel, C. A. Cantrell, S. Madronich, and J. G. Calvert, Actinometer and eppley radiometer measurements of the NO_2 photolysis rate coefficient during the Mauna Loa Observatory Photochemistry Experiment, *J. Geophys. Res.*, *97*, 10,349–10,359, 1992.

Shetter, R. E., et al., Actinometric and radiometric measurement and modeling of the photolysis rate coefficient of ozone to $O(^1D)$ during Mauna Loa Observatory Photochemistry Experiment 2, *J. Geophys. Res.*, *101*, 14,631–14,641, 1996.

Shetter, R. E., W. Junkermann, W. H. Swartz, G. J. Frost, J. H. Crawford, B. L. Lefer, J. D. Barrick, S. R. Hall, A. Hofzumahaus, A. Bais, J. G. Calvert, C. A. Cantrell, S. Madronich, M. Müller, A. Kraus, P. S. Monks, G. D. Edwards, R. McKenzie, P. Johnston, R. Schmitt, E. Griffioen, M. Krol, A. Kylling, R. R. Dickerson, S. A. Lloyd, T. Martin, B. Gardiner, B. Mayer, G. Pfister, E. P. Röth, P. Koepke, A. Ruggaber, H. Schwander, and M. van Weele, Photolysis frequency of NO_2: Measurement and modeling during the International Photolysis Frequency Measurement and Modeling Intercomparison (IPMMI), *J. Geophys. Res.*, submitted, 2002.

Shifrin, K. S., Simple relationship for the Ångström parameter of disperse systems, *Appl. Opt.*, *34*, 4480–4485, 1995.

Shindell, D. T., D. Rind, and P. Lonergan, Increased polar stratospheric ozone losses and delayed eventual recovery owing to increased greenhouse-gas concentrations, *Nature*, *392*, 589–592, 1998.

Sinnhuber, B.-M., et al., Large loss of total ozone during the Arctic winter of 1999/2000, *Geophys. Res. Lett.*, *27*, 3473–3476, 2000.

Solomon, S., Stratospheric ozone depletion: A review of concepts and history, *Rev. Geophys.*, *37*, 275–316, 1999.

Solomon, S., R. R. Garcia, F. S. Rowland, and D. J. Wuebbles, On the depletion of Antarctic ozone, *Nature*, *321*, 755–758, 1986.

Stamnes, K., S.-C. Tsay, W. Wiscombe, and K. Jayaweera, Numerically stable algorithm for discrete-ordinate-method radiative transfer in multiple scattering and emitting layered media, *Appl. Opt.*, *27*, 2502–2509, 1988.

Stedman, D. H., and H. Niki, Photolysis of NO_2 in air as measurement method for light intensity, *Environ. Sci. Technol.*, *7*, 735–739, 1973.

Stimpfle, R. M., et al., The coupling of $ClONO_2$, ClO, and NO_2 in the lower stratosphere from in situ observations using the NASA ER-2 aircraft, *J. Geophys. Res.*, *104*, 26,705–26,714, 1999.

Stockwell, W. R., P. Middleton, J. S. Chang, and X. Tang, The second generation Regional Acid Deposition Model: Chemical mechanism for regional air quality modeling, *J. Geophys. Res.*, *95*, 16,343–16,367, 1990.

Stolarski, R. S., and R. J. Cicerone, Stratospheric chlorine: A possible sink for ozone, *Can. J. Chem.*, *52*, 1610–1615, 1974.

Stolarski, R. S., A. J. Krueger, M. R. Schoeberl, R. D. McPeters, P. A. Newman, and J. C. Alpert, Nimbus 7 satellite measurements of the springtime Antarctic ozone decrease, *Nature*, *322*, 808–811, 1986.

Swartz, W. H., and P. A. Newman, SOLVE flight base analysis, *SRA-R98-002*, Applied Physics Laboratory, The Johns Hopkins University Applied Physics Laboratory, Laurel, Maryland, 1998.

Swartz, W. H., S. A. Lloyd, T. L. Kusterer, D. E. Anderson, C. T. McElroy, and C. Midwinter, A sensitivity study of photolysis rate coefficients during POLARIS, *J. Geophys. Res.*, *104*, 26,725–26,735, 1999.

Swartz, W. H., J.-H. Yee, R. J. Vervack, Jr., S. A. Lloyd, and P. A. Newman, Photochemical ozone loss in the Arctic as determined by MSX/UVISI stellar occultation observations during the 1999/2000 winter, *J. Geophys. Res.*, *107*(D20), 8296, doi:10.1029/2001JD000933, 2002.

Swinbank, R., and A. O'Neill, A stratosphere–troposphere data assimilation system, *Mon. Wea. Rev.*, *122*, 686–702, 1994.

Talukdar, R. K., J. B. Burkholder, M. Hunter, M. K. Gilles, J. M. Roberts, and A. R. Ravishankara, Atmospheric fate of several alkyl nitrates, 2, UV absorption cross-sections and photodissociation quantum yields, *J. Chem. Soc., Faraday Trans.*, *93*, 2797–2805, 1997.

Talukdar, R. K., C. A. Longfellow, M. K. Gilles, and A. R. Ravishankara, Quantum yields of $O(^1D)$ in the photolysis of ozone between 289 and 329 nm as a function of temperature, *Geophys. Res. Lett.*, *25*, 143–146, 1998.

Thompson, A. M., The effect of clouds on photolysis rates and ozone formation in the unpolluted troposphere, *J. Geophys. Res.*, *89*, 1341–1349, 1984.

Thompson, A. M., The oxidizing capacity of the Earth's atmosphere: Probable past and future changes, *Science*, *256*, 1157–1165, 1992.

Tie, X., G. P. Brasseur, B. Briegleb, and C. Grainer, Two-dimensional simulation of Pinatubo aerosol and its effect on stratospheric ozone, *J. Geophys. Res.*, *99*, 20,545–20,562, 1994.

Torres, O., Z. Ahmad, and J. R. Herman, Optical effects of polar stratospheric clouds on the retrieval of TOMS total ozone, *J. Geophys. Res.*, *97*, 13,105–13,024, 1992.

Tsay, S.-C., and K. Stamnes, Ultraviolet radiation in the Arctic: The impact of potential ozone depletions and cloud effects, *J. Geophys. Res.*, *97*, 7829–7840, 1992.

van Weele, M., et al., From model intercomparison toward benchmark UV spectra for six real atmospheric cases, *J. Geophys. Res.*, *105*, 4915–4925, 2000.

Vervack, R. J., Jr., J.-H. Yee, J. F. Carbary, and F. Morgan, Atmospheric remote sensing using a combined extinctive and refractive stellar occultation technique, 3, Inversion method for refraction measurements, *J. Geophys. Res.*, *107*(D15), 4061, doi:10.1029/2001JD000796, 2002.

Volz-Thomas, A., A. Lerner, H.-W. Pätz, M. Schultz, D. S. McKenna, R. Schmitt, S. Madronich, and E. P. Röth, Airborne measurements of the photolysis frequency of NO_2, *J. Geophys. Res.*, *11*, 18,613–18,627, 1996.

Vömel, H., D. W. Toohey, T. Deshler, and C. Kröger, Sunset observations of ClO in the Arctic polar vortex and implications for ozone loss, *Geophys. Res. Lett.*, *28*, 4183–4186, 2001.

Wallace, J. M., and P. V. Hobbs, *Atmospheric Science: An Introductory Survey*, Academic Press, San Diego, 1977.

Ware, R., et al., GPS sounding of the atmosphere from low Earth orbit: Preliminary results, *Bull. Amer. Meteor. Soc.*, *77*, 19–40, 1996.

Weihs, P., and A. R. Webb, Accuracy of spectral UV model calculations, 1, Consideration of uncertainties in input parameters, *J. Geophys. Res.*, *102*, 1541–1550, 1997.

Wennberg, P. O., R. J. Salawitch, D. J. Donaldson, T. F. Hanisco, E. J. Lanzendorf, K. K. Perkins, S. A. Lloyd, V. Vaida, R. S. Gao, E. J. Hinsta, R. C. Cohen, W. H. Swartz, T. L. Kusterer, and D. E. Anderson, Twilight observations suggest unknown sources of HO_x, *Geophys. Res. Lett.*, *26*, 1373–1376, 1999.

Wild, O., X. Zhu, and M. J. Prather, Fast-J: Accurate simulation of in- and below-cloud photolysis in tropospheric chemical models, *J. Atmos. Chem.*, *37*, 245–282, 2000.

WMO, Atmospheric ozone 1985, *Tech. Rep. World Meteorological Organization Global Ozone Research and Monitoring Project Report No. 16*, WMO, Geneva, 1986.

Wofsy, S. C., M. B. McElroy, and Y. L. Yung, The chemistry of atmospheric bromine, *Geophys. Res. Lett.*, *2*, 215–218, 1975.

Woods, T. N., et al., Validation of the UARS solar ultraviolet irradiances: Comparison with ATLAS 1 and 2 measurements, *J. Geophys. Res.*, *101*, 9541–9469, 1996.

Yee, J.-H., et al., Atmospheric remote sensing using a combined extinctive and refractive stellar occultation technique, 1, Overview and proof-of-concept observations, *J. Geophys. Res.*, *107*(D14), 4213, doi:10.1029/2001JD000794, 2002.

Zafonte, L., P. L. Rieger, and J. R. Holmes, Nitrogen dioxide photolysis in the Los Angeles atmosphere, *Environ. Sci. Technol.*, *11*, 483–487, 1977.